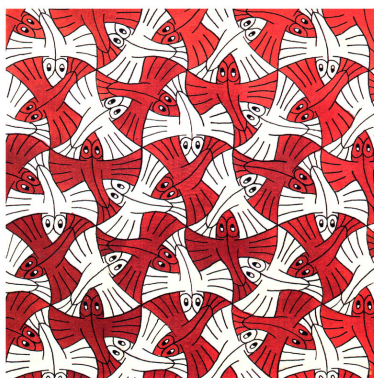




**SAPIENZA**  
UNIVERSITÀ DI ROMA

DOTTORATO DI RICERCA IN BIOCHIMICA  
CICLO XXIX (A.A. 2013-2016)

***Biostructural studies on PPAR  
nuclear receptors***



**Dottorando**  
Davide Capelli

**Docente guida**  
Prof.ssa Roberta Chiaraluce

**Coordinatore**  
Prof. Francesco Malatesta

**Correlatore**  
Dott. Giorgio Pochetti

**Gennaio 2017**



# Ringraziamenti

La ricerca delle parole più adatte per ringraziare tutti coloro che mi hanno accompagnato lungo questo percorso è emozionante e richiede grande impegno, segno che molte sono le persone che hanno contribuito al raggiungimento di questo obiettivo.

Innanzitutto, ringrazio la Prof.ssa Roberta Chiaraluce dell'Università degli Studi di Roma "La Sapienza" per avermi offerto l'opportunità di svolgere il dottorato sotto la sua esperta guida, nonché tutte le persone del suo staff, in particolare il Prof. Valerio Consalvi e la Dott.ssa Clorinda Lori per la competenza, la gentilezza e la disponibilità che hanno sempre dimostrato nei miei confronti.

Ringrazio il Prof. Francesco Malatesta, coordinatore del Dottorato di Ricerca in Biochimica, per avermi trasmesso quell'entusiasmo e quella curiosità che ogni uomo di scienza dovrebbe possedere e divulgare.

Un ringraziamento speciale è dedicato al Dott. Giorgio Pochetti, correlatore di questa tesi, e alla Dott.ssa Roberta Montanari dell'Istituto di Cristallografia del CNR, dove ho svolto gran parte del lavoro raccontato in questa tesi e non solo. Senza di loro non avrei mai raggiunto i traguardi finora ottenuti e, per questo motivo, il mio obiettivo è di poter ricambiare quanto prima la fiducia e la stima che da sempre ripongono nei miei confronti, in ogni caso consapevole di rimanere per sempre in debito.

Un ringraziamento sincero va anche a tutti i colleghi dell'Istituto di Cristallografia del CNR, sempre presenti e coinvolti in tutti gli aspetti della mia vita professionale e privata.

Infine ringrazio gli amici più cari, compagni fedeli di tante avventure, e la mia famiglia nella sua interezza, esempio massimo di armonia e di amore.

A Marta e a nostro figlio Valerio è dedicato questo lavoro e, più in generale, a loro è dedicata tutta la mia vita.

*A Marta e Valerio*



# Table of contents

Abstract.....	I
<b>1 Introduction.....</b>	<b>1</b>
1.1 Nuclear receptors.....	1
1.1.1 DNA Binding Domain and Ligand Binding Domain .....	3
1.1.2 Co-activators and co-repressors .....	7
1.1.3 The role of NRs in the activation and repression of transcription.....	9
1.1.4 Ligand-Receptor interaction.....	11
1.2 Peroxisome Proliferator-Activated Receptors (PPARs).....	13
1.2.1 PPARs structure and function .....	15
1.2.2 The ligand binding domain.....	16
1.2.3 The role of the AF-2 helix H12 .....	20
1.2.4 The role of the helix H3 and the $\beta$ -sheet.....	22
1.2.5 Binding to co-regulators.....	23
1.2.6 Heterodimer formation with RXR.....	26
1.2.7 Non-genomic actions .....	30
1.2.8 Regulation by post-translational modifications (PTM) .....	32
1.2.9 Drugs and active compounds on PPARs .....	35
1.2.10 Novel active PPAR ligands .....	38
1.2.11 Selective PPAR Modulators (SPPARMs) .....	42
1.2.12 PPAR antagonists.....	43
1.3 Structure-based drug discovery .....	45
<b>2 Aim of the study.....</b>	<b>51</b>
<b>3 Experimental methods.....</b>	<b>53</b>
3.1 Expression and purification of PPARs LBD.....	53

3.2	Crystallization , data collection and structure determination ...	55
3.3	Isothermal titration calorimetry (ITC) .....	62
3.4	Surface plasmon resonance (SPR) .....	63
<b>4</b>	<b>Results and discussion</b> .....	<b>65</b>
4.1	The pan agonist AL29-26.....	65
4.1.1	Crystallization and structure determination of the complexes PPAR $\alpha$ -LBD/AL29-26 and PPAR $\gamma$ -LBD/AL29-26.....	67
4.1.2	PPAR $\gamma$ -LBD/AL29-26 structure: new position of the carboxylate in the region of partial agonists .....	69
4.1.3	PPAR $\alpha$ -LBD/AL29-26 structure: ligand occupation of a new pocket. ....	72
4.1.4	Specificity of the new cavity: a steric clash with S289 prevents AL29-26 to occupy the diphenyl pocket of PPAR $\gamma$ -LBD determining its partial agonist properties .....	77
4.2	Saponins and sapogenins as potential PPAR $\gamma$ agonists.....	80
4.2.1	Fast screening of saponins and sapogenins from <i>Medicago</i> species by SPR.....	81
4.2.2	Toxicity and transcriptional activity on the most affine compounds .....	87
4.2.3	Crystal structure of the PPAR $\gamma$ -LBD/caulophyllogenin complex.....	90
4.2.4	Isothermal titration calorimetry (ITC) assay: comparison between caulophyllogenin and the fatty acid 13-( <i>S</i> )-HODE.....	93
4.3	The metabolically active form of Metaglidasen .....	95
4.3.1	PPAR activity .....	96
4.3.2	Crystal structure of ( <i>R</i> )- and ( <i>S</i> )-halofenic acid in the PPAR $\gamma$ - LBD.....	100



4.4	Transactivation deficiency of the PPAR $\gamma$ F360L mutant associated with familial partial lipodystrophy.....	107
4.4.1	Overall structure of PPAR $\gamma$ -LBD F360L and conformational changes induced by the mutation.....	108
4.4.2	Ligand interactions.....	114
4.4.3	Crystal structure of the complex between PPAR $\gamma$ -LBD R357A and rosiglitazone.....	117
4.4.4	The co-activator SRC-1 has a lower binding affinity for the mutants.....	120
4.5	Resveratrol and its metabolites.....	122
4.5.1	Binding affinity of resveratrol towards PPARs LBD.....	123
4.5.2	Crystal structure of PPAR $\gamma$ -LBD/resveratrol complex.....	126
4.5.3	Antagonistic activity of resveratrol.....	129
4.6	Betulinic acid: a PPAR $\gamma$ antagonist.....	133
4.6.1	Crystal structure of PPAR $\gamma$ -LBD in complex with betulinic acid: two molecules of the ligand bind the LBD simultaneously....	134
4.6.2	Sub-optimal stabilization of helices 11 and 12.....	136
4.6.3	Comparison with the antagonist SR1664 and the agonist SR1663: the F282/F363 switch mechanism.....	139
<b>5</b>	<b>Summary and conclusions.....</b>	<b>144</b>
	<b>References.....</b>	<b>149</b>
	<b>Appendix.....</b>	<b>181</b>



## Abstract

The peroxisome proliferator-activated receptors (PPARs) represent a family of nuclear receptors that function as ligand-activated transcription factors, regulating genes involved in cell differentiation and various metabolic processes, especially lipid and glucose homeostasis. The PPAR family comprises three isoforms: PPAR $\alpha$ , PPAR $\beta/\delta$  and PPAR $\gamma$ , with different tissue distribution, ligand specificity and physiological role. Because of their wide range of actions on glucose homeostasis, lipid metabolism and vascular inflammation, PPARs represent promising targets for the development of new drugs for the treatment of metabolic disorders such as type 2 diabetes mellitus (T2DM), dyslipidemia and atherosclerosis. Among all the subtypes, despite the undesirable side effects associated to the drug treatment, PPAR $\gamma$  is still the most widely studied for its crucial role in the complex cross-talk between metabolically active tissues essential for energy balance. Then, new combination strategies using dual or pan agonists, as well as selective modulators, are currently in development.

This study is aimed to understand in deep the dynamic personality of the nuclear receptors PPAR in complex with both natural and synthetic ligands that, interacting with different regions of the LBD, confer a differentiated biological response in cellular and animal models. PPARs could be then described as a ‘functionally pluripotent’ proteins being their activity mediated by ligands that, causing the functional site to adopt an active/inactive conformations, activate different structural and biological pathways depending on the co-activator/co-repressor recruited.

Through a structural approach we propose to get more insights on how the biological response is variably affected by ligands depending on their binding mode and even the mutation of a single residue responsible for

a structural destabilization of the LBD could be associated to rare genetic disorder.

The understanding of such a mechanism required the use of more than one biophysical technology. X-ray diffraction was used as the main approach to investigate the binding mode of the selected ligands. In addition, the binding has been also characterized using other biophysical techniques such as Isothermal Titration Calorimetry (ITC) and Surface Plasmon Resonance (SPR) to obtain thermodynamic and kinetic parameters of the binding.





# 1. Introduction

## 1.1 Nuclear receptors

Nuclear receptors (NRs) are a large superfamily of transcription factors involved in important physiological functions such as control of embryonic development, organ physiology, cell differentiation and homeostasis [1–3]. Apart from the normal physiology, nuclear receptors have been identified to play a role in many pathological processes, such as cancer, diabetes, rheumatoid arthritis, asthma or hormone-resistance syndromes [4, 5]. Therefore, despite their already long history, these transcriptional regulators are still of great interest in modern biomedical research and drug discovery.

Nuclear receptors are soluble proteins that can bind to specific DNA-regulatory elements and act as cell-type and promoter-specific regulators of transcription [6]. In contrast to other transcription factors, the activity of nuclear receptors can be modulated by binding to the corresponding ligands – small lipophilic molecules that easily penetrate biological membranes. Natural ligands already known include steroid and thyroid hormones, retinoic acid, oxysterols, vitamins and eicosanoids.

The receptors are commonly categorized into seven subfamilies based on sequence homology [7], but they can also be classified into three subgroups based on characteristics of ligand binding. These subgroups include classic hormone receptors, sensor or metabolic receptors and orphan receptors. The classic hormone receptors include the glucocorticoid, estrogen, thyroid, retinoic acid and vitamin D receptors. In general, these receptors bind specific, endogenous ligands with high affinity. Peroxisome proliferator-activated receptors (PPARs), liver X receptor (LXR), farnesol X

receptor (FXR), liver receptor homolog-1 (LRH-1) and retinoid X receptor (RXR) belong to the subgroup known as the sensor receptors. As a result of their role in maintaining glucose and lipid homeostasis, these receptors are also known as ‘metabolic’ nuclear receptors. In contrast to the classic and orphan receptors, the sensor/metabolic receptors bind with lower affinity to a broad range of physiological ligands encompassing compounds from dietary origin. Ligands have not been identified to date for some receptors, thus they are referred to as orphans.

Nuclear receptors share a common structure composed of five conserved regions or domains (A/B – F): the N-terminal A/B domain, a medial DNA-binding domain (DBD), a hinge region (D), the ligand-binding domain (LDB) and the C-terminal domain (F) as shown in Figure 1 [8]. The N-terminal A/B domain is the least conserved among members of the superfamily, with the length of this region varying significantly between receptors. The A/B region contains a weak ligand-independent transcriptional activation function-1 (AF-1) and is often a site for post-translational modification that can dramatically affect receptor activity. In contrast, the C region is the most highly conserved and contains the DBD with its two zinc finger motifs, the hallmark characteristic of nuclear receptors. The D region functions as a hinge, allowing the more conserved and structured C and E domains to swivel slightly to accommodate multiple conformations. Region E contains the LBD. The ligand-dependent activation function-2 (AF-2) and the receptor dimerization interface are embedded within this region. Binding of ligands to the receptor induces a conformational change within the LBD that initiates a series of events within the receptor resulting in transcriptional activation of specific target genes.

The functions of nuclear receptors can also be modulated by post-translational modifications that include phosphorylation, ubiquitylation, and



sumoylation. Phosphorylation can activate some nuclear receptors independently of ligand binding and function as the major mechanism regulating activities of orphan receptors. Receptor ubiquitylation can occur in response to ligand binding and may contribute to termination of hormonal signaling. sumoylation typically reduces the activation function of nuclear receptors and/or promotes repressor activity [9].

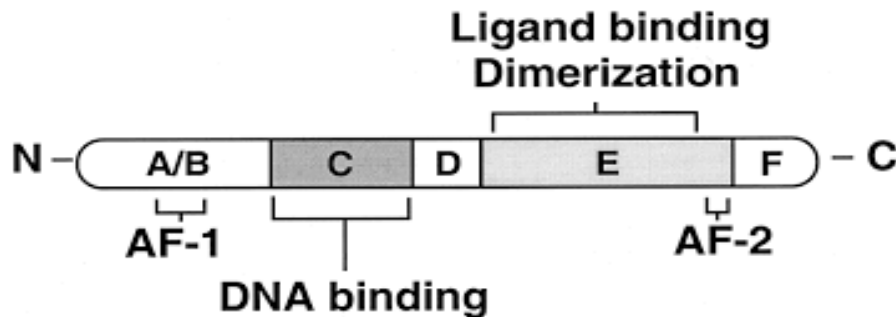


**Figure 1.** The five conserved domains (A/B – F) that compose the protein structure for nearly all members of the nuclear hormone receptor superfamily.

### 1.1.1 DNA Binding Domain and Ligand Binding Domain

The C region containing the DBD is the most well conserved region; through this domain, nuclear receptors bind to specific DNA sequences, called hormone response elements (HREs), within the regulatory region(s) of target genes. DBD consists of a highly conserved 66-residue core made up of two typical cysteine-rich zinc finger motifs, two  $\alpha$  helices, and a COOH extension. It includes several sequence elements, referred to as P, D, T, and A boxes, that have been shown to define or contribute to the response element specificity, to a dimerization interface within the DBDs, and to contacts with the DNA backbone and residues flanking the DNA core recognition sequence [10] (Figure 2). The DBD is also the target of post-translational

modifications. Furthermore, it is involved in nuclear localization and functions in interactions with transcription factors and co-activators.

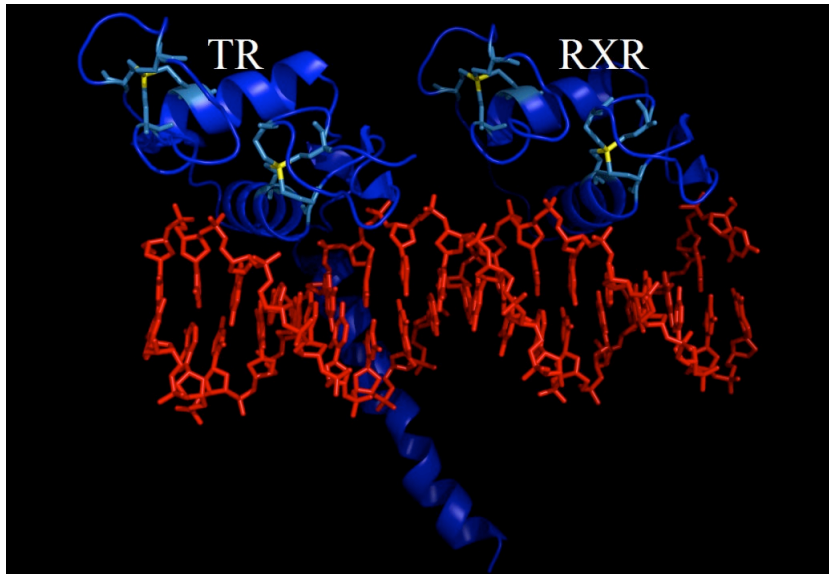


**Figure 2.** Heterodimer of thyroid receptor (TR) and RXR DBDs (PDB ID: 2NLL). Zinc ions are depicted in yellow, DNA in red.

Several *in vitro* studies have shown that the LBD, which is less conserved than the DBD, is functionally complex as it mediates ligand binding and dimerization and contains a ligand-dependent transactivation function. The LBD consists of 250 residues and contains four structurally distinct but functionally linked surfaces: 1) a dimerization surface, which mediates interaction with partner LBDs, 2) the ligand-binding pocket (LBP), which interacts with diverse lipophilic small molecules in the case of liganded NRs, 3) a co-regulator binding surface, which binds to regulatory protein complexes that modulate positively or negatively transcriptional activity, and 4) an activation function helix, termed AF-2, which mediates ligand-dependent transactivation. Within the AF-2, the integrity of a conserved amphipathic  $\alpha$ -helix called AF-2 activation domain has been

shown to be required for ligand-dependent transactivation and co-activator recruitment. Moreover, some NRs can also interact with transcriptional co-repressors through their LBD [11].

The first resolution of a NR LBD crystal structure, the unliganded RXR $\alpha$ , revealed that this domain is highly structured [12]. This crystal structure, together with the elucidation of the 3D structures of multiple other NR LBDs, showed a common fold comprising 12  $\alpha$  helices (H) and a short  $\beta$ -turn (Figure 3A), arranged in three layers to form an antiparallel ' $\alpha$ -helical sandwich'. Note that some variability exists; for example, no helix H2 was found in RAR $\gamma$  [13], while an additional short helix H2' is present in PPAR $\gamma$  [14]. Helices 1 through 3 constitute one face of the LBD. H4, H5,  $\beta$ -turn, H8, and H9 correspond to the central layer of the domain and H6, H7, and H10 form the second face. The superposition of all available LBD structures reveals a clear overall similarity, particularly in the top half of the LBD, that includes H1, H4, H5, and H7 through H10 and corresponds to a structurally rather invariable region. The lower part of the LBD harbors a variable region, which contains the LBP.

Structural and functional studies of the LBD of NRs revealed that the dynamics of their C-terminal helix (H12, also termed AF-2) is fundamental for NR activity. Together the various apo- and holo-LBD structures suggest a common mousetrap-like mechanism by which AF-2 becomes competent to activate transcription: upon ligand binding, H11 is repositioned in the continuity of H10, and the concomitant swinging of H12 unleashes the  $\Omega$ -loop (between H2 and H3) which flips over underneath H6, carrying along the amino-terminal part of H3 (Figure 3B). In its final position, H12 seals as a 'lid' the ligand-binding cavity and further stabilizes ligand binding (in some but not all NRs) by contributing to additional ligand-protein interactions. The transconformation of H12, together with additional structural changes (such

as bending of helix H3), brings it into a distinct receptor environment, thus creating the surface(s) which allow binding of co-activators and thereby generates the transcriptional activity of the AF-2 domain. In the absence of ligand some NRs recruit a complex of opposite functionality, composed of co-repressors or silencing mediator, which is responsible for the gene silencing ability of some NRs [15]. Furthermore, many receptors are able to promote transcription even in the absence of ligand, suggesting that the structures of LBDs mediating each functional response persist in a dynamic equilibrium, which exists independently but is affected by ligand binding [16].

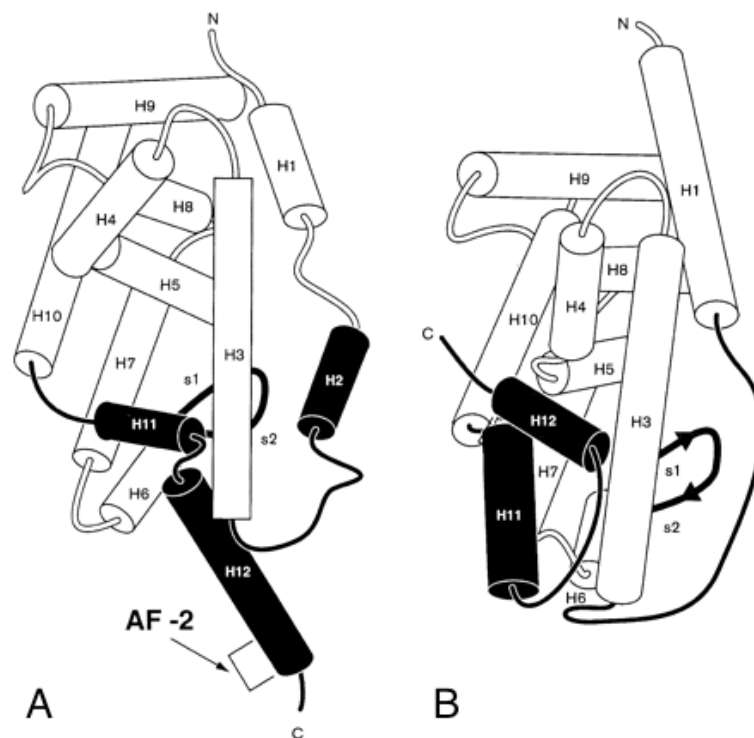


**Figure 3.** A) apo-RXR $\alpha$  structure with helix 12 in the inactive conformation. B) holo-RXR $\alpha$  structure showing the helix 12 in the active conformation, according to the mousetrap model.

### 1.1.2 Co-activators and co-repressors

The first step of nuclear receptor activation is initiated by ligand binding, and thus the ligand binding pocket is an important structural feature of nuclear receptors. The second step of nuclear receptor activation is ligand-induced recruitment of co-activator complexes, which contain chromatin-modifying enzymes required for transcription.

Nuclear co-activators such as steroid receptor co-activator 1 (SRC-1, also known as NCoA1) contain multiple LXXLL motifs (where X is any amino acid and L is leucine in single-letter code for amino acids) that interact with LBDs. X-ray structures of various LBDs bound to agonists and peptides with LXXLL motifs reveal a conserved mode of co-activator binding [15]. The LXXLL co-activator motif adopts a two-turn  $\alpha$  helix with its three-leucine side chains fitting into the hydrophobic pocket between two charged residues - the so-called charge clamp - which further stabilize the co-activator helix by capping both helical ends. The high degree of amino acid sequence conservation in the co-activator binding pocket (Figure 4) suggests that this mode of co-activator binding represents a general mechanism for the activation of nuclear receptors. In addition, nuclear receptors can achieve specific recognition of co-activators by interacting with the variable residues within or flanking the LXXLL motifs.

On the other hand, the position of the AF-2 helix also plays a key role in recruiting co-repressors such as nuclear receptor co-repressor 1 (NCoR1) and silencing mediator for retinoid and thyroid hormone receptors (SMRT, also known as NCoR2). These nuclear co-repressors bind to LBDs via a conserved LXXXIXXXL/I motif, which is similar to the LXXLL co-activator motif but has an N-terminal extension. In comparison to co-activators, the longer co-repressor motif adopts a three-turn  $\alpha$  helix instead of two turns for

the co-activator motif, and binds to the same overlapped site as for the LXXLL helix. The additional turn of the co-repressor helix extends into space that would normally be occupied by the AF-2 helix when it is in the active conformation. Thus the binding of co-repressors and the active AF-2 conformation is mutually exclusive: the AF-2 helix must shift to some alternative position to accommodate the larger co-repressor helix. The binding mode of co-repressors, similar to that of co-activators, is also highly conserved among nuclear receptors. It seems clear that binding of co-activators and co-repressors is tightly modulated by the position of the AF-2 helix. The conformational flexibility of this helix allows it to sense the presence of the bound ligand, either an agonist or an antagonist, and to recruit the co-activators or co-repressors that ultimately determine the transcriptional output of nuclear receptors [17, 18].

		Helix-3	3'	Helix-4	Helix-5	AF-2
NGFIB	410	YDLLSGSLDVIRKWA	EKIPGFI	ELCPGDQD	LLLES	SAFLELFILR...
DHR38	360	YQLLTSSVDVIKQFA	EKIPGYFD	LLPEDQEL	LFQSASLE	LFVLR...
LRH-1	365	CKMADQTLFSIV	EWARSSIF	FR	ELKVDDQ	MKLLQNCWSELLILD...
GR	564	NMLGGRQVIAAVK	WAKAIPGFR	NLHLDDQ	M	TLLQYSWMFLMAFA...
PPAR $\alpha$	277	QCTSVETVTE	TEFAKAI	PGFANL	DLNDQV	TLLKYGVEAIFAM...
RXR $\alpha$	269	CQAADKQLFTL	EWAKRIP	HFSE	ELPLDDQ	VILLRAGWNELLIAS...
ER $\alpha$	347	TNLADREL	VHMINWAK	RVPGFV	DLTLHDQ	VHLLCAWLEIILMIG...
PXR	244	ADMSTYMF	KGIISFA	KVISYFR	DLPIEDQ	ISLLKGAAFELCQLR...
RAR $\gamma$	231	SELATKCI	IKIVEFA	KRLPGF	TGLSIAD	QITLLKAACLDILMLR...
TR $\alpha$	219	TKIITPAIT	TRVVDFA	KKLPMF	SELPCED	QIILLKGCCMEIMSLR...

**Figure 4.** Conservation of the Charge Clamp Pocket. Sequence alignment of co-factor binding pockets in nuclear receptors reveals the conserved nature of the charge clamp pocket and the AF-2 helix. Positively charged residues are labeled in blue, negatively charged residues are in red, polar residues are in green, and the hydrophobic residues are in black. The arrows indicate the positions of the charged clamp residues.

### **1.1.3 The role of NRs in the activation and repression of transcription**

NRs repress or activate transcription by participating in the constitution of large, multimeric protein complexes on the promoter of their target genes [19]. The functional state of NRs is changed upon the binding of ligand such that co-repressors are released and co-activators are recruited. In the unliganded state, NRs are associated to co-repressor complexes. These complexes are composed of a subunit (SMRT/NCoR2 or NCoR1) directly interacting with the receptor through a degenerated LXXLL motif, also called the CoRNR box, which interact with amino acids from the LBD hydrophobic groove [20, 21]. Co-repressor complexes are built around the SMRT or NCoR subunits, which harbor a conserved repression domain on which the core repressive machinery (including HDAC3, GPS2 and TBL1 or TBLR1) is assembled. HDAC3 negatively affects transcription factor access to DNA condensing the nucleosome. Upon ligand binding the co-repressor complex is released and the co-activator complex is recruited, allowing the transcriptional complex to access the gene. In Eukaryotes a group of transcriptional factors, the so-called *General Transcriptional Factors* (GTF), bind to RNA Polymerase II at the promoter of the DNA sequence (*e.g.*, TATA box) to form a large transcription Preinitiation Complex (PIC) and activate transcription (Figure 5).

In 1995, SRC-1 was cloned as the first authentic NR co-activator. SRC-1 was found to interact with steroid receptors in a hormone-dependent manner and robustly increase the transcriptional activities of steroid receptors. Soon after, two other homologous proteins, SRC-2 (also known as TIF2, GRIP1 and NCoA2) and SRC-3 (also known as p/CIP, RAC3, AIB1, ACTR, TRAM1 and NCoA3), were characterized as NR co-activators. These

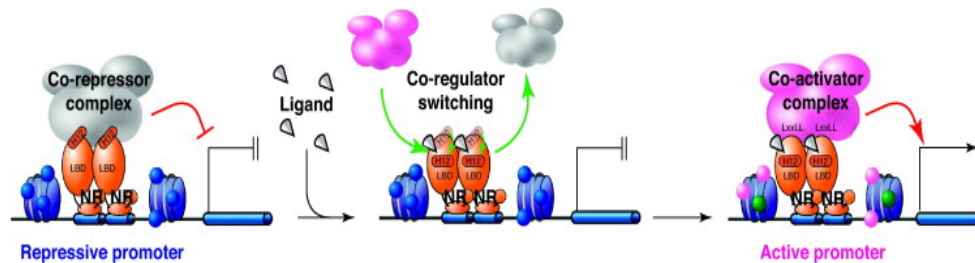


**Figure 5.** Ligand-dependent NR switching of co-regulators. In the absence of a ligand, co-repressor complexes maintain repressive states of NR-mediated transcription. Transactivation is triggered by binding of the cognate ligand to the LBD, which induces co-activators binding while co-repressors dissociate from the LBD.

three homologous proteins comprise the p160 SRC family. SRCs contain three structural domains. The amino-terminal domain is the most conserved region and is required for protein–protein interactions. The central region of the SRC proteins contains three LXXLL motifs, which form amphipathic  $\alpha$ -helices and are responsible for interacting with NRs. The carboxyl terminus contains two transcriptional activation domains (AD1 and AD2). AD1 binds CREB-binding protein (CBP) and the histone acetyltransferase p300 (also known as EP300), and the recruitment of CBP or p300 by SRCs to the chromatin is essential for SRC-mediated transcriptional activation. AD2 interacts with co-activator-associated arginine methyltransferase 1 (CARM1) and protein arginine N-methyltransferase 1 (PRMT1), which are histone methyltransferases. The C-terminal end of SRC-1 and SRC-3 contain HAT activity domains, although their cellular substrates are incompletely identified. These molecular features provide SRCs with a suitable structural base for recruiting additional co-regulators and general transcription factors, which in turn results in chromatin remodelling, assembly of general transcription factors and recruitment of RNA polymerase II for transcriptional activation [22].



### 1.1.4 Ligand-Receptor interaction

Occupation of a receptor by a ligand may or may not result in *activation* of the receptor. By activation, it means that the receptor is affected by the bound molecule in such a way as to elicit a tissue response. Binding and activation represent two distinct steps in the generation of the receptor-mediated response by an *agonist* (Figure 6). If a ligand binds to the receptor without causing activation and thereby prevents the agonist from binding, it is termed a *receptor antagonist*. The tendency of a ligand to bind to the receptors is governed by its *affinity*, whereas the tendency for it, once bound, to activate the receptor is denoted by its *efficacy*. Ligands of high potency generally have a high affinity for the receptors and thus occupy a significant proportion of the receptors even at low concentrations. Agonists also possess significant efficacy, whereas antagonists, in the simplest case, have zero efficacy. Ligands with intermediate levels of efficacy, such that even when 100% of the receptors are occupied the tissue response is submaximal, are known as *partial agonists*, to distinguish them from *full agonists*, the efficacy of which is sufficient that they can elicit a maximal tissue response [23].

One of the most exciting messages for nuclear receptor-based drug development arises from the observation that chemistry can provide us not only with receptor-selective and various types of full/partial agonists and antagonists, but also with compounds that activate only a subset of the functions induced by the cognate ligand or with ligands that act in a cell-type-selective manner [*selective nuclear receptor modulators* (SNURMs)]. Importantly, recent studies have shed light on the molecular mechanisms underlying SNURM action, which has made it possible to design screening and target validation. Moreover, recent data indicate that several other factors and mechanisms have to be considered for a full understanding of nuclear

receptor pharmacology. For example, we have just begun to recognize the importance of the so-called *non-genomic action* of nuclear receptor ligands and the impact of factors that re-direct nuclear receptor signalling. In all of these cases, molecular biology has provided us with a variety of concepts by which nuclear receptors and/or their ligands can induce or modulate important physiological programs. The challenge now is to generate chemical compounds that address one or only some of these functions to achieve the pharmacologically desired effect [24].

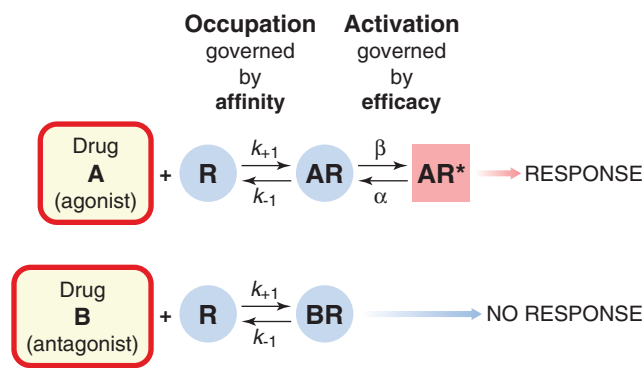


**Figure 6.** The distinction between ligand binding and activation. Ligand A is an agonist, because when it is bound, the receptor (R) tends to become activated, whereas ligand B is an antagonist, because binding does not lead to activation. The rate constants for the binding and activation steps vary between ligands. For an antagonist, which does not activate the receptor,  $\beta = 0$ .

## 1.2 Peroxisome Proliferator-Activated Receptors (PPARs)

Peroxisome proliferator-activated receptors (PPARs) are ligand-activated transcription factors that regulate genes involved in cell differentiation and various metabolic processes, especially lipid and glucose homeostasis. In molecular terms, PPARs represent a family of ligand-activated nuclear hormone receptors belonging to the steroid receptor superfamily. The family of PPARs comprises three isoforms: PPAR $\alpha$ , PPAR $\beta/\delta$  and PPAR $\gamma$ . These three isotypes differ from each other in terms of tissue distributions, ligand specificities and physiological roles. Each of them either activates or suppresses different genes with only partial overlap in activity. All isoforms participate in lipid homeostasis and glucose regulation (energy balance) and, until recently, their actions were thought to be limited to specific tissue types (Figure 7).

PPAR $\alpha$  is highly expressed in metabolically active tissues, such as liver, heart, skeletal muscle, intestinal mucosa and brown adipose tissue. This receptor is implicated in fatty acid (FA) metabolism and its activation reduces lipid levels. Synthetic PPAR $\alpha$  ligands such as fibrates are recommended in clinical practice in the dyslipemic state (hypertriglyceridemia) (Figure 8). The two PPAR $\gamma$  isoforms  $\gamma$ 1 and  $\gamma$ 2 (the latter having an extra 28 amino acids at the N-terminus) act in the white and brown adipose tissues to promote adipocyte differentiation and lipid storage and biosynthesis, while only the expression of PPAR $\gamma$ 1 extends to other tissues such as the gut or immune cells. This receptor also participates in lipoprotein metabolism and insulin sensitivity. Thiazolidinediones are PPAR $\gamma$  synthetic agonists used in the treatment of diabetes mellitus. The least known isoform is PPAR $\beta/\delta$ , which has not been so intensely studied as PPAR $\alpha$  and

PPAR $\gamma$ . PPAR $\beta/\delta$  is expressed ubiquitously in virtually all tissues; however, it is particularly abundant in the liver, intestine, kidney, abdominal adipose tissue, and skeletal muscle, all of which are involved in lipid metabolism. It participates in fatty acid oxidation, mainly in skeletal and cardiac muscles, regulates blood cholesterol concentrations and glucose levels [25]. A recent report that the synthetic molecule GW501516 can suppress insulin level in a primate model implies that ligands specific to PPAR $\beta/\delta$  might have therapeutic potential by themselves or in combination with PPAR $\gamma$  agonists [26].

In conclusion, PPAR $\alpha$  and PPAR $\beta/\delta$  mainly facilitate energy combustion, whereas PPAR $\gamma$  contributes to energy storage by enhancing adipogenesis.

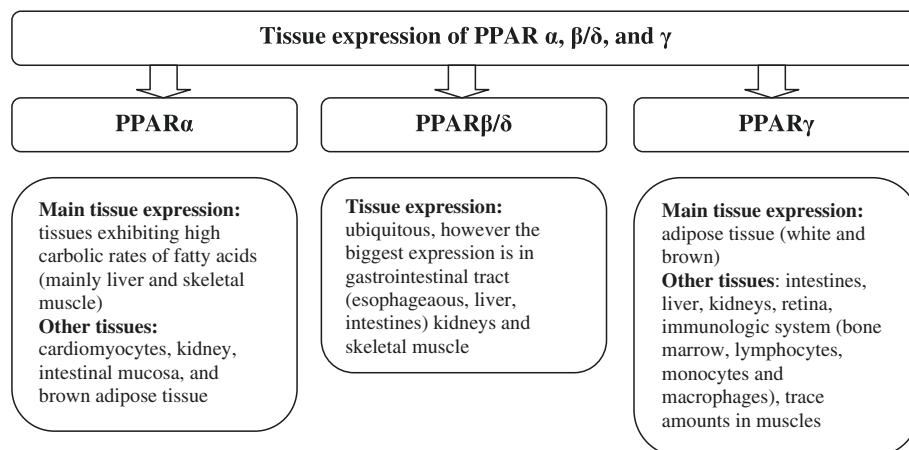


**Figure 7.** Expression of PPARs in specific tissues.

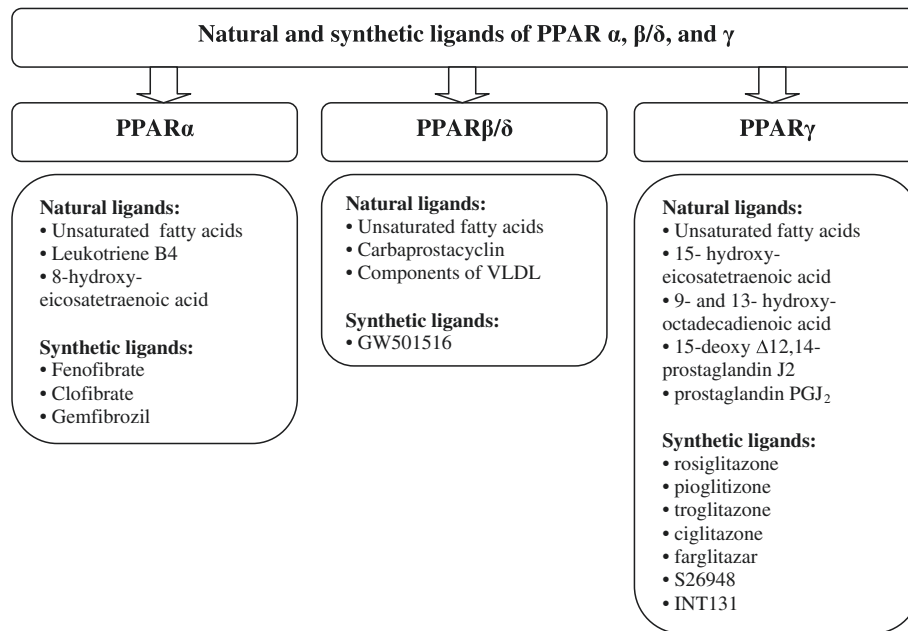


**Figure 8.** Natural and synthetic ligands of PPARs.

### 1.2.1 PPARs structure and function

The PPARs have a domain structure common to other members of the nuclear receptor gene family (Figure 9). Sequence comparison of their DNA-binding domains (DBD) shows that they are highly conserved, while the ligand-binding domains (LBD) have a slightly lower level of conservation across the subtypes [27]. After interaction with agonists, PPARs are translocated to the nucleus and heterodimerize with another nuclear receptor - the retinoid X receptor (RXR) - which forms a heterodimer with a number of other receptors (*e.g.*, vitamin D or thyroid hormones). The specific DNA regions of target genes that bind with PPARs are termed peroxisome proliferator hormone response elements (PPREs; Figure 10). The PPREs are found in the promoters of PPAR responsive genes, such as the fatty acid-binding protein (aP2). In most cases, this process activates transcription of various genes involved in diverse physiological and pathophysiological

processes. The function of PPARs is modified by a number of co-activators and co-repressors, the presence of which can either stimulate or inhibit receptor function, respectively. Ligands that activate PPAR $\gamma$ -RXR cause an exchange of co-repressors for co-activators. Human cells are characterized by a different availability of co-factors that depends on the type of cell and the association of specific co-factors to other genes [25].

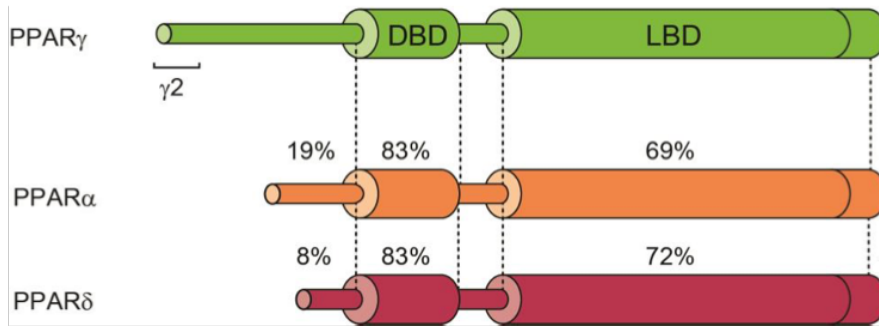


**Figure 9.** Functional domains of the PPARs: DBD, DNA-binding domain; LBD, ligand-binding domain. Numbers represent the percent (%) identity between the human subtypes.

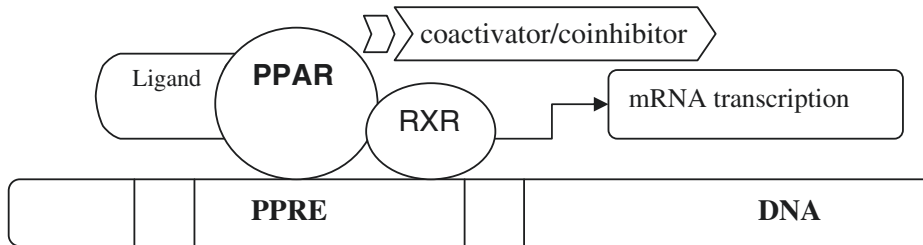


**Figure 10.** Mechanism of gene transcription by PPARs.

### 1.2.2 The ligand binding domain

In addition to ligand binding, the LBD is required for heterodimerization and interaction with transcriptional co-factors. Due to their importance as pharmaceutical targets for regulating the fatty acid metabolism and antidiabetic drugs, and since they provide an interesting

example of receptors interacting with other molecular partners in a ligand-dependent manner, the PPARs LBD structure has been intensively studied at the atomic level in the past decade. Numerous structures have been determined for PPAR $\alpha$ , PPAR $\gamma$  and PPAR $\beta/\delta$ , in both liganded and apo forms, with or without a co-activator or a co-repressor, and in presence or absence of RXR.

The overall structure is common to all three isotypes of PPAR LBD and resembles the LBDs of other nuclear receptors, like RXR and the retinoic acid receptor (RAR). In terms of secondary structure, the molecules fold into a single domain that contains a bundle of 13 helices and a small four-stranded  $\beta$ -sheet (Figure 11). On the contrary to other NRs LBD, the PPARs LBD contains an extra helix, called H2', between the first  $\beta$ -strand and H3. Also, helices H10 and H11 are in fact one continuous helix in PPAR. Helices H4, H5, H8, and H9 are sandwiched between helices H1, H3, H7, and H10/H11. The ligand binding site - the so-called *ligand binding pocket* (LBP) - is a very large cavity within the protein with a total volume of 1300 to 1400  $\text{\AA}^3$ , which is substantially larger than those found in other NRs. It is enclosed by helices H2', H3, H4, H5, H7, H10/H11, H12, and  $\beta$ -strands S3 and S4. The cavity is Y-shaped (Figure 12) and consists of an entrance extending from the surface of the protein then branching off to two pockets, arm I and arm II (Figure 13), which are both approximately 12  $\text{\AA}$  in length: arm I extends toward the AF-2 helix H12 and consists of polar residues, while arm II is situated between helix H3 and the  $\beta$ -sheet, showing hydrophobic features, which are not surprising given the hydrophobic nature of the natural ligands. The solvent accessible part of the entrance is essentially composed of polar residues, *e.g.* Pro227, Arg288, Glu295 and Glu343 for PPAR $\gamma$  (Figure 14). The loop between helices H2' and H3, situated at the entrance of the binding

site, is very flexible in all PPAR structures and is even disordered in some structures. This suggests that the binding site entrance can potentially adapt, allowing large ligands to enter the binding pocket without significantly changing the overall structure of the LBD [28]. Thirty four residues define the wall of the binding cavity, 80% of which are conserved across the three isotypes.

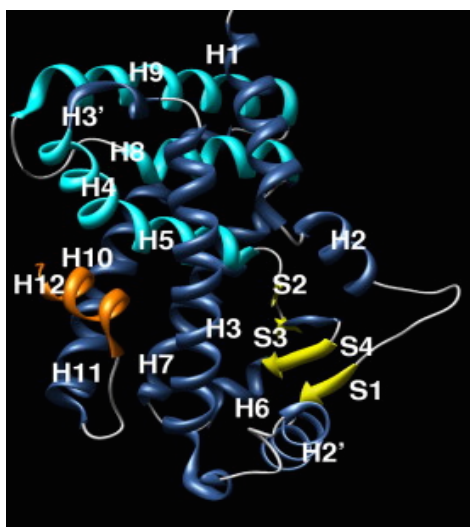


**Figure 11.** secondary structure elements of PPAR $\gamma$  LBD.



**Figure 12.** PPAR $\gamma$  Ligand Binding Pocket.

However, the differences can be linked to ligand specificity. A comparison of the experimental 3D structures of the three PPAR LBDs indicates that, although the overall size of the cavity is similar, there are marked differences in the detailed topology [29]. It is interesting to note the conservation of four polar residues in arm I of each PPAR isotype. These residues are part of a hydrogen-bonds network involving the carboxylate group of FAs and eicosanoic acids, with Ser280 (H3), Tyr314 (H5), His440 (H11) and Tyr464 (H12) of PPAR $\alpha$  (respectively Thr289, His323, His449 and Tyr473 of PPAR $\beta/\delta$ , and Ser289, His323, His449 and Tyr473 of PPAR $\gamma$ ).



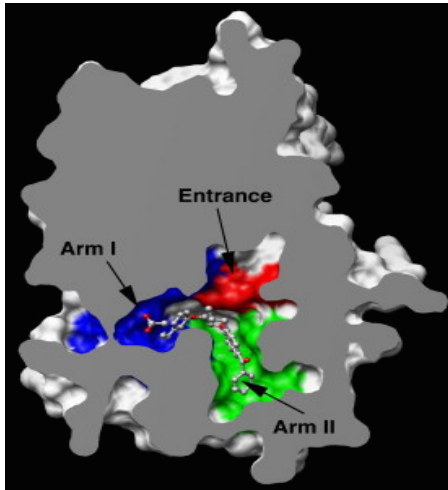


**Figure 13.** Arm I (blue), arm II (green) and entrance (red) of PPAR $\gamma$  LBP are shown.

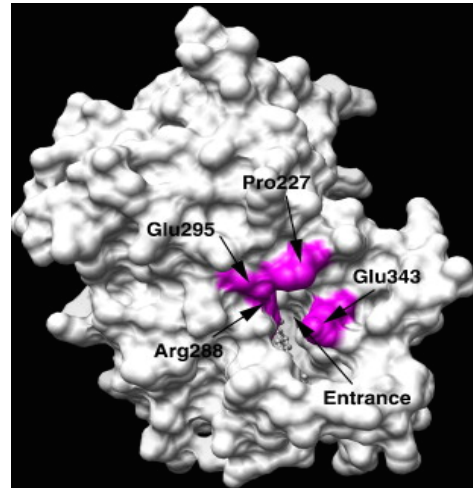


**Figure 14.** PPAR $\gamma$  surface, showing binding site entrance.

A similar hydrogen-bonds network, that involves the Tyr473 residue of H12, may exist in PPAR complexes with synthetic ligands and helps holding the AF-2 helix in the active conformation, thus promoting the binding of co-activator proteins (Figure 15) [28].

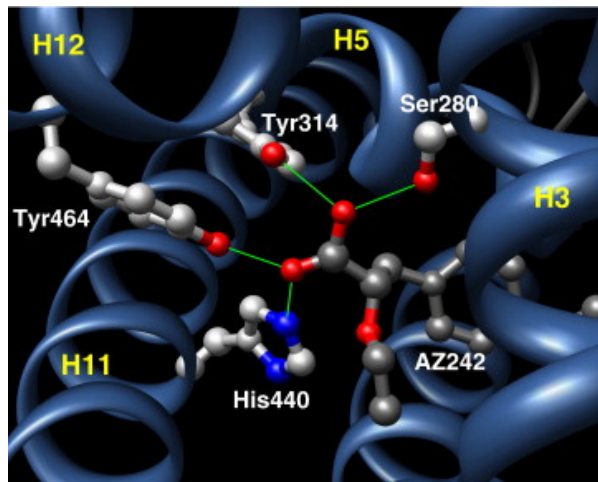


**Figure 15.** Hydrogen-bonds network between a ligand of PPAR $\alpha$  and residues Ser280, Tyr314, His440 and Tyr464. Hydrogen-bonds are shown in green lines.

A structure–activity relationship between the ligand/PPAR interaction and the partial or full agonism character of the ligand seems to be provided by the hydrogen-bonds network taking place in arm I, involving one residue of the AF-2 helix H12. Indeed, a series of experimental 3D structures seem to show that partial agonists do not form this hydrogen-bonds network, on the contrary to most of the full agonists [30-33]. However, a recent X-ray structure shows that a partial PPAR $\gamma$  agonist does make this hydrogen-bonds network [34]. Thus, the origin of partial agonism might be more complex and a direct interaction with helix H12 does not seem sufficient to have a full agonism.

### **1.2.3 The role of the AF-2 helix H12**

In line with the 'mousetrap' model proposed by D. Moras *et al.* [15], several studies performed on the PPAR LBD proved that not only the LBD shows conformational changes upon ligand binding, but it also changes dynamically. NMR studies on the apo- and holo-PPAR $\alpha/\gamma$  showed an overall stabilization of the LBD upon ligand binding [35, 36], resulting in a more compact and rigid structure. This stabilization is more relevant for full agonists than for partial agonists and was confirmed by Hydrogen/Deuterium exchange (HDX) experiments, showing that full agonists stabilize helices H11 and H12 through a hydrogen-bonding network, which is lacking in partial agonists and antagonists [37]. Moreover, fluorescence anisotropy measurements on PPAR $\gamma$  [38] showed that helix 12 is very dynamic in the absence of ligand, with movements on the nanosecond timescale, suggesting that its mobility is independent of the rest of the LBD. Upon ligand binding, it becomes immobilized on the surface of the receptor. Furthermore, the structures of apo-PPAR $\gamma$  and  $\beta/\delta$  LBDs suggest that the receptors can adopt the active conformation even in the absence of agonists [39, 40], in

accordance with the existence of a basal activity in absence of ligand [41, 42]. All these data indicate that PPAR LBD does not adopt a well-defined structure in the absence of ligand, but rather shows an equilibrium of conformations [36]. Ligand binding would shift this equilibrium to a state that favors co-activator recruitment, through direct contacts between the ligand and the helix 12 and a global stabilization of the LBD. In this model, co-activators with high affinity for the receptor could bind to LBD in the absence on any agonist. The high constitutive activity of PPARs [41, 42] seems closely related to a ligand-independent stabilization of the active position of the AF-2 helix H12, allowing recruitment of co-activators. It has been found by comparing several PPAR experimental structures [43] and by Molecular Dynamics (MD) simulations [44] that residues Glu324 (H4/H5 junction) Arg397 (loop between H8 and H9) and Arg443 (H11) are involved, together with Tyr477 (H12), in a hydrogen-bonds network that stabilizes the AF-2 helix H12 in the active conformation in a ligand-independent manner (Figure 16A). MD simulations, together with experimental mutagenesis, showed that residues Leu469, Tyr473, Leu476 and Tyr477 significantly stabilize the AF-2 helix H12 in the active conformation through interactions with the ligand and some adjacent residues of the PPAR LBD [44] (Figure 16B). Most of these interactions are actually ligand independent. All these residues are highly conserved in the PPAR isotypes.

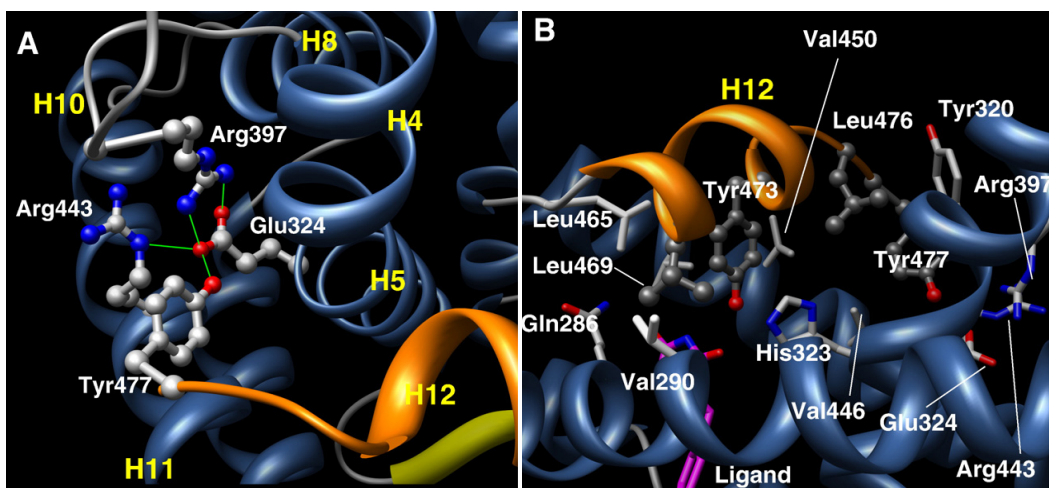


**Figure 16.** A) PPAR $\gamma$  residues involved in a hydrogen-bonds network stabilizing the AF-2 domain in a ligand-independent manner (2PRG [39]). Hydrogen-bonds are shown in green lines, AF-2 helix H12 is coloured in orange. B) Interactions between residues Leu469, Tyr473, Leu476 and Tyr477 and some neighboring residues of PPAR that stabilize the active conformation of AF-2 helix H1. Rosiglitazone is shown in magenta.

### 1.2.4 The role of the helix H3 and the $\beta$ -sheet

X-ray structures of the PPAR $\gamma$  LBD in complex with full agonists indicate the critical role of helix 12 in transcriptional regulation of these nuclear receptors. The structures of PPAR $\gamma$  bound to partial agonists show that these ligands occupy the region between H3 to the  $\beta$ -sheet, forming hydrogen-bonds with the first strand of the  $\beta$ -sheet (*e.g.* -NH of S342) and no direct interactions with H12. This observation demonstrates the importance of other regions such as H3 and  $\beta$ -sheet in the transcriptional response suggesting a distinct co-activator binding surface, consistent with the finding that stabilization of regions outside the LXXLL motifs contribute to receptor binding [45-50]. Moreover, the recently solved structure of full-length PPAR $\gamma$ -RXR heterodimer demonstrated that the  $\beta$ -sheet region of PPAR $\gamma$  binds directly to the RXR DBD [51]. Thus, differential binding of ligands in the region between  $\beta$ -sheet and H3 of PPAR $\gamma$  may also affect transcriptional

activity through modulation of its interaction with RXR.

Another X-ray and molecular dynamics work explained at molecular level the different pharmacological profile of the enantiomers of a novel PPAR $\alpha/\gamma$  dual agonist [52], confirming that a differential stabilization of H3 plays an important role in determining the partial agonist character of a ligand. In particular, partial agonism seems to be ascribed to closer contacts with the residue Q286 belonging to H3, whereas full agonism could be related to stronger interactions with H11, H12 and the loop 11/12.

Also, H/D exchange kinetics and X-ray experiments have been performed for six complexes of PPAR $\gamma$  with full and partial agonists [45]. On the basis of the structures of these complexes, ligands were broadly grouped into those that occupy the portion of LBD spanning from H11 and H12 beyond H3 to those that occupy the region between H3 and the  $\beta$ -sheet only. Among both classes of compounds, the partial agonists showed differential stabilization of H3 when compared to full agonists. With the first class of compounds, stronger transactivation was achieved with a corresponding decrease in stabilization of H3; this can perhaps be explained by the ability of the compounds in this area to achieve increase in transactivation by directly stabilizing H12. In contrast, compounds unable to directly contact H12 showed increased stabilization of H3 in proportion with transactivation efficacy.

### **1.2.5 Binding to co-regulators**

It is well established that the transcriptional activity of nuclear receptors is regulated by their interactions with co-factors that positively regulate target gene expression, such as the co-activators SRC-1 or CBP, or with negative regulatory proteins that inhibit target gene transcription, such as the co-repressors SMRT or N-CoR.

Recruitment of co-activator proteins depends on allosteric changes in the AF-2 helical domain. The NR interaction domain of these activators contains a LXXLL motif that forms two turns of  $\alpha$ -helix and binds into a hydrophobic cleft on the surface of the receptor, which is formed upon stabilization of the active conformation of the FA-2 helix H12. Many crystal structures of PPARs complexed with co-activators have been obtained that allow a detailed analysis of the binding [29, 31, 32, 39, 53]. In the 3D structure of PPAR $\gamma$  in complex with rosiglitazone and SCR-1 [39], the hydrophobic face of the LXXLL helix of the co-activator packs into a hydrophobic surface formed by some residues situated between Glu471 and Lys301 of PPAR $\gamma$ , interacting mainly with L468 and L318 of the PPAR $\gamma$  LBD (Figure 17). In addition to the hydrophobic contacts described above, an important and conserved set of hydrogen-bond interactions, the so-called charge clamp, is formed between the Glu471 and Lys301 side chains and the co-activator backbone. It is interesting to note that the residues involved in the charge clamp or defining the hydrophobic pocket where the LXXLL binds are highly conserved among other members of the NR family.

To understand the molecular basis of co-repressor recruitment, the crystal structure of a ternary complex containing the PPAR $\alpha$  LBD bound to the antagonist GW6471 and a peptide derived from the C-terminal receptor-interacting motif of SMRT (LXXXIXXXL) has been studied [54]. In this structure the co-repressor peptide adopts a three-turn  $\alpha$ -helix and docks into a hydrophobic groove formed by helices H3, H3', H4 and H5. Superposition of the agonist- and antagonist-bound PPAR $\alpha$  (Figure 18A) reveals that the co-repressor binding site partially overlaps with the co-activator binding site. The additional helical turn in the SMRT motif extends into the space usually occupied by AF-2 helix H12 and prevents this helix from folding back into its active conformation.

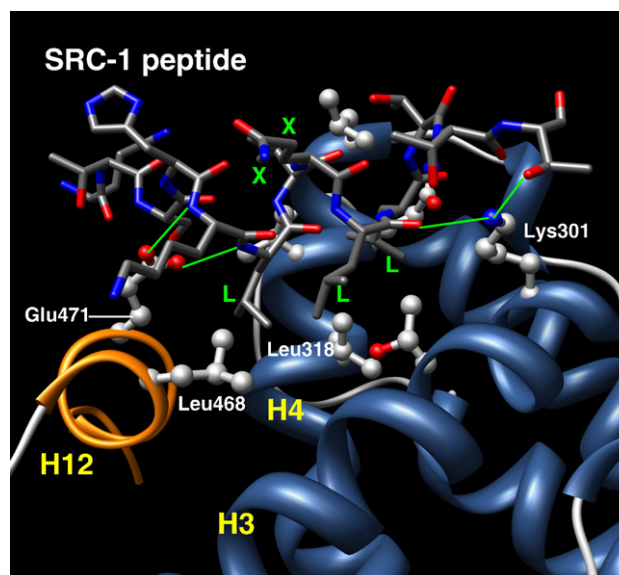


**Figure 17.** interactions between the SRC-1 peptide and PPAR $\gamma$  (2PRG [39]). The LXXLL motif of the co-activator is shown in green. The hydrogen-bonds of the charge clamp are shown in green thin lines.

Also, the ligand GW6471 was obtained by replacing the carboxylate head of the GW409544 agonist by a larger ethylamide group that prevents any hydrogen-bond with the side chain of Tyr464 of AF-2 helix H12 and pushes it out of the agonist bound position. In this way, the integrity of the charge clamp is also destroyed.

This study also suggests two main differences between the binding modes of the co-activator and co-repressor [54]. First, the additional helical turn in the co-repressor motif result in a larger interaction surface with PPAR $\alpha$  than the two helical turns of the co-activator motif and could partially explain the preference for co-repressor instead of co-activator binding to PPAR in presence of an antagonist. Moreover, superposition of the PPAR $\alpha$ /GW409544/SRC-1 [29] and the PPAR $\alpha$ /GW6471/SMRT [54] complexes indicates that the +5 and +8 positions of the LXXXIXXXL co-repressor motif, respectively occupied by Ile and Ala residues, correspond to

the first and second Leu residues in the LXXLL co-activator motifs (Figure 18B). The presence of the two larger Leu residues in the co-activator prevents it from binding tightly to the LBD surface when AF-2 helix H12 is in its inactive conformation, so they become strong contributors to the interaction in the context of the active conformation due to interactions with H12. Second, as already described, the charge clamp between PPAR and the co-activator is destroyed in the complex with co-repressor due to the repositioning of Glu462 (H12). However, Lys301 still makes hydrogen-bonds with the co-repressor backbone [54].

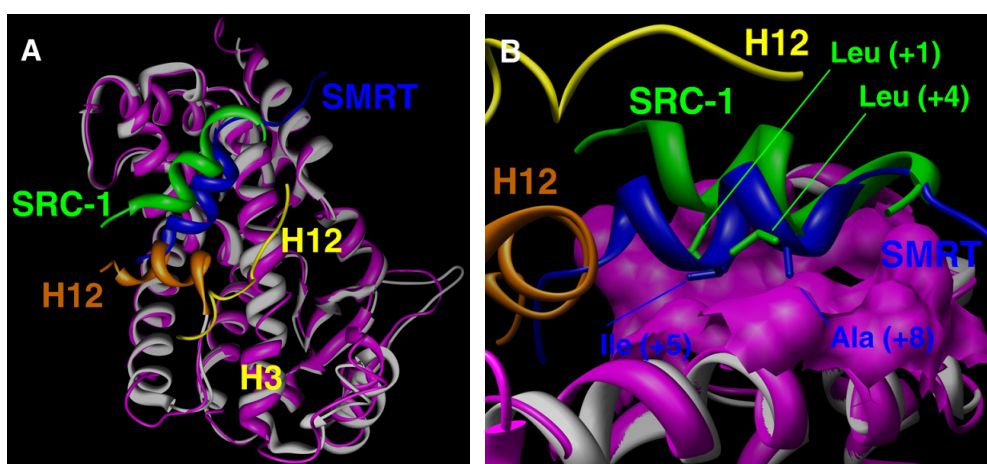


**Figure 18.** Structural superposition of PPAR $\alpha$ -LBD/GW409544/SRC-1 [29] (white) and the PPAR $\alpha$ -LBD/GW6471/SMRT [54] (magenta). In the PPAR $\alpha$ -LBD/GW409544/SRC-1 structure, the AF-2 helix H12 and the SRC-1 co-activator are orange and green, respectively. In the PPAR $\alpha$ -LBD/GW6471/SMRT structure, the AF-2 helix H12 and the SMRT co-repressor are yellow and blue, respectively. (A) The co-repressor occupies partly the position of the active conformation of AF-2. (B) The Ile (+ 5) and Ala (+ 8) residues of the LXXXIXXXL co-repressor motif correspond to the Leu (+1) and Leu (+4) residues of the LXXLL co-activator motif. The larger size of the Leu residues prevents the co-activator to bind tightly to the LBD surface in the inactive conformation, on the contrary to the co-repressor.

### 1.2.6 Heterodimer formation with RXR

Although some evidence suggests that the PPARs can form homodimers and bind to DNA response elements such as the Pal3 motif [55], it is widely accepted that the PPARs must heterodimerize with RXR to carry



out most of their functions. Therefore, like other RXR's partners, the PPARs are integral parts of the RXR-dependent signaling network. The crystal structure of the PPAR $\gamma$  and RXR $\alpha$  LBDs complexed to the RXR ligand 9-*cis*-retinoic acid (9cRA), the PPAR $\gamma$  agonist rosiglitazone and the co-activator peptides has been described [53]. The structural analysis of domains E present principles of heterodimerization in comparison to homodimerization. Homodimers of domain E of RXRs and PPARs are symmetric around a twofold rotation axis parallel to the core of the dimerization interface formed by helix 10. Further, residues are located in helices 7, 9, and 11 as well as in loops 7/8 and 9/10. These structural elements contribute to the dimerization in the same manner from both molecules in homodimers. This symmetry is not maintained in the interface of the heterodimers of RXRs with PPARs. The PPAR $\gamma$ /RXR $\alpha$  interface is asymmetric where the PPAR $\gamma$  LBD is rotated about 10° from the C2 symmetry axis of the RXR LBD. The interface is comprised of a complex network of hydrophobic and polar interactions mediated by H7, H9, and H10 and the loop between H8 and H9 of both receptors (Table 1). The majority of the heterodimerization interactions are mediated through H10 of both receptors (Table 1 and Figure 19a).

Non polar interactions		Polar Interactions	
RXR $\alpha$	PPAR $\gamma$	RXR $\alpha$	PPAR $\gamma$
(H9)	Y397 – A433 (H10)	(H7)	K356 – E407 (H9)
(H10)	F415 – A433 (H10)	(H7)	K356 – G395 (L8)
(H10)	A416 – L414 (H9)	(H7)	D379 – K438 (H10)
(H10)	A416 – F432 (H10)	(H7)	D379 – D441 (H10)
(H10)	A416 – L436 (H10)	(H9)	E390 – K434 (H10)
(H10)	L419 – L436 (H10)	(H9)	E394 – K434 (H10)
(H10)	L420 – L414 (H10)	(H9)	E401 – Q430 (H9)
(H10)	L420 – L436 (H10)	(H9)	R393 – D441 (H10)
(H10)	L420 – Q437 (H10)	(H9)	Y397 – Q437 (H10)
(H10)	L420 – M439 (H10)	(H10)	K417 – E407 (H9)
(H10)	L422 – T440 (H10)	(H10)	R421 – E407 (H9)
(H10)	P423 – T440 (H10)	(H10)	R421 – D396 (L8)
(H10)	P423 – M439 (H10)	(H10)	R426 – Q444 (H10)
(H10)	S427 – Q444 (H10)	(H10)	S427 – R443 (H10)
(H10)	L430 – Q444 (H10)	(H10)	K431 – Y477 (AF2)
(H10)	L430 – T447 (H10)		
(H7)	E352 – P398 (L8)		
(H7)	R348 – Y477 (AF2)		

**Table 1.** Interactions in the RXR $\alpha$ /PPAR $\gamma$  dimer interface.

Members of the nuclear receptor subfamily 2, which includes RXR, are unique in having a glutamic acid residue (E352 in RXR $\alpha$ ) in the middle of H7. Close examination of the 9cRA-RXR $\alpha$  portion of the heterodimer structure reveals an unwinding of H7 that is absent in the published apo-RXR $\alpha$  structure [12]. The unwinding of H7 by the E352 give rise to a complex series of charge-driven interactions along the heterodimer interface. The E352 rotates K356 one residue around H7 of RXR, which places it close to a negatively charged region at E407 on the surface of PPAR $\gamma$  (Figure 19b). E352 also makes a salt bridge with R348 on H7, holding this residue in close proximity to K431 on H10 of RXR $\alpha$ . An unexpected consequence of these interactions is the formation of a salt bridge between K431 of RXR $\alpha$  and the free carboxylate of Y477 in PPAR $\gamma$  (Figure 19b). This salt bridge is further reinforced by a packing interaction between the side chains of Y477 and R348. Thus, E352 of RXR $\alpha$  forms an intradimer salt bridge with R348, which facilitates an interdimer salt bridge between K431 of RXR $\alpha$  and the C-terminal residue of the PPAR $\gamma$ . These salt bridges stabilize the PPAR $\gamma$  AF-2 helix in a position that facilitates the recruitment of co-activators. Notably, the corresponding interaction between the RXR $\alpha$  AF-2 helix and H10 of PPAR $\gamma$  was not observed. These charge-driven interactions, which are asymmetric with respect to the heterodimer, suggest a structural basis for the permissiveness of the PPAR $\gamma$ /RXR $\alpha$  complex. Indeed the existence of two types of nuclear receptor heterodimers, nonpermissive and permissive, has been already described. No response of RXRs to agonists is detected in nonpermissive heterodimers formed with RARs, TRs, VDR. Agonists will induce a signal via RXRs in heterodimers formed with RARs if a ligand of RARs is present.

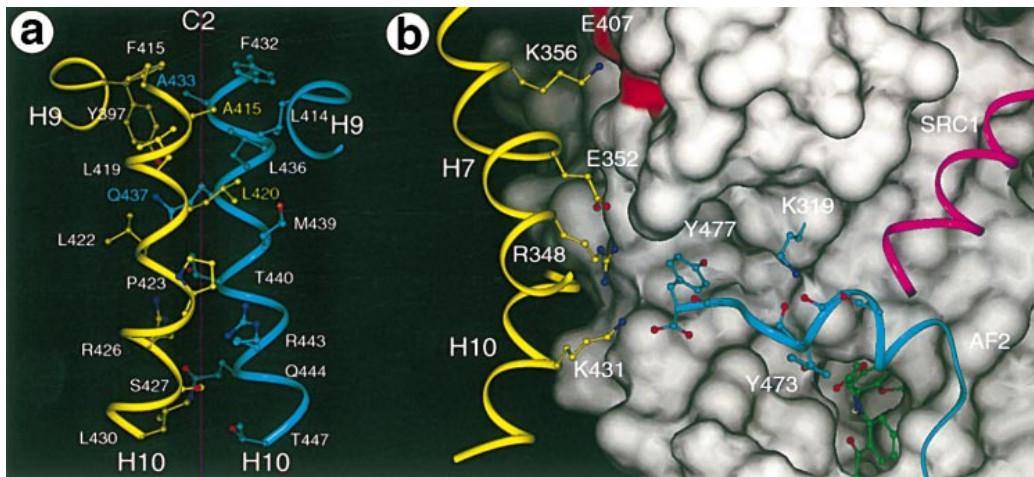


**Figure 19.** Interactions between RXR $\alpha$  and PPAR $\gamma$ . (a) Intermolecular interactions mediated by helices 10 of RXR $\alpha$  and PPAR $\gamma$ . Key residues that form the core hydrophobic interface of the parallel coiled coil are labeled, along with the C2 axis of symmetry. (b) Interactions between the PPAR $\gamma$  AF-2 helix and RXR $\alpha$ . Helices 7 and 10 of RXR $\alpha$  are shown in yellow, with residues that form key charge interactions with PPAR $\gamma$  indicated, including the E insert, E352. The surface of PPAR $\gamma$  is shown in gray, with the AF-2 helix of PPAR $\gamma$  indicated in cyan. PPAR $\gamma$  residues Y477, the C-terminal residue that interacts with K431 and R348 of RXR $\alpha$ ; K319, which caps the C-terminal carbonyls of the AF-2 helix; and Y473, which interacts with the PPAR $\gamma$  ligands, are indicated. The LxxLL motif of SRC-1 is shown in magenta.

However, RXRs can be activated by agonists in permissive heterodimers formed with PPARs, LXR and FXR independently of the presence of a ligand in the heterodimeric partner. Addition of an agonist of PPARs results in an additive effect on transcriptional activation in the case of RXR/PPAR heterodimers. The crystal structure of the heterodimer of RXR $\alpha$  and PPAR $\gamma$  in complex with 9cRA, rosiglitazone and peptides derived from SRC-1 suggests some features of the structural basis for permissiveness of RXR heterodimers. The interconnection of hydrogen-bonds and salt bridges stabilizes the formation of a salt bridge between the  $\epsilon$ -amino group of K431 in helix 10 of RXR $\alpha$  and the carboxylate group of Y477, which is the C-terminus of domain E of PPAR $\gamma$ . Thus, this salt bridge may permit the stabilization of helix 12 in transcriptionally active form of PPAR $\gamma$ , even in the absence of a PPAR agonist [53].

### 1.2.7 Non-genomic actions

Studies on the role of PPARs in integrating and modulating inflammatory stimuli have highlighted many unknown mechanisms of action of the receptors at the non-genomic level. Indeed, PPARs can mediate indirect repressive effects termed transrepression by inhibiting the activity of key transcription factors. As shown in Figure 20, transrepression can occur either by inhibiting the binding of transcription factors to DNA through direct protein-protein interactions (tethering) or by sequestering co-factors necessary to their activity (squelching).

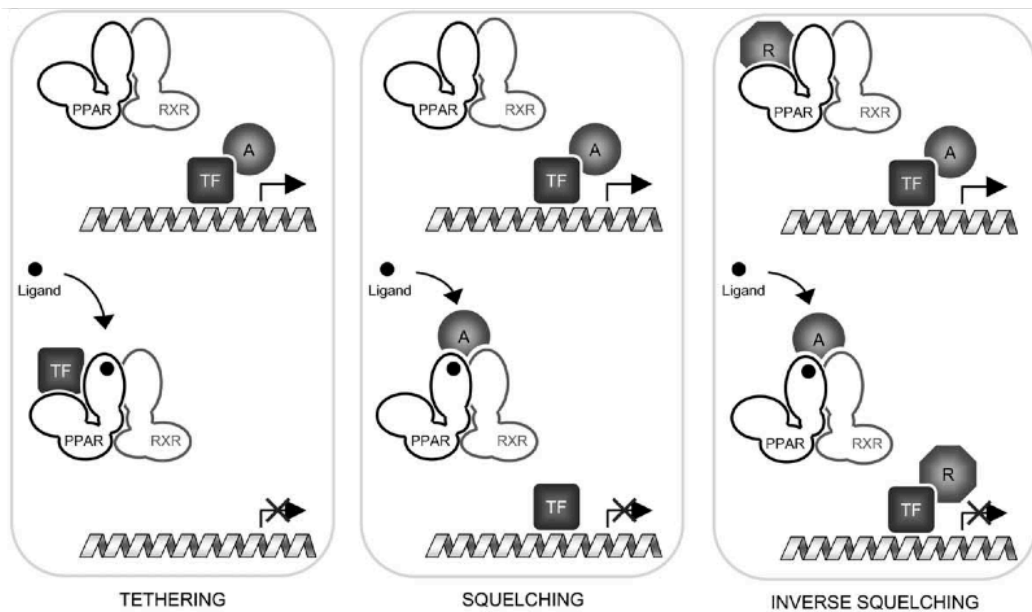
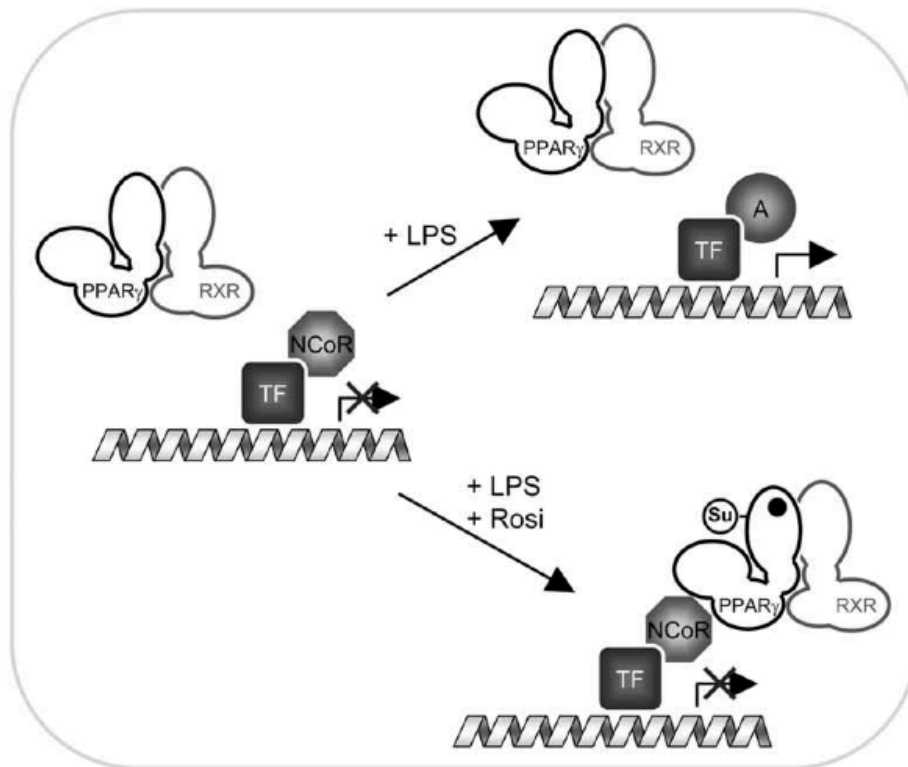


**Figura 20.** General mechanisms of transrepression by PPAR/RXR heterodimers. Tethering (interaction with transcriptional factors that inhibit their DNA binding), squelching (titration of a co-activator in the presence of a ligand) and inverse squelching (titration of a co-repressor in the absence of a ligand) are schematically described.

Tethering of transcriptional factors is illustrated by the inhibition of interleukin-2 (IL-2) expression in response to PPAR $\gamma$ . The ligand-dependent binding of PPAR $\gamma$  to nuclear factor of activated T cells (NFAT) correlates

with the dissociation of NFAT from the IL-2 promoter [58]. Another example is the repression of the  $\alpha$ 1-acid glycoprotein (AGP) promoter by PPAR $\alpha$  which inhibits the binding of the CCAAT/enhancer binding protein  $\beta$  (C/EBP $\beta$ ) to the promoter through a direct interaction [59]. Tethering of the p65/RelA subunit of NF $\kappa$ B and of the c-jun subunit of the activator protein 1 (AP-1) by PPAR $\alpha$  is also plausible since both of these factors interact with PPAR $\alpha$  and are necessary to the fibrate-dependent inhibition of the IL-6 promoter [60, 61]. Finally, in enterocytes, the nuclear export of the p65/RelA and the consequent anti-inflammatory effect induced by exposure to a specific commensal bacterium is caused by the translocation of PPAR $\gamma$  from the nucleus to the cytoplasm [62]. This example suggests that under some circumstances, tethering seems to involve direct interactions which promote the nuclear export of the transcription factor tethered.

Recently, a model explaining the ligand-dependent squelching of NcoR and the subsequent repression of the iNOS promoter has been proposed [63]. In response to rosiglitazone, PPAR $\gamma$  is sumoylated and indirectly recruited to the iNOS promoter through ligand-dependent association with the nuclear receptor co-repressor (NcoR). This association prevents NcoR dissociation and therefore repress transcription of iNOS (Figure 21). Another example of co-factor squelching is the repression of the cyclin D1 promoter by PPAR $\gamma$  ligands which promote PPAR $\gamma$ /p300 versus AP-1/p300 interactions [64]. PPAR $\alpha$  also competes with C/EBP $\beta$  for binding to their common co-activator GRIP1/TIF-2/SRC-2 and thereby represses the action of C/EBP $\beta$  on the fibrinogen promoter [65]. Finally, inverse squelching has also been observed between PPAR $\gamma$  and STAT3. Troglitazone inhibits the interaction between PPAR $\gamma$  and the co-repressor SMRT, thereby inducing the redistribution of SMRT to activated STAT3 and repressing STAT3 signaling [66].



Transrepression of the *iNOS* promoter

**Figure 21.** On the *iNOS* promoter, LPS relieves the repression by NCoR in the absence of PPAR $\gamma$  ligands. However, rosiglitazone-induced PPAR $\gamma$  lysine 365 sumoylation induces the binding of sumoylated PPAR $\gamma$  to the repressive complex and thereby stabilizes the association of NCoR with the promoter to maintain the gene in an inactive state [63].

### 1.2.8 Regulation by post-translational modifications (PTM)

PPARs function, as well as that of other nuclear receptors, is regulated by post-translational modifications (PTM) including phosphorylation, ubiquitylation and sumoylation.

Several phosphorylation sites spanning all across the receptor have been characterized using *in vitro* or cellular assays. At the molecular level, the effects of PPAR phosphorylation are mediated by different mechanisms including changes in the affinity for ligands, RXR, co-factors and target genes, which often result from long-range conformational changes across the

entire receptor. For instance, phosphorylation of PPAR $\gamma$ 2 serine112 by MAP kinase induces conformational changes which are transmitted to the LBD and result in a weakened affinity for ligands [67], causing a lower transcriptional activity [68]. The interaction between PPAR and RXR also seems to be modulated by phosphorylation in the hinge region as mutation of the PKC phosphorylation sites T129 and S179 of PPAR $\alpha$  reduces heterodimerization [69]. The effects of phosphorylation on the interactions with co-factors are illustrated by the MAP kinase-mediated phosphorylation of the AF-1 which activates PPAR $\alpha$  in response to insulin, probably by relieving inhibition by co-repressors [41]. Since PPAR $\alpha$  interact with NCoR through its C terminus [70], this co-repressor release would be mediated by interdomain communication. Phosphorylation may also regulate binding to response elements as observed upon phosphorylation of the PPAR $\alpha$  DBD by PKA [42]. Moreover, phosphorylation of serine245 (PPAR $\gamma$ 2 residue S273) by Cdk5 could be responsible of the dysregulation of a large number of genes, whose expression is altered in obesity, including a reduction in the expression of the insulin-sensitizing adipokine and adiponectine [71]. Finally, besides these direct effects of phosphorylation, PPAR activity can also be modulated by changing the expression level of the receptor.

Ubiquitin is an 8 kDa protein which covalently binds to proteins to target them for degradation by the 26S proteasome. Ubiquitylation of proteins occurs on lysine residues and requires the action of a sequential activation cascade composed of an activating enzyme (E1), a conjugating enzyme (E2) and finally an ubiquitin ligase (E3). Ubiquitylation and proteasome-mediated degradation are linked to the transcriptional activity of nuclear receptors through the regulation of cellular levels of the receptor but also through the intrinsic crosstalk between proteasome activity and transcription [72]. Both PPAR $\alpha$  and PPAR $\gamma$  can be targeted for degradation

by ubiquitylation. The degradation of PPAR $\gamma$  is enhanced by ligand binding through a mechanism that requires an intact AF-2 structure and probably an active conformation of the receptor as the association of the RIP140 co-repressor reverses the effect of the ligand on degradation [73]. In contrast, PPAR $\alpha$  agonists stabilize the receptor [74, 75]. Finally, it should be noted that PPAR $\beta/\delta$  can affect ubiquitylation by regulating the expression of ubiquitin C, possibly through direct transcriptional control [76].

Small ubiquitin-like modifiers (SUMO) compose a family of three 11 kDa proteins homologous to ubiquitin which can be reversibly conjugated to proteins through covalent binding to regulate various cellular mechanism including transcriptional repression [77]. Sumoylation is catalyzed by the coordinated action of specific E1, E2 and E3 enzymes and occurs on lysine residues located in  $\Psi$ KXE/D motifs (where  $\Psi$  is a large hydrophobic residue and X is any residue). K77 sumoylation occurs in a ligand-independent and exerts inhibitory effects on the activity of the receptor [63, 78, 79]. Indeed, both the basal and the ligand-dependent activity of the PPAR $\gamma$  K107R mutant are increased and this mutant can enhance physiological effects such as apoptosis in response to TZDs [78] or adipogenesis [79]. In contrast, sumoylation at lysine 365 is ligand-dependent and leads to complex transrepressive effects on the iNOS promoter by promoting the interaction with NCoR [63]. The mechanism controlling this sumoylation event involves a direct ligand-independent interaction between PPAR $\gamma$  and the protein inhibitor of activated STAT 1 (PIAS1), an E3 SUMO ligase. In this model, rosiglitazone binding induces a conformational change which guides K365 towards the surface of the LBD and thereby allows PIAS to exert its sumo ligase activity on this residue (Figure 21) [63]. However, PIAS proteins can also be recruited in a ligand-dependent manner and coactivate nuclear receptors including PPAR $\gamma$  [78, 80]. Thus, PIAS proteins could exert a dual



action on PPAR $\gamma$  signaling by promoting transpression through sumoylation of PPAR $\gamma$  K365 and by acting as a co-activator of PPAR $\gamma$  on direct target genes, possibly through sumoylation of other co-factors or histones. Finally, since transcriptional repression by SUMO is generally mediated by the recruitment of co-repressors and histone deacetylases (HDACs) [81] and since sumoylation of PPAR $\gamma$  K365 promotes the association of PPAR $\gamma$  and NCoR, studying the influence of K77 sumoylation on the recruitment of co-repressors to target gene promoters could allow to better understand the mechanisms of PPAR target gene silencing.

### **1.2.9 Drugs and active compounds on PPARs**

The broad roles of PPARs in regulating metabolism, inflammation, differentiation and cellular growth, have made them a central focus of pharmacological and genetic research for more than a decade [82, 83].

Agonists of PPAR $\alpha$  and PPAR $\gamma$  are currently approved for use in treating, respectively, dyslipidemia and type 2 diabetes. Agonists of PPAR $\beta/\delta$  are currently in development by many pharmaceutical companies. Despite their therapeutic importance, there are dose limiting side effects associated with PPAR drug treatment, thus a new generation of safer PPAR drugs are being actively sought after [83, 84]. Initial strategies aimed to develop new highly potent PPAR agonists specific for only one isotype. Therefore, pure PPAR $\gamma$  agonists have been or are in development while, surprisingly, only few pure PPAR $\alpha$  ligands are in the pipeline. However, combination therapy with drugs acting on different PPAR isotypes may have synergistic and wider therapeutic effects improving both glucose and lipid metabolism of patients suffering from metabolic syndrome and/or type 2 diabetes. Based on this hypothesis, new dual and pan agonists are currently developed aiming to

obtain synergism on lipid and glucose homeostasis from simultaneous activations of the three PPAR isotypes (Figure 23).

- **Fibrates**

All marketed PPAR $\alpha$  agonists belong to the fibrate class (clofibrate, ciprofibrate, fenofibrate, bezafibrate, gemfibrozil; Figure 22). these compounds have been used therapeutically for more than 30 years, and are well established effective agents for managing dyslipidemia, in particular

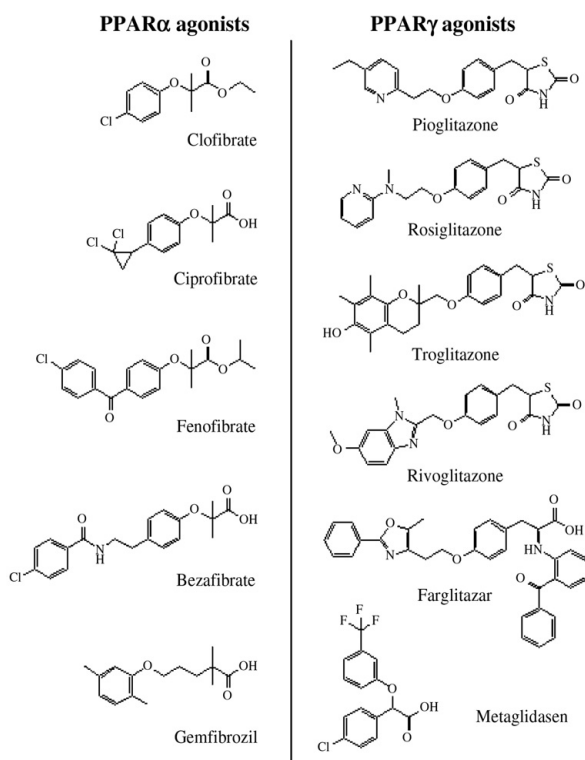


**Figure 22.** Chemical structures of some PPAR ligands.

elevated concentrations of triglyceride-rich lipoproteins (VLDL) and low levels of HDL-C that are typically associated with the mixed dyslipidemia characteristic of type 2 diabetes and the metabolic syndrome. They are generally considered as safe drugs with only few side effects, although some

adverse effects might be related to PPAR $\alpha$  activation in humans including rare cases of myopathy, increase in creatinine and homocysteine, lithogenicity and gastro intestinal disorders. To date, no fibrate has been withdrawn from the market or interrupted at late stage of development due to any of these side effects. However, such safety issues may become relevant when developing more potent PPAR $\alpha$  agonists. Recently, the development of the dual PPAR $\alpha/\gamma$  agonist tesaglitazar was suspended due to an unexpected increase in plasma creatinine levels [84].

- **Thiazolidinediones (TZDs)**

This class of compounds includes rosiglitazone, pioglitazone (which are currently approved for the treatment of type 2 diabetes) and troglitazone (Figure 22). Although they are efficacious in ameliorating hyperglycemia, their administration is associated with several adverse effects which have been categorized as either unique to individual TZDs or common to the class of drug. Of the unique effects, the best characterized is hepatotoxicity, which has been associated to date specifically with troglitazone [85]. Studies with other glitazones indicate that hepatotoxicity is not a class effect [86]. Class side effects include body weight gain, decrease in hematocrit and hemoglobin and peripheral edema, mild anemia and possible increased risk for congestive heart failure, which limit their clinical use [84].

- **PPAR $\beta/\delta$  agonists**

While several studies have been performed to investigate the effects of PPAR $\alpha$  and PPAR $\gamma$  activation by specific ligands, the role of the third member of the PPAR family, PPAR $\beta/\delta$ , has not been extensively studied until recently. As a consequence, less is known about the potential safety issues that could be associated to the use of PPAR $\beta/\delta$ -specific ligands.

Contradictory results have been published regarding the role of PPAR $\beta/\delta$  in carcinogenesis. Intestinal tumorigenesis, but not colon carcinogenesis, is reported to increase in response to GW501516 in a genetically modified animal model [87]. However, other reports suggest that ligand activation of PPAR $\beta/\delta$  will inhibit colon carcinogenesis [88, 89].

### **1.2.10 Novel active PPAR ligands**

The development of new PPAR drugs that reduce the reported adverse side effects is a major area of research in the pharmaceutical industry. The ability of each PPAR subtype to regulate distinct metabolic pathways has led to the investigation of combination approaches. The final purpose of the combination agonist strategy is to activate each receptor subtype to provide maximal efficacy on appropriate target genes associated with specific pharmacological pathways while minimizing undesired adverse side effects. Initial efforts have focused on developing PPAR $\alpha/\gamma$  dual agonists, but other subtype combinations such as PPAR $\gamma/\beta(\delta)$  dual agonists and PPAR $\alpha/\gamma/\beta(\delta)$  pan agonists are emerging. Given that PPAR subtype selective compounds each have specific documented side effect issues, it remains to be seen whether or not combination agonists will have increased risk of safety liabilities compared to selective agonists. One of the key challenges facing the development of a dual agonist in a single molecule is identifying the optimal receptor subtype specific functional activity ratio as the intrinsic potencies at each receptor subtype will ultimately determine the overall efficacy with respect to metabolic effects and minimized side effects.

- **PPAR $\alpha/\gamma$  dual agonists**

PPAR $\alpha/\gamma$  dual agonists have been hypothesized as a combination strategy to achieve a broad spectrum of metabolic effects and reduce

mortality rates associated with type 2 diabetes by improving insulin resistance, hyperglycemia and reducing atherogenic dyslipidemia. Moreover, PPAR $\alpha$  agonists stimulate lipid oxidation and decrease adiposity in rodent obesity models. Thus, the propensity of PPAR $\gamma$  activation to induce weight gain through its adipogenic effects may be offset by the ability of PPAR $\alpha$  activation to stimulate lipid catabolism thereby providing a compound with reduced propensity for inducing undesired weight gain [86]. In recent years, a number of structurally diverse PPAR $\alpha/\gamma$  dual agonists have been reported. Many of these have been evaluated in the clinic and some have advanced into late stage development. The clinical efficacy of the initially discovered dual PPAR $\alpha/\gamma$  agonists has been encouraging. However, the discontinuation of the development of the most promising PPAR $\alpha/\gamma$  dual agonists, including muraglitazar, tesaglitazar, ragaglitazar, TAK559 and KRP297 [91–94] (Figure 23) due to various safety liability issues has been disconcerting. Other dual agonists are advancing through different stages of development.

- **PPAR $\gamma/\beta(\delta)$  dual agonists**

Based on the central roles that both PPAR $\gamma$  and PPAR $\beta/\delta$  play in lipid metabolism, PPAR $\gamma/\beta(\delta)$  dual agonists have been postulated as a beneficial combination therapy for type 2 diabetes. Such a combination is predicted to effectively lower glucose and improve insulin sensitivity while simultaneously improving the dyslipidemia common in diabetic patients [95, 96]. The beneficial effects on lipid homeostasis and ability to stimulate reverse cholesterol transport are expected to significantly prevent the progression of atherosclerosis which should contribute to reducing the mortality rates of type 2 diabetic patients. Furthermore, the propensity of PPAR $\beta/\delta$  activation to improve insulin sensitivity and increase fatty acid oxidation suggests that a dual PPAR $\gamma/\beta(\delta)$  agonist could attenuate the

undesired weight gain realized with selective PPAR $\gamma$  agonists. Reports of PPAR $\gamma/\beta(\delta)$  dual agonists have been limited. The design and characterization of a ligand with predominately dual PPAR $\gamma/\beta(\delta)$  activity has been described by GlaxoSmithKline [97] and more recently by Eli Lilly and Co. [98] (compound 23 and compound 20, respectively; Figure 23). The pre-clinical studies provide evidence supporting the hypothesis that a dual PPAR $\gamma/\beta(\delta)$  agonist can attenuate the undesired weight gain side effect prevalent with marketed TZDs. It remains to identify the appropriate  $\gamma/\beta(\delta)$  ratios that will deliver optimal glucose control with minimized adverse side effects.

- **PPAR pan agonists**

The development of dual PPAR $\alpha/\gamma$  and PPAR $\gamma/\beta(\delta)$  agonists has highlighted the potential therapeutic benefits gained from targeting multiple PPAR receptors in a single molecule. Combining the agonist activity of all three PPAR subtypes - the so called PPAR pan agonist - into a single chemical entity could potentially deliver a drug that treats a broad spectrum of metabolic diseases by improving insulin sensitization, obesity, dyslipidemia and hypertension as well as providing beneficial effects on inflammatory markers. Improved management of overall adverse safety events may be realized through the synergistic effects of PPAR $\alpha$  and PPAR $\beta/\delta$  on fatty acids oxidation to sequester the undesired weight gain induced through PPAR $\gamma$  activation as well as improved cardiovascular health through the beneficial anti-atherogenic effects of PPAR $\beta/\delta$ . This strategy has led several pharmaceutical companies to pursue the design and development of PPAR pan agonists for the treatment of type 2 diabetes and metabolic syndrome [83]. The development of PPAR pan agonists is in its early stages and only a few compounds have progressed into clinical trials.

GlaxoSmithKline's PPAR pan agonist GW677954 (Figure 23) is currently being investigated in Phase II trials for the treatment of insulin resistance, hyperglycemia and dyslipidemia associated with type 2 diabetes and metabolic syndrome [98]. LY465608 (Figure 23) was originally reported as a dual PPAR $\alpha/\gamma$  agonist by researchers at Eli Lilly Pharmaceuticals [99].

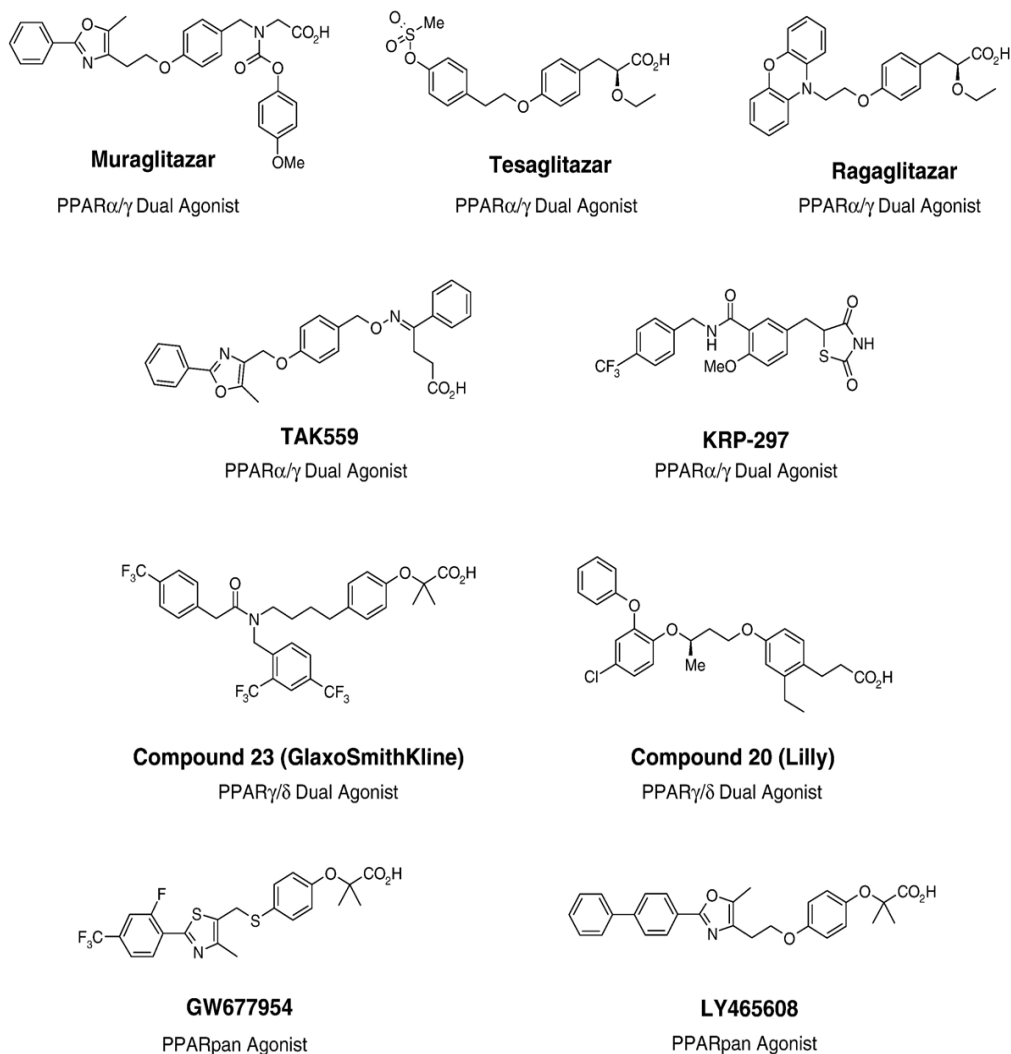


**Figure 23.** PPARs dual and pan agonist compounds.

Further detailed studies demonstrated that this compound also possesses significant PPAR $\beta/\delta$  activity and now LY465608 is classified as a PPAR pan agonist. The prospect of PPAR pan agonists to combat multiple aspects of the diabetic phenotype has high expectations. The key issue for the development of PPAR pan agonists, as well as PPAR dual agonist combinations, is whether they can deliver an improved therapeutic index compared to the existing PPAR subtype selective agonists. More clinical information on these PPAR pan agonists is anxiously anticipated and will be closely examined as the first generation of these compounds advance through development.

### **1.2.11 Selective PPAR Modulators (SPPARMs)**

Another potential approach to minimize side effects is to identify new selective PPAR modulating drugs that can deliver improved therapeutic indexes. The design of selective modulators requires consideration of the many factors that control the functional properties of a ligand. For example, the level of agonism induced by a ligand is regulated in part by the ability to recruit co-activators as well as the relative abundance of specific co-activators present in a given tissue. The functional profile of a ligand is thus dependent upon the context of tissue, available concentrations of co-factor proteins and target gene [100, 101]. A ligand, therefore, can function as a full agonist in one tissue where sufficient concentrations of co-activators are present and as a partial agonist or antagonist in selective tissues with insufficient levels of co-activator proteins. The kinetics of co-factor recruitment plays a defining role in the assembly of transcriptional complexes and can also influence the level of agonism. Finally, the unique structural receptor conformations induced by a ligand plays a key role in determining differential co-activator recruitment. Hence, ligands that modulate the



activity of PPARs in a tissue and pharmacological specific manner would offer opportunities to regulate desired biological pathways while reducing undesired side effects pathways. Based on this concept, selective estrogen receptor modulator (SERMs) drugs with improved therapeutic benefits compared to the natural estrogen receptor ligand estradiol have been successfully developed [102]. The success of the SERMs has inspired the development of selective PPAR modulators (SPPARMs), in particular selective PPAR $\gamma$  modulators able to uncouple insulin sensitizing and adipogenesis properties [103]. Microarray studies investigating the gene expression profile of TZDs in a variety of organs has shown that some genes are universally regulated by TZDs while the regulation of other genes is ligand specific [104]. These results provide hope that the rational design of novel PPAR $\gamma$  ligands which activate target genes that mediate glucose disposal but are neutral toward genes involved in undesired side effects such as weight gain, fluid retention or edema can be developed. In recent years, several unique PPAR $\gamma$  modulators with differential potency and selectivity have been described. The limited characterization of these ligands, however, has not definitively demonstrated that these compounds possess efficacy with improved safety profiles compared to existing PPAR $\gamma$  antidiabetic agents. Nevertheless, a collection of exciting results observed with various PPARs modulators has encouraged several pharmaceutical companies to increase their research efforts to identify novel SPPARMs with pharmacological efficacy and minimized adverse effects.

### **1.2.12 PPAR antagonists**

Genetic studies in humans and mice paradoxically suggest that a moderate reduction of PPAR $\gamma$  activity may confer a reduced risk for the development of type 2 diabetes. New research efforts have begun to explore

the potential utility of PPAR antagonists to deliver therapeutic benefit with reduced side effect profiles [83]. Therefore, a number of pure PPAR $\gamma$  antagonists and a series of triazolone based PPAR $\alpha$  antagonists useful as tool compounds have been reported.

### 1.3 Structure-based drug discovery

Discovering new drugs is crucial in providing novel treatments to improve the health of the developed world's increasingly aging population as well as in combating the threats posed by emerging new diseases. The fast pace of development and increased prosperity of large areas of the world will lead to increases in incidence of various chronic conditions (such as diabetes, cancer and cardiovascular problems), but also the expectation of improved healthcare, life expectancy and quality of life. These necessities continue to challenge and inspire the huge scientific and financial resources of the pharmacological industry [105].

The potential of detailed structural knowledge to provide a molecular basis of disease was first demonstrated by Max Perutz in his studies relating mutations to the structure of haemoglobin in the 1960s. By the mid-1970s, structural insight were being used not only to rationalise structure-activity relationship but also to provide guidance in the design of compounds with improved properties against such targets as dihydrofolate reductase and angiotensin converting enzyme. These early descriptions of structure-based design illustrate the two long-standing applications of structural methods in drug discovery. The first is to provide detailed understanding of the mechanism of action of the protein and how this relates to its biological function. Such understanding can be significant in designing the most appropriate strategy for modulating the activity of the target and the design of the *in vitro* and *in vivo* assays on which drug discovery depends. The second conventional use of structural methods is to employ the structure of a lead molecule bound to the target to guide the design of modifications to improve compound affinity, selectivity or drug-like properties.

These protein crystal structures were an important driver in moving drug discovery to be more rational and target oriented. As more structural information has become available, an increasing number of drug-discovery projects use rational, target-oriented approaches that rely on either explicit or model structures of the target.

Nowadays, an appreciation of the 3D structure of both the compounds and their target are a part of just about every drug-discovery project. This target structure can be experimentally determined, a model constructed on the basis of homology or a virtual model of the receptor created on the basis of the chemical structure of the known active compounds. In addition, computational methods such as virtual screening and experimental methods such as fragment screening can generate many new ideas for compound templates and possible interactions with the active site. The major advantage of experimentally determining the structure of these different compounds bound to the target is to increase the confidence in the hypotheses and increase the scope of subsequent design. This encourages the medicinal chemists to embark on novel and often challenging syntheses in the search for novel, distinctive and drug-like lead compounds. Our ability to predict conformational changes in proteins and the binding energy of protein-ligand complexes remains relatively poor, so there is still plenty of scope for experience, inspiration and guess work in the details of design.

The determination of the structure of a protein target, perhaps complexed to a substrate or a ligand, can provide a clear insight into its mechanism of action, which can often be related to the biological or therapeutic role. Modern structural biology, particularly protein crystallography, is generating the structure of an increasing number of therapeutically important targets. The two main issues limiting the number of

structures are the ability to produce sufficient quantities of pure, soluble, functional, homogenous protein for crystallography trials and the ability of the protein to form regular crystals suitable for diffraction experiments. This combination of limitations often means that a structure is not available for the whole therapeutic target. However, even the structure of individual domains can be sufficient to make a real impact on a discovery project and provide conditions to understand the overall function of the protein. The members of PPAR family provide one example. Although each receptor consists of a number of domains, the detailed structure of just the ligand-binding domain is sufficient to successfully design selective ligands. However, the complexities of the function of the receptor in the cell can only be understood in terms of the interaction between the different domains that have an influence on receptor activity.

The crystal structure of a ligand bound to a protein provides a detailed insight into the interactions made between the two molecules. Such understanding can be used to design changes to the ligand introducing new interactions to modify the affinity and specificity of the ligand for a particular protein. In addition, the structure can be used to identify where the ligand can be changed to modulate the physicochemical and ADME (absorption, distribution, metabolism, and excretion) properties of the compound, by showing which parts of the compound are important for affinity and which parts can be altered without affecting binding.

As the availability of crystal structures increased in the early 1990s, a number of experimental and computational methods were developed to use the structure of the protein target as a route to discover novel hit compounds. The methods include *de novo* design, virtual screening and fragment-based discovery. *Virtual screening* use computational docking methods to assess

which of the large database of compounds will fit into the unliganded structure of the target protein. Current protocols and methods can, with up to 80% success, predict the binding position and orientation of ligands that are known to bind a protein. However, identifying which ligands bind into a particular binding site is much less successful, with many more false positive hits being identified. *De novo design* attempts to use the unliganded structure of the protein to generate novel chemical structures that can bind. There are varying algorithms, most of which depend on identifying initial hot spots of interactions that are then grown into complete ligands. *Fragment-based drug discovery* is founded on the premise that most ligands that bind strongly to a protein active site can be considered as a number of smaller fragments or functionalities, which can be identified by screening a small library of molecules by X-ray crystallography, NMR spectroscopy or functional assay. The structures of the fragments binding to the protein can be used to design new ligands by adding functionality to the fragment, by merging together or linking various fragments or by grafting features of the fragments onto existing ligands.

Selection of promising, well characterized hits and leads is essential for success in the drug discovery process. Furthermore, information on the interaction of potential drug candidates with the targeted biomolecule is important as a basis for the understanding of more complex schemes. Binding assays are the type of assays that provide such information on affinity, kinetics and thermodynamics [106]. Until recently, obtaining reliable data was often difficult and time consuming, because most of the methods available used labeled compounds that had to be specially synthesized. Many of the methods were not able to follow a binding event in real time. Stop flow technologies have for a long time been the only possibility to get kinetic

information on an interacting system, but this technology is time and material consuming.

High-throughput screening (HTS) set-ups are preferentially used to perform functional and binding assays in order to be able to test a large number of compounds in a short time. It is well known that often a very large portion of false positive [107] hits are identified for many reasons: interference with the labeling method, interaction with substrate or other auxiliary reagents, general and/or promiscuous protein binding.

Biophysical binding assays are alternative tools in generating label free, high quality data on the interaction between a target and a potential drug candidate. Label free screening methods include mass spectroscopy [108], analytical ultracentrifugation (AUC) [109], nuclear magnetic resonance spectroscopy [110], isothermal titration calorimetry (ITC) [111] and biosensor [112, 113].

Biosensors based on optical detection principles are the type of sensors most often used. They offer a rapid way to determine relevant binding data without the need for labeling of the interacting molecules. These biosensors measure in real time the quantity of complex formed between a molecule immobilized on the sensor surface and a molecule in solution. The optical biosensor type most often used in such experiments is based on determining small changes in refractive index induced at the interface upon binding. A huge number of different optical techniques to monitor such refractive index changes have already been introduced in the past and this number is still increasing [114, 115]. Surface plasmon resonance (SPR) is currently the most widely used. When first launched, the technology was most frequently applied in the characterization of diagnostic antibodies used in immunological testing. With the growing interest in biomolecular drugs,

the technique was more and more applied in the drug discovery. A real challenge, however, was to apply the technique for the discovery of low molecular weight drugs. It is only more recently that interactions of small synthetic molecules with biomolecules were described. This type of application became possible due to increased sensitivity through improvements in hardware, software and data evaluation [116].

Of all the techniques that are currently available to measure binding, ITC is the only one capable of measuring not only the magnitude of the binding affinity but also the magnitude of the two thermodynamic terms that define the binding affinity: the enthalpy ( $\Delta H$ ) and entropy ( $\Delta S$ ) changes. Several reports examine issues concerning drug design and the correlation of thermodynamic and X-ray structural data. New instruments allow volumetric effects in biochemical systems to be evaluated calorimetrically and to substantially expand the throughput of differential scanning calorimetry measurements in drug discovery and other high-throughput applications [117].



## 2. Aim of the study

The aim of this study has been the biostructural characterization of the ligand binding domain (LBD) of the three PPAR isotypes complexed with both natural (resveratrol, betulinic acid, saponins and sapogenins) and synthetic (halofenic acid and AL29-26) ligands, indeed a better understanding of the ligand binding mode and its relation to the activity could suggest novel basis for ligand design and enable the development of safer drugs with minimized unwanted side-effects. The development of more balanced drugs interacting with PPARs, devoid of the side effects showed by the currently marketed PPAR $\gamma$  full agonists, is considered the major challenge for the pharmaceutical companies. Therefore, alternative strategies have been used to develop ligands with a modulated and selective pharmacological profile among PPARs in order to reduce the undesired effects and obtain more beneficial responses (*e.g.* dual or pan agonists with an optimal receptor subtype selectivity ratio: partial agonists towards PPAR $\gamma$  and full agonists towards PPAR $\alpha$  and/or PPAR $\beta/\delta$ ).

This study arises from the participation to several research projects, supported from both private and public organizations, concerning the screening of a compounds collection for the identification of novel ligands for PPAR nuclear receptors, which also made it possible financing my PhD.

To this purpose, X-ray crystallography represents one of the most powerful approaches providing information for structure-based ligand design. Indeed, knowledge of the 3D structures of protein targets is now playing a major role in all stages of drug discovery. Therefore, the complex of PPARs with several ligands has been solved in order to investigate the binding mode in the LBD of these nuclear receptors.

In addition to these structural studies, the binding between PPARs and some of the examined ligands has been further characterized by Isothermal Titration Calorimetry (ITC) and Surface Plasmon Resonance (SPR). ITC is a powerful technique that allows to obtain all the thermodynamic parameters associated to the protein/ligand interaction at equilibrium, such as the affinity constant  $K_a$ ,  $\Delta H$  and  $\Delta G$ . SPR technology has been used to measure the kinetic parameters of the binding, including the rate constants ( $K_{on}$  and  $K_{off}$ ), and to reveal the antagonist character of some ligands. Compared to ITC, SPR allows to consume less sample and to perform high-throughput experiments, as in the case of the screening of a large number of saponins/sapogenins in a single experiment.

Moreover, structural studies on PPAR $\gamma$  mutant F360L, which is associated with familial partial lipodystrophy, have been also performed in complex with the partial agonist LT175 to provide insights into the structural basis of the transactivation deficiency of this pathological mutant.

For all these experiments, the ligand binding domain of the three PPAR isoforms has been expressed as soluble fusion protein using *E.coli* as heterologous host and then purified through many steps of liquid chromatography.

## 3. Experimental methods

### 3.1 Expression and purification of PPARs LBD

The recombinant ligand binding domain (LBD) of human PPAR $\gamma$  (gene ID 5468, amino acids 174–477, expected molecular mass 34.5 kDa), PPAR $\alpha$  (gene ID 5465, amino acids 180–468, expected molecular mass 33.3 kDa) and PPAR $\beta/\delta$  (gene ID 5467, amino acids 185–477, expected molecular mass 33.27 kDa) was expressed as N-terminal His-tagged protein using the pET28a vector (Novagen) and then purified as follows. Freshly transformed *E. coli* BL21 (DE3) were grown in LB medium with 30  $\mu\text{g/ml}$  of kanamycin at 310 K to an OD<sub>600</sub> of 0.6. The culture was then induced with 0.2 mM isopropyl- $\beta$ -D-thio-galactopyranoside (IPTG) and further incubated at 291 K for 20 hours (overnight). Cells were harvested with centrifugation and resuspended in a 20 ml/liter culture of Buffer A [20 mM Tris, pH 8.0, 150 mM NaCl, 10% (v/v) glycerol, 1 mM Tris 2-carboxyethylphosphine HCl (TCEP)] in the presence of protease inhibitors (Complete Mini EDTA-free; Roche Applied Science). Cells were sonicated in an ice bath and the soluble fraction was isolated by centrifugation (35000 rpm for 45 minutes). The supernatant was loaded onto an Ni<sup>2+</sup>-nitrilotriacetic acid column following the procedure recommended by the manufacturer (GE Healthcare, UK) and eluted stepwise with a gradient of imidazole 10–500 mM in Buffer A (batch method). The fractions containing the pure protein were analyzed by SDS gel electrophoresis with Coomassie blue staining. The protein was then dialyzed over Buffer A to remove imidazole and cleaved with 10 units/mg of thrombin protease (GE Healthcare, UK) at room temperature for 2,5 hours. The cleavage was monitored by SDS-PAGE and the identity of the native and digested protein was determined on the basis of the molecular weight. The

digested mixture was reloaded onto a Ni<sup>2+</sup>-nitrilotriacetic acid column to remove the His-tags and the undigested protein. The flow-through was dialyzed with Buffer B [20 mM Tris, pH 8.0, 10% (v/v) glycerol, 1 mM Tris 2-carboxyethylphosphine HCl (TCEP)] to remove NaCl and then loaded onto a HiTrap™ Q HP anion-exchange column (GE Healthcare, UK) and eluted with a linear gradient of 0.01-500 mM sodium chloride in Buffer B using a BioLogic DuoFlow™ FPLC system (BioRad Laboratories, USA). The pooled fractions were analyzed by SDS gel electrophoresis and those containing PPARs were concentrated using Amicon® Ultra centrifugal filter with a 10 kDa cutoff membrane (EMD Millipore, USA). Finally, the protein was purified by gel-filtration chromatography on a Superdex™ 75 10/300 GL column (GE Healthcare, UK) eluted with Buffer C [20 mM Tris, pH 8.0, 0,5 mM EDTA, 1 mM Tris 2-carboxyethylphosphine HCl (TCEP)]. In the case of the PPARβ/δ LBD, the cell-lysis supernatant was treated and partially purified as for the PPARγ/α LBD and the protein was further purified by two steps of column chromatography. After the addition of thrombin protease to cleave the N-terminal His-tag, the pooled fraction from the nickel-chelate column was dialyzed against buffer D (20 mM MES, 10 mM DTT, 100 mM ammonium acetate, pH 6.0) and loaded onto a HiTrap™ SP HP cation-exchange column (GE Healthcare, UK). The protein was eluted with a linear gradient of 0.01–1.0 M Ammonium acetate. Finally, the protein was purified by gel-filtration chromatography on a Superdex™ 75 10/300 GL column (GE Healthcare, UK) eluted with buffer E (20 mM HEPES, 10 mM DTT, 500 mM Ammonium acetate, pH 7.5).

For crystallization, PPARγ, PPARα and PPARβ/δ LBDs were then concentrated at 8-10 mg mL<sup>-1</sup> using Microcon® centrifugal filter with a 10 kDa cutoff membrane (EMD Millipore, USA) and the concentration was estimated by Bradford Assay (BioRad Laboratories, USA) with calibration

against a set of Bovine Serum Albumine (BSA) standards of known concentration. The purity of the proteins was determined to be greater than 95% using SDS gel electrophoresis with Coomassie blue staining.

The QuickChange Site-Directed Mutagenesis Kit (Stratagene) was used to introduce the point mutations F360L and R357A into the bacterial expression vectors.

## **3.2 Crystallization, data collection and structure determination**

- **Soaking experiment of PPAR $\gamma$ -LBD and co-crystallization of PPAR $\alpha$ -LBD with AL29-26**

Crystals of apo-PPAR $\gamma$ -LBD (0.3 x 0.3 x 0.2 mm) were obtained by vapour diffusion at 291 K using a sitting drop made by mixing 2  $\mu$ l of protein solution [8 mg mL<sup>-1</sup>, in 20 mM Tris, pH 8.0, 0.5 mM EDTA, 1 mM Tris 2-carboxyethylphosphine HCl (TCEP)] with 2  $\mu$ l of reservoir solution (0.8 M Sodium citrate and 0.15 M Tris, pH 8.0). The crystals were soaked for several days in a storage solution (1.2 M Sodium citrate and 0.15 M Tris, pH 8.0) containing the ligand (0.25 mM) and then flash-cooled in liquid nitrogen. The ligand dissolved in DMSO was diluted in the storage solution so that the final concentration of DMSO was 0.5% (v/v). The storage solution with 20% (v/v) glycerol was used as cryoprotectant. Preliminary PPAR $\alpha$ -LBD co-crystallization were performed by using a Phoenix liquid-handling robot (Art Robbins Instruments, USA) with the ligand AL29-26 in a threefold excess with respect to the protein. Crystals (0.7 x 0.2 x 0.2 mm), obtained at the condition A12 of the Qiagen JCSG Core I Suite [PEG 3350 20% (w/v), 0.2 M Magnesium acetate], were freeze-dried using the mother solution with 35% (w/v) PEG 3350 as cryoprotectant and used for data collection. Co-crystallization trials were also performed for PPAR $\beta/\delta$ -LBD/AL29-26 and

small crystals were obtained at the conditions G5 [PEG 6000 10% (w/v), citric acid 0.1 M, pH 5.0], G6 [PEG 6000 5% (w/v), citric acid 0.1M, pH 5.0] and H5 [PEG 3000 10% (w/v), Sodium chloride 0.2 M, Phosphate/citrate 0.1 M, pH4.2] of the Qiagen JCSG Core I Suite. X-ray data set were collected at 100 K under a nitrogen stream by using synchrotron radiation (beamline ID 23-2 at ESRF, Grenoble, France). The collected data were processed with the programs *MOSFLM* and *SCALA* [118]. Structure solution was performed with *AMoRe* [119] using the coordinates of PPAR $\gamma$ -LBD/LT175(*R*) (PDB ID: 3D6D) [52] and PPAR $\alpha$ -LBD/APHM13 [125] complexes as the starting models for PPAR $\gamma$ -LBD and PPAR $\alpha$ -LBD, respectively. The coordinates were then refined with *CNS* [120]. All data between 50.0 and 2.0 Å were included for PPAR $\gamma$ -LBD/AL29-26 complex belonging to *C2* space group, whereas all data between 50.0 and 1.83 Å were used for PPAR $\alpha$ -LBD/AL29-26 complex appertaining to the space group *P4<sub>1</sub>2<sub>1</sub>2*. A final step of refinement was performed with the software *PHENIX* [121]. The coordinates of PPAR $\gamma$ -LBD/AL29-26 and PPAR $\alpha$ -LBD/AL29-26 complexes have been deposited in the *Protein Data Bank* (PDB) with the code 5HZC and 5HYK, respectively. Diffraction data were also collected for PPAR $\beta/\delta$ -LBD/AL29-26 at low resolution (4-5 Å), but no interpretable electron density maps could be obtained.

- **Soaking experiments of PPAR $\gamma$ -LBD with Caulophyllogenin (SAP19)**

Crystals of apo-PPAR $\gamma$ -LBD (0.2 x 0.2 x 0.2 mm) were obtained by vapour diffusion at 291 K using a sitting drop made by mixing 2  $\mu$ L of protein solution [8 mg mL<sup>-1</sup>, in 20 mM Tris, pH 8.0, 0.5 mM EDTA, 1 mM Tris 2-carboxyethylphosphine HCl (TCEP)] with 2  $\mu$ L of reservoir solution (0.8 M Sodium citrate and 0.15 M Tris, pH 8.0) and equilibrating against 500

$\mu\text{L}$  reservoir solution. The crystals were soaked for eight days in storage solution (1.2 M Sodium citrate and 0.15 M Tris, pH 8.0) containing the ligand (0.25 mM) and then flash-cooled in liquid nitrogen. The ligand dissolved in DMSO was diluted in the storage solution so that the final concentration of DMSO was 0.5% (v/v). The storage solution with 20% (v/v) glycerol was used as cryoprotectant. X-ray data set were collected at 100 K under a nitrogen stream by using synchrotron radiation (beamline ID 23-2 at ESRF, Grenoble, France). The collected data were processed with the programs *MOSFLM* and *SCALA*. Structure solution was performed with *AMoRe*, using the coordinates of PPAR $\gamma$ -LBD/LT175(*S*) (PDB ID: 3B3K) [52] as the starting model. The coordinates were then refined with *CNS*. All data between 50.00 and 2.25 Å were included for PPAR $\gamma$ -LBD/SAP19 complex belonging to *C2* space group. A final step of refinement was performed with the software *PHENIX*. The coordinates of PPAR $\gamma$ -LBD/SAP19 complex have been deposited in the *Protein Data Bank* (PDB) with the code 5F9B.

- **Soaking experiments of PPAR $\gamma$ -LBD with metaglidasen's metabolically active form halofenic acid (*R*) and (*S*)**

Crystals of apo-PPAR $\gamma$ -LBD (0.3 x 0.2 x 0.2 mm) were obtained by the vapour diffusion method at 291 K using a sitting drop made by mixing 2  $\mu\text{L}$  of protein solution [10 mg mL<sup>-1</sup>, in 20 mM Tris, pH 8.0, 1 mM Tris 2-carboxyethylphosphine HCl (TCEP)] with 2  $\mu\text{L}$  of reservoir solution (0.8 M Sodium citrate and 0.15 M Tris, pH 8.0). Crystals were soaked for two weeks in a storage solution (1.2 M Sodium citrate and 0.15 M Tris, pH 8.0) containing the ligand (0.25 mM). The ligand was dissolved in DMSO and added to the storage solution so that the final concentration of DMSO was 0.5% (v/v). The storage solution with 20% (v/v) glycerol was used as a

cryoprotectant.

X-ray crystallographic data were collected at 100 K under a nitrogen stream by using synchrotron radiation (beamline ID29 at ESRF, Grenoble, France). The diffracted intensities were processed with the programs *MOSFLM* and *SCALA*. Structure solution was performed with *AMoRe*, using the coordinates of PPAR $\gamma$ -LBD/LT175(*S*) complex (PDB ID: 3B3K) [52] as the starting model. The coordinates were then refined with the software *PHENIX*. All data between 58 and 2.6 Å were included for both structures. The coordinates of PPAR $\gamma$ -LBD/(*R*)-2 and PPAR $\gamma$ -LBD/(*S*)-2 complexes have been deposited in the *Protein Data Bank* with access codes 4PVU and 4PWL, respectively.

- **Co-crystallization of PPAR $\gamma$ -LBD F360L with LT175 and PPAR $\gamma$ -LBD R357A with rosiglitazone**

The protein complexes with the ligands were formed by mixing 98  $\mu$ l protein solution (10 mg mL<sup>-1</sup>) with 2  $\mu$ l ligand stock solution (50 mM in DMSO) so that the ligands were in a threefold excess with respect to the protein and the final concentration of DMSO was 2% (v/v). The mutant complexes in buffer C [20 mM Tris, pH 8.0, 0.5 mM EDTA, 1 mM Tris 2-carboxyethylphosphine HCl (TCEP)] were used for crystallization at 291K by the vapour-diffusion method in 96-well sitting-drop plates (MRC plates; Molecular Dimensions, UK). Preliminary crystallization trials of the mutant complexes were performed with a Phoenix liquid-handling robot (Art Robbins Instruments, USA) by mixing 200 nl protein solution with an equal volume of reservoir solution (Biocrystal Facility at the CNR Institute of Biology and Molecular Pathology, Sapienza University of Rome). Crystals of PPAR $\gamma$ -LBD F360L with LT175 (referred to in the following as F360L) appeared in well No. 18 (0.49 M Sodium dihydrogen phosphate, 0.91 M



dipotassium hydrogen phosphate, pH 6.9) and No. 25 (3.5 M Sodium formate, pH 7.0) of the Index crystallization screen (Hampton Research). More suitable crystals for X-ray analysis were then obtained by the vapour-diffusion method at 291 K using a sitting drop made by mixing 2  $\mu$ l protein–ligand solution (8 mg ml<sup>-1</sup> in 20 mM Tris, 1 mM TCEP, pH 8.0) with 2  $\mu$ l reservoir solution (3.5 M Sodium formate, pH 7.0, or 1.4 M Sodium/Potassium phosphate, pH 6.9) and equilibrating against 0.5  $\mu$ l reservoir buffer. Crystals appeared after a few days from both tested conditions and belonged to space group  $P2_12_12$  or  $I222$ , respectively. Crystals were flash-cooled in liquid nitrogen after brief soaking in a cryoprotectant buffer composed by mother-liquor solution with 20% (v/v) glycerol. Crystals of R357A with rosiglitazone (referred to in the following as R357A) belonging to space group  $C222_1$  appeared in well No. 5 [50% (w/v) PEG 500 MME/PEG 20K, 0.06 M MgCl<sub>2</sub> and CaCl<sub>2</sub>, 0.1 M Sodium HEPES and MOPS, pH 7.5] of the Morpheus crystallization screen (Molecular Dimensions, UK). Suitable crystals for X-ray data collection were directly flash-cooled in liquid nitrogen after brief soaking in a cryoprotectant buffer composed by mother-liquor solution with 20% (v/v) glycerol.

X-ray data were collected at 100 K under a nitrogen stream by using synchrotron radiation (beamlines ID23-2 for F360L and ID29 for R357A at ESRF, Grenoble, France). The collected data were processed with *MOSFLM* and *SCALA* for the crystal of F360L belonging to space group  $I222$  and *XDS* and *XSCALE* [122] for that belonging to space group  $P2_12_12$ . Structure solution was performed with *AMoRe* using the coordinates of PPAR $\gamma$ -LBD/LT175(S) complex (PDB ID: 3B3K) [52] as the starting model. The coordinates were then refined with *CNS*. Finally, both refined models were optimized by the *PDB\_REDO* web server using *REFMAC 5.8.0049* [123]. The coordinates of F360L complexed with LT175 have been deposited in the

*Protein Data Bank* (PDB ID: 4L98 for space group  $P2_12_12$  and 4L96 for space group  $I222$ ). *MOSFLM* and *SCALA* were used to process the data regarding the mutant R357A in complex with rosiglitazone. Structure solution was performed with *AMoRe* using the coordinates of PPAR $\gamma$ -LBD/rosiglitazone complex (PDB ID: 2PRG) [39]. The coordinates were then refined with *PHENIX* and the quality of the structure was validated using *MolProbity* [124]. The coordinates of this complex have been deposited in the *Protein Data Bank* with access code 4O8F.

- **Soaking experiment of PPAR $\gamma$ -LBD with resveratrol**

Crystals of apo-PPAR $\gamma$ -LBD (0.2 x 0.3 x 0.2 mm) were obtained by vapour diffusion at 291 K using a sitting drop made by mixing 2  $\mu$ L of protein solution [10 mg mL<sup>-1</sup>, in 20 mM Tris, pH 8.0, 0.5 mM EDTA, 1 mM Tris 2-carboxyethylphosphine HCl (TCEP)] with 2  $\mu$ L of reservoir solution (0.8 M Sodium citrate and 0.15 M Tris, pH 8.0) and equilibrating against 500  $\mu$ l reservoir solution. The crystals were soaked for three days in storage solution (1.2 M Sodium citrate and 0.15 M Tris, pH 8.0) containing the ligand (0.25 mM) and then flash-cooled in liquid nitrogen. The ligand (Cayman Chemicals, USA) was dissolved in Dimethyl sulfoxide (DMSO) and added to the storage solution so that the final concentration of DMSO was 0.5% (v/v). The storage solution with 20% (v/v) glycerol was used as cryoprotectant.

X-ray data were collected at 100 K under a nitrogen stream by using synchrotron radiation (beamline XRD1 at Elettra, Trieste, Italy). The diffracted intensities were processed with the softwares *MOSFLM* and *SCALA*. Structure solution was performed with *AMoRe* using the coordinates of PPAR $\gamma$ -LBD complexed with the agonist LT175(S) (PDB ID: 3B3K) as a starting model [52]. The coordinates were then refined with *CNS*. All data

between 52.10–2.85 Å were included. The coordinates of PPAR $\gamma$ -LBD complexed with resveratrol have been deposited in the *Protein Data Bank* with access code 4JAZ.

- **Soaking experiment of PPAR $\gamma$ -LBD with betulinic acid**

Crystals of apo-PPAR $\gamma$ -LBD (0.2 x 0.2 x 0.2 mm) were obtained by the vapour diffusion method at 291 K using a sitting drop made by mixing 2  $\mu$ L of protein solution [10 mg mL<sup>-1</sup>, in 20 mM Tris, pH 8.0, 1 mM Tris 2-carboxyethylphosphine HCl (TCEP)] with 2  $\mu$ L of reservoir solution (0.8 M Sodium citrate and 0.15 M Tris, pH 8.0) and equilibrating against 500  $\mu$ l reservoir solution. The crystals were soaked for one week in storage solution (1.2 M Sodium citrate and 0.15 M Tris, pH 8.0) containing the ligand (0.5 mM) and then flash-cooled in liquid nitrogen. The ligand was dissolved in Dimethyl sulfoxide (DMSO) and added to the storage solution so that the final concentration of DMSO was 1% (v/v). The storage solution with 20% (v/v) glycerol was used as cryoprotectant.

X-ray data were collected at 100 K under a nitrogen stream by using synchrotron radiation (beamline BM14U at ESRF, Grenoble, France). The diffracted intensities were processed with the softwares *XDS* and *XSCALE*. Structure solution was performed with *AMoRe* using the coordinates of PPAR $\gamma$ -LBD complexed with the agonist LT175(R) (PDB ID: 3D6D) as a starting model [52]. The coordinates were then refined with *CNS*. All data between 50.00–2.00 Å were included in the refinement. The coordinates of PPAR $\gamma$ -LBD complexed with BA have been deposited in the *Protein Data Bank* with access code 5LSG.

### 3.3 Isothermal titration calorimetry

ITC experiments were performed at 298 K by using an ITC200 microcalorimeter (MicroCal, Inc., USA). The PPAR $\gamma$  and PPAR $\alpha$  LBDs were extensively dialyzed against a solution of HEPES (20 mM, pH 8.0) and Tris 2-carboxyethylphosphine HCl (TCEP, 1 mM) with Amicon<sup>®</sup> Ultra centrifugal filter, and the final exchange buffer was used to dilute the ligand stock solution (50 mM in DMSO). DMSO was added to the protein solution at the same percentage of the ligand solution (1%, *v/v*). Samples were centrifuged before the experiments to eliminate possible aggregates. Protein and ligand solutions were also degassed before use. The protein solution (50  $\mu$ M) was placed in the sample cell, and ligand solution (500  $\mu$ M) was loaded into the syringe injector. The titrations involved 19 injections of 2  $\mu$ L each at 180 second intervals. The syringe stirring speed was set to 1000 rpm. A reference titration of ligand into buffer was used to correct for heats of dilution. In the experiments with betulinic acid, a reverse titration was performed with the protein solution (500  $\mu$ M) injected into the cell containing the ligand (50  $\mu$ M), both with 0.1% DMSO (*v/v*).

Thermodynamic data was processed with the software Origin 7.0 provided by MicroCal. The  $\Delta H$  values were measured for both titrations, and fitting the isotherms with one-site binding model yielded the values of the association constant ( $K_a$ ). From the Gibbs-Helmholtz equation is also calculated the change of entropy ( $\Delta S$ ). The inflection point in the calorimetric isotherm gives the stoichiometry value  $n$ , indicating the ligand:protein ratio of the binding. To correct for any discrepancies in the baseline outlined by the software, a manual adjustment was performed. In all of the experiments with PPAR $\gamma$ -LBD F360L mutant, the protein solution (25–50  $\mu$ M) was placed in the sample cell and the co-activator SRC-

1 (500  $\mu\text{M}$ ) was loaded into the syringe injector. The experiments with SRC-1 (purchased from GL Biochem Ltd, Shanghai, People's Republic of China) were performed after equilibrating the protein with LT175 in a twofold excess.

In the experiment of PPAR $\gamma$ -LBD with 13-(*S*)-HODE, the ligand solution (400  $\mu\text{M}$ ) was obtained by dissolving 10  $\mu\text{g}$  of the ligand in 83  $\mu\text{l}$  of exchange buffer and titrated against the protein solution (40  $\mu\text{M}$ ).

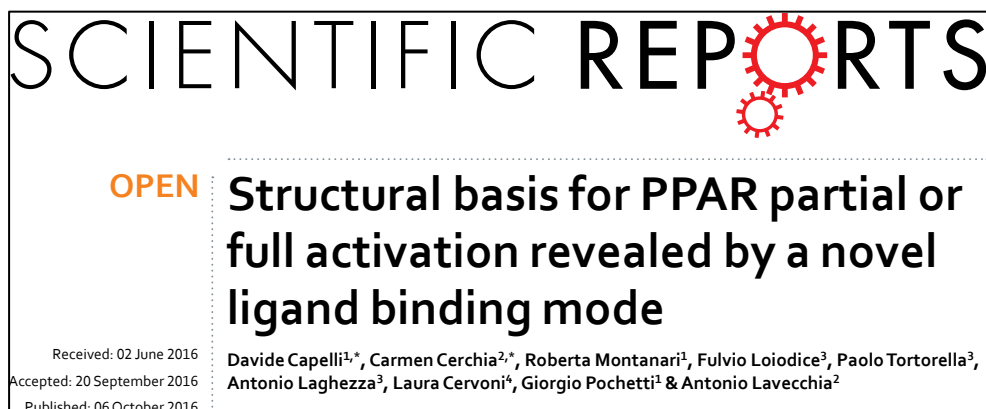
In the experiment of PPAR $\gamma$ -LBD with caulophyllogenin, exchange buffer was used to dilute the ligand stock solution (25 mM in DMSO) and the same percentage of DMSO (2%, *v/v*) was added to the protein solution. The titrations involved 19 injections of 2  $\mu\text{L}$  each at 150 second intervals.

### 3.4 Surface Plasmon Resonance

Surface plasmon resonance analyses were performed by using Pioneer *AE* optical biosensor equipped with COOH5 sensor chips (SensiQ Technologies, Inc., USA). PPAR $\gamma$ -LBD surfaces were prepared by using standard amine-coupling procedures [126] and HBS [Hepes-buffered saline: 20 mM Hepes, pH 7.4, 150 mM Sodium chloride, 0.005% (*v/v*) P20] as the running buffer. Flow cells were activated for 7 minutes by injecting 140  $\mu\text{L}$  of 50 mM *N*-hydroxysuccinimide (NHS):200 mM ethyl-3(3-dimethylamino) propyl carbodiimide (EDC). Fifty  $\mu\text{L}$  of a 0.25 mg  $\text{mL}^{-1}$  PPAR $\gamma$ -LBD solution (in 10 mM Sodium acetate, pH 5.0) were injected for 5 minutes at 10  $\mu\text{L}/\text{min}$  on channels 1 and 3 (channel 2 was used as ref. 3, for a duplicate experiment), followed by a 70- $\mu\text{L}$  injection of ethanolamine to block any remaining activated groups on the surface. More than 13,500 RU of protein were immobilized on both channels. The stability of the PPAR $\gamma$  surface was demonstrated by the flat baseline achieved at the beginning (0–60 seconds) of each sensorgram. The screening of the analytes (saponins and sapogenins)

was performed using HBS without P20, with 1 mM DTT and 2% (v/v) DMSO. To collect detailed kinetic data the OneStep [127-129] protocol was used, injecting the analytes at a flow rate of 50  $\mu\text{L}/\text{min}$  and at the concentration of 100  $\mu\text{M}$  (50  $\mu\text{M}$  for SAP14 and SAP15) over the three channels at 293 K (association phase of 180 seconds). Five buffer blanks were injected for double referencing. The regeneration of the surfaces between binding cycles was not necessary because all the analytes dissociate quickly in the 120 second dissociation phase. A DMSO calibration plot was constructed [buffer sample containing 1–3% (v/v) DMSO] to correct for bulk refractive index shifts [130]. Data were collected at a rate of 20 Hz. All sensorgrams were processed by using double referencing [131]. First, the responses from the reference surface (channel 2) were subtracted from the binding responses collected over the reaction surfaces to correct for bulk refractive index changes. Second, the response from an average of the blanks was subtracted to remove any systematic artifact observed between the reaction and the reference flow cells. To obtain kinetic rate constants and affinity constants the corrected response data were fit in the QDAT software provided by SensiQ Technologies. A kinetic analysis of each ligand/analyte interaction was obtained by fitting the response data to a reversible 1:1 bimolecular interaction model (but for few analytes a 2:1 interaction model was used). The equilibrium dissociation constant ( $K_d$ ) was determined by the ratio  $k_{off}/k_{on}$ .

## 4. Results and discussion



### 4.1 The pan agonist AL29-26

In this study a novel PPAR pan agonist (AL29-26; Figure 24) has been identified using a structure-based virtual screening (SBVS) approach and its crystal structure in the complex with PPAR $\alpha$  and PPAR $\gamma$  LBDs has been solved. This naphthalenic derivative showed a very attractive PPAR pan agonist activity profile in transactivation assay: potent full agonist on PPAR $\alpha$  and partial agonist on  $\gamma$  and  $\beta/\delta$  subtypes (Table 2). The structural investigation revealed that this ligand occupies a new pocket of PPAR $\alpha$  LBD whose filling is allowed by the ligand-induced switching of the F273 side chain from a closed to an open conformation. The comparison between this pocket and the corresponding cavity in PPAR $\gamma$  provides a rationale for the different activation of the ligand towards PPAR $\alpha$  and PPAR $\gamma$ , suggesting a novel basis for ligand design. To date, indeed, the data show that an appropriate dual PPAR $\gamma/\alpha$  activation results in improved metabolic profile.

However, an over-activation of PPAR $\gamma$  can lead to serious side effects including weight gain and steatosis, for this reason PPAR $\gamma$  partial agonists are more advisable. On the other hand, a strong activation of PPAR $\alpha$  is also beneficial because improves dyslipidemia, lowering plasma tryglicerides and increasing HDL cholesterol levels. Therefore, the search for the optimal pharmacological profile of a ligand plays an important role and for this purpose is required the understanding, at molecular level, of the mechanism by which the ligand behaves as full or partial agonist on PPARs.

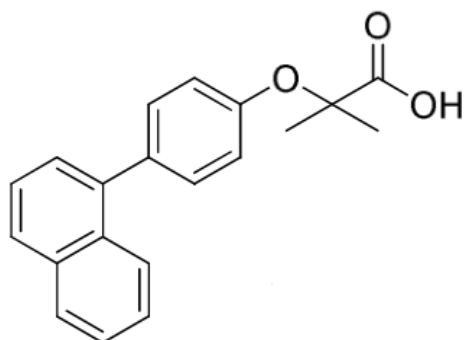


**Figure 24.** Chemical structure of AL29-26.

Compound	PPAR $\alpha$		PPAR $\gamma$		PPAR $\beta/\delta$	
	EC <sub>50</sub> ( $\mu$ M)	E <sub>max</sub> <sup>a</sup>	EC <sub>50</sub> ( $\mu$ M)	E <sub>max</sub> <sup>a</sup>	EC <sub>50</sub> ( $\mu$ M)	E <sub>max</sub> <sup>a</sup>
AL29-26	0.31 $\pm$ 0.13	87 $\pm$ 8	5.3 $\pm$ 1.6	27 $\pm$ 3	11 $\pm$ 2	54 $\pm$ 6
Wy14,643	1.6 $\pm$ 0.3	100 $\pm$ 10	i	i	i	i
rosiglitazone	i	i	0.04 $\pm$ 0.02	100 $\pm$ 9	i	i
L165,041	i	i	i	i	1.6 $\pm$ 1.3	100 $\pm$ 10

**Table 2.** Results of transactivation assays performed on the three PPAR isotypes with AL29-26 and the reference agonist compounds. <sup>a</sup> Efficacy values were calculated as the percentage of the maximum obtained fold induction with the reference compounds. i = inactive at tested concentrations.



#### **4.1.1 Crystallization and structure determination of the complexes PPAR $\alpha$ -LBD/AL29-26 and PPAR $\gamma$ -LBD/AL29-26**

Crystals (0.3 x 0.3 x 0.2 mm) of apo-PPAR $\gamma$ -LBD (Figure 25) were obtained by vapour diffusion using the sitting drop method and then soaked for several days in storage solutions containing the ligand (0.25 mM). As regards PPAR $\alpha$ -LBD, co-crystallization trials were performed using the Phoenix liquid-handling robot with the ligand in three-fold excess with respect to the protein. Suitable crystal (0.7 x 0.2 x 0.2 mm) for X-ray data collection were obtained at the condition A12 of the Qiagen JCSG Core I suite (see Experimental Methods). Preliminary co-crystallization trials were also performed for PPAR $\beta/\delta$ -LBD and small crystals were obtained at the conditions G5, G6 and H5 (see Experimental Methods) of the same crystallization screen. X-ray diffraction data were collected at ESRF of Grenoble (France), but only the crystal structures of PPAR $\alpha$ -LBD and PPAR $\gamma$ -LBD complexes were solved since the ligand could be unambiguously modelled in the electron density maps (Figures 26A-C).

The solved structures for PPAR $\alpha$ - and PPAR $\gamma$ -LBD have been deposited in the PDB with codes 5HYK and 5HZC, respectively, and the crystallographic statistics are shown in Table 3. Diffraction data were also collected for PPAR $\beta/\delta$ -LBD/AL2926 complex at low resolution (4 - 5 Å), but no interpretable electron density maps could be obtained. With the aim to obtain more suitable crystal for X-ray analysis of the latter complex, the three conditions identified in the trials were reproduced on a larger scale but they have not been successful.

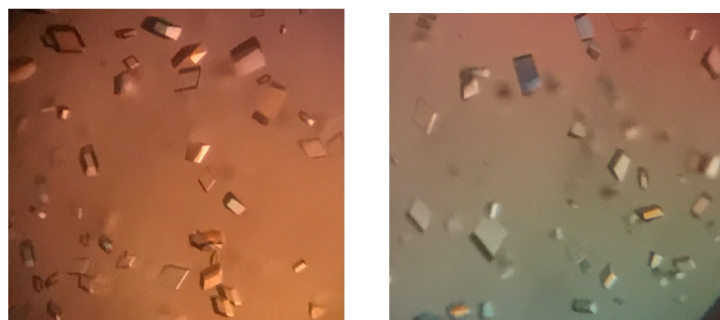


**Figure 25.** Crystals of apo-PPAR $\gamma$ -LBD.

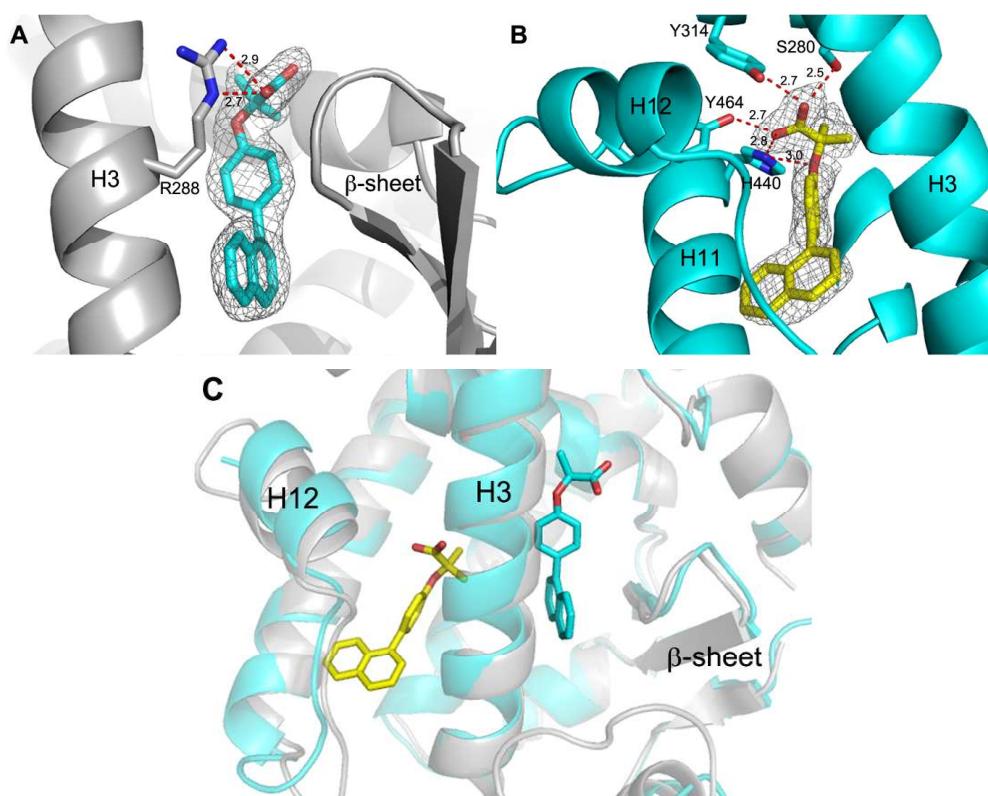


**Figure 26.** Ligand binding of AL29-26 to A) PPAR $\gamma$ -LBD (grey) and B) PPAR $\alpha$ -LBD (cyan). *2Fo-Fc* electron density maps are shown in mesh and countered at  $1\sigma$ . C) Superposition of PPAR $\alpha$ -LBD/AL2926 (ligand in yellow) and PPAR $\gamma$ -LBD/AL2926 (ligand in cyan) crystal structures.

### 4.1.2 PPAR $\gamma$ -LBD/AL29-26 structure: new position of the carboxylate in the region of partial agonists

As known, the apo-form of PPAR $\gamma$ -LBD crystallizes as a dimer, where the molecule A of the asymmetric unit has its activation function-2 helix (H12) in the active conformation and the molecule B in the inactive conformation, due to the crystal packing. AL29-26 was very easily modelled in the density of the molecule B and its binding mode in the LBD of PPAR $\gamma$  is shown in Figure 26A. A second molecule of the ligand could be also fitted in molecule A of the dimer with a similar binding mode. The protein-ligand interactions observed in chains A and B were essentially the same, therefore the two complexes of the asymmetric unit will be described hereafter as a generic model. Notably, the ligand occupies the conventional region of PPAR $\gamma$  partial agonists, between helix 3 and the  $\beta$ -sheet, even though its position is significantly different from that of all the partial agonists known in literature (Figure 27).

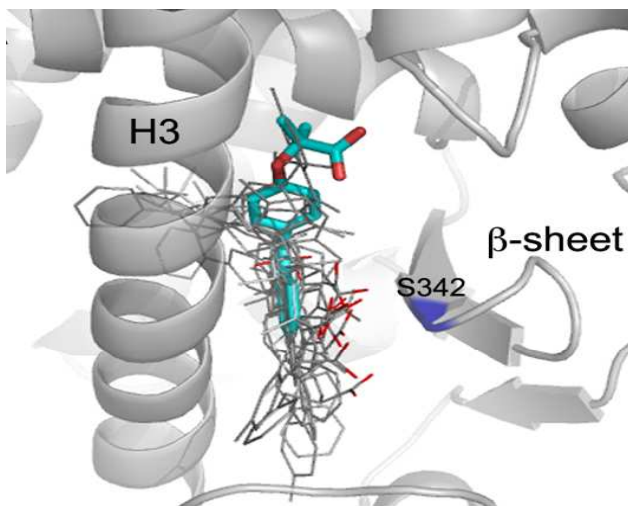


**Figure 27.** Superposition of PPAR $\gamma$  complexes (grey) with known partial agonists (PDB IDs: 3D6D, 4PVU, 4PWL, 4JL4, 4JAZ, 4E4K, 2Q5P, 2Q6S, 2Q5S, 4E4Q, 5F9B) onto the PPAR $\gamma$  complexes with AL29-26 (cyan). The carboxylate groups are depicted in red, the residue S342 in blue.

	PPAR $\gamma$ -LBD/AL29-26	PPAR $\alpha$ -LBD/AL2926
<b>Data collection</b>		
space group	<i>C2</i>	<i>P4<sub>1</sub>2<sub>1</sub>2</i>
cell dimension <i>a, b, c</i> [Å]	93.40, 60.79, 119.00	63.65, 63.65, 126.00
wavelength [Å]	0.873	0.873
resolution range [Å]	50.00 - 2.00	50.00 - 1.83
last shell [Å]	2.21 - 2.00	2.05 - 1.83
<i>R</i> <sub>merge</sub> [%]	5.9 (64.6) <sup>a</sup>	7.1 (51.8) <sup>a</sup>
unique reflections	23665	43099
mean ( <i>I</i> )/ $\sigma$ ( <i>I</i> )	10.1 (1.2) <sup>a</sup>	22.7 (5.0) <sup>a</sup>
completeness	98.0 (97.0) <sup>a</sup>	100 (100) <sup>a</sup>
No. of molecules in asymmetric unit	2	1
<b>Refinement</b>		
resolution range [Å]	50.00 - 2.00	50.00 - 1.83
<i>R</i> <sub>work</sub> [%]	22.5	21.1
<i>R</i> <sub>free</sub> [%]	26.8	26.2
Bond lengths r.m.s.d. [Å]	0.009	0.007
Bond angles r.m.s.d. [deg]	1.519	1.108

**Table 3.** Summary of crystallographic analysis for crystals of the PPAR $\gamma$ -LBD/AL2916 and PPAR $\alpha$ -LBD/AL29-26 complexes. <sup>a</sup> The values in parentheses refer to the outer shell.

Conversely from the other PPAR $\gamma$  partial agonists, which form a more or less efficient H-bond interaction through the carboxylate group with the NH of S342 belonging to inner strand of the  $\beta$ -sheet, the carboxylate of AL29-26 is significantly shifted along the axis of H3 toward H5, with one of its oxygens forming two H-bonds with the side chain of R288 (2.7 and 2.9 Å; Figure 26A). The other carboxylate oxygen makes H-bonds (2.7 Å) with two

water molecules bridged to CO of L228 on the loop 1/2 (2.8 Å) and to CO of M329 on the helix 5 (2.9 Å), respectively. One of the two methyl groups of the ligand makes van der Waals (vdW) interactions with the methyls of the A292 and M329 side chains (3.8 and 4.3 Å, respectively), the other one with those of L330 and L333 (4.2 and 4.1 Å, respectively). The single aromatic ring is sandwiched between the R288 and L330 side chains. The naphthalene ring is positioned between I341 and C285 side chains, facing the NH of S342, usually H-bound to the carboxylate group of canonical partial agonists. The naphthalene system of the ligand is almost perpendicular to the plane of the single aromatic ring.

It would be interesting to determine whether this unusual position of a partial agonist could be associated to a different stabilization of the  $\beta$ -sheet and, consequently, to a different degree of inhibition of the S245 phosphorylation with respect to other partial agonists. In the recent years, indeed, a new antidiabetic mechanism depending upon the inhibition of S245 phosphorylation (PPAR $\gamma$ 2 residue S273) by cyclin-dependent kinase 5 (Cdk5) has been proposed [71]. This inhibition maintains the transcription of many insulin-responsive genes, such as adiponectin and adipon [71]. Interestingly, obesity and other pro-inflammatory signals induce the phosphorylation of PPAR $\gamma$  at S245, explaining why obese people also develop insulin resistance. Given that the Cdk5 recognition site extends into the first  $\beta$ -strand of PPAR $\gamma$ , structural stabilization of the  $\beta$ -sheet region, caused by partial agonists, presumably makes the residue S245 less accessible to the kinase, protecting the receptor from phosphorylation, an event well correlated with glucose-lowering effects. This might explain how PPAR $\gamma$  partial agonists can exhibit similar or higher antidiabetic effects than

those of TZDs and other full agonists. At this regard, it has been recently published the crystal structure of PPAR $\gamma$ -LBD complexed with the ligand SR2067 (PDB ID: 4R06), which interacts with the  $\beta$ -sheet exclusively through hydrophobic interactions mediated by a naphthalene group, revealing a unique kinetic and structural signature for PPAR $\gamma$  partial agonism [132]. The superposition of this structure with that of PPAR $\gamma$ -LBD/AL29-26 shows an equivalent position of the naphthalene groups of the two ligands in front of the  $\beta$ -sheet (Figure 28).

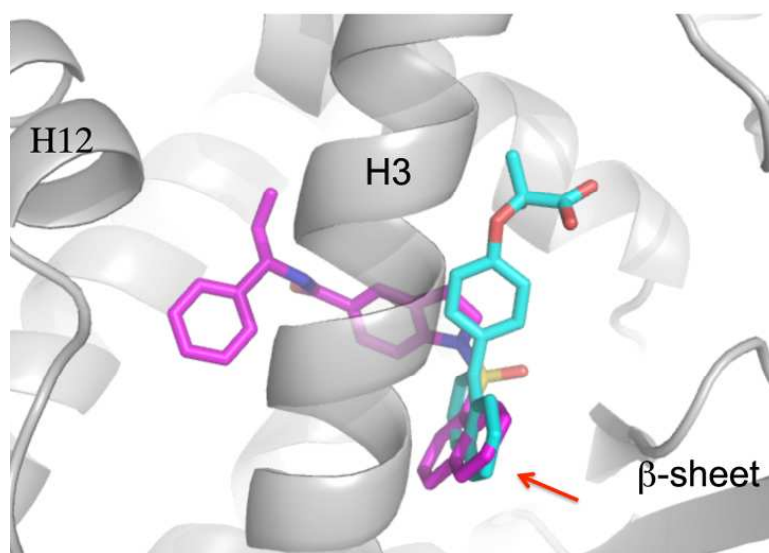


**Figure 28.** Superposition of SR2067 (magenta; PDB ID: 4R06) onto PPAR $\gamma$ -LBD/AL2926 complex (cyan). The red arrow indicates the naphthalene groups of the two ligands.

#### 4.1.3 PPAR $\alpha$ -LBD/AL29-26 structure: ligand occupation of a new pocket

In the complex with PPAR $\alpha$ -LBD, the polar head of AL29-26 is engaged in a very efficient H-bonds network with the side chain of Y464 (2.7

Å) on the helix 12, as well as Y314 (2.7 Å), H440 (2.8 Å) and with OH of S280 (2.5 Å) (Figure 26B). All of the PPAR $\alpha$  agonists already reported in the PDB share the same standard polar interactions. The two methyl groups of the ligand form vdW contacts with M355, F318, H440 and C276, in the upper portion of the binding pocket. The rigid and bulky aromatic groups of the ligand occupy a new region of the hydrophobic pocket within PPAR $\alpha$  ligand binding domain, between H3 and H11, never occupied by other known PPAR $\alpha$  agonists (Figure 29), with the only exception of the ligand BMS-631707 (PDB ID: 2REW) [133]. The opening of this usually inaccessible region is allowed by the ligand-induced switching of the F273 from the commonly adopted extended conformation to the folded gauche\* one ( $\chi^1 = -67^\circ$ ). As a consequence, the aromatic moiety of the ligand occupies the position usually assumed by the aromatic ring of F273, that operates as a gate-keeper for the accommodation of rigid and bulky substituents at the carbon atom linked to the carboxylate group.

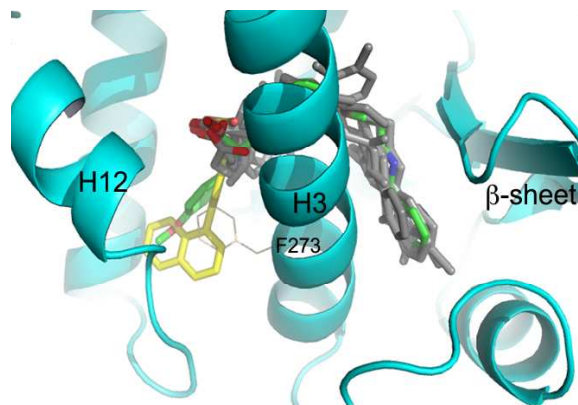


**Figure 29.** Superposition of PPAR $\alpha$  complexes with known partial agonists (gray; PDB IDs: 2REW, 4BCR, 1K7L, 3SP6, 3FEI, 2GTK, 3G8I, 3ET1, 3KDT, 1I7G) onto the PPAR $\alpha$  complex with AL29-26 (ligand yellow, protein cyan). The ligand BMS-631707 (PDB ID: 2REW) is shown in green. The “closed” (trans) conformation of F273 side-chain is also shown (gray).

The above mentioned ligand BMS-631707, containing the conformationally constrained azetidinone ring linked to the carboxylate, behaves in the same manner replacing the side chain of F273, forced to assume a gauche conformation. A similar situation was also observed in the complex of PPAR $\gamma$ -LBD with LT175 (PDB ID: 3B3K) where the rigid and straight diphenyl group of the ligand caused the flipping-out of the corresponding F282 side chain, toward the 'benzophenone pocket', making available a new region of the LBD, the so-called 'dyphenil pocket' [52]. In that case, it was observed that the dyphenil group of LT175 occupied only the first branch (Figure 30). In PPAR $\alpha$  the similar, but more spherical new region of the LBD is totally filled by the single aromatic ring of AL29-26, that occupies the first branch, whereas the naphthalene rings fill the second branch of the cavity (Figure 30).

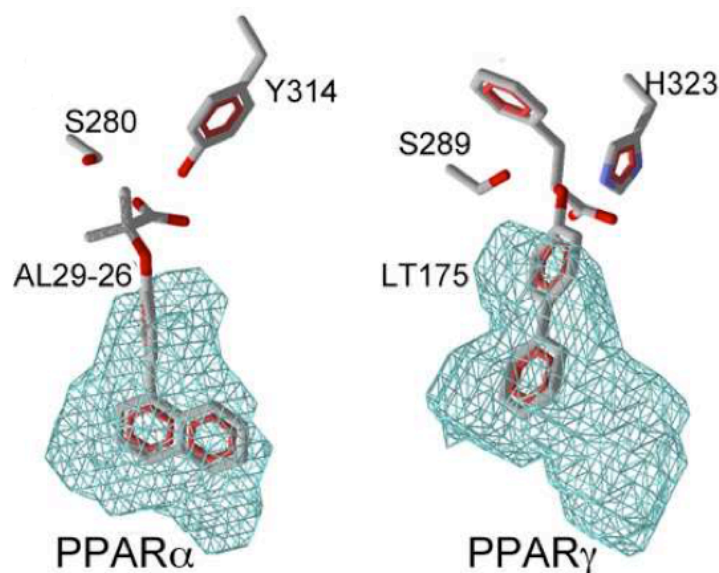


**Figure 30.** New PPAR $\alpha$  (left) and PPAR $\gamma$  (right) hydrophobic pockets allowed by the ligand-induced switching of the F273 side-chain (F282 in PPAR $\gamma$ ). The cavities were calculated using the software Molegro [134].



The positioning of the ligand in this new region induces a significant conformational change of the loop 11/12 that forms the edges of the pocket with H3 and H11. It is worth noting that in all the known structures of PPAR $\alpha$  complexes this loop always assumes a different and ordered conformation in which the residue A454 would make a steric clash with the bulky naphthalene rings of AL29-26. Consequently, the ligand provokes a rearrangement of the loop 11/12 whose new conformation, closer to helix 3, is strongly stabilized by a vdW interaction between A454 and the two methyls of V270, on helix 3 (3.4 and 3.6 Å, respectively) (Figure 31). A further stabilization is achieved through vdW interactions of the methyl groups of A454 and L456 with carbon atoms of the naphthalene ring system (3.4 and 3.6 Å, respectively). This novel and distinct interaction between H3 and the loop 11/12, indirectly, also contributes to further stabilize the active conformation of H12.

The discovery of this new cavity of PPAR $\alpha$ -LBD, analogue to the PPAR $\gamma$ -LBD diphenyl pocket, whose accessibility is regulated by the side chain of the gate-keeper F273, was never observed before and its structural characterization provides new opportunities to rational design of more balanced PPAR modulators. Moreover, we confirmed in this work the many possibilities used by PPARs to modulate the stabilization of the activation function 2 (AF-2) region through a subtle mechanism of molecular cross-talk, mediated by the ligand, among different regions of the protein. It is known the unique mode of binding to PPAR $\alpha$ -LBD of the ligand WY14643 (PDB ID: 4BCR) [135] that revealed a new pattern of nuclear receptor ligand recognition in which a second molecule of ligand is involved in the interaction with the protein, providing additional stabilization to the AF-2

region. This molecule strongly stabilizes the highly mobile  $\omega$ -loop by the formation of a charge cluster that involves the ligand itself, the helix 3 and the loop 11/12, providing in this way a more subtle stabilization of helix 12.

At the same way, in this work we showed that the bulky AL29-26, occupying a new hydrophobic pocket, perturbs the PPAR $\alpha$  standard conformation of the loop 11/12 forcing it to a different and stable conformation in which A454 of the loop strongly interacts with V270 on helix 3. This novel interaction between H3 and the loop 11/12, mediated by the ligand, also contributes to further stabilize the active conformation of H12. Similar mechanisms have been proposed to explain actions of PPAR $\gamma$  partial agonists, that activate H12 to a lesser extent stabilizing H3 and the  $\beta$ -sheet and/or modifying the dynamics of the flexible  $\omega$ -loop [135].

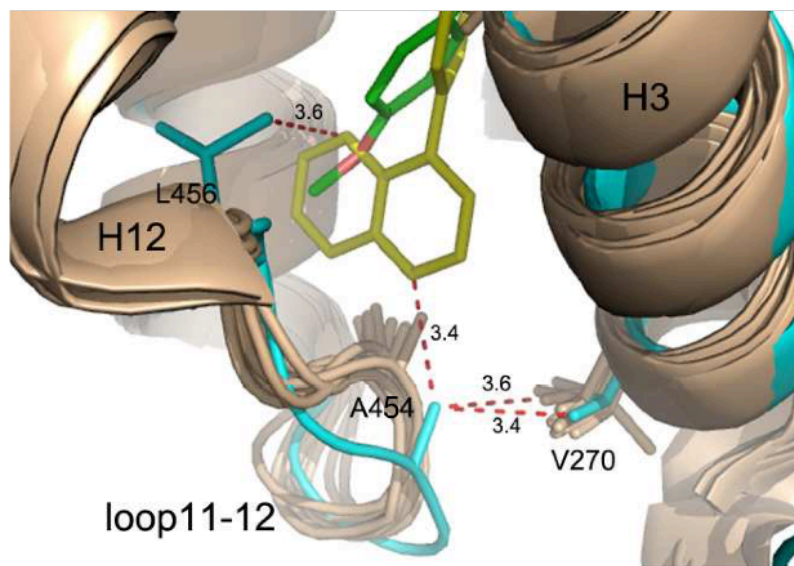


**Figure 31.** New conformation of the loop 11/12 in the PPAR $\alpha$ -LBD/AL29-26 complex: superposition of the loops 11/12 of known PPAR $\alpha$  structures (light-brown) (same PDB IDs of Figure 29) with that of PPAR $\alpha$ -LBD/AL29-26 (ligand yellow, protein cyan). The ligand BMS-631707 (PDB ID: 2REW) is shown in green. Additional vdW interactions realized by AL29-26 are shown as red dashed lines.

#### **4.1.4 Specificity of the new cavity: a steric clash with S289 prevents AL29-26 to occupy the diphenyl pocket of PPAR $\gamma$ -LBD determining its partial agonist properties**

Within PPAR $\gamma$ -LBD the ligand AL29-26 doesn't occupy the diphenyl pocket, preferring to accommodate in the region of partial agonists. In order to investigate the reason of this behaviour, the ligand was modelled in the PPAR $\gamma$  diphenyl pocket considering the different hydrogen-bond network realized by the carboxylate group with respect to PPAR $\alpha$ -LBD, for the presence of H323 instead of Y314. For this purpose the structure of PPAR $\gamma$ -LBD/LT175 complex was used as template, given the structural similarity of the two ligands. AL29-26 could occupy the diphenyl pocket, completely filling the second branch of the cavity even though with very short vdW distances with some residues of the protein (2.7 Å with M463, 2.6 Å with L453 and 3.0 Å with I456 side chains). In this position, however, one of its methyls would make a steric clash with the OH of S289 (2.2 Å), preventing H-bonding with the carboxylate group and perturbing in this way the efficient H-bond network of the ligand (Figure 32A).

On the contrary, in the PPAR $\alpha$  LBD the new hydrophobic pocket has more space to accommodate the ligand due to the presence of the shorter A454 in place of M643 of PPAR $\gamma$ -LBD, the shorter V444 instead of L453 and the side chain of I447 less close to the ligand compared to the corresponding I456. The global volume of the two cavities, calculated by the software Molegro [134], seems to be very similar (200.7 vs 198.1 Å<sup>3</sup> for PPAR $\alpha$ - and PPAR $\gamma$ -LBD, respectively) although showing differences concerning the shape. Unlike the L-shaped PPAR $\gamma$ -LBD diphenyl pocket, indeed, the PPAR $\alpha$  cavity shows an almost spherical shape that better allows the accommodation of a bulkier ligand (Figure 30). In this situation, the two

methylys of the ligand have no clashes with the side chain of S280 (S289 in PPAR $\gamma$ -LBD), due to the shifted positioning of the ligand in the pocket caused by the presence of the bulkier Y314 on helix 12, with respect to PPAR $\gamma$  H323 (Figure 32B).

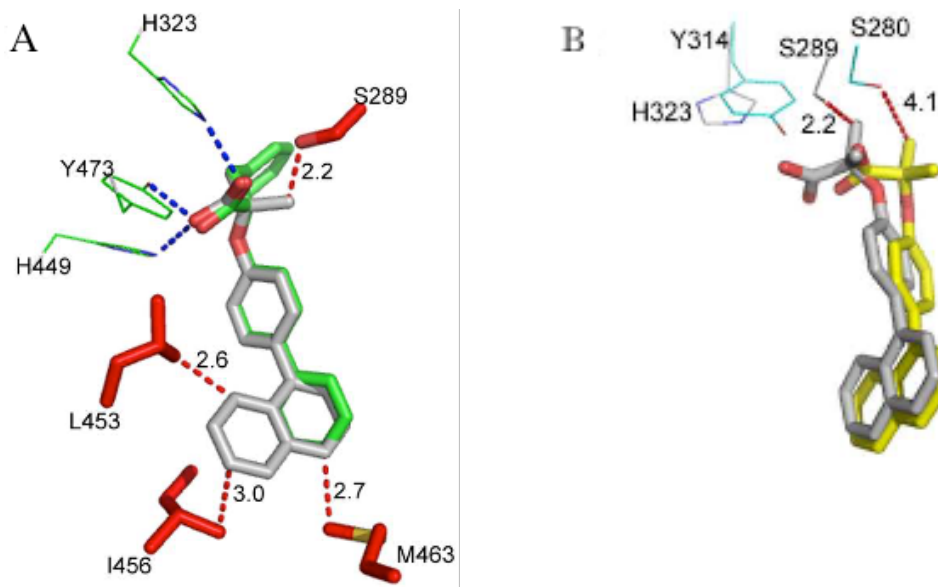
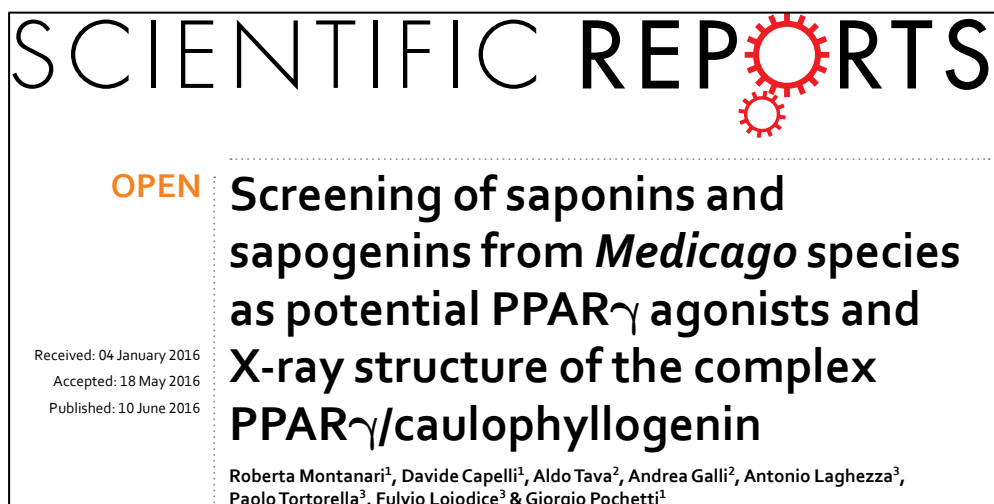


**Figure 32.** A) Modelled AL29-26 (gray) onto LT175 (green) (PDB ID: 3B3K) in the complex with PPAR $\gamma$ -LBD. Residues belonging to the “diphenyl pocket” are shown in red (vdW interactions with AL29-26 as red dashed lines). The residues interacting with the carboxylate group are shown in green (H-bonds are shown as blue dashed lines). B) Superposition of PPAR $\gamma$ -modelled AL29-26 (gray) onto the PPAR $\alpha$ /AL29-26 complex (the ligand is shown in yellow). Two representative residues of PPAR $\gamma$  are shown in gray, the corresponding residues of PPAR $\alpha$  in cyan.

At this regard, we noticed that in the molecule A of PPAR $\gamma$ , whose helix 12 is in its active conformation, there is weak electron density in correspondence of the side chain of F282 in its closed conformation, and some residual *Fo-Fc* electron density is visible in the region corresponding to its “flipped-out” conformation; moreover, there is some poor, not easily interpretable, additional density in the diphenyl pocket that cannot be merely attributed to water molecules and that let hypothesize a small percentage of

occupation of this region by a second molecule of ligand with lower affinity. This could also be a consequence of the soaking method used to bind AL29-26 in the crystal of apo-PPAR $\gamma$ , whereas the ligand is in large excess with respect to the protein. However, this event is not visible in the molecule B of PPAR $\gamma$  where H12, in its inactive conformation, cannot interact with the ligand. In this case the side chain of F282 assumes unambiguously the extended conformation, blocking the entrance of the new pocket. In conclusion, AL29-26 in the PPAR $\gamma$ -LBD complex prefers to occupy the region facing the  $\beta$ -sheet, behaving as a partial agonist. It could be hypothesized that the substitution of one of the two methyl groups of AL29-26 with a H atom could relieve the steric clash with S289 of PPAR $\gamma$  changing the pharmacological character of this ligand and turning it in a more potent agonist.



## 4.2 Saponins and sapogenins as potential PPAR $\gamma$ agonists

Some medicinal plants have been traditionally used to treat metabolic diseases such as insulin resistance, steatosis and diabetes, because of their hypoglycemic and antidiabetic properties. Saponins are a class of chemical compounds found in particular abundance in various plant species which have been reported to exhibit hypoglycemic potential in diabetic states [136, 137], and attracted a lot of interest because of their potent, hypolipidemic and insulin-like properties [138-141]. Saponins are amphipathic glycosides consisting of a sugar moiety linked to a hydrophobic aglycone (sapogenin) with a triterpenoid or a steroid structure. The number of saccharide chains attached to the sapogenin/aglycone core can vary, giving rise to another dimension of nomenclature (monodesmosidic, bidesmosidic, etc.) as can the length of each chain. Due to their variety of chemical structures, naturally occurring saponins display a broad diversity of polarity, hydrophobicity and acidity that determine their various biological and pharmacological features [142]. Saponins from *Platycodi radix* have been shown to improve

homeostasis in type 2 diabetic states, partly by enhancing hepatic and adipocyte insulin sensitivity which is achieved by activating PPAR $\gamma$  [143]. They also inhibit lipogenesis through AMPKa-PPAR $\gamma$ 2 in 3T3-L1 cell and modulate fat accumulation in obese mice [144]. Saponins and sapogenins were recently studied for their anti-inflammatory effect due to the inhibition of NF-kB and for their effect on PPAR transcriptional activity [145, 146]. Particularly, several oleanane-type triterpenoid saponins from the roots of *Pulsatilla koreana* inhibited TNF $\alpha$ -stimulated NF-kB activation in a dose-dependent manner, with IC<sub>50</sub> values ranging from 0.75–8.30  $\mu$ M, repressing the expression of the iNOS and ICAM-1 genes, which play important roles in the inflammatory response [147, 148]. The same compounds also significantly activated the transcriptional activity of PPARs in a dose-dependent manner, with EC<sub>50</sub> values up to 1  $\mu$ M. Moreover, protopanaxatriol, a monoglucoside sapogenin present in the root of *Panax ginseng*, showed antagonist activity towards PPAR $\gamma$  [146]. It specifically inhibited the transactivation activity of PPAR $\gamma$ , but not that of PPAR $\alpha$ ,  $\beta/\delta$  and LXR  $\alpha,\beta$ , by repressing the adipocyte differentiation and ameliorating obesity, insulin resistance, steatosis and hyperlipidemia in diet-induced obesity mice.

#### **4.2.1 Fast screening of saponins and sapogenins from *Medicago* species by SPR**

In the present study a series of previously purified and characterized saponins and sapogenins from *Medicago* species were tested by Surface Plasmon Resonance (SPR) experiments for their ability to bind and activate PPAR $\gamma$ , in order to select the most promising compounds for further activity tests and for X-ray analysis. Compounds of this genus have been shown to possess a broad spectrum of biological properties such as fungicidal,

molluscicidal, insecticidal, nematocidal, allelopathic, antiviral cytotoxic and hemolytic activity [149].

The affinity ( $K_d$ ) and rate constants ( $K_{on}$ ,  $K_{off}$ ) for PPAR $\gamma$ -LBD/saponin or saponin interactions are reported in Table 4 and compared with the reference ligand LT175, whose  $K_d$  obtained by this analytical method (2.34  $\mu$ M) basically confirmed that previously achieved from experiments (3.66  $\mu$ M) [150]. The compounds used in this study (Figure 33) are both saponins (compounds 1–17) and saponinins (compounds 18–24), all having the same pentacyclic triterpene structure with differences in number and position of hydroxyl and carboxylic groups on the triterpene skeleton and nature and number of the sugars linked at C-3 and C-28 position. For saponins, different values of affinity towards PPAR $\gamma$ -LBD were registered: higher affinity ( $K_d$  less than 100  $\mu$ M) were found for saponins 1 (that shows the lowest equilibrium dissociation constant  $K_d = 18.33 \mu$ M), 3, 4, 6–8, 10, and 17; a middle affinity ( $K_d$  125–150  $\mu$ M) was found for saponins 2, 5 and 9, while a very low or no affinity ( $K_d$  from about 500 to >1000  $\mu$ M) was observed for saponins 11–16 (see Table 4). The first group of saponins, including compounds with high and middle PPAR $\gamma$ -LBD affinity, was composed by mono- and bidesmosides of oleanolic acid, 2 $\beta$ -hydroxy oleanolic acid, echinocystic acid, hederagenin, bayogenin and soyasapogenol B, whereas the second group of saponins showing low or no affinity with PPAR $\gamma$ -LBD, are all derivatives of medicagenic and zanhic acid. Concerning saponinins, only echinocystic acid (18) and caulophyllogenin (19) showed considerable affinities for PPAR $\gamma$ -LBD, with  $K_d = 9.70$  and 54.82  $\mu$ M, respectively, whereas the other tested saponinins had very low or no affinity ( $K_d > 500$ , see Table 4).



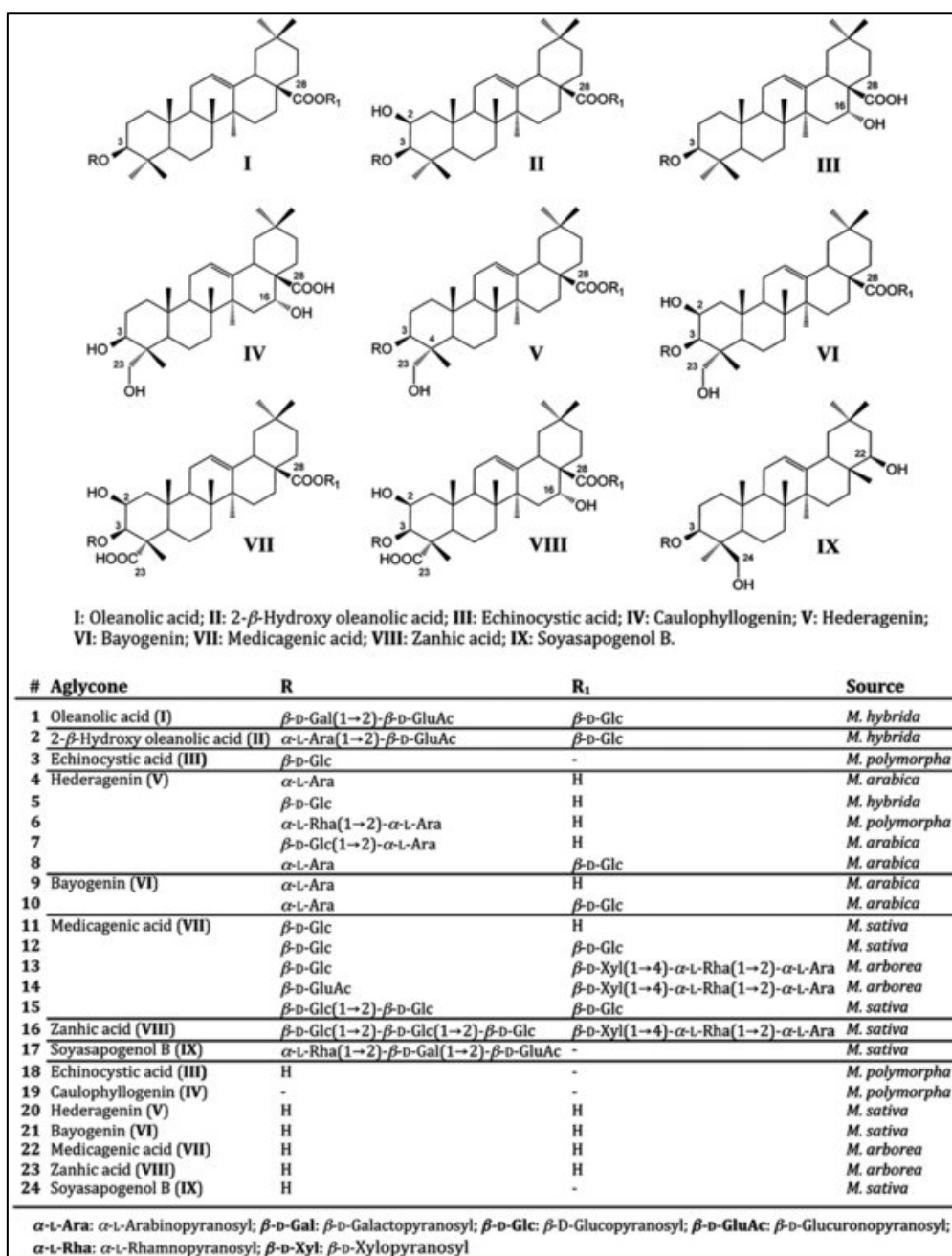
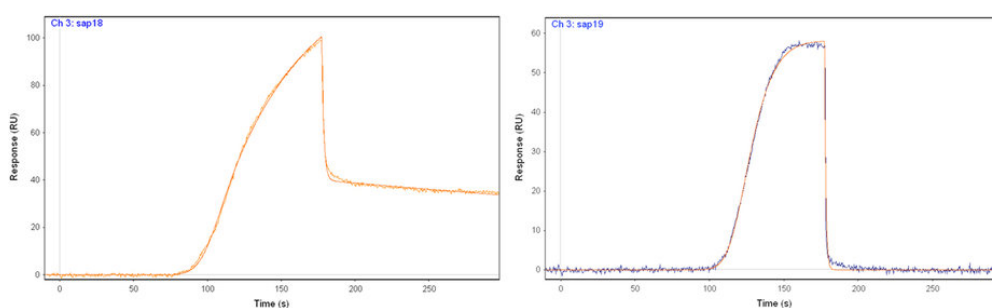


Figure 33. Structure and classification of saponins (1–17) and sapogenins (18–24) used in this study.

Interaction	$K_{on}$ ( $M^{-1} s^{-1}$ ) <sup>a</sup>	$K_{off}$ ( $s^{-1}$ ) <sup>a</sup>	$K_d$ ( $\mu M$ ) <sup>a</sup>
LT175 <sup>b, c</sup>	$3.5(0.1)e^5$ $9.5(0.2)e^2$	0.82(0.04) 0.81(0.02)	2.34(0.04) 850(30)
SAP1	$6.12(0.04)e^4$	1.122(0.002)	18.33(0.09)
SAP2	$1.254(0.003)e^4$	1.572(0.004)	125.34(0.04)
SAP3	$1.567(0.003)e^4$	1.264(0.003)	80.67(0.03)
SAP4	$1.333(0.003)e^4$	0.694(0.002)	52.05(0.05)
SAP5	$1.040(0.002)e^3$	1.381(0.003)	132.71(0.05)
SAP6	$1.346(0.004)e^4$	0.913(0.002)	67.85(0.06)
SAP7	$2.928(0.007)e^4$	1.260(0.003)	43.03(0.03)
SAP8	$3.74(0.01)e^4$	2.139(0.008)	57.18(0.04)
SAP9	$5.18(0.02)e^3$	0.769(0.002)	148.25(0.09)
SAP10	$1.626(0.004)e^4$	1.451(0.004)	89.28(0.04)
SAP11	$1.949(0.006)e^3$	0.970(0.003)	497.4(0.2)
SAP12 <sup>d</sup>	-	-	-
SAP13	$5.64(0.03)e^3$	4.13(0.03)	731.2(0.2)
SAP14	-	-	>1000
SAP15	-	-	>1000
SAP16	-	-	>1000
SAP17 <sup>c</sup>	$5.1(0.1)e^4$	1.68(0.04)	32.5(0.02)
SAP18 <sup>c</sup>	$144.8(0.2)$ $1.98(0.01)e^4$	$1.405(0.004)e^{-3}$ 0.715(0.002)	9.70(0.03) 36.1(0.2)
SAP19	$2.053(0.005)e^4$	1.126(0.002)	54.82(0.03)
SAP20	-	-	>1000
SAP21 <sup>d</sup>	-	-	-
SAP22	$4.65(0.04)e^3$	2.47(0.02)	513(7)
SAP23	$4.76(0.08)e^3$	3.33(0.05)	699.2(0.6)
SAP24 <sup>d</sup>	-	-	-

**Table 4.** Affinity ( $K_d$ ) and rate constants ( $K_{on}$ ,  $K_{off}$ ) for PPAR $\gamma$  receptor/saponin (or sapogenin) interactions. <sup>a</sup> Experimental error is reported in parentheses. <sup>b</sup> LT175 was chosen as reference compound because its  $K_d$  is known from ITC experiments ( $K_d = 3.66 \mu M$ ). <sup>c</sup> For this compound data were fit to a 2:1 molecular interaction model. <sup>d</sup> For this compound data didn't fit to models.

Interestingly, echinocistic acid (18) showed a binding profile that differed from all the other tested compounds. Indeed, the data obtained from kinetic analysis of 18 were more suitable for a 2:1 molecular interaction model (Figure 34), suggesting that two molecules of 18 could simultaneously bind the receptor LBD. In addition, the high affinity binding site has a very small kinetic association rate constant  $K_{on}$  compared to that of the other compounds ( $144.8 \text{ M}^{-1}\text{s}^{-1}$  vs values ranging from  $1 \times 10^3$  to  $7.6 \times 10^4 \text{ M}^{-1}\text{s}^{-1}$ ) and a lower dissociation rate constant  $K_{off}$  ( $1.4 \times 10^{-3}$  vs  $0.3 - 64 \text{ s}^{-1}$ ), therefore a slow kinetics of association and dissociation can be hypothesized. A similar behavior has been observed for other nuclear receptor antagonists [151]. By contrast, caulophyllogenin (19) showed a kinetic behavior characterized by a rapid association and dissociation time (Figure 34).



**Figure 34.** Representative data sets for kinetic analysis of saponins 18 (left) and 19 (right) in the interaction with PPAR $\gamma$ -LBD. Red lines represent the global fits of the data to a 1:1 bimolecular interaction model for SAP19 and a 2:1 model for SAP18. The kinetic parameters obtained from each interaction are reported in Table 4.

The SPR experiment showed that, among saponins, the compounds with higher affinity were, in general, short sugar chains mono- and bidesmoside saponins characterized by the presence of a methyl or alcoholic group at C-23 position on the triterpenic nucleus. On the contrary, a carboxylic group in the same position, as in the derivatives of medicagenic

and zanhic acid, significantly reduced the affinity. In addition, the hydroxyl group at the  $2\beta$  position of the aglycone seemed to lower the affinity. Saponins of  $2\beta$ -hydroxy oleanolic acid (2) and bayogenin (compounds 9 and 10) showed, in general, higher dissociation constants  $K_d$  compared to saponins of oleanolic acid (1) and hederagenin (compounds 4, 6 and 7) in which the  $2\beta$ -hydroxy group was not present. The glycosidic portion of the molecule seemed to be an additional important feature for the interaction with PPAR $\gamma$ -LBD. As reported in Table 4, most saponins with higher affinity were glycosides of hederagenin (compounds 4, 6, 7 and 8), bayogenin (compounds 9 and 10) and soyasapogenol B (17) even though their aglycone portion, hederagenin (20), bayogenin (21) and soyasapogenol B (24), didn't show affinity to the nuclear receptor. This allows to suggest that sugars, in particular when linked at the C-3 position, are of relevance for the interaction mechanisms with the binding site of PPAR $\gamma$ . Sugar chains could either allow a correct positioning of the aglycone moiety in the affinity site of the nuclear receptor or favor its accommodation into an alternative binding site. Also the sugar chain length, in particular at C-28 position, seems to be of importance to improve affinity. The most active saponins are both monodesmosidic or monosaccharide C-28 substituted compounds.

As regards sapogenins, the SPR experiment showed that only echinocystic acid (18) and caulophyllogenin (19) possessed a good affinity for the PPAR $\gamma$ -LBD (for 19 this was also confirmed by ITC analysis). Both compounds are characterized by the presence of a  $16\alpha$ -hydroxyl group in the molecule that probably is another important feature in conferring affinity to PPAR $\gamma$ . The same  $16\alpha$ -hydroxy substituent is also present in zanhic acid but this character is probably not sufficient to contrast the strong binding

inhibition performed by the carboxylic group at C-23 position.

In conclusion, some chemical characteristics of substrates were of relevance in conferring binding affinity to PPAR $\gamma$ . The presence of a methyl or hydroxyl at C-23 position of the triterpenic nucleus strongly increased affinity, which was inhibited from the presence of a carboxylic group at the same position. The 2 $\beta$ -hydroxy substitution seemed to lower the affinity, while the 16 $\alpha$ -hydroxy substitution had some positive effects on affinity only if no carboxylic group was present at C-23 position. Moreover, the glycosylation at C-3 seemed to increase the activity, although it should be taken into account the possibility that oral administrations of saponins might lead to hydrolysis of glycosides from terpenoid. Finally, the SPR analysis has been proved to be a very powerful and fast method for screening a large number of compounds with the aim to select the better candidates as agonists and also antagonists of nuclear receptors.

#### **4.2.2 Toxicity and transcriptional activity on the most affine compounds**

MTT assay was performed by Loiodice and collaborators in order to evaluate the toxicity on HepG2 cells of saponins/sapogenins showing higher affinity, such as compounds 3, 6, 7, 8, 17, 18 and 19. As shown in Table 5, only caulophyllogenin (19) and soyasaponin I (17) did not show cytotoxicity at concentrations up to 100  $\mu$ M, whereas the other tested compounds showed cytotoxic activities at values ranging from 3 to 20  $\mu$ M.

Concerning PPAR $\gamma$  activity, the same compounds were tested at doses lower than that at which they showed cytotoxicity (100  $\mu$ M for soyasaponin I 17 and caulophyllogenin 19, 50  $\mu$ M for saponin 8, 12.5  $\mu$ M for saponins 3 and 7, 6.25  $\mu$ M for saponin 6 and echinocystic acid (18), as

reported in Figure 35A. Only caulophyllogenin (19) behaved as a partial agonist with  $EC_{50} = 12.6 \pm 2.7 \mu\text{M}$  and efficacy =  $9.4 \pm 0.6\%$  (Figure 35B). Its low potency and efficacy should not be underestimated because very similar to those of the well-known selective modulator metaglidasen [152, 153], a compound already investigated as a useful agent for the treatment of type 2 diabetes and hyperglycemia, showing reduced adverse side effects. Echinocystic acid (18) displayed similar activity only at concentrations up to  $6.25 \mu\text{M}$ .

The antagonist behaviour of the above compounds was also evaluated in displacement experiments against rosiglitazone, indicating that only echinocystic acid (18) shows moderate activity reducing the effects of the reference compound by 40% at  $5 \mu\text{M}$ . This property could be useful to inhibit the adipocyte differentiation which is a typical adverse effect of PPAR $\gamma$  agonists. The cytotoxic activity *in vitro* of compound 18 against human cancer cell lines (HepG2) deserves to be deepened to establish a possible role of this sapogenin as potential anti-cancer in combination with other anti-tumorigenic drugs, as already evidenced in previous papers [154, 155]. Echinocystic acid (18) and caulophyllogenin (19) used in this investigation were extracted from *M. polimorpha* (*Leguminose* family), but they are also components of *Crysantellum americanum*, a plant of the *Asteraceae* family which contains several triterpen saponins, whose therapeutic properties as hypolipidemic and hepatoprotective agents are known [156]. Further studies should be also performed to evaluate the anti-inflammatory activity of these sapogenins as possible inhibitors of NF- $\kappa$ B.

Compound	IC <sub>50</sub> (μM)
3	7.8 ± 0.3
6	3.5 ± 0.1
7	12.3 ± 0.2
8	20.2 ± 1.8
17	> 100
18	4.1 ± 0.4
19	> 100

**Table 5.** Cytotoxicity values (MTT assay) on HepG2 from saponins/sapogenins showing higher affinities. IC<sub>50</sub> represents the concentration that reduces the cell viability by 50%.

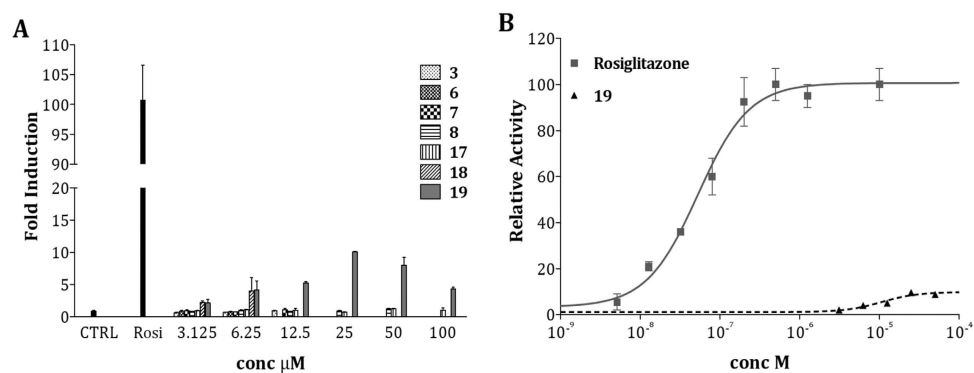


**Figure 35.** A) PPAR<sub>γ</sub> activity from saponins/sapogenins showing higher affinities (Rosi corresponds to the reference compound rosiglitazone); B) Dose-response curve on PPAR<sub>γ</sub> from rosiglitazone and sapogenin 19.

### 4.2.3 Crystal structure of the PPAR $\gamma$ -LBD/caulophyllogenin complex

In order to provide an explanation at molecular level for the different behavior of echinocystic acid (18) and caulophyllogenin (19) as antagonist and partial agonist, respectively, crystals (0.2 x 0.2 x 0.2 mm) of apo-PPAR $\gamma$ -LBD were obtained by vapour diffusion using the sitting drop method and then soaked for eight days in a storage solution containing the ligand (0.25 mM). X-ray data collection for the PPAR $\gamma$  complexes with the two sapogenins was performed at ESRF of Grenoble (France). Unfortunately, for the PPAR $\gamma$ -LBD/echinocystic acid complex the electron density in the region of the ligand could not be clearly interpreted, so that only the structure of the PPAR $\gamma$ -LBD/caulophyllogenin complex was solved and deposited in the PDB with the code 5F9B. The summary of the crystallographic analysis is shown in Table 6.

The final omit map in Figure 36 showed clear electron density in the LBD of PPAR $\gamma$  where one molecule of caulophyllogenin (19) can be easily fitted. The ligand was accommodated between the helix 3 and the  $\beta$ -sheet, where its carboxylic oxygens formed a hydrogen bond (2.1 Å) with the NH group of S342, belonging to the  $\beta$ -sheet, and the CO of L340 (3.3 Å), respectively. The 16 $\alpha$ -hydroxy group is H-bound to the CO of G284 on helix 3 (2.7 Å). The 3 $\beta$ -hydroxy group made a H-bond with the hydroxyl group of the Y327 side-chain (2.9 Å). Moreover, there were extensive van der Waals interactions between the sulphur atom of C285, on the helix 3, and the carbon atoms of the rings C and E of the ligand. The ring E was also engaged in van der Waals interactions with the aromatic ring of F363, on helix 7. Hypothetically, in this orientation of the ligand it could be very easy to



accommodate glycoside moieties linked to the carbon atom 3 that protrude towards the helix 12, in the region occupied by full agonists.

PPAR $\gamma$ -LBD/caulophyllogenin	
<b>Data collection</b>	
space group	<i>C</i> 2
cell dimension <i>a</i> , <i>b</i> , <i>c</i> [Å]	93.21, 61.66, 118.9
monoclinic angle $\beta$ [deg]	102.8
wavelength [Å]	0.8726
resolution range [Å]	50.00 - 2.25
last shell [Å]	2.30 - 2.25
$R_{\text{merge}}$ [%]	6.0 (34.9) <sup>a</sup>
unique reflections	31203 (2012) <sup>a</sup>
mean $\langle I \rangle / \sigma(I)$	9.2 (2.8) <sup>a</sup>
completeness	99.3 (99.5) <sup>a</sup>
multiplicity	3.6 (3.4) <sup>a</sup>
<b>Refinement</b>	
$R_{\text{work}}$ [%]	23.2
$R_{\text{free}}$ [%]	28.1
Bond lengths r.m.s.d. [Å]	0.010
Bond angles r.m.s.d. [deg]	1.389

**Table 6.** Summary of crystallographic analysis for the PPAR $\gamma$ -LBD/caulophyllogenin complex; <sup>a</sup> The values in parenthesis refer to the outer shell.

As demonstrated by the superposition of the crystal structures, the position of caulophyllogenin (19) in the LBD of PPAR $\gamma$  was very similar to that of the partial agonist (*R*) enantiomer of LT175 (PDB ID: 3D6D) [52] (Figure 37A) and also to that of the fatty acid 13-(*S*)-HODE (PDB ID: 2VST) [157], a natural agonist of PPAR $\gamma$  (Figure 37B).

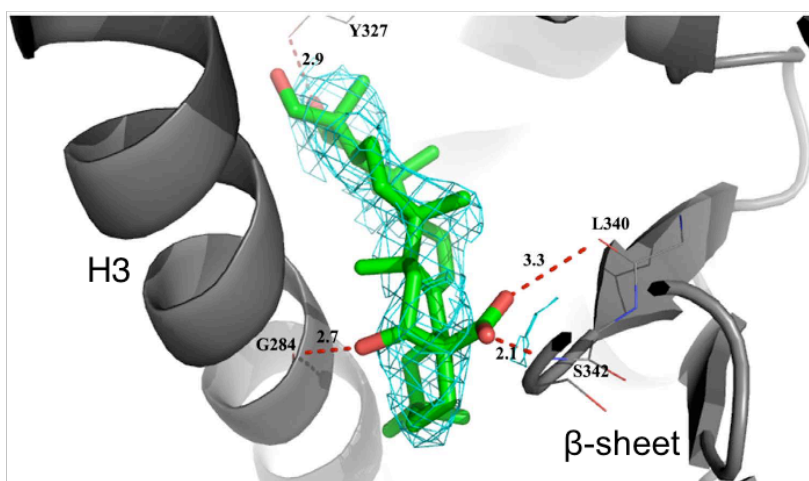


**Figure 36.** Binding of caulophyllogenin in the LBD of PPAR $\gamma$  with  $2F_o-F_c$  electron density map calculated around the ligand.

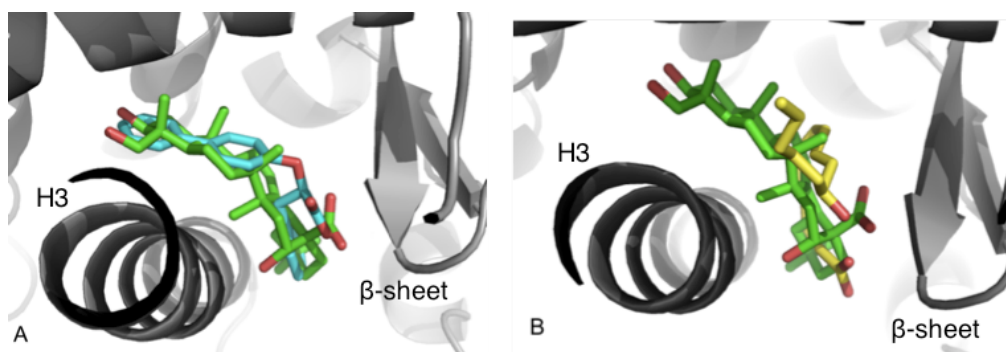


**Figure 37.** Superposition of (A) SAP19 (green) and LT175R (cyan) (PDB ID: 3D6D) and (B) SAP19 (green) and 13-(*S*)-HODE (yellow) (PDB ID: 2VST), in the LBD of PPAR $\gamma$ .

#### **4.2.4 Isothermal titration calorimetry (ITC) assay: comparison between caulophyllogenin and the fatty acid 13-(S)-HODE**

To further confirm the interaction of caulophyllogenin 19 with PPAR $\gamma$ -LBD, ITC experiments were performed comparing the thermodynamic parameters ( $\Delta H$ ,  $\Delta S$  and  $K_d$ ) of this rigid sapogenin with those of the more flexible fatty acid 13-(S)-HODE. This technique is one of the most powerful methods for characterizing protein-ligand interactions, which are observed directly from the change in intrinsic heat (binding enthalpy) of the reaction. The results (Figure 38) indicated that caulophyllogenin (19) binds to the PPAR $\gamma$ -LBD with a  $K_d$  not far from that calculated by SPR techniques (6.5 vs 54.8  $\mu\text{M}$ , respectively). Moreover, the comparison of the thermodynamic parameters between the two compounds showed that although they have similar  $K_d$  values [6.5 and 9.4  $\mu\text{M}$  for caulophyllogenin (19) and 13-(S)-HODE, respectively], the binding of 13-(S)-HODE, whose higher flexibility allows better interactions with the protein, shows a more favorable enthalpic contribution ( $\Delta H = -2.21$  vs  $-1.55$  kcal/mol, respectively), instead the binding of caulophyllogenin (19) is associated to a more favorable entropic term ( $-T\Delta S = -5.46$  vs  $-4.56$  kcal/mol, respectively), also due to the minor loss of translational and rotational degrees of freedom of this more rigid ligand upon binding. In any case, both binding interactions seem to be entropy-driven and more hydrophobic in character.

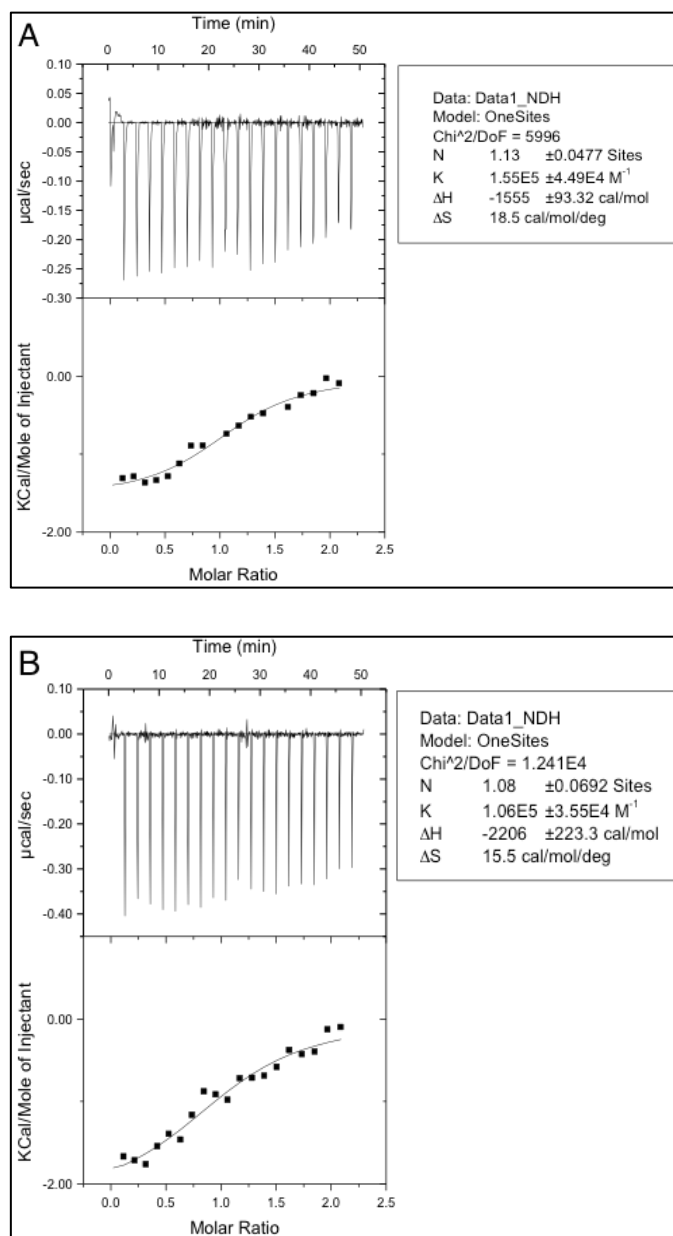


**Figure 38.** Titration of (A) caulophyllogenin (19) (500  $\mu\text{M}$ ) and (B) 13-(S)-HODE (400  $\mu\text{M}$ ) to PPAR $\gamma$ -LBD (50  $\mu\text{M}$ ). The upper panel of each figure shows the raw data of the ITC experiment. The lower panel shows the corresponding binding isotherm fitted according to the “one binding site” model.

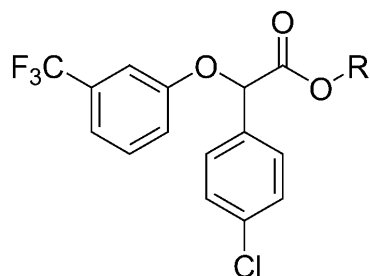
## On the Metabolically Active Form of Metaglidasen: Improved Synthesis and Investigation of Its Peculiar Activity on Peroxisome Proliferator-Activated Receptors and Skeletal Muscles

Antonio Laghezza,<sup>[a]</sup> Roberta Montanari,<sup>[b]</sup> Antonio Lavecchia,<sup>[c]</sup> Luca Piemontese,<sup>[a]</sup> Giorgio Pochetti,<sup>[b]</sup> Vito Iacobazzi,<sup>[d, e]</sup> Vittoria Infantino,<sup>[d, f]</sup> Davide Capelli,<sup>[b]</sup> Michela De Bellis,<sup>[a]</sup> Antonella Liantonio,<sup>[a]</sup> Sabata Pierno,<sup>[a]</sup> Paolo Tortorella,<sup>[a]</sup> Diana Conte Camerino,<sup>[a]</sup> and Fulvio Loiodice\*<sup>[a]</sup>

### 4.3 The metabolically active form of Metaglidasen

Because of the mechanism-based side-effects associated with the use of PPAR $\gamma$  full agonists already developed and marketed, such as rosiglitazone and pioglitazone, emphasis has shifted in the recent years to the development of partial agonists or selective PPAR $\gamma$  modulators (SPPAR $\gamma$ Ms). This approach proposes that diverse PPAR $\gamma$  ligands, depending on their structure, would bind in a distinct manner to PPARs, inducing various levels of activation and distinct conformational changes of the receptors, leading to differential interactions with co-activators and co-repressors. This may enable uncoupling of the benefits of PPAR activation from the adverse effects associated with full agonism. According to this concept, a number of these modulators have already demonstrated desirable pharmacological profiles in various rodent models with significantly decreased side effects relative to those generally observed with existing full agonists [31, 104, 158, 159]. One key representative is metaglidasen, a selective PPAR $\gamma$  partial agonist that structurally, mechanistically and preclinically differs from the glitazones [160].

Metaglidasen is the (*R*) enantiomer of halofenate (compound 1; Figure 39) and both of them are prodrugs esters that are rapidly and completely modified *in vivo* by non specific esterases to give the corresponding free acid form (compound 2; Figure 39).



1: R = CH<sub>2</sub>CH<sub>2</sub>NHCOCH<sub>3</sub> (halofenate)  
2: R = H (halofenic acid)

**Figure 39.** Structure of halofenate and its metabolically active form, halofenic acid.

Metaglidasen showed promising therapeutic potential for the treatment of type 2 diabetes and hyperglycemia, as demonstrated by some recent patents [161, 162]. Metaglidasen and (*S*)-halofenate also showed the same activity both *in vitro* and *in vivo*, suggesting a lack of stereoselectivity for PPAR $\gamma$  [158, 160, 163]. The reason of the clinical development of (*R*)-1 in place of the most accessible (*S*)-halofenate seems to be its decreased inhibitory activity toward cytochrome P450 2C9 (CYP2C9) relative to the corresponding *dextro* isomer (*S*)-1 [164].

#### 4.3.1 PPAR activity

Two stereoisomers of halofenic acid were evaluated for their agonist activity on the human PPAR $\gamma$ -LBD and PPAR $\alpha$ -LBD subtypes. To this

purpose, transactivation assays were performed by Antonio Laghezza and the results were compared to corresponding data for rosiglitazone and Wy14,643 used as reference compounds in the PPAR $\gamma$  and PPAR $\alpha$  assays, respectively (Figure 40). The maximum induction obtained with the reference agonist was defined as 100%. As concerns PPAR $\gamma$ , the results showed this receptors to lack any stereoselectivity between (*R*)- and (*S*)-halofenic acid, since both isomers behaved as partial agonists with similar potency ( $EC_{50}$ : 4.8 and 7.6  $\mu$ M, respectively) and efficacy ( $E_{max}$ :  $\sim$  10%) confirming previously reported data [160] (Figure 40A).

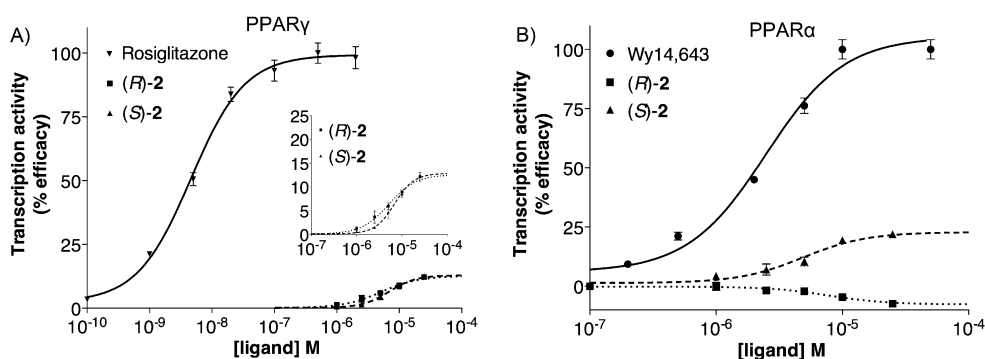


**Figure 40.** Transactivation assay data for A) human PPAR $\gamma$  and B) human PPAR $\alpha$ . Gal4-hPPAR $\gamma$  or Gal4-hPPAR $\alpha$  ligand binding domain expression plasmid was co-transfected with a luciferase reporter plasmid in HepG2 cells. The insert in panel A) is a magnification of the curves that relate only to compounds (*R*)-2 and (*S*)-2. Data are normalized with respect to control, and values are the mean  $\pm$  SEM of n=3 experiments performed in duplicate.

In addition, isothermal titration calorimetry (ITC) was used to calculate the thermodynamic parameters relating to the formation of the complexes of both stereoisomers with the PPAR $\gamma$  ligand binding domain (LBD). The results obtained for the enantiomers (*R*) and (*S*) were  $1.36 \times 10^5$   $M^{-1}$  and  $1.72 \times 10^5$   $M^{-1}$ , respectively, demonstrating that these ligands bind to PPAR $\gamma$ -LBD with similar affinity in according with their functional activity.

Calorimetric data (raw and integration data) for both isomers are shown in Figure 41A.

Although previous experiments reported no activity on PPAR $\alpha$  from racemic halofenic acid [152, 158, 161, 162, 163], the effects on PPAR $\alpha$ -LBD of both (*R*)- and (*S*)-halofenic acid were investigated because of their great similarity with some chiral  $\alpha$ -aryloxy- $\alpha$ -aryacetic acids previously claimed as highly stereoselective PPAR $\alpha$  agonists [165]. Surprisingly, (*S*)-halofenic acid acted as a partial agonist (EC<sub>50</sub>: 11 $\mu$ M, E<sub>max</sub>: 31%), whereas its enantiomer behaved as antagonist (Figure 41B). The antagonist activity was confirmed by a competitive binding assay, in which (*R*)-halofenic acid displayed a dose-dependent inhibition of Wy14,643-mediated PPAR $\alpha$  activity, with a half-maximal inhibitory concentration of  $\sim$  21  $\mu$ M (Figure 42). These data suggest that (*R*)-halofenic acid is able to interact with PPAR $\alpha$ -LBD in such a way to displace the agonist Wy14,643 from the ligand binding domain and inhibit its activity in a cellular context. It is reasonable to assume that this compound is able to similarly displace its enantiomer, thus explaining why racemic halofenic acid does not show PPAR $\alpha$  activity. Due to the absence of crystal structures of PPAR $\alpha$ -LBD complexed with carboxylic antagonists to be used as a starting point for docking, crystallization of the complexes with both (*R*)- and (*S*)-halofenic acid will be crucial to confirm the obtained results. These study are still in progress for PPAR $\alpha$ -LBD, whereas they have already been achieved for PPAR $\gamma$ -LBD with the aim to provide a molecular explanation for the lack of stereoselectivity of this receptors towards the two enantiomers.



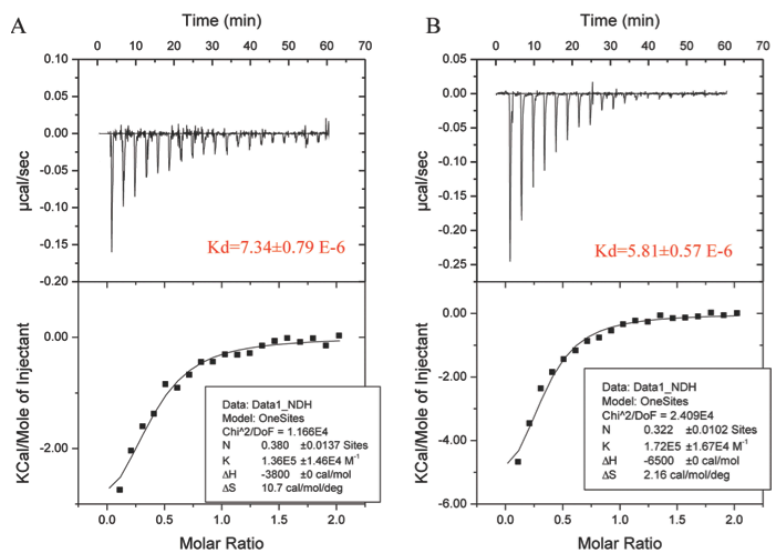


**Figure 41.** Binding of A) (*R*)-halofenic acid and B) (*S*)-halofenic acid to PPAR $\gamma$ -LBD. The upper panel shows the raw data, the lower panel shows the corresponding binding isotherm fitted according to the “one binding site” model.

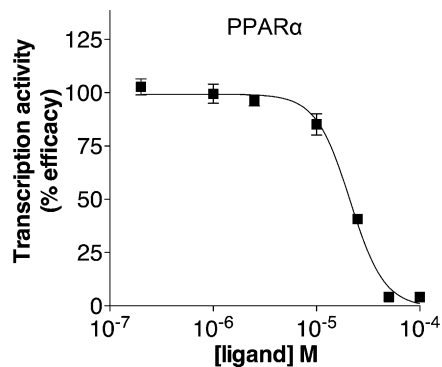


**Figure 42.** PPAR $\alpha$  antagonist effect of (*R*)-2. PPAR $\alpha$  activity was measured in Gal4-hPPAR $\alpha$ -LBD transfected cells treated with Wy 14,643 at 10  $\mu$ M and increasing concentrations of (*R*)-2. Data are normalized with respect to control, and values are the mean  $\pm$  SEM of  $n=2$  experiments performed in triplicate.

### 4.3.2 Crystal structure of (*R*)- and (*S*)-halofenic acid in the PPAR $\gamma$ -LBD

Crystals (0.3 x 0.2 x 0.2 mm) of apo-PPAR $\gamma$ -LBD were obtained by vapour diffusion using the sitting drop method and then soaked for two weeks in storage solutions containing the ligands (0.25 mM). X-ray data collection for the PPAR $\gamma$ -LBD in complex with the two enantiomers was performed at ESRF of Grenoble (France) and the solved structures have been deposited in the PDB with codes 4PVU and 4PWL for the enantiomers (*R*) and (*S*), respectively. Crystals of the PPAR $\gamma$ -LBD complexes belong to the *C*2 space group, with cell parameters shown in Table 7.

As regards (*R*)-halofenic acid, the final omit map (Figure 43) showed clear electron density where one molecule can be easily fitted. This isomer was accommodated between H3 and the  $\beta$ -sheet, where one of its carboxylic oxygen atoms was found to form a hydrogen bond (2.7 Å) with the NH group of S342 belonging to the  $\beta$ -sheet (Figure 44A). This interaction has often been observed in other PPAR $\gamma$  complexes with partial agonists. Upon binding, the ligand forced the side chains of R288 and E291 to assume different conformations. In this new orientation, the charged guanidinium group of R288 interacts with the electronegative trifluoromethyl group of the ligand (3.5 Å) and made van der Waals interactions with the residue A292 belonging to helix 3. The chlorine atom, at the opposite extremity of the ligand, is directed toward a hydrophobic core of the LBD formed by the side chains of I281, L353, F363, and M364. The shortest distances of the chlorine atom were with one methyl group of I281 (3.7 Å) and a carbon atom of the aromatic ring of F363 (3.7 Å).

	PPAR $\gamma$ -LBD/( <i>R</i> )	PPAR $\gamma$ -LBD/( <i>S</i> )
<b>Data collection</b>		
space group	<i>C</i> 2	<i>C</i> 2
cell dimension <i>a</i> , <i>b</i> , <i>c</i> [Å]	93.4, 60.2, 119.1	93.1, 61.7, 118.7
monoclinic angle $\beta$ [deg]	103.4	102.3
wavelength [Å]	0.97623	0.97623
resolution range [Å]	57.91 - 2.60	57.99 - 2.60
last shell [Å]	2.72 - 2.60	2.72 - 2.60
$R_{\text{merge}}$ [%]	4.3 (37.3) <sup>a</sup>	6.4 (48.9) <sup>a</sup>
observation	59572 (6467) <sup>a</sup>	54799 (5959) <sup>a</sup>
unique reflections	19580 (2296) <sup>a</sup>	19771 (2273) <sup>a</sup>
mean $\langle I \rangle / \sigma(I)$	11.8 (2.3) <sup>a</sup>	7.9 (1.8) <sup>a</sup>
completeness	98.0 (95.2) <sup>a</sup>	96.7 (92.6) <sup>a</sup>
multiplicity	3.0 (2.8) <sup>a</sup>	2.8 (2.6) <sup>a</sup>
<b>Refinement</b>		
resolution range [Å]	57.9 - 2.60	58 - 2.60
$R_{\text{work}}$ [%]	20.0	21.8
$R_{\text{free}}$ [%]	25.1	30.8
Bond lengths r.m.s.d. [Å]	0.008	0.027
Bond angles r.m.s.d. [deg]	1.321	1.594

**Table 7.** Summary of crystallographic analysis for the PPAR $\gamma$ -LBD/(*R*)-halofenic acid and PPAR $\gamma$ -LBD/(*S*)-halofenic acid complexes. <sup>a</sup> The values in parentheses refer to the outer shell.

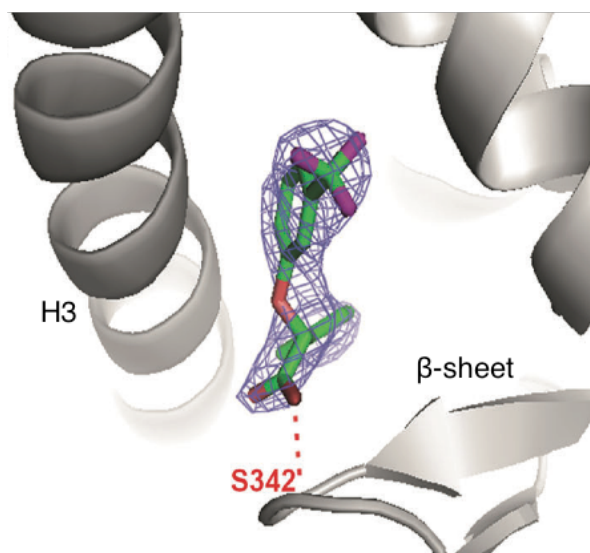


**Figure 43.**  $2F_oF_c$  omit map calculated around (*R*)-halofenic acid (green).

Enantiomer (*S*)-halofenic acid also bound to PPAR $\gamma$  assuming the typical position of partial agonists, although more shifted toward the entrance of the LBD with respect to the (*R*) isomer. (*S*)-halofenic acid faced the  $\beta$ -sheet and both its carboxylic oxygens were found to be engaged in two hydrogen bonds with the NH group of S342 and the side chain OH of S342, respectively (Figure 44B). The side chain of R288 maintained its typical position (*t* conformation), and its guanidinium group made two hydrogen bonds with one of the ligand carboxylic oxygen atoms and the NH group of E343, respectively. The ligand electronegative CF<sub>3</sub> group interacted with the positively charged side chain of R288 through a water molecule also bridged with the CO of L340 (Figure 44B). One of the fluorine atoms also contacted the residue C285 at distances of  $\sim 3.0$  Å. The (*S*) enantiomer formed more and stronger interactions with H3 and the  $\beta$ -sheet than (*R*), better stabilizing these regions of the LBD as shown by the Ligplot analysis [166] (Figure 45).

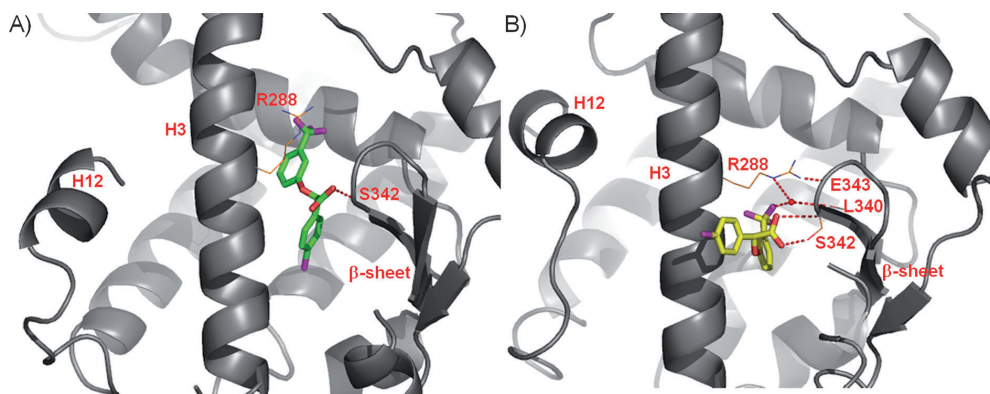


**Figure 44.** Hydrogen bond network of A) (*R*)-halofenic acid (green) and B) (*S*)-halofenic acid (yellow) in complex with PPAR $\gamma$ -LBD

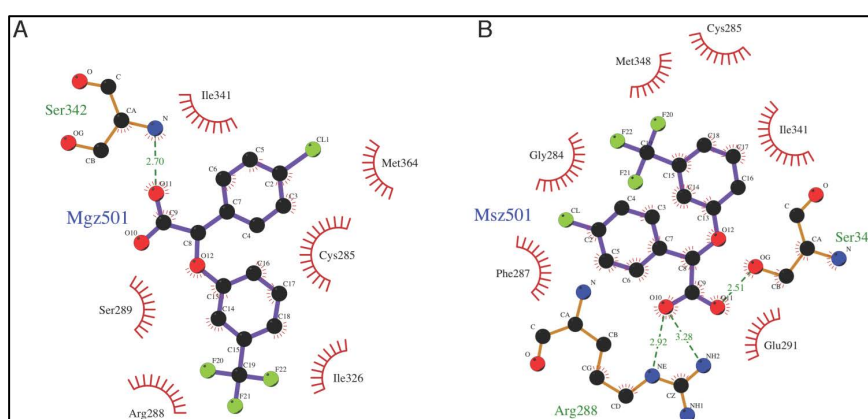


**Figure 45.** The Ligplot diagrams illustrate the protein-ligand interactions for A) (*R*)-halofenic acid and B) (*S*)-halofenic acid in complex with PPAR $\gamma$ -LBD

The largest number of hydrogen bonds and vdW interactions realized by this ligand, in comparison with (*R*)-halofenic acid, was in accordance with the more favorable enthalpic contribution observed in the ITC experiment upon binding to PPAR $\gamma$ -LBD (-6.5 vs -3.8 kcalmol<sup>-1</sup>, respectively). The omit map around (*S*)-halofenic acid is shown in Figure 46. Superimposition of (*R*)- and (*S*)-halofenic acid in the PPAR $\gamma$  LBD (Figure

47A) shows that the two enantiomers, although both interacting with the NH group of S342 through their carboxylic oxygen atoms, occupy slightly different positions between H3 and the  $\beta$ -sheet, with the (*S*) enantiomer less inserted into the LBD cavity. The superimposition with other known PPAR $\gamma$  partial agonists showed that (*R*)-halofenic acid occupied the same position of MRL24 [167] (PDB ID: 2Q5P) and (*S*)-halofenic acid, that of the partial agonist FS214 [168] (PDB ID: 4E4Q) (Figures 47B and 47C). Both stereoisomers seem to be able to stabilize, even though in different ways, the same region of the receptor (H3 and  $\beta$ -sheet), thus explaining their similar affinity and activity toward PPAR $\gamma$ .

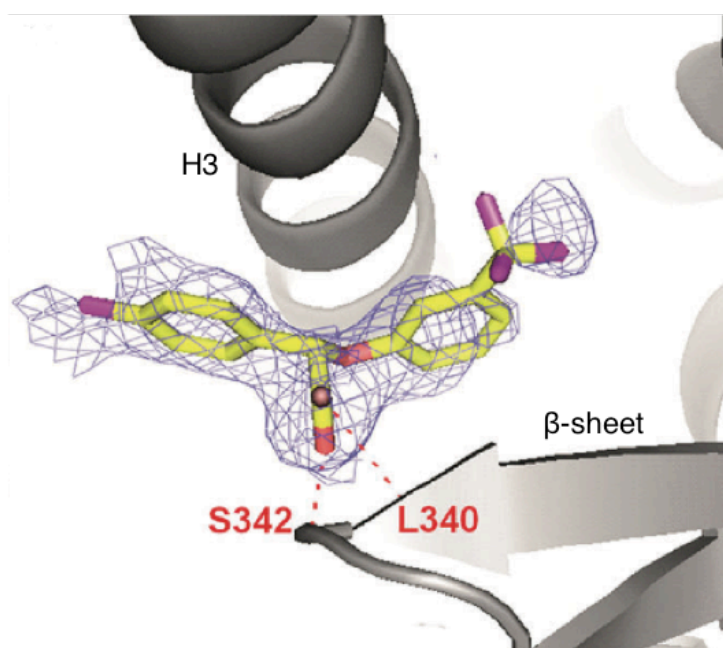


**Figure 46.**  $2F_o - F_c$  omit map calculated around (*S*)-halofenic acid (yellow).

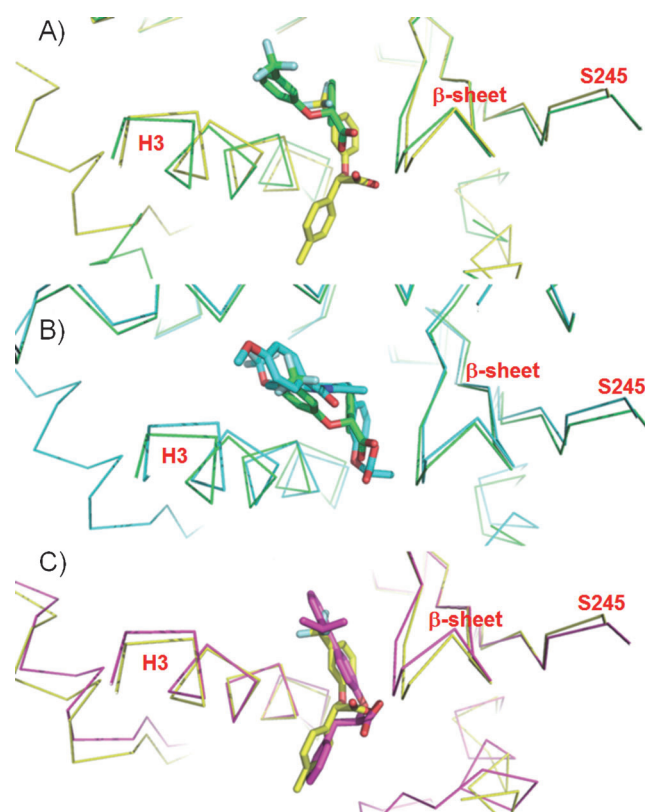


**Figure 47.** Superpositions of A) (*R*)-halofenic acid (green) and (*S*)-halofenic acid (yellow); B) (*R*)-halofenic acid (green) and MRL24 (cyan); C) (*S*)-halofenic acid (yellow) and FS214 (magenta) into the LBD of PPARγ1. S245 of PPARγ1 corresponds to S273 of PPARγ2.

The binding mode of (*R*)-halofenic acid would also explain its ability to inhibit the Cdk5-mediated phosphorylation of PPARγ. Recently, indeed, Choi et al. reported this biochemical effect at the level of S273 of PPARγ2 (corresponding to S245 of PPARγ1) for rosiglitazone and some PPARγ partial agonists including (*R*)-halofenic acid [71]. This study suggests that both thiazolidinediones (TZDs) and partial agonists with antidiabetic effects improve insulin sensitivity primarily by this mechanism. Inhibition of S273 phosphorylation seems to be distinct from classical transcriptional activation,

which involves the stabilization of the highly dynamic activation of helix 12 and appears to mediate at least some of the undesirable side effects of chronic PPAR $\gamma$  activation. In this study, using amide hydrogen/deuterium exchange kinetics, the authors showed that binding of the PPAR $\gamma$  partial agonist MRL24 significantly decreases flexibility of the loop region around S273 and that both rosiglitazone and MRL24 decrease the mobility of H3 and the adjacent  $\beta$ -sheet, which are sites for potential interaction with co-regulatory proteins. These findings suggest that ligand-induced decreases in the dynamic nature of H3, the  $\beta$ -sheet, and the Cdk5 site, may “freeze” this region into a conformation less favorable to Cdk5-mediated phosphorylation. According to this hypothesis, it is likely that (*R*)-halofenic acid decreases the dynamics of H3,  $\beta$ -sheet, and Cdk5 site, explaining the consequent decrease of PPAR $\gamma$  phosphorylation at S273. This could be the principal molecular mechanism responsible for its antidiabetic activity and lack of undesirable side effects typical of classical PPAR $\gamma$  full agonists. A similar behavior could also be suggested for (*S*)-halofenic acid, which binds to the same region of PPAR $\gamma$ -LBD, although slightly shifted with respect to the (*R*) enantiomer. In conclusion, it appears that a more careful investigation of the structural determinants of the metabolically active form of metaglidase could allow the identification of new analogues with improved pharmacological properties, that is a dual PPAR $\alpha/\gamma$  activity. In this perspective, particular attention must be paid to the stereochemistry, which, as widely reported for PPAR ligands, plays a key role in the biological activity of these compounds.



**Structural basis of the transactivation deficiency of the human PPAR $\gamma$  F360L mutant associated with familial partial lipodystrophy**

**Clorinda Lori, Alessandra Pasquo, Roberta Montanari, Davide Capelli, Valerio Consalvi, Roberta Chiaraluce, Laura Cervoni, Fulvio Liodice, Antonio Laghezza, Massimiliano Aschi, Alessandra Giorgi and Giorgio Pochetti**

*Acta Cryst.* (2014). D70, 1965–1976

#### **4.4 Transactivation deficiency of the PPAR $\gamma$ F360L mutant associated with familial partial lipodystrophy**

There is evidence that some rare missense mutations in PPAR $\gamma$  have serious phenotypic effects, contributing to the risk of insulin resistance, dyslipidaemia, type 2 diabetes [169] and colon cancer [170, 171] in affected individuals. Some of these mutations can also be associated with familial partial lipodystrophy (FPLD) [172, 173], which is an autosomal dominant skin condition characterized by adipose-tissue repartitioning associated with multiple metabolic diseases such as severe insulin resistance, hypertriglyceridaemia and diabetes [174, 175]. In this study the effect of the F360L mutation on the structure and thermal stability of human PPAR $\gamma$ -LBD has been investigated, in order to gain more insight into the effects of such a mutation at a molecular level. To date, indeed, the structurally disruptive effect of this missense mutation is unknown.

#### **4.4.1 Overall structure of PPAR $\gamma$ -LBD F360L and conformational changes induced by the mutation**

Initially we unsuccessfully tried to crystallize the apo form of the mutant in the same conditions of wild-type (WT) PPAR $\gamma$ -LBD [39], so we decided to find the right conditions performing co-crystallization trials with the partial agonist LT175 with the aim of making the LBD more stable and favouring its crystallization. This ligand was selected because it occupies the diphenyl pocket [52], a region of the LBD which is also formed by the loop containing the mutated Phe360 residue. A comparison of this structure with the previously solved complex structure [52] of the WT receptor with the same ligand (PDB ID: 3B3K) would have allowed us to verify the consequences of the mutation for ligand binding.

Co-crystallization trials has been performed at Biocrystal Facility of the CNR Institute of Biology and Molecular Pathology (Sapienza University of Rome) using a Phoenix liquid-handling robot (Art Robbins Instruments, USA), which allows to rapidly screen a large number of different conditions with a small sample consumption. Small crystals of the complex with LT175 appeared in well Nos. 18 and 25 of the Index crystallization kit (see Experimental Methods), which have been reproduced on a larger scale to obtain more suitable crystals for X-ray analysis. Crystals appeared after a few days from both tested conditions and X-ray data were collected at ESRF of Grenoble (France). The solved structures have been deposited in the PDB with codes 4L98 and 4L96 and the summary of crystallization analysis for crystals of both conditions, belonging to space group  $P2_12_12$  or  $I222$ , respectively, is shown in Table 8. Crystallization trials were also performed with the full agonist rosiglitazone, but they did not produce crystals suitable

for X-ray analysis. Accurate observation of both of the structures revealed that the crystal packing is almost the same with an identical arrangement of the single monomers (r.m.s.d. of 0.53 and 0.63 Å , respectively, for the two monomers in  $P2_12_12$  superimposed onto the monomer of  $I222$ ) and of the homodimer. Comparing the PPAR $\gamma$ -LBD F360L/LT175 crystal structure (space group  $P2_12_12$ ) with that of the WT receptor also complexed with LT175 (PDB ID: 3B3K) [52], it can be noticed that the interface between the two monomers of the homodimer in PPAR $\gamma$ -LBD F360L/LT175 is different from that of PPAR $\gamma$ -LBD/LT175 and of all the known crystal structures of the wild type receptor complexed with other ligands. The WT interface is formed by helices 11 and 10 of the two monomers, which face each other (Fig. 48A), while the PPAR $\gamma$  F360L interface is formed by H3, H12 and loop 11/12 of each molecule (Fig. 48B). An analysis of the dimerization interface of F360L with the program *PSAP* (Protein Structure Analysis Package) [176] revealed that this new arrangement of the dimer in PPAR $\gamma$  F360L is very stable, with five salt bridges and 21 hydrogen bonds and a more extended surface of interaction between the two monomers with respect to the WT.

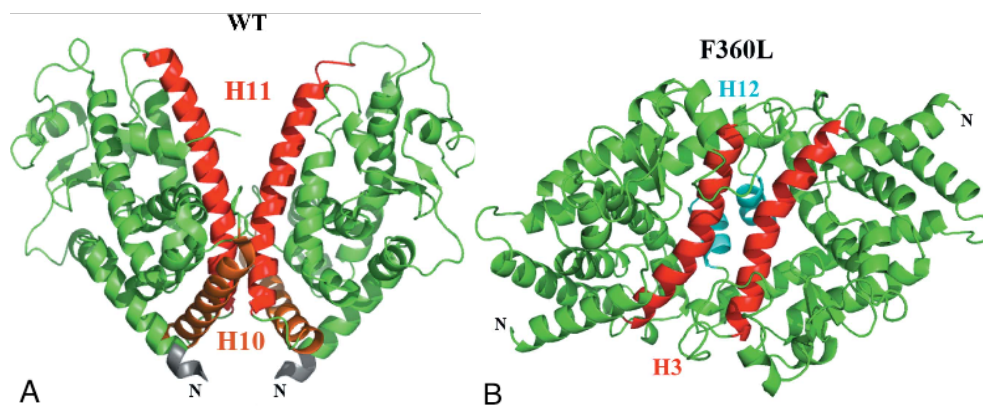
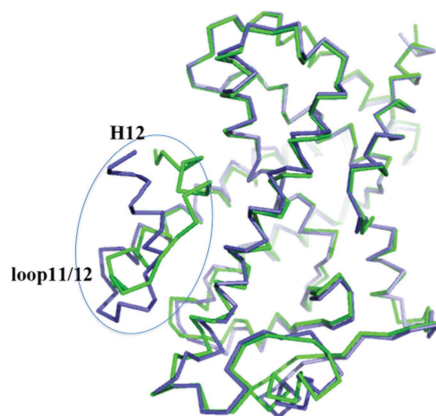


**Figure 48.** Homodimer of the A) wild type and B) the F360L mutant. The interface between the monomers is drawn in red, orange and cyan.

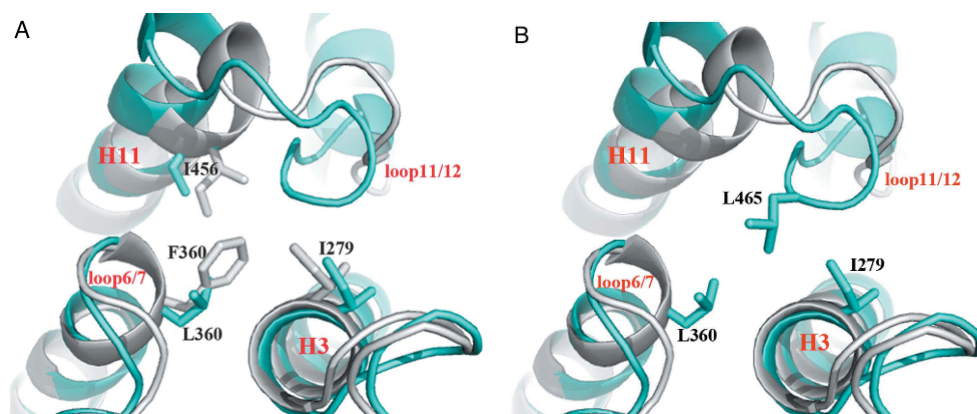
The superposition of a single monomer of WT and F360L mutant shows that the two molecules have comparable conformations, except for the terminal end of H11, loop 11/12 and H12 (Figure 49). The strong van der Waals interaction made by the side chain of Phe360 in the WT with those of Ile279 in helix 3 and Ile456 in helix 11 (3.2 and 3.7 Å, respectively) are lost in the mutant (6.2 and 5.4 Å, respectively), suggesting a key role of Phe360 in stabilizing the diphenyl pocket of the LBD (Figure 50A). Destabilization of the terminal end of H11 caused by the mutation and the resulting rearrangement of the following loop 11/12 permits a different stabilization of this region, with the side chain of Leu465 in loop 11/12 which forms vdW interaction with Leu360 and Ile279 (3.8 and 3.2 Å, respectively; Figure 50B). Moreover, the very strong salt bridge formed in the WT between Arg357 (loop 6/7) and Glu460 (loop 11/12) is partially lost in the mutant, with an increase of the shortest distance from 2.6 to 5.2 Å, respectively (Figure 51). Another salt bridge between Arg357 and Glu276 in helix 3 is also weakened (the shortest distance increases from 2.8 to 4.1 Å, respectively). This could be also due to the loss of interaction between the positively charged Arg357 and the polarizable  $\pi$ -electron cloud of the aromatic ring of Phe360 (the shortest distance between the two residues is 3.4 Å). This is a common interaction in proteins that provides conformational tethering of the arginine side chain while leaving its hydrogen-bond capacity intact for use in the binding of acidic residues [177]. The shorter leucine is not able, using only van der Waals interactions, to stabilize the side chain of Arg357, which loses the salt bridge with Glu460, in this way destabilizing loop 11/12 in which Glu460 is located. In addition, as shown in Figure 52, the side chain of His466 also plays a critical role in the different stabilization of this loop and of helix 12.

PPAR $\gamma$ -LBD F360L/LT175		
<b>Data collection</b>		
space group	<i>P2<sub>1</sub>2<sub>1</sub>2</i>	<i>I222</i>
cell dimension <i>a, b, c</i> [Å]	64.41, 112.46, 117.74	67.17, 112.00, 116.8
wavelength [Å]	0.973	0.973
resolution range [Å]	50.00 - 2.28	41.00 - 2.38
last shell [Å]	2.50 - 2.28	2.47 - 2.38
<i>R</i> <sub>merge</sub> [%]	8.8 (42.4) <sup>a</sup>	11.0 (60.1) <sup>a</sup>
unique reflections	39713	17959
mean ( <i>I</i> )/ $\sigma$ ( <i>I</i> )	18.9 (4.8) <sup>a</sup>	11.3 (2.9) <sup>a</sup>
completeness	99.9 (99.9) <sup>a</sup>	100 (99.3) <sup>a</sup>
No. of molecules in asymmetric unit	2	1
<b>Refinement</b>		
resolution range [Å]	50.00 - 2.28	41.00 - 2.38
<i>R</i> <sub>work</sub> [%]	21.4	18.9
<i>R</i> <sub>free</sub> [%]	25.6	22.7
Bond lengths r.m.s.d. [Å]	0.011	0.011
Bond angles r.m.s.d. [deg]	1.506	1.435

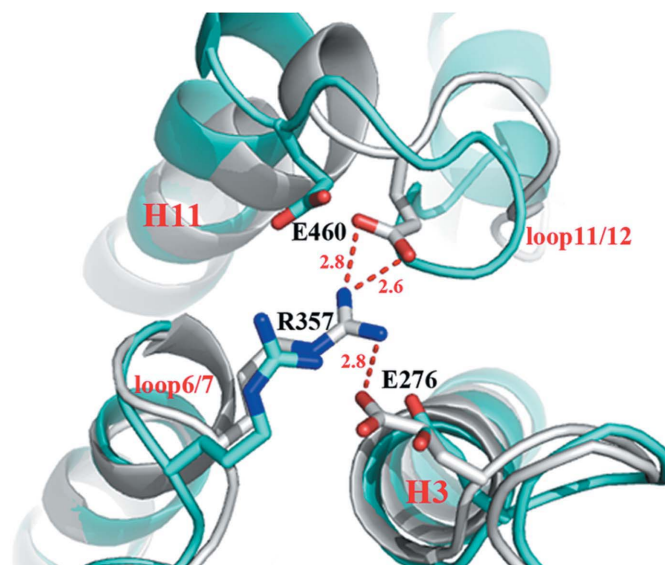
**Table 8.** Summary of crystallographic analysis for crystals of the PPAR $\gamma$ -LBD F360L/LT175 complex obtained with conditions Nos. 18 and 25 of Index crystallization screen. <sup>a</sup> The values in parentheses refer to the outer shell



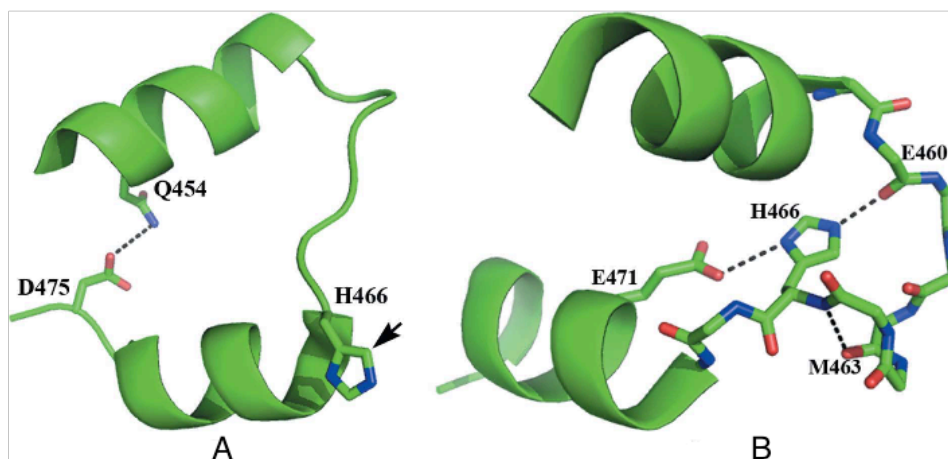
**Figure 49.** Superposition of the crystal structures of the WT (green) and the F360L mutant (cyan) complexed with the ligand LT175. The regions with the main conformational differences are included in the ellipse.



**Figure 50.** Superposition of the crystal structures of the WT (grey) and the F360L mutant (cyan) complexed with the ligand LT175. A) Van der Waals interactions between residues of H3, H11 and loop 6/7; B) van der Waals interactions of loop 6/7 with loop 11/12 and helix 3 in the F360L mutant.

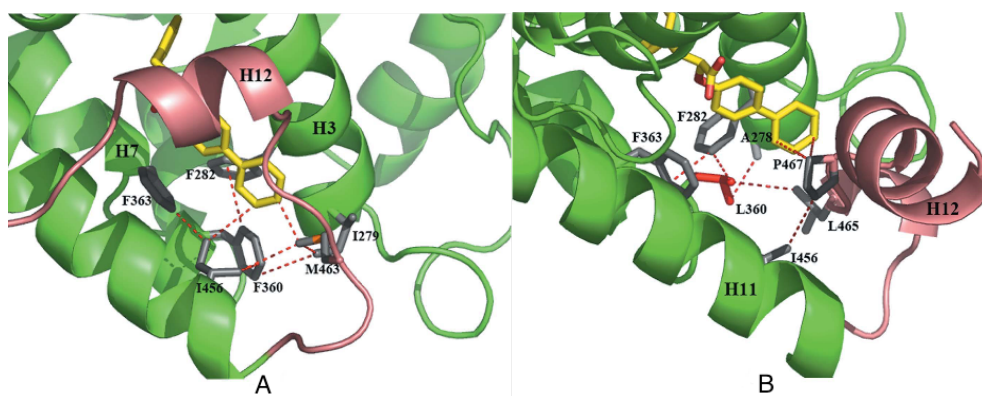


**Figure 51.** Superposition of the crystal structures of the WT (grey) and the F360L mutant (cyan) complexed with the ligand LT175, showing the electrostatic interactions of Arg357 with Glu460 and Glu276. Hydrogen bonds are represented as red dashed lines.



**Figure 52.** Conformation of loop 11/12 in A) the WT and B) the F360L mutant. Hydrogen bonds are drawn as black dashed lines; the black arrow indicates the different position of the His466 side chain in the WT.

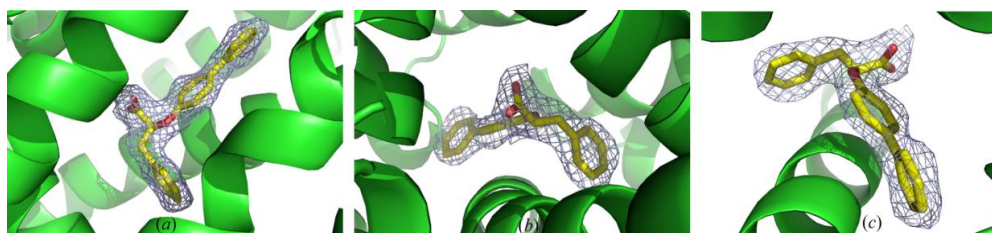
Figure 53 shows the different networks of van der Waals interaction at the bottom of diphenyl pocket for the WT and the mutant. It can be noticed that the mutated Leu360 makes van der Waals contacts with Phe282 and Ala278 in helix 3 (3.1 and 3.4 Å, respectively) and Leu465 in loop 11/12 (3.8 Å), whereas in the WT the shortest van der Waals contacts of Phe360 are with the side chain of Phe282 and Ile279 belonging to H3 (3.5 and 3.3 Å, respectively) and Ile456 in helix 11 (3.6 Å). Phe360 and Phe282 are also involved in a typical 'edge-to-ring face' interaction between the two aromatic rings. Furthermore, the important role played by Met463 of the WT in the interaction with the terminal end of the ligand (Figure 53A) is assumed by Pro467 (Figure 53B) in the mutant. The final result of all of these conformational changes induced by the F360L mutation is that the transactivation helix 12 assumes a different and inactive conformation (Figures 49 and 53B).



**Figure 53.** Van der Waals interactions in the diphenyl pocket of A) the WT and B) the F360L mutant. The mutated residue Leu360 is represented in red and the ligand LT175 in yellow.

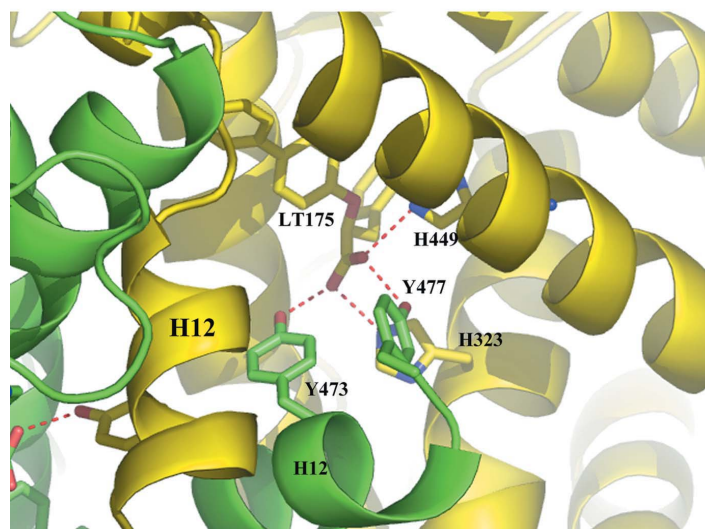
#### 4.4.2 Ligand interactions

Figure 53 shows that LT175 maintains the same position in the F360L LBD (the OMIT maps calculated around the ligand are shown in Figure 54), although inserted more deeply in the pocket, with similar van der Waals contacts; the only exception is provided by the already discussed interaction with Pro467 at the bottom of the diphenyl pocket. Conversely, many differences can be found in the hydrogen-bond network made by its carboxylate O atoms. In addition to the canonical interaction with His449 and His323, the two O atoms make H-bonds with Tyr473 and Tyr447 in helix 12, both belonging to the facing molecule of the homodimer (Figure 55).



**Figure 54.**  $2F_o - F_c$  omit maps calculated around (a) molecule A and (b) molecule B of the ligand LT175 ( $P2_12_12$ ), and (c) molecule A of LT175 ( $I222$ ). All the maps are contoured at the  $1\sigma$  level.





**Figure 55.** Hydrogen-bonds made by residues of monomer A (yellow) and monomer B (green) of the homodimer with the carboxylate group of the ligand LT175 (yellow).

Therefore, there is an additional tyrosine, Tyr477, that is engaged in hydrogen bonds to the carboxylate group besides the canonical Tyr473, which, however, in the WT homodimer belongs to the same monomer where the ligand is bound. This very stable arrangement, as denoted by well defined electron densities of all the residues of H12, is made possible by the new interface between the two monomers, in which H12 of one molecule protrudes towards the ligand inserted into the LBD of the facing molecule. This is probably an artifact of the crystal packing: the destabilization of H12 caused by the mutation allows this helix to find a new conformation that favours a new stable interface between two monomers in the crystal.

It is worth noting that despite several trials it was not possible to crystallize the apo form of the mutant in the conditions generally used to crystallize the WT apo form, suggesting that the mutation destabilizes the LBD of PPAR $\gamma$  and the active conformation of H12 and only the presence of

the ligand allows the complex to crystallize, although in consequence of a new dimer interface. However, in order to check the results obtained by X-ray analysis, molecular dynamics (MD) simulations were also performed by Aschi and collaborators on the apo form of the mutant and the WT. Table 9 contains the basic data concerning the simulated system. The backbone root-mean-square deviation (r.m.s.d.) evaluated for both the WT and F360L with respect to the initial structure of the WT (PDB ID: 1PRG) [39], characterized by a relatively low value, indicates that the average structure of both the macromolecules in solution is not dramatically different from that found in the crystalline state. Also, the close values of the radius of gyration reported in Table 9 suggest a strong average morphological similarity of the WT and the F360L mutant. On the other hand, the high difference in the trace of the backbone covariance matrix, which concisely provides us with the whole internal fluctuation of the macromolecules, clearly shows that the point mutation produces a sharp mechanical destabilization of the whole system accompanied by a very large increase in the whole fluctuation. This is further confirmed by analysis of the root mean square fluctuation (r.m.s.f.) per residue, which highlighted the increase of fluctuation of the F360L mutant in the marked regions which specifically correspond to H12 and residues 280 - 287 of H3.

	WT	F360L
Backbon r.m.s.d. (nm)	$2.59 \times 10^{-1}$ ( $1.57 \times 10^{-2}$ )	$2.75 \times 10^{-1}$ ( $2.44 \times 10^{-2}$ )
Radius of gyration (nm)	1.95 ( $1.0 \times 10^{-2}$ )	1.95 ( $1.1 \times 10^{-2}$ )
Trace of the covariance matrix (nm <sup>2</sup> )	10.9 (0.5)	13.2 (0.6)

**Table 9.** Results of MD simulations for PPAR $\gamma$  WT and the F360L mutant. The standard deviations are reported

### 4.4.3 Crystal structure of the complex between PPAR $\gamma$ -LBD R357A and rosiglitazone

In order to evaluate the importance of the residue Arg357 in the stabilization of the diphenyl pocket within the LBD, the PPAR $\gamma$  mutant R357A was also expressed and co-crystallization trials with the full agonist rosiglitazone has been performed using the Phoenix liquid-handling robot. Suitable crystals for X-ray data collection appeared in well No. 5 of the Morpheus crystallization screen (see Experimental Methods) and the summary of the crystallographic analysis performed at ESRF is shown in Table 10. The solved structure has been deposited in the PDB with code 4O8F. On the contrary, co-crystallization trials of the R357A mutant with the ligand LT175 was not successful.

The complex crystallized in space group  $C222_1$ , with two molecules in the asymmetric unit. OMIT maps calculated around the two molecules of the ligand are shown in Figure 56. A comparison with the crystal structure of the WT with the same ligand (PDB ID: 2PRG) [39] showed that the complex of the mutant maintains the same dimer interface and the same monomer conformation with helix 12 in the active form. However, an accurate examination of the B factors of the mutant reveals a general increase in the thermal parameters with respect to the WT, particularly for the atoms in loop 6/7 containing the mutation, in the region 276–282 of H3 and in the region 453–475 including the terminal part of H11 and loop 11/12 (Figure 57), as found in the MD simulation of apo F360L and in the crystal structure of F360L/LT175. In particular, the electron density around the side chains of Ile279 and Ile456, contacting Phe360, is very weak. Superposition of the crystal structures of R357A and the WT shows that the ligands occupy the

same position in the LBD, making identical interactions with H12; however, the N-methyl group of R357A assumes a different conformation (C14—C15—N16—C17 torsion angle of  $-86^\circ$  vs  $70^\circ$ , respectively), with its methyl group pointing towards the Leu353 side chain (Figure 58).

PPAR $\gamma$ -LBD R357A/rosiglitazone	
<b>Data collection</b>	
space group	$C222_1$
cell dimension $a, b, c$ [Å]	85.70, 87.10, 163.80
wavelength [Å]	0.976
resolution range [Å]	82.00 - 2.56
last shell [Å]	2.72 - 2.60
$R_{\text{merge}}$ [%]	6.1 (43.5) <sup>a</sup>
unique reflections	18994
mean $\langle I \rangle / \sigma(I)$	9.3 (1.3) <sup>a</sup>
completeness	98.8 (97.5) <sup>a</sup>
No. of molecules in asymmetric unit	2
<b>Refinement</b>	
resolution range [Å]	82.00 - 2.56
$R_{\text{work}}$ [%]	23.8
$R_{\text{free}}$ [%]	29.6
Bond lengths r.m.s.d. [Å]	0.011
Bond angles r.m.s.d. [deg]	1.602

**Table 10.** Summary of crystallographic analysis for crystals of the PPAR $\gamma$ -LBD R357A/rosiglitazone complex obtained with conditions No. 5 of Morpheus crystallization screen. <sup>a</sup> The values in parentheses refer to the outer shell

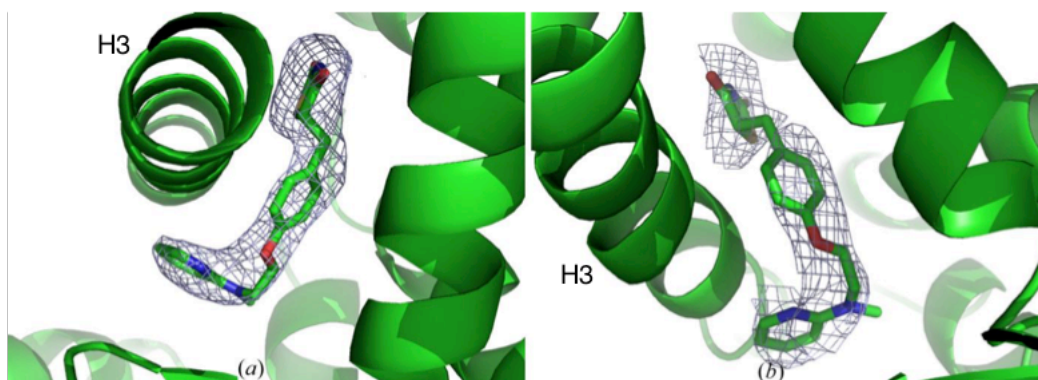


**Figure 56.**  $2F_o-F_c$  omit maps calculated around (a) molecule A and (b) molecule B of the ligand rosiglitazone. All the maps are contoured at the  $1\sigma$  level.

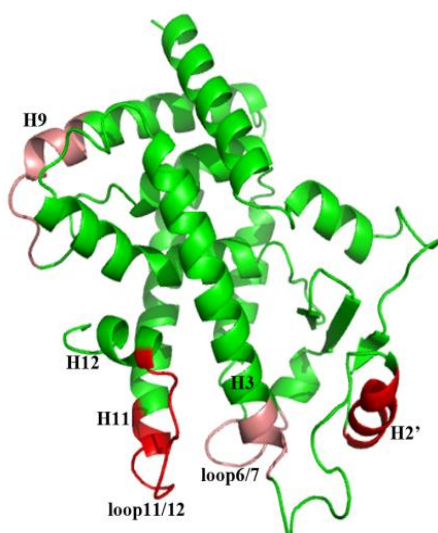


**Figure 57.** Regions of the PPAR $\gamma$ -LBD R357A complexed with rosiglitazone with markedly (red color) and less markedly (pink color) higher B-factors with respect to the corresponding WT crystal structure with the same ligand. The variation of B-factors regarding H8 is less relevant because in the WT structure this helix is affected by crystal packing interactions.

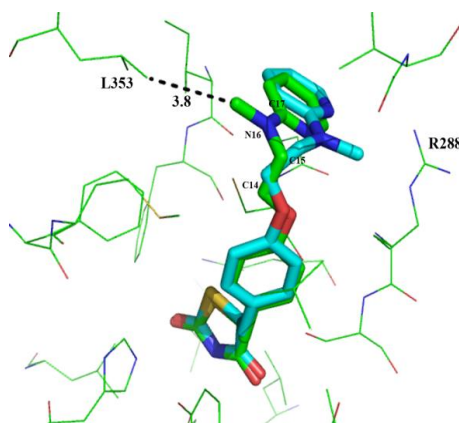


**Figure 58.** Superposition of molecules A of rosiglitazone in R357A (green color) and WT (cyan color), respectively.

#### **4.4.4 The co-activator SRC-1 has a lower binding affinity for the mutants**

As previously discussed, the inactive conformation of helix 12 observed in the crystal structure of the complex with F360L mutant is clearly an artefact of the crystal packing, since the new dimer interface allows helix 12 of one monomer to protrude towards the ligand bound to the other monomer forming an hydrogen bond with it. However, such a marked deviation of H12 from its active conformation would not be possible without the F360L mutation, which strongly destabilizes the region of the diphenyl pocket allowing the formation of a new dimer interface. In the absence of ligands with agonistic activity an increase in the H12 dynamics and a stronger fluctuation of some regions of the LBD is probable, as indicated for instance by the MD simulation. A more disordered conformation of H12 in the classic heterodimer interface with RXR $\alpha$  would impair efficient recruitment of the co-activator, because, as is known, this helix forms part of the hydrophobic cleft used to bind the co-activator [39]. As shown in Figure 59, ITC experiments reveal a less efficient recruitment of co-activator SRC-1 for the F360L and R357A mutants. The co-activator SRC-1 was injected into a cell containing the ligand binding domain of the WT and the mutants pre-equilibrated with the ligand LT175. The results showed that the WT is able to recruit the co-activator with higher affinity with respect to the mutants F360L and R357A ( $K_a = 7.64 \pm 1.17 \times 10^5 \text{ M}^{-1}$  vs  $K_a = 3.01 \pm 0.54 \times 10^5 \text{ M}^{-1}$  and  $K_a = 1.79 \pm 0.28 \times 10^5 \text{ M}^{-1}$ , respectively), thus explaining the lower transactivation activity of the mutated receptors.

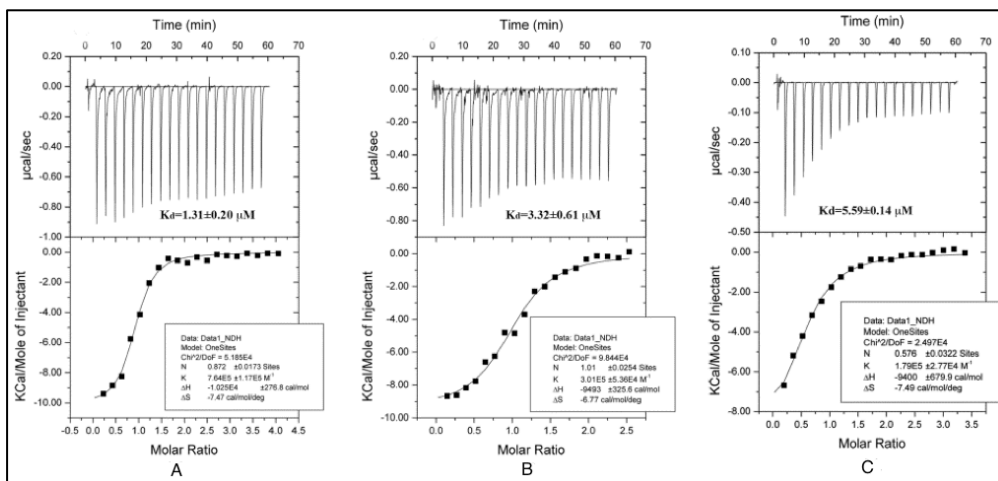


**Figure 59.** ITC experiments: binding of SRC-1 to A) WT, B) F360L and C) R357A after equilibration with LT175.

## Resveratrol and Its Metabolites Bind to PPARs

Enrica Calleri,<sup>[a]</sup> Giorgio Pochetti,<sup>[b]</sup> Katina S. S. Dossou,<sup>[c]</sup> Antonio Laghezza,<sup>[d]</sup>  
Roberta Montanari,<sup>[b]</sup> Davide Capelli,<sup>[b]</sup> Ellen Prada,<sup>[a]</sup> Fulvio Liodice,<sup>[d]</sup> Gabriella Massolini,<sup>[a]</sup>  
Michel Bernier,<sup>[c]</sup> and Ruin Moaddel\*<sup>[c]</sup>

### 4.5 Resveratrol and its metabolites

Resveratrol (3,5,4'-trihydroxystilbene, Figure 60) is a type of natural phenol which can be found in the skin and seeds of grapes and is the active component of red wine that has led to the "French paradox" [178], according to which French people have a relatively low incidence of coronary heart disease (CHD), while having a diet relatively rich in saturated fats. It is a known activator of the NAD<sup>+</sup>-dependent deacetylase SIRT1 and, for this reason, has been the subject of intense studies for its potential role in diabetes and aging [179]. In addition, the SIRT1-dependent repression of visceral white adipocyte genes involves deacetylation of PPAR $\gamma$  [180]. This dietary polyphenol also inhibits platelets aggregation [181], promotes vasodilatation [182, 183] and shows anti-inflammatory activity [184]. However, recent data have revealed that resveratrol can affect PPAR activity and modulate many biological actions of PPAR agonists [185]. Resveratrol also has inhibitory effect on adipogenesis [186], that is believed to occur through down-regulation of PPAR $\gamma$  mRNA expression in human visceral adipocytes [187]. To date, there is no evidence about the direct interaction between resveratrol and/or its metabolites with PPARs.



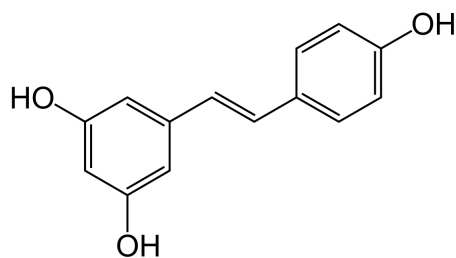


**Figura 60.** Chemical structure of resveratrol.

#### **4.5.1 Binding affinity of resveratrol towards PPARs LBD**

Frontal affinity chromatographic (FAC) [188] studies were carried out by Calleri and collaborators in order to determine whether resveratrol and its metabolites bind to the LBD of PPAR $\gamma$  and PPAR $\alpha$ . Resveratrol, the high-affinity full agonist of PPAR $\gamma$  GW1929 ( $K_a$  value of  $\sim 40$  nM) [189] and the dual agonist R-1 ( $K_a$  values of  $\sim 270$  nM) [188, 190] have been used as marker ligands on the PPAR $\gamma/\alpha$ -open tubular (OT) silica capillary stationary phase. As shown in Table 11, resveratrol and its metabolite 4-*O*-glucuronide had similar binding affinities towards PPAR $\gamma$ -LBD when resveratrol and GW1929 were used as marker ligands, suggesting that the binding site of resveratrol overlaps with GW1929. Conversely, a significant decrease in the affinity of resveratrol 3-*O*-glucuronide to PPAR $\gamma$ -LBD was observed when GW1929 was used as marker ligand. Moreover, resveratrol 3-*O*-sulfate did not displace resveratrol although it displaced GW1929, indicating that the sulfated analogue does not compete with resveratrol for binding.

Compound	$K_i$ [ $\mu\text{M}$ ]		
	Resveratrol	GW1929	R-1
resveratrol	$1.37 \pm 0.57$	$1.80 \pm 0.43$	no displacement
resveratrol-3- <i>O</i> -glucuronide	$1.07 \pm 0.22$	$16.6 \pm 5.81$	no displacement
resveratrol-4- <i>O</i> -glucuronide	$0.77 \pm 0.23$	$1.75 \pm 0.71$	no displacement
resveratrol-3- <i>O</i> -sulfate	no displacement	$3.80 \pm 1.29$	no displacement

**Table 11.** Binding affinity of resveratrol, resveratrol-3-*O*-glucuronide, resveratrol-4-*O*-glucuronide, and resveratrol-3-*O*-sulfate was determined by frontal displacement affinity chromatography by using the PPAR $\gamma$ -OT column. Resveratrol, GW1929, and R-1 were used as markers.

As shown in Table 12, only resveratrol showed affinity for PPAR $\alpha$ -LBD, indicating that the metabolites do not bind PPAR $\alpha$ -LBD at the same site as resveratrol. Neither resveratrol nor its metabolites (concentrations up to 10  $\mu\text{M}$ ) were able to dose-dependently displace compound R-1 from both PPAR $\gamma$ -OT and PPAR $\alpha$ -OT columns, suggesting a lack of overlap between the binding sites for R-1 and resveratrol.

Compound	$K_i$ [ $\mu\text{M}$ ]	
	Resveratrol	R-1
resveratrol	$2.69 \pm 0.18$	no displacement
resveratrol-3- <i>O</i> -glucuronide	no displacement	no displacement
resveratrol-4- <i>O</i> -glucuronide	no displacement	no displacement
resveratrol-3- <i>O</i> -sulfate	no displacement	no displacement

**Table 12.** Binding affinity of resveratrol, resveratrol-3-*O*-glucuronide, resveratrol-4-*O*-glucuronide, and resveratrol-3-*O*-sulfate was determined by frontal displacement affinity chromatography by using the PPAR $\alpha$ -OT column. Resveratrol and R-1 were used as markers.

Isothermal titration calorimetry experiments were used to confirm the interaction of resveratrol with PPAR $\gamma$ -LBD. The association constants ( $K_a$  values) of the binding and the thermodynamic parameters, such as  $\Delta G$ ,  $\Delta H$ ,  $\Delta S$  and  $n$ , were determined from the thermograms (Figure 61) using the

software Origin 7.0 provided by the manufacturer. The results indicated that resveratrol bound to the PPAR $\gamma$ -LBD with an affinity constant similar to that calculated by frontal affinity chromatography ( $1.09 \pm 0.08 \mu\text{M}$  vs  $1.37 \pm 0.57 \mu\text{M}$ , respectively; Tables 11, 12 and 13).

	$K_d \times 10^5 [\text{M}^{-1}]$	$n^{[a]}$	$\Delta H [\text{Kcal M}^{-1}]$	$-T\Delta S [\text{Kcal M}^{-1}]$
PPAR $\gamma$ -LBD/resveratrol	$1.09 \pm 0.08$	0.91	$-3.40^{[b]} \pm 0$	-3.49

**Table 13.** Thermodynamic parameters of the formation of the PPAR $\gamma$ -LBD/resveratrol complex determined by isothermal titration calorimetry. [a] Molar binding ratio of the ligand–protein interaction (observed stoichiometry). [b] This value was kept fixed during the fitting by Origin.

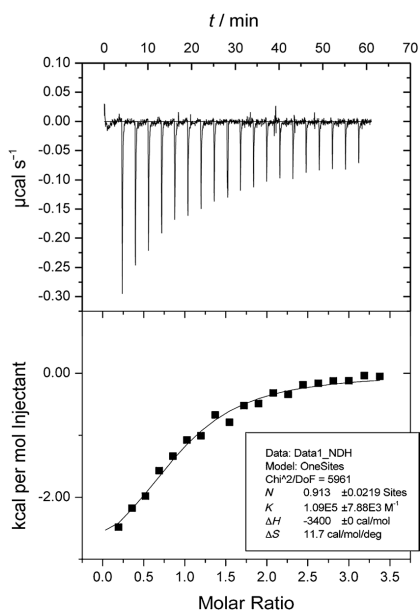


**Figure 61.** Titration of PPAR $\gamma$  (50  $\mu\text{M}$ ) with resveratrol (500  $\mu\text{M}$ ). The upper panels show the raw data; the lower panels show the corresponding binding isotherm, fitted according to the “one binding site” model. The thermodynamic parameters ( $K_d$ ,  $\Delta H$ , and  $\Delta S$ ) are indicated in the boxes.

#### 4.5.2 Crystal structure of PPAR $\gamma$ -LBD/resveratrol complex

To gain more insights into the interaction of PPAR $\gamma$ -LBD with resveratrol, X-ray studies were performed. Crystals (0.2 x 0.3 x 0.2 mm) of apo-PPAR $\gamma$ -LBD were obtained by vapor diffusion using the sitting drop method and then soaked for three days in a storage solution containing the ligand (0.25 mM). X-ray data were collected at Elettra Synchrotron of Trieste (Italy). Crystals of the PPAR $\gamma$ -LBD/resveratrol complex belong to the *C*2 space group, with cell parameters shown in Table 14. The crystal structure of the complex between PPAR $\gamma$ -LBD and resveratrol was solved (PDB ID: 4JAZ) with a resolution of 2.85 Å. The electron density map (Figure 62) clearly reveals the presence of one molecule of the ligand bound to the LBD of PPAR $\gamma$ . The ligand occupies a region close to the  $\beta$ -sheet in a position similar to that of other known PPAR $\gamma$  partial agonists [45, 52, 168], in which a strong hydrogen bond was formed between the Ser342 amide and one of the hydroxy groups of resveratrol (Figure 63A). The side chain of Arg288 was displaced by the ligand from its usual position and, consequently, the side chain of Glu291 was also forced to assume a new orientation. Van der Waals interactions were present between resveratrol and the side chains of Phe264, His266, and Arg288, with electrostatic forces between the charged side chains of Arg288 and Arg280 and the negative dipoles of the ligand hydroxy groups. Unlike other known partial agonists of PPAR $\gamma$ , the terminal end of resveratrol occupied a small pocket close to the entrance of the LBD to form a hydrogen bond with the side chain of Arg280. This new pattern of receptor–ligand recognition could be exploited for ligand design. The crystal structure of PPAR $\gamma$ , complexed with amorfrutin 1, a ligand structurally related to resveratrol, was recently published [191]. The superposition of the

two crystal structures illustrates that both ligands occupied the same position and formed similar interactions with the PPAR $\gamma$ -LBD (Figure 63B). The crystal structure of the PPAR $\gamma$ -LBD in complex with resveratrol was further examined in order to explain the results obtained from frontal displacement chromatography. Superposition of the PPAR $\gamma$ -LBD with resveratrol and farglitazar, a high-affinity PPAR $\gamma$  ligand that is structurally very similar to GW1929 [53], showed that the latter compound partially occupies the same region as resveratrol, which could explain the displacement of GW1929 by resveratrol (Figure 63C). In contrast, compound R-1, a full PPAR $\gamma$  agonist [192], occupied a different position within the PPAR $\gamma$ -LBD when compared to resveratrol (Figure 63D). Superposition of the two molecules demonstrated that, although the fused ring moiety of compound R-1 was very close to the terminal part of resveratrol, the two did not occupy the same region. This result supports the notion that resveratrol is unable to displace compound R-1 from the PPAR $\gamma$ -LBD, as evidenced by frontal displacement chromatography.

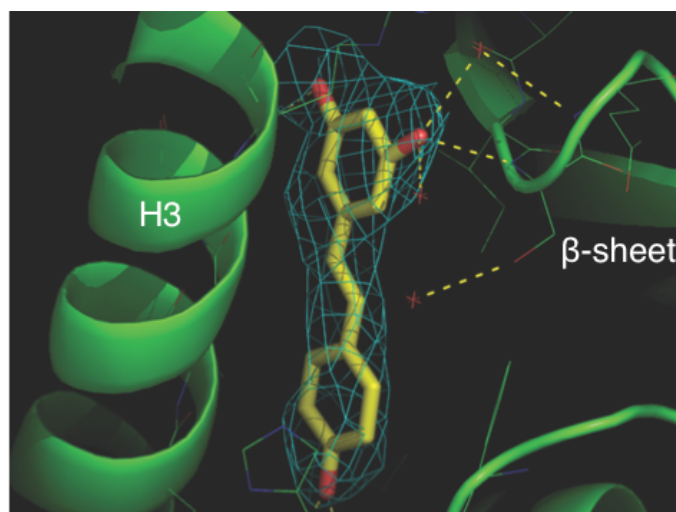


**Figure 62.**  $F_0-F_C$  omit map calculated around the ligand and contoured at 2.5  $\sigma$ .

PPAR $\gamma$ -LBD/Resveratrol	
<b>Data collection</b>	
space group	<i>C</i> 2
cell dimension <i>a</i> , <i>b</i> , <i>c</i> [Å]	93.72, 63.38, 119.8
monoclinic angle $\beta$ [deg]	102.9
wavelength [Å]	1
resolution range [Å]	52.10 - 2.85
last shell [Å]	3.00 - 2.85
$R_{\text{merge}}$ [%]	7.2 (42.2) <sup>a</sup>
observation	32406 (4415) <sup>a</sup>
unique reflections	13805 (2012) <sup>a</sup>
mean $\langle I \rangle / \sigma(I)$	7.2 (1.8) <sup>a</sup>
completeness	86.2 (86.3) <sup>a</sup>
multiplicity	2.3 (2.2) <sup>a</sup>
<b>Refinement</b>	
resolution range [Å]	10 - 2.85
$R_{\text{work}}$ [%]	23.7
$R_{\text{free}}$ [%]	26.3
Bond lengths r.m.s.d. [Å]	0.012
Bond angles r.m.s.d. [deg]	null

**Table 14.** Summary of crystallographic analysis for the PPAR $\gamma$ -LBD/resveratrol complex; <sup>a</sup> The values in parenthesis refer to the outer shell.

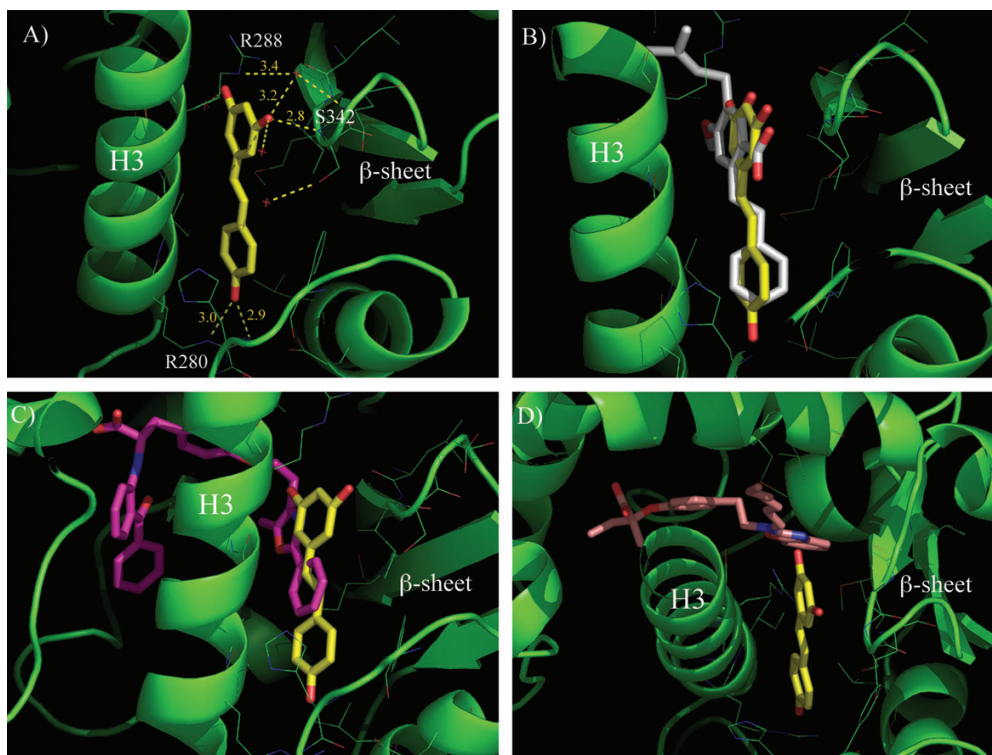


**Figure 63.** A) Hydrogen-bond network of resveratrol in the PPAR $\gamma$ -LBD. B) Superposition of the complexes of PPAR $\gamma$  with resveratrol (yellow) and amorfrutin 1 (white). For the sake of clarity, the cartoon of PPAR $\gamma$ -LBD complexed with resveratrol is shown (green). C) Superposition of the complexes of PPAR $\gamma$ -LBD with resveratrol (yellow) and farglitazar (purple). D) Superposition of the complexes of PPAR $\gamma$ -LBD with resveratrol (yellow) and compound R-1 (pink).

### 4.5.3 Antagonistic activity of resveratrol

Inoue et al. initially reported PPAR $\alpha/\gamma$  dual agonism of resveratrol, excluding any activity toward the PPAR $\beta/\delta$  isoform and other nuclear receptors [185], and subsequently updated their work and reported the pan-agonism of resveratrol for PPARs [193]. Surprisingly, there was no PPAR transactivation observed in response to resveratrol treatment at concentrations up to 100  $\mu$ M (Figure 64A and 64B) in luciferase-based transactivation assays performed on HepG2 cells by Loiodice and collaborators. Similarly,

no apparent effect was seen on the transactivation potential of PPAR $\alpha$  and PPAR $\gamma$  treated with two fixed concentration (10 and 25  $\mu$ M) of its metabolites. However, the incongruity of these data and the previously reported could result from the type of cell line used. Specifically, different cell lines might provide different results depending on the presence of recruitable co-factors (co-activators or co-repressors) and/or metabolic processes, such as cellular metabolism of resveratrol during the experiment. Actually, these *in vitro* assays might not be the most suitable for studying the effects of resveratrol on PPARs, and might require a more careful investigation *in vivo*.

Nevertheless, the demonstration of direct binding of resveratrol to PPAR resulting from frontal affinity chromatography, ITC and X-ray experiments, led us to investigate whether resveratrol exhibited PPAR antagonistic activity. For this purpose, transiently transfected HepG2 cells were coincubated with or without resveratrol in the presence of either rosiglitazone or Wy-14643 for 20 h. Data from the luciferase reporter assay indicated that resveratrol was able to displace rosiglitazone from PPAR $\gamma$  and Wy-14643 from PPAR $\alpha$  with IC<sub>50</sub> values of  $27.4 \pm 1.8 \mu$ M and  $31.7 \pm 2.5 \mu$ M, respectively (Figure 65A and 65B). Taken together, these results suggest that resveratrol acts on both PPAR $\gamma$  and PPAR $\alpha$  as an antagonist.

A comparison of the structure of resveratrol with structures of the ligands used as positive controls in the cell-based reporter assays was also carried out (Figures 66A and 66B). Rosiglitazone is a PPAR $\gamma$  full agonist whose crystal structure in complex with the PPAR $\gamma$ -LBD showed a standard agonist position with direct interaction with H12 through a hydrogen bond with Tyr473 [135].



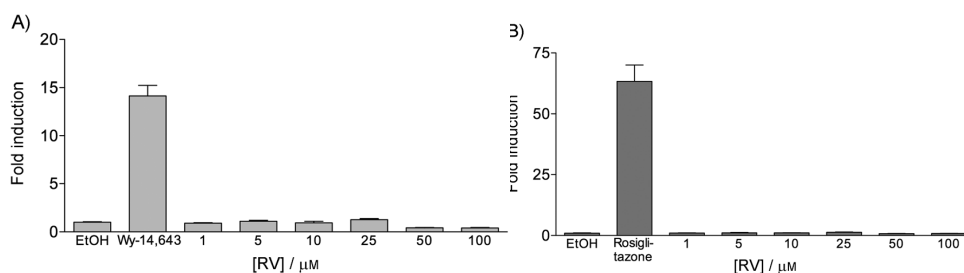


**Figure 64.** Transactivation assay on PPAR $\alpha$  and PPAR $\gamma$  of resveratrol in HepG2 cells. Fold induction by resveratrol (RV) over vehicle (EtOH, 0.1%) on A) PPAR $\alpha$  and B) PPAR $\gamma$  as determined by luciferase-based transactivation assays. Reference compounds: Wy-14643 (10  $\mu$ M) and rosiglitazone (2  $\mu$ M).

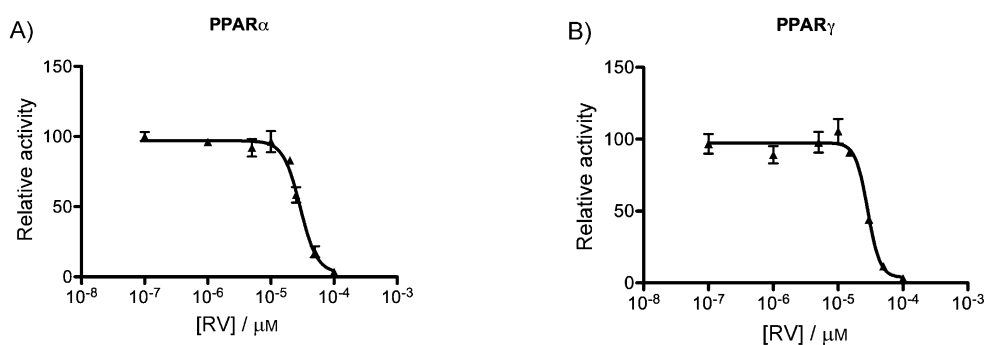


**Figure 65.** Inhibition of agonist-induced transactivation of PPAR $\alpha$  and PPAR $\gamma$  by resveratrol in HepG2 cells. Transiently transfected HepG2 cells were incubated with increasing concentrations of resveratrol (1–100  $\mu$ M) in the presence of either A) 10  $\mu$ M Wy-14643 or B) 2  $\mu$ M rosiglitazone. Luciferase reporter activity was measured in cell lysates 20 h later. Data represent mean  $\pm$  SEM from two independent experiments, each performed in triplicate wells.

However rosiglitazone and resveratrol partially occupy the same region (Figure 66A), so that the latter compound is able to displace rosiglitazone from its position as demonstrated by luciferase reporter assay. Moreover, the X-ray crystal structure of the PPAR $\alpha$ -LBD/Wy-14643 complex showed one molecule of the ligand directly interacting with H12, similar to rosiglitazone and many other PPAR full agonists, and, more interestingly, a second molecule that interacted with a secondary site between

H2' and H3, called the  $\omega$ -loop. It seems that the occupation of this second site can better activate PPAR $\alpha$  by stabilizing H12 in the active conformation without any direct contact with the helix but only through interactions connecting the  $\omega$ -loop, H3, and loop 11/12, which precedes H12. Interestingly, superposition of the PPAR $\gamma$ -LBD/resveratrol and PPAR $\alpha$ -LBD/Wy-14643 crystal structures (Figure 66B) showed that one aromatic ring of resveratrol occupied almost the same position as an aromatic ring of Wy-14643.

In conclusion, the binding mode of resveratrol reveals a new pattern of receptor-ligand recognition and suggests a novel basis for ligand design. Moreover, the fact that resveratrol binds to PPAR $\gamma$ -LBD and conveys antagonistic activity on both PPAR $\gamma$  and PPAR $\alpha$  highlights the need for better understanding the role of cellular metabolism in resveratrol signalling.

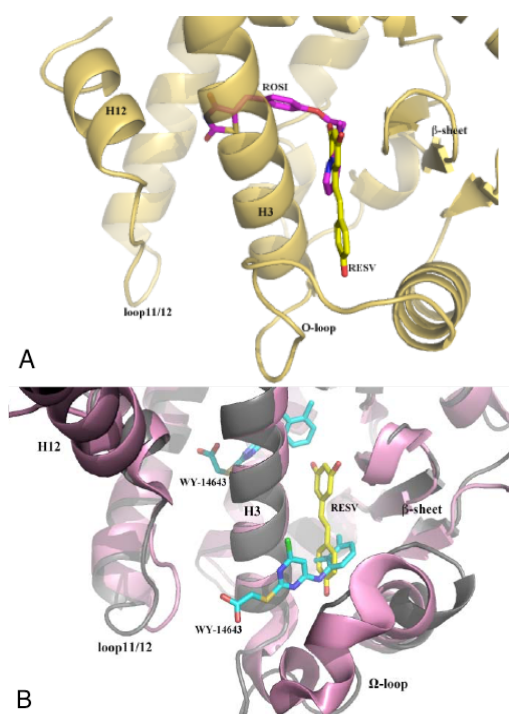


**Figure 66.** The superposition of A) resveratrol (yellow) and rosiglitazone (purple) within LBD of PPAR $\gamma$  and B) PPAR $\gamma$ /resveratrol and PPAR $\alpha$ /Wy-14,643 (cyan) crystal structures.

#### 4.6 Betulinic acid: a PPAR $\gamma$ antagonist

In this study to be published some medicinal plants commonly used by the pygmies Baka, a community living in the south of Cameroon and possessing a consolidate tradition in the use of medicinal natural compounds, were selected as candidates to be PPARs ligands. Among them, *Diospyros bapidensis* has been identified as the most interesting plant for PPARs receptors considering that some plants of the same family are kown to have anti-inflammatory, anti-diabetic and hypoglicemic properties [194 - 197]. All the active components have been tested using affinity-based assay and further analyzed for their *in vitro* activity (agonist and/or antagonist assay) toward PPAR $\alpha$  and PPAR $\gamma$  receptors by employing GAL4-PPAR transactivation assay. Plumbagin was the only ligand showing PPAR $\gamma$  partial agonism, while no transactivation activity was observed in response to all other ligands. With the aim to investigate whether they exhibited PPAR antagonistic activity, competitive displacement experiments were performed. The results showed that betulinic acid (BA; Figure 67) was able to displace rosiglitazone from PPAR $\gamma$ -LBD and Wy-14643 from PPAR $\alpha$ -LBD with micromolar IC<sub>50</sub> values of  $3.1 \pm 1.2 \mu\text{M}$  and  $7.4 \pm 1.8 \mu\text{M}$ , respectively. Betulinic acid, which has been proved to have a variety of pharmacological and biochemical effects including anti-inflammatory and anti-cancer activities [198], as well as anti-adipogenic action in high-fat diet-fed mice [196], was also the ligand with higher affinity. Subsequently, X-ray-studies were performed on the complex between PPAR $\gamma$ -LBD and betulinic acid and a possible structural mechanism by which BA antagonizes PPAR $\gamma$  was proposed.

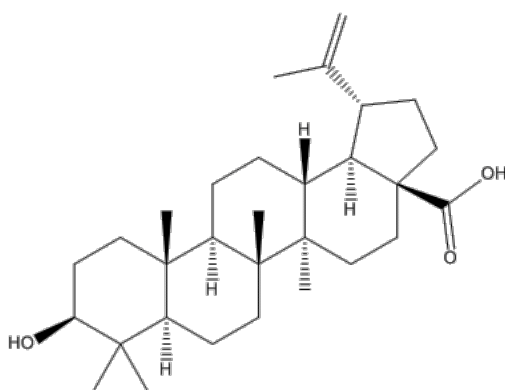


Figure 67. Chemical structure of betulinic acid.

#### 4.6.1 Crystal structure of PPAR $\gamma$ -LBD in complex with betulinic acid: two molecules of the ligand bind the LBD simultaneously

Crystals (0.2 x 0.2 x 0.2 mm) of apo-PPAR $\gamma$ -LBD were obtained by vapour diffusion using the sitting drop method and then soaked for one week in storage solutions containing the ligand (0.5 mM). X-ray data were collected at ESRF of Grenoble (France). Crystals of the PPAR $\gamma$ -LBD/BA complex belong to the *C2* space group, with cell parameters shown in Table 15. The solved structure has been deposited in the PDB with code 5LSG.

In the molecule A of the asymmetric unit the electron density map clearly revealed the presence of one molecule of BA in the region usually occupied by full agonists (Figure 68). Additional less evident electron density was also observed in the region occupied by partial agonists, between H3 and the  $\beta$ -sheet, where a second molecule of the ligand could be accommodated and refined. The presence of a second potential BA binding site was also suggested by docking studies (data not shown), which predicted an

energetically favourable pose in this second cleft. The first BA molecule has all its methyl groups engaged in vdW interactions with the protein environment (L453, F282, M364, C285, L330 and V339). The carboxylate group makes H-bonds bridging the OH of Y327 and that of S289. One of the two oxygen atoms is also involved in a H-bond with the carboxylate group of the second BA molecule, which is also H-bound to the CO of I281. The 3-OH group of the second BA molecule makes a H-bond with the side-chain of E343, while the methyl groups interact at short distance with R280, G284, I341, F287, E291 and one carbon atom of the first BA molecule (3.3 Å). Unlikely most of the partial agonists, this second molecule of BA doesn't form H-bonds with residues belonging to the backbone of the  $\beta$ -sheet. H-bonds interaction of both molecules of the ligand in the LBD of PPAR $\gamma$  are shown in Figure 69.

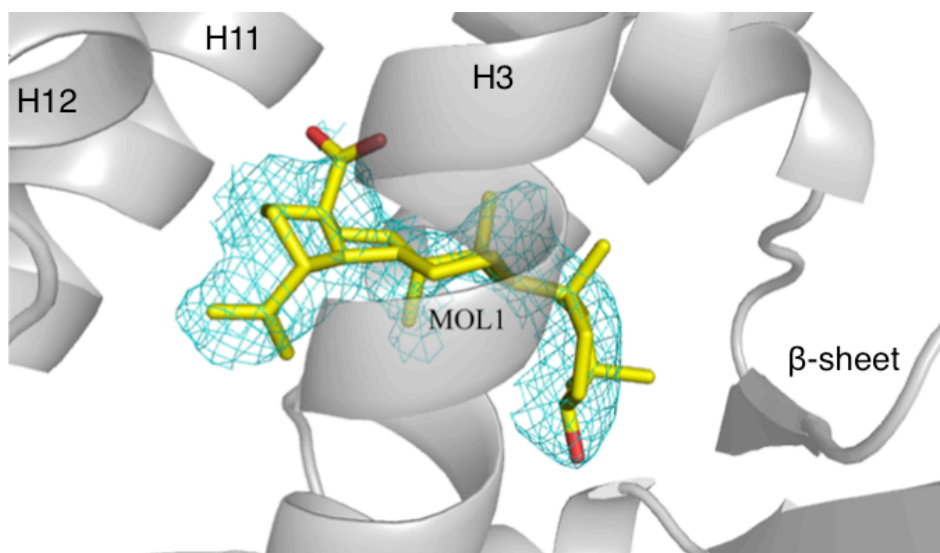


**Figura 68.** *2Fo-Fc* omit map around molecule 1 of BA (yellow) is shown in mesh and contoured at 0.7  $\sigma$

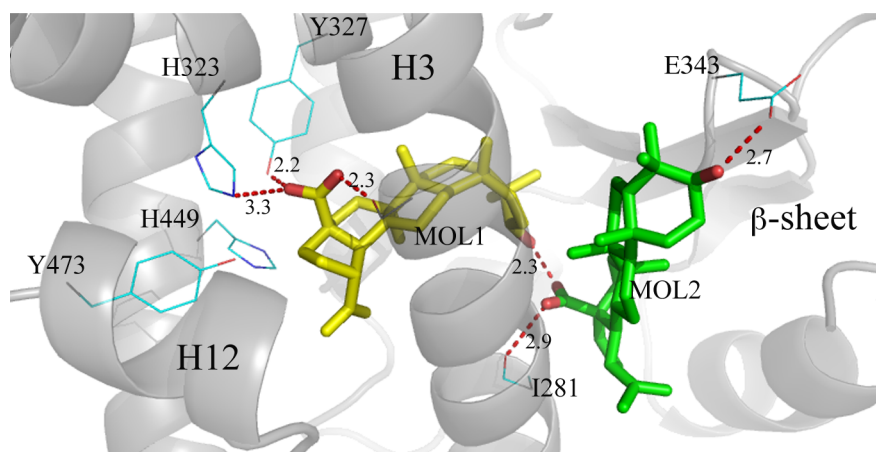


**Figura 69.** H-bonds interactions (red dashed lines) of molecule 1 (yellow) and 2 (green) of BA, bound simultaneously to the LBD of PPAR $\gamma$ .

#### 4.6.2 Sub-optimal stabilization of helices 11 and 12

Unlike the strong agonist rosiglitazone (PDB ID: 2PRG) the ligand BA doesn't interact directly with Y473 by H-bonds with its carboxylate group, which instead is engaged in H-bonds with Y327, H323 and the side-chain of S289. On the contrary, BA contacts the Y473 OH by vdW interactions through a carbon atoms of its 5-membered ring (shortest C-O distance: 3.1 Å). The H-bond network realized by the triad Y473, H323 and H449 is less stable than that of complexes with full agonists such as rosiglitazone, as denoted by the slightly shifted position of the activation function-2 helix (AF-2 or H12) from its active conformation with the consequent loss of the H-bond between the H449 ring and the Y473 OH (distance of 3.6 Å). From the crystal structure it can be noticed a steric clash between carbon atoms of the ligand and the ring of H449 (shortest distance 2.9 Å). Moreover, the environment around H449 is different compared to the

PPAR $\gamma$ -LBD/BA	
<b>Data collection</b>	
space group	<i>C</i> 2
cell dimension <i>a</i> , <i>b</i> , <i>c</i> [Å]	92.86, 60.85, 118.30
monoclinic angle $\beta$ [deg]	102.482
wavelength [Å]	0.9537
resolution range [Å]	50.00 - 2.00
last shell [Å]	2.20 - 2.00
$R_{\text{merge}}$ [%]	2.7 (41.3) <sup>a</sup>
unique reflections	84071
mean $\langle I \rangle / \sigma(I)$	20.33 (2.63) <sup>a</sup>
completeness	98.6 (97.6) <sup>a</sup>
<b>Refinement</b>	
resolution range [Å]	50.00 - 2.00
$R_{\text{work}}$ [%]	22.9
$R_{\text{free}}$ [%]	27.0
Bond lengths r.m.s.d. [Å]	0.009
Bond angles r.m.s.d. [deg]	1.367

**Table 15.** Summary of crystallographic analysis for PPAR $\gamma$ -LBD/BA complex.  
<sup>a</sup> The values in parentheses refer to the outer shell

structure of the complex with rosiglitazone, because the side-chain of F363 has changed its conformation, due to a steric clash with one methyl of BA (3.0 Å), and now approaches H449 (3.3 Å), L453 (3.6 Å), L452 (3.7 Å), and the methyl group of I456 (3.5 Å) which is slightly displaced from its original position (Figure 70). Therefore, the dynamics of the helix 11 around H449 is changed, a helix which is part of the AF-2 surface and directly affects H12. A loss of stabilization of the region including H11, near H449, has been also observed in HDX experiments for the complex of PPAR $\gamma$  with the antagonist SR1664 [199]. We suggest that the antagonist character of BA is due to the loss of direct H-bonds with Y473 and the consequent destabilization, or sub-optimal stabilization, of helices 11 and 12. In any case, the micromolar affinity ( $K_d = 4 \mu\text{M}$ ) of BA for the LBD of PPAR $\gamma$ , as determined by ITC (Figure 71), was sufficient to displace rosiglitazone as observed in the competitive test performed by Loiodice and collaborators ( $\text{IC}_{50}$  value of  $3.0 \pm 1.7 \mu\text{M}$ ).

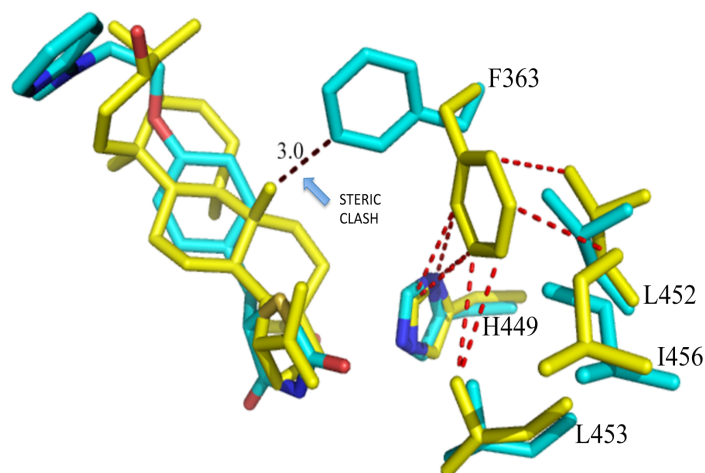


**Figure 70.** Superpose of the crystal structures of the complexes PPAR $\gamma$ -LBD/BA (yellow) and PPAR $\gamma$ -LBD/rosiglitazone (PDB ID: 2PRG) (cyan). The F363 side-chain in gauche conformation (cyan) would make a steric clash (black dashed lines) with a methyl group of BA. The gauche\* conformation of F363 allows vdW interactions (ranging from 3.3 to 3.7 Å) with hydrophobic residues on H11 (red dashed lines).



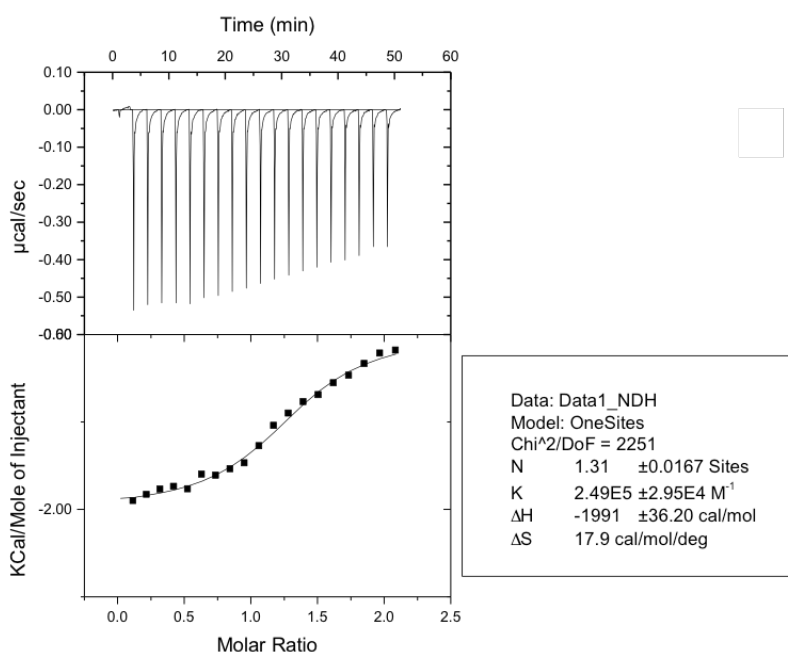


**Figure 71.** Reverse titration of PPAR $\gamma$ -LBD to BA. The upper panel of the figure shows the raw data of the ITC experiment. The lower panel shows the corresponding binding isotherm fitted according to the “one binding site” model.

#### 4.6.3 Comparison with the antagonist SR1664 and the agonist SR1663: the F282/F363 switch mechanism.

It is interesting to compare the crystal structure of PPAR $\gamma$ /BA with that of the complex with another PPAR $\gamma$  antagonist available in the PDB. Figure 72 shows the superposition of the structures of BA and SR1664 [199, 200] in the complex with PPAR $\gamma$ . The two compounds occupy a similar position in the LBD, both contacting Y473 only through vdW interactions, and forming instead a H-bond with Y327. In the case of the bulkier SR1664 the authors observed steric clashes, not present in the (*R*) enantiomer SR1663, with the F282 aromatic ring and the hydrophobic side chains of

H11, such as that of Leu 453 as well as that of Leu 465 of the loop 11/12. Therefore, the authors suggested that SR1664 actively antagonizes PPAR $\gamma$  through a stereo-specific AF2-mediated, F282-dependent clash. Moreover, they confirmed the role of F282 in the antagonism of SR1664, showing that this ligand turns into an agonist upon mutation F282A. Anyway, the shortest distance of SR1664 with F282 is 3.0 Å (NO<sub>2</sub>-C) that is consistent with a strong vdW interaction rather than a steric clash. As discussed hereafter, the F282A mutation may result in a different position of the ligand into the pocket, explaining its agonism towards the mutant. The corresponding (*R*) enantiomer SR1663 shows agonist properties (80% efficacy compared to rosiglitazone). Observing the interaction of the ligand with the the protein molecule A in the complex with PPAR $\gamma$ , the molecule whose H12 is in the active conformation (H12 of the molecule B of the dimer is in a inactive conformation and it should not be considered to discuss its interaction with an agonist), it can be seen a deeper protruding of the NO<sub>2</sub> group towards F282, due to the different stereochemistry, that would give a strong clash with F282 if this residue would assume its usual conformation. Actually, there is poor electron density in the position of F282 and the authors could assign only the position of the C $\beta$  atom of the F282 side-chain.

A more accurate observation of the electron density maps reveals a possible different conformation of the F282 side-chain, switching from *trans* to *gauche\** (Figure 73). A similar situation was already observed in the structure with the ligand LT175 (PDB ID: 3B3K) where the bulky and rigid diphenyl group of the ligand displaced the side-chain of F282, shifting in turn those of F363 and I456 and opening a new hydrophobic pocket in the LBD between H11 and H3 (Figure 74).

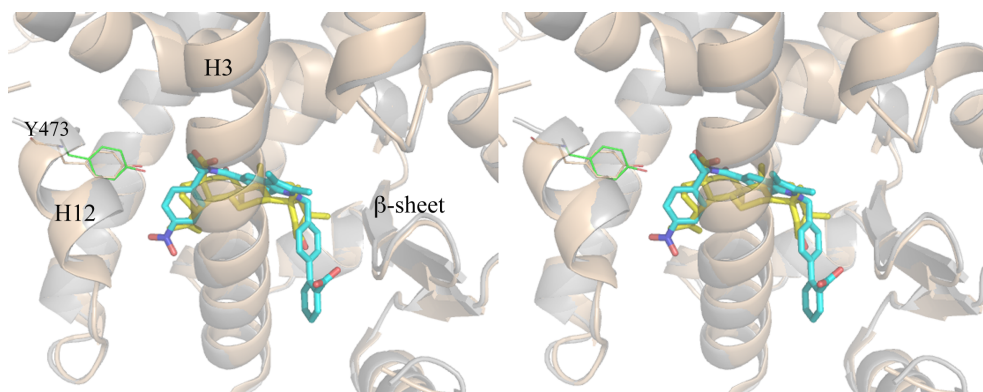


**Figure 72.** Stereoview of the superposed crystal structures of PPAR $\gamma$ /BA (cartoon gray, BA yellow) and PPAR $\gamma$ /SR1664 complexes (cartoon wheat, SR1664 cyan).

This is also confirmed in the PPAR $\gamma$ /SR1663 structure by the shifted conformation of F363, with respect to that observed in the apo-PPAR $\gamma$ , and the alternate conformation of C285, that in this new conformation can interact with the side-chain of F282. This role of gate-keeper of F282 was recently observed also in the PPAR $\alpha$  complex with the ligand AL29-26 (in this case the PPAR $\alpha$  corresponding residue is F273; see chapter 4.1). The accommodation of the nitro-substituted ring of SR1663 in the new pocket, as well as the diphenyl moiety of LT175, can determine the agonist character of the ligand with an additional stabilization of H11 and H3. It is possible that SR1664 in the F282A mutant could assume a similar deeper position in the pocket, becoming an agonist, but only its crystal structure in the complex with the mutant could unveil it. Looking at the structures of the the two compounds BA and SR1664, both lacking the H-bond interaction with Y473 on H12, it would seem that this feature could be responsible of their antagonist character. In any case, also SR1663 showed no direct interactions, other than vdW contacts, with Y473. This would suggest that a direct hydrogen bond with Y473 is not necessarily required for some agonist

activity, but rather stabilizing H12 in its active conformation seems more important, as well as keeping the proper conformations of the other helices composing the AF-2 surface together with H12, for the co-activator recruitment. In the case of the antagonist BA, the loosening of the interaction with H12, associated with a different stabilization of H449 on the helix 11, could be responsible for different dynamics of the helices forming the co-activator binding site, determining the antagonist character of the ligand. In conclusion, it can be noted that the PPAR $\gamma$  LBD is formed by closely related domains whose dynamics, upon ligand binding into different regions of the LBD (between H3, H12, H11 and the loop 11/12, as in the case of full agonists, or between H3, the  $\beta$ -sheet and the  $\omega$  loop, as in the case of partial agonists), can produce long range allosteric effects affecting the recruitment of co-activators or the phosphorylation of S245 (S273 in PPAR $\gamma$ 2) and other post-translational modifications, modulating in this way the biological response.

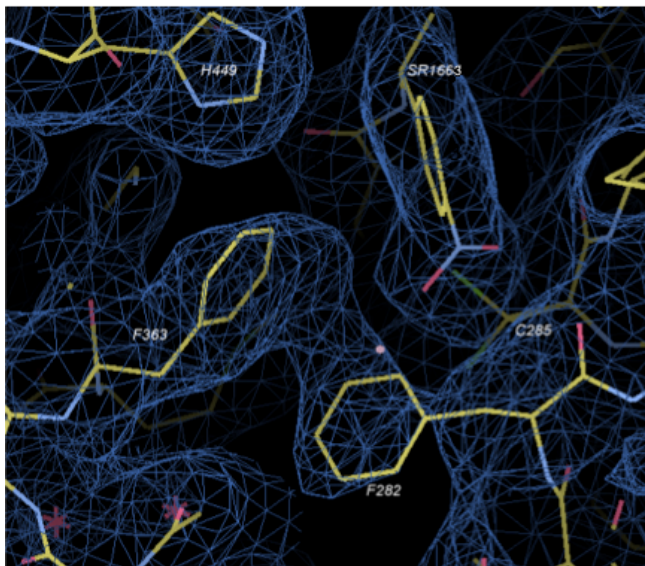


**Figure 73.** *2Fo-Fc* electron density map of SR1663 after a new refinement by Phenix with the side-chain of F282 in  $g^*$  conformation ( $\chi^1 = -87^\circ$ ). The conformation of F363 side-chain is also changed, with respect to the structure of apo-PPAR $\gamma$  or of the complex with rosiglitazone, after the shift of F282.

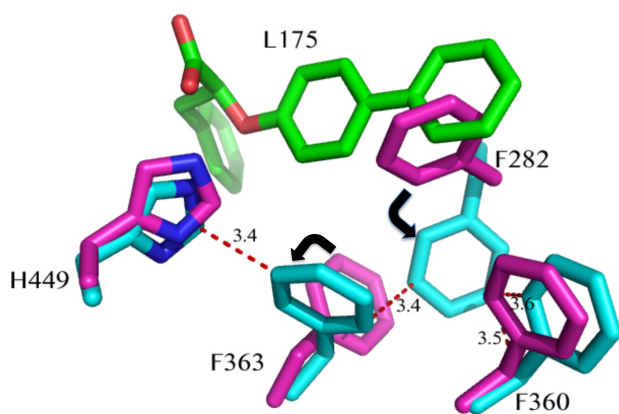


**Figure 74.** F282/F363 switch mechanism: in the structure of the complex between PPAR $\gamma$ -LBD (cyan) and LT175, the ligand (green) forces the F282 side-chain to switch from the trans to the gauche\* conformation, and in turn the F363 side-chain also changes its conformation by 180°, contacting H449. In the new conformation the F282 aromatic ring makes favorable pi-stacking interactions with the rings of F360 and F363.

## 5. Summary and conclusions

In this thesis the PPARs LBD in complex with both natural and synthetic ligands have been investigated using X-ray crystallography, with the aim to determine a structure-activity relationship between the ligand/receptor interaction and the partial/full agonism or antagonism character of the ligands, thus providing information for the design of novel compounds with a better pharmacological profile. In addition, the interaction with the receptors for some of these ligands has been further characterized through SPR and ITC techniques, which provided information on binding affinity, kinetics and thermodynamics. In particular, SPR has proved to be a potent and fast tool for high-throughput screening of a large number of compounds, as in the case of saponins and sapogenins, also being able to reveal the antagonistic character of some ligands (*e.g.* echinocistic acid).

PPARs represent a central point of pharmacological and medical research, due to the broad roles of the three isotypes in regulating metabolism, inflammation, differentiation and cellular growth. In particular, all isoforms are involved in lipid homeostasis and glucose regulation (energy balance), with PPAR $\alpha$  and PPAR $\beta/\delta$  facilitating energy combustion and PPAR $\gamma$  contributing to energy storage by enhancing adipogenesis. For this reason PPAR $\gamma$  ligands, in particular full agonists for the receptor such as TZDs, were used in the clinic for treatment of type 2 diabetes mellitus (T2DM). However, they showed serious life-threatening side effects so that in the recent years the research have been focused on partial agonists and selective modulators with a weaker effect in specific tissues.

In the strategy for searching safer therapeutic agonists of PPAR $\gamma$ , devoided of the side effects of the full agonists, new drug candidates called

selective PPAR $\gamma$  modulators (SPPARMs), able to differentially induce specific effects, have been developed and clinically tested. Ideal SPPARMs would be potent and highly efficacious inducers of insulin sensitivity (*e.g.* up-regulation of adiponectin or adiponectin target genes) with low potency and/or low maximal activity (partial agonists) on adipogenesis (*e.g.* down-regulation of aP2 and LPL target genes).

It has been observed that specific binding of a ligand to the PPAR $\gamma$  LBD can be associated to a different recruitment of co-activators and to different gene expression profiles. A preliminar NMR structural dynamics study performed on the apo-PPAR $\gamma$  LBD [36] indicated that the LBD is in very high molecular motion when not bound to the ligand. The converse was shown upon addition of rosiglitazone, indicating that full agonists are able to greatly stabilize the mobility of the receptor. Further HDX studies showed that full agonists strongly and selectively stabilize H3 and H12, and the activation function-2 (AF-2) surface for the recruitment of co-activators. X-ray crystallography studies showed that this stabilization is obtained mainly by a H-bond network between the acidic head of the ligand and three key residues of the nuclear receptor: H449, H323 and Y474, the latter belonging to the helix 12. HDX and X-ray crystallography also showed that, surprisingly, partial agonists cause no direct stabilization of H12 even though in some cases have a transactivation output nearly 80% of that of rosiglitazone (*e.g.* BVT.13) [32], suggesting that a non-H12-dependent mechanism exists to control co-activator recruitment. Instead, partial agonists were shown to preferentially stabilize other regions of the LBD, especially the  $\beta$ -sheet region and H3. Helix 3 occupies a central position in the LBD and through different ligand binding modes is able to allosterically propagate a conformational exchange between different regions that may alter the surface of the receptor, eliciting different biological responses. Among these, the

inhibition of the phosphorylation of S245 (PPAR $\gamma$ 2 residue S273) is very desirable as an antidiabetic effect: most of partial agonists bind to the region in front of the inner strand of the  $\beta$ -sheet, making H-bonds with S342, strongly stabilizing the  $\beta$ -sheet and reducing in this way the flexibility of the loop region around the phosphorylatable S245 and making less favorable its phosphorylation by Cdk5 [71]. But, while it is easy to assume that ligands directly stabilizing the phosphorylation region could affect the phosphorylation rate, less clear is the case of other ligands such as LT175 [52] that, although occupying a region far from the consensus motif, also affect the phosphorylation rate. Then we are currently demonstrating, through different techniques (NMR, phosphorylation assays, protein-protein docking, MD simulation), a new cross-talk mechanism able to allosterically inhibit PPAR $\gamma$  phosphorylation. Our future objective is to explore, through HDX technology, structural changes remote from the ligand binding site with the aim to describe a novel mechanism of ligand inhibition of Cdk5-mediated PPAR $\gamma$  phosphorylation and to probe that the protection of the consensus region is variably affected by ligands depending on their binding mode.

However, so far it is not yet possible to establish a straightforward relation between a given ligand binding mode and a specific pharmacological profile. Generally, it can be said that compounds strongly stabilizing the H12 in its active conformation (through direct H-bonds with this helix) are unable to uncouple the insulin sensitizing activity from the adipogenic effect. There are also partial agonists or antagonists facing the helix 12, but not interacting directly with it, that form different H-bond networks compared to TZDs, for example making H-bonds with Y327 and S289. These compounds (betulinic acid, benzimidazoles, SR1663) showed a reduced adipogenic effect, maintaining at the same time the insulin sensitizing action. Partial agonists occupying the region between H3 and the  $\beta$ -sheet (caulophyllogenin,



halofenic acid, AL29-26) can, in principle, inhibit the phosphorylation of S245 and the level of inhibition could be associated to the degree of stabilization of the  $\beta$ -sheet induced by the ligand. This question can be better addressed by HDX experiments, that measure the degree of exposition to the solvent (and to Cdk5) of the  $\beta$ -sheet, rather than X-ray studies.

A further research direction under consideration is to explore the therapeutic potential of PPAR pan agonists that would combine the agonistic activities toward PPAR $\gamma$ , PPAR $\alpha$  and PPAR $\beta/\delta$  in a single ligand with a balanced activation profile; these compounds may prove to be the ultimate combination of PPAR activities for treatment of T2DM and its further complications. Indeed, pan agonists would regroup the beneficial effects of the three PPAR subtypes by normalizing insulin resistance, plasma lipids and adiposity [201]. To this purpose, the ligand AL29-26 has been identified using a SBVS approach and it has been shown to be a potent full agonist on PPAR $\alpha$ , and a partial agonist on PPAR $\gamma$  and  $\beta/\delta$  subtypes. To date, the data show that an appropriate dual PPAR $\gamma/\alpha$  activation results in improved metabolic profile. However, as already hinted, partial agonists of PPAR $\gamma$  are more desirable to avoid the serious side-effects caused by full agonists. On the contrary, a strong activation of PPAR $\alpha$  is also advantageous because improves dyslipidemia, lowering plasma triglycerides and increasing HDL cholesterol levels. Therefore, the search for the optimal pharmacological profile of a ligand plays an important role and for this purpose it is required the understanding, at molecular level, of the mechanism by which the ligand behaves as full or partial agonist on PPARs. In the paper concerning the ligand AL29-26, a rationale for the difference of ligand activity toward  $\alpha$  and  $\gamma$  subtypes has been provided and a new cavity of PPAR $\alpha$ -LBD never observed before has been discovered, thus opening new opportunities to rational design of more balanced PPAR modulators.

In this thesis, crystal structure of PPAR $\gamma$  mutants were also characterized. Particularly, the structure of the human pathological PPAR $\gamma$  F360L mutant showed as a simple conservative mutation to leucine leads to dramatic conformational changes in the C-terminal region of the receptor LBD, revealing the impact of mutations on dynamics and communication pathways among PPAR $\gamma$  domains. In particular, F360L mutation is responsible of the lack of van der Waals interactions and the weakening of two important salt bridges connecting H3 and the loop 11/12, with a consequent destabilization and rearrangement of this loop resulting in the increased dynamics of the helix 12 and in a less efficient co-activators recruitment. In conclusion, the elucidation of the crystal structure of the PPAR $\gamma$ -LBD F360L mutant has provided considerable insight into the structural basis of the transactivation deficiency of this mutant, which has been associated with familial partial lipodystrophy. The study of other known pathological mutants, associated to metabolic disorder and different types of cancer, has been continued using spectroscopic techniques (fluorescence and CD spectroscopy) to investigate the effects of a single aminoacidic substitution on PPAR $\gamma$  thermal, thermodynamic and spectral properties (manuscript in preparation).

## References

- . 1 Novac N. and Heinzl T. Nuclear receptors: overview and classification. *Curr Drug Targets Inflamm Allergy* (2004) 3(4):335–346.
- . 2 Mohan R. and Heyman R.A. Orphan nuclear receptor modulators. *Curr Top Med Chem* (2003) 3(14):1637–1647.
- . 3 Bonet M.L., Ribot J., Felipe,E., Palou A. Vitamin A and the regulation of fat reserves. *Cell Mol Life Sci* (2003) 60(7):1311–1321.
- . 4 Shao W. and Brown M. Advances in estrogen receptor biology: prospects for improvements in targeted breast cancer therapy. *Breast Cancer Res* (2004) 6(1):39–52.
- . 5 Di Croce L., Okret S., Kersten S., Gustafsson J.A., Parker M., Wahli W., Beato, M. Steroid and nuclear receptors. *EMBO Journal* (1999) 18, 6201–6210.
- . 6 Gronemeyer H., Gustafsson J.-A., Laudet, V. Principles for modulation of the nuclear receptor superfamily. *Nat Rev Drug Discov* (2004) 3(11):950–964.
- . 7 Auwerx J., Baulieu E., Beato M. et al. A unified nomenclature system for the nuclear receptor superfamily. *Cell* (1999) 97(2):161–163.
- . 8 Burris T.P. The nuclear receptor superfamily, in *Nuclear Receptors and Genetic Disease* (eds T.P. Burris and E.R.B. McCabe, 2001), Academic Press, San Diego, CA.
- . 9 Sever R., Glass C.K. Signaling by nuclear receptors. *Cold Spring Harb Perspect Biol* (2013) 5(3):a016709.

- . 10 Umesono K. and Evans R.M. Determinants of target gene specificity for steroid/thyroid hormone receptors. *Cell* (1989) 57(7):1139-1146.
- . 11 Germain P., Staels B., Dacquet C., Spedding M., Laudet V. Overview of nomenclature of nuclear receptors. *Pharmacol Rev* (2006) 58(4):685-704
- . 12 Bourguet W., Ruff M., Chambon P., Gronemeyer H., Moras D. Crystal structure of the ligand-binding domain of the human nuclear receptor RXR- $\alpha$ . *Nature* (1995) 375(6530):377-382.
- . 13 Renaud R.L., Rochel N., Ruff M., Vivat V., Chambon P., Gronemeyer H., Moras D. Crystal structure of the RAR $\gamma$  ligand-binding domain bound to all-trans retinoic acid. *Nature* (1995) 378(6558):681-689
- . 14 Milburn M.V., Charifson P., Lambert M., Cobb J., Wisely G.B. Ligand binding and activation of PPARs - crystal structures of PPAR $\gamma$ . [Abstract]. EMBO Workshop on 'Structure and Function of Nuclear Receptors', May 2-5, 1997, Erice, Italy.
- . 15 Moras D., Gronemeyer H. The nuclear receptor ligand-binding domain: structure and function. *Curr Opin Cell Biol* (1998) 10(3):384-391
- . 16 Mackinnon J.A.G, Gallastegui N., Osguthorpe D.J., Hagler A.T., Estebanez-Perpina E.E. Allosteric mechanism of nuclear receptors: insights from computational simulations. *Mol Cell Endocrinol* (2014) 393(1-2):75-82
- . 17 Li Y., Lambert M.H., Xu H.E. Activation of Nuclear Receptors: A Perspective from Structural Genomics. *Structure* (2003) 11(7):741-746
- . 18 Lazar M.A. Nuclear receptor corepressors. *Nucl Recept Signal* (2003) 1:e001.

- . 19 Glass C.K., Rosenfeld M. G. The coregulator exchange in transcriptional functions of nuclear receptors. *Genes Dev* (2000) 14(2):121-141.
- . 20 Hu X., Li Y., Lazar M.A. Determinants of CoRNR-dependent repression complex assembly on nuclear hormone receptors. *Mol Cell Biol* (2001) 21(5):1747-58.
- . 21 Hu X., Lazar M.A. The CoRNR motif controls the recruitment of corepressors by nuclear hormone receptors. *Nature* (1999) 402(6757):93-6.
- . 22 Xu J., Wu R.-C., O'Malley B.W. Normal and Cancer-related Functions of the p160 Steroid Receptor Co-activator (SRC) Family. *Nat Rev Cancer* (2009) 9(9):615-30
- . 23 Rang H.P., Dale M.M., Ritter J.M. *Pharmacology* 7th Ed. Elsevier
- . 24 Gronemeyer H., Gustafsson J.A., Laudet V. Principles for modulation of the nuclear receptor superfamily. *Nat Rev Drug Discov* (2004) 3(11):950-64.
- . 25 Grygiel-Górniak B. Peroxisome proliferator-activated receptors and their ligands: nutritional and clinical implications - a review. *Nutr J* (2014) 13:17.
- . 26 Risérus U., Sprecher D., Johnson T., Olson E., Hirschberg S., Liu A., Fang Z., Hegde P., Richards D., Sarov-Blat L., Strum J.C., Basu S., Cheeseman J., Fielding B.A., Humphreys S.M., Danoff T., Moore N.R., Murgatroyd P., O'Rahilly S., Sutton P., Willson T., Hassall D., Frayn K.N., Karpe F. Activation of peroxisome proliferator-activated receptor (PPAR) $\delta$  promotes reversal of multiple metabolic abnormalities, reduces

oxidative stress, and increases fatty acid oxidation in moderately obese men. *Diabetes* (2008) 57(2):332-9.

. 27 Willson T.M., Brown P.J., Sternbach D.D., Henke B.R. The PPARs: From Orphan Receptors to Drug Discovery. *J Med Chem* (2000) 43(4):527-50.

. 28 Zoete V., Grosdidier A., Michielin O. Peroxisome proliferator-activated receptor structures: ligand specificity, molecular switch and interactions with regulators. *Biochim Biophys Acta* (2007) 1771(8):915-25.

. 29 Xu H.E., Lambert M.H., Montana V.G., Plunket K.D., Moore L.B., Collins J.L., Oplinger J.A., Kliewer S.A., Gampe R.T. Jr, McKee D.D., Moore J.T., Willson T.M. Structural determinants of ligand binding selectivity between the peroxisome proliferator-activated receptors. *Proc Natl Acad Sci U.S.A.* (2001) 98(24):13919-24.

. 30 Lu I.L., Huang C.F., Peng Y.H., Lin Y.T., Hsieh H.P., Chen C.T., Lien T.W., Lee H.J., Mahindroo N., Prakash E., Yueh A., Chen H.Y., Goparaju C.M., Chen X., Liao C.C., Chao Y.S., Hsu J.T., Wu S.Y. Structure-based drug design of a novel family of PPAR partial agonists: virtual screening, X-ray crystallography, and in vitro/in vivo biological activities. *J Med Chem* (2006) 49(9):2703–2712.

. 31 Burgermeister E., Schnoebelen A., Flament A., Benz J., Stihle M., Gsell B., Rufer A., Ruf A., Kuhn B., Marki H.P., Mizrahi J., Sebokova E., Niesor E., Meyer M. A novel partial agonist of peroxisome proliferator-activated receptor-gamma (PPARgamma) recruits PPARgamma-Coactivator-1alpha, prevents triglyceride accumulation, and potentiates insulin signaling in vitro. *Mol Endocrinol* (2006) 20(4):809–830.

- . 32 Ostberg T., Svensson S., Selen G., Uppenberg J., Thor M., Sundbom M., Sydow-Backman M., Gustavsson A.-L., Jendeberg L. A new class of peroxisome proliferator-activated receptor agonists with a novel binding epitope shows antidiabetic effects. *J Biol Chem* (2004) 279(39):41124–41130.
- . 33 Oberfield J.L., Collins J.L., Holmes C.P., Goreham D.M., Cooper J.P., Cobb J.E., Lenhard J.M., Hull-Ryde E.A., Mohr C.P., Blanchard S.G., Parks D.J., Moore L.B., Lehmann J.M., Plunket K., Miller A.B., Milburn M.V., Kliewer S.A., Willson T.M. A peroxisome proliferator-activated receptor gamma ligand inhibits adipocyte differentiation. *Proc Natl Acad Sci* (1999) 96(11):6102–6106.
- . 34 Shi G.Q., Dropinski J.F., McKeever B.M., Xu S., Becker J.W., Berger J.P., MacNaul K.L., Elbrecht A., Zhou G., Doebber T.W., Wang P., Chao Y.-S., Forrest M., Heck J.V., Moller D.E., Jones A.B. Design and synthesis of aryloxyphenylacetic acid derivatives: a novel class of PPAR dual agonists with potent antihyperglycemic and lipid modulating activity. *J Med Chem* (2005) 48(13):4457–4468.
- . 35 Cronet P., Petersen J.F.W., Folmer R., Blomberg N., Sjoblom K., Karlsson U., Lindstedt E.-L., Bamberg K. Structure of the PPAR[alpha] and [gamma] ligand binding domain in complex with AZ 242; ligand selectivity and agonist activation in the PPAR family. *Structure* (2001) 9(8):699–706.
- . 36 Johnson B.A., Wilson E.M., Li Y., Moller D.E., Smith R.G., Zhou G. Ligand-induced stabilization of PPAR[gamma] monitored by NMR spectroscopy: implications for nuclear receptor activation. *J Mol Biol* (2000) 298(2):187–194.

- . 37 Hamuro Y., Coales S.J., Morrow J.A., Molnar K.S., Tuske S.J., Southern M.R., Griffin P.R. Hydrogen/deuterium-exchange (H/D-Ex) of PPARgamma LBD in the presence of various modulators. *Protein Sci* (2006) 15(8):1883–1892.
- . 38 Kallenberger B.C., Love J.D., Chatterjee V.K., Schwabe J.W.R. A dynamic mechanism of nuclear receptor activation and its perturbation in a human disease. *Nat Struct Biol* (2003) 10(2):136–140.
- . 39 Nolte R.T., Wisely G.B., Westin S., Cobb J.E., Lambert M.H., Kurokawa R., Rosenfeld M.G., Willson T.M., Glass C.K., Milburn M.V. Ligand binding and co-activator assembly of the peroxisome proliferator-activated receptor-gamma. *Nature* (1998) 395(6698):137–143.
- . 40 Uppenberg J., Svensson C., Jaki M., Bertilsson G., Jendeberg L., Berkenstam A. Crystal structure of the ligand binding domain of the human nuclear receptor PPARgamma. *J Biol Chem* (1998) 273(47):31108–31112.
- . 41 Juge-Aubry C.E., Hammar E., Siegrist-Kaiser C., Pernin A., Takeshita A., Chin W.W., Burger A.G., Meier C.A. Regulation of the transcriptional activity of the peroxisome proliferator-activated receptor alpha by phosphorylation of a ligand-independent trans-activating domain. *J Biol Chem* (1999) 274(15):10505–10510.
- . 42 Lazennec G., Canaple L., Saugy D., Wahli W. Activation of peroxisome proliferator-activated receptors (PPARs) by their ligands and protein kinase A activators. *Mol Endocrinol* (2000) 14(12):1962–1975.
- . 43 Molnár F., Matilainen M., Carlberg C. Structural determinants of the agonist-independent association of human peroxisome proliferator-activated receptors with coactivators. *J Biol Chem* (2005) 280(28):26543–26556.



- . 44 Michalik L., Zoete V., Krey G., Grosdidier A., Gelman L., Chodanowski P., Feige J.N., Desvergne B., Wahli W., Michielin M. Combined simulation and mutagenesis analyses of PPAR[alpha] AF-2 unveil the basis of helix 12 dynamics. *J Biol Chem* (2007) 282(13):9666-77.
- . 45 Bruning J.B., Chalmers M.J., Prasad S., Busby S.A., Kamenecka T.M., He Y., Nettles K.W., Griffin P.R. Partial agonists activate PPARgamma using a helix 12 independent mechanism. *Structure* (2007) 15(10):1258-71.
- . 46 Oberfield J.L., Collins J.L., Holmes C.P., Goreham D.M., Cooper J.P., Cobb J.E., Lenhard J.M., Hull-Ryde E.A., Mohr C.P., Blanchard S.G., Parks D.J., Moore L.B., Lehmann J.M., Plunket K., Miller A.B., Milburn M.V., Kliewer S.A., Willson T.M. A peroxisome proliferator-activated receptor gamma ligand inhibits adipocyte differentiation. *Proc Natl Acad Sci U.S.A.* (1999) 96(11):6102–6106.
- . 47 Burgermeister E., Schnoebelen A., Flament A., Benz J., Stihle M., Gsell B., Rufer A., Ruf A., Kuhn B., Marki H.P., Mizrahi J., Sebokova E., Niesor E., Meyer M. A novel partial agonist of peroxisome proliferator-activated receptor-gamma (PPARgamma) recruits PPARgamma-coactivator-1alpha, prevents triglyceride accumulation, and potentiates insulin signaling in vitro. *Mol Endocrinol* (2006) 20(4):809–830.
- . 48 Nettles K.W. Insights into PPARgamma from structures with endogenous and covalently bound ligands. *Nat Struct Mol Biol* (2008) 15(9):893–895.
- . 49 Xu H.E., Li Y. Ligand-dependent and -independent regulation of PPAR gamma and orphan nuclear receptors. *Sci Signal* (2008) 1(48):52.

- . 50 Li Y., Zhang J., Schopfer F.J., Martynowski D., Garcia-Barrio M.T., Kovach A., Suino-Powell K., Baker P.R., Freeman B.A., Chen, Y. E., Xu, H. E. Molecular recognition of nitrated fatty acids by PPAR gamma. *Nat Struct Mol Biol* (2008) 15(8):865–867.
- . 51 Chandra V., Huang P., Hamuro Y., Raghuram S., Wang Y., Burris T.P., Rastinejad, F. Structure of the intact PPAR-gamma-RXR-alpha nuclear receptor complex on DNA. *Nature* (2008) 456(7220):350–356.
- . 52 Montanari R., Saccoccia F., Scotti E., Crestani M., Godio C., Gilardi F., Liodice F., Fracchiolla G., Laghezza A., Tortorella P., Lavecchia A., Novellino E., Mazza F., Aschi M., Pochetti G. Crystal structure of the peroxisome proliferator-activated receptor gamma (PPARgamma) ligand binding domain complexed with a novel partial agonist: a new region of the hydrophobic pocket could be exploited for drug design. *J Med Chem* (2008) 51(24):7768-76.
- . 53 Gampe R.T. Jr., Montana V.G., Lambert M.H., Miller A.B., Bledsoe R.K., Milburn M.V., Kliewer S.A., Willson T.M., Xu H.E. Asymmetry in the PPARgamma/RXRalpha crystal structure reveals the molecular basis of heterodimerization among nuclear receptors. *Mol Cell* (2000) 5(3):545-555.
- . 54 Xu H.E., Stanley T.B., Montana V.G., Lambert M.H., Shearer B.G., Cobb J.E., McKee D.D., Galardi C.M., Plunket K.D., Nolte R.T., Parks D.J., Moore J.T., Kliewer S.A., Willson T.M., Stimmel J.B. Structural basis for antagonist-mediated recruitment of nuclear co-repressors by PPARalpha. *Nature* (2002) 415(6873):813-7.
- . 55 Okuno M., Arimoto E., Ikenobu Y., Nishihara T., Imagawa M. Dual DNA-binding specificity of peroxisome-proliferator-activated receptor  $\gamma$

controlled by heterodimer formation with retinoid X receptor  $\gamma$ . *Biochemical Journal* (2001) 353(Pt. 2):193–198.

. 56 Aranda A. and Pascual A. Nuclear hormone receptors and gene expression. *Physiol Rev* (2001) 81(3):1269–1304.

. 57 Forman B.M., Umesono K., Chen J., Evans R.M.. Unique response pathways are established by allosteric interactions among nuclear hormone receptors. *Cell* (1995) 81(4):541–550.

. 58 Yang X.Y., Wang L.H., Chen T., Hodge D.R., Resau J.H., DaSilva L., Farrar W.L. Activation of human T lymphocytes is inhibited by peroxisome proliferator-activated receptor gamma (PPARgamma) agonists. PPARgamma co-association with transcription factor NFAT. *J Biol Chem* (2000) 275(7):4541-4.

. 59 Mouthiers A., Baillet A., Deloménie C., Porquet D., Mejdoubi-Charef N. Peroxisome proliferator-activated receptor alpha physically interacts with CCAAT/enhancer binding protein (C/EBPbeta) to inhibit C/EBPbeta-responsive alpha1-acid glycoprotein gene expression. *Mol Endocrinol* (2005) 19(5):1135-46.

. 60 Delerive P., De Bosscher K., Besnard S., Vanden Berghe W., Peters J.M., Gonzalez F.J., Fruchart J.C., Tedgui A., Haegeman G., Staels B. Peroxisome proliferator-activated receptor alpha negatively regulates the vascular inflammatory gene response by negative cross-talk with transcription factors NF-kappaB and AP-1. *J Biol Chem* (1999) 274(45):32048-54.

. 61 Staels B., Koenig W., Habib A., Merval R., Lebret M., Torra I.P., Delerive P., Fadel A., Chinetti G., Fruchart J.C., Najib J., Maclouf J., Tedgui

A. Activation of human aortic smooth-muscle cells is inhibited by PPARalpha but not by PPARgamma activators. *Nature* (1998) 393(6687):790-3.

. 62 Kelly D., Campbell J.I., King T.P., Grant G., Jansson E.A., Coutts A.G., Pettersson S., Conway S. Commensal anaerobic gut bacteria attenuate inflammation by regulating nuclear-cytoplasmic shuttling of PPAR-gamma and RelA. *Nat Immunol* (2004) 5(1):104-12.

. 63 Pascual G., Fong A.L., Ogawa S., Gamliel A., Li A.C., Perissi V., Rose D.W., Willson T.M., Rosenfeld M.G., Glass C.K. A SUMOylation-dependent pathway mediates transrepression of inflammatory response genes by PPAR-gamma. *Nature* (2005) 437(7059):759-63.

. 64 Wang C., Fu M., D'Amico M., Albanese C., Zhou J.N., Brownlee M., Lisanti M.P., Chatterjee V.K., Lazar M.A., Pestell R.G. Inhibition of cellular proliferation through I $\kappa$ B kinase-independent and peroxisome proliferator-activated receptor gamma-dependent repression of cyclin D1. *Mol Cell Biol* (2001) 21(9):3057-70.

. 65 Gervois P., Vu-Dac N., Kleemann R., Kockx M., Dubois G., Laine B., Kosykh V., Fruchart J.C., Kooistra T., Staels B. Negative regulation of human fibrinogen gene expression by peroxisome proliferator-activated receptor alpha agonists via inhibition of CCAAT box/enhancer-binding protein beta. *J Biol Chem* (2001) 276(36):33471-7.

. 66 Wang L.H., Yang X.Y., Zhang X., Huang J., Hou J., Li J., Xiong H., Mihalic K., Zhu H., Xiao W., Farrar W.L. Transcriptional inactivation of STAT3 by PPARgamma suppresses IL-6-responsive multiple myeloma cells. *Immunity* (2004) 20(2):205-18.

- . 67 Shao D., Rangwala S.M., Bailey S.T., Krakow S.L., Reginato M.J., Lazar M.A. Interdomain communication regulating ligand binding by PPAR-gamma. *Nature* (1998) 396(6709):377-80.
- . 68 Hu E., Kim J.B., Sarraf P., Spiegelman B.M. Inhibition of adipogenesis through MAP kinase-mediated phosphorylation of PPARgamma. *Science* (1996) 274(5295):2100-3.
- . 69 Gray J.P., Burns K.A., Leas T.L., Perdew G.H., Vanden Heuvel J.P. Regulation of peroxisome proliferator-activated receptor alpha by protein kinase C. *Biochemistry* (2005) 44(30):10313-21.
- . 70 Dowell P., Ishmael J.E., Avram D., Peterson V.J., Nevriy D.J., Leid M. Identification of nuclear receptor corepressor as a peroxisome proliferator-activated receptor alpha interacting protein. *J Biol Chem* (1999) 274(22):15901-7.
- . 71 Choi J.H., Banks A.S., Estall J.L., Kajimura S., Boström P., Laznik D., Ruas J.L., Chalmers M.J., Kamenecka T.M., Blüher M., Griffin P.R., Spiegelman B.M. Anti-diabetic drugs inhibit obesity-linked phosphorylation of PPARgamma by Cdk5. *Nature* (2010) 466(7305):451-6.
- . 72 Dennis A.P., O'Malley B.W. Rush hour at the promoter: how the ubiquitin-proteasome pathway polices the traffic flow of nuclear receptor-dependent transcription. *J Steroid Biochem Mol Biol* (2005) 93(2-5):139–51.
- . 73 Hauser S., Adelmant G., Sarraf P., Wright H.M., Mueller E., Spiegelman B.M. Degradation of the peroxisome proliferator-activated receptor gamma is linked to ligand-dependent activation. *J Biol Chem* (2000) 275(24):18527-33.

- . 74 Blanquart C., Barbier O., Fruchart J.C., Staels B., Glineur C. Peroxisome proliferator-activated receptor alpha (PPARalpha) turnover by the ubiquitin-proteasome system controls the ligand-induced expression level of its target genes. *J Biol Chem* (2002) 277(40):37254–9.
- . 75 Hirotsani M., Tsukamoto T., Bourdeaux J., Sadano H., Osumi T. Stabilization of peroxisome proliferator-activated receptor alpha by the ligand. *Biochem Biophys Res Commun* (2001) 288(1):106–10.
- . 76 Kim D.J., Akiyama T.E., Harman F.S., Burns A.M., Shan W., Ward J.M., et al. Peroxisome proliferator-activated receptor beta (delta)-dependent regulation of ubiquitin C expression contributes to attenuation of skin carcinogenesis. *J Biol Chem* (2004) 279(22):23719–27.
- . 77 Hay R.T. SUMO: a history of modification. *Mol Cell* (2005) 18(1):1–12.
- . 78 Ohshima T., Koga H., Shimotohno K. Transcriptional activity of peroxisome proliferator-activated receptor gamma is modulated by SUMO-1 modification. *J Biol Chem* (2004) 279(28):29551–7.
- . 79 Yamashita D., Yamaguchi T., Shimizu M., Nakata N., Hirose F., Osumi T. The transactivating function of peroxisome proliferator-activated receptor gamma is negatively regulated by SUMO conjugation in the amino-terminal domain. *Genes Cells* (2004) 9(11):1017–29.
- . 80 Kotaja N., Aittomaki S., Silvennoinen O., Palvimo J.J., Janne O.A. ARIP3 (androgen receptor-interacting protein 3) and other PIAS (protein inhibitor of activated STAT) proteins differ in their ability to modulate steroid receptor-dependent transcriptional activation. *Mol Endocrinol* (2000) 14(12):1986–2000.

- . 81 Gill G. SUMO and ubiquitin in the nucleus: different functions, similar mechanisms? *Genes Dev* (2004) 18(17):2046–59.
- . 82 Berger J.P., Akiyama T.E., Meinke P.T. PPARs: therapeutic targets for metabolic disease. *Trends Pharmacol Sci* (2005) 26(5):244-51.
- . 83 Shearer B.G., Billin A.N. The next generation of PPAR drugs: do we have the tools to find them? *Biochim Biophys Acta* (2007) 1771(8):1082-93.
- . 84 Rubenstrunk A., Hanf R., Hum D.W., Fruchart J.C., Staels B. Safety issues and prospects for future generations of PPAR modulators. *Biochim Biophys Acta* (2007) 1771(8):1065-81.
- . 85 Watkins P.B., Whitcomb R.W. Hepatic dysfunction associated with troglitazone. *N Engl J Med* (1998) 338(13):916–917.
- . 86 Lebovitz H.E., Kreider M., Freed M.I. Evaluation of liver function in type 2 diabetic patients during clinical trials: evidence that rosiglitazone does not cause hepatic dysfunction. *Diabetes Care* (2002) 25(5):815–821.
- . 87 Gupta R.A., Wang D., Katkuri S., Wang H., Dey S.K., DuBois R.N. Activation of nuclear hormone receptor peroxisome proliferator-activated receptor-delta accelerates intestinal adenoma growth. *Nat Med* (2004) 10(3):245–247.
- . 88 Marin H.E., Peraza M.A., Billin A.N., Willson T.M., Ward J.M., Kennett M.J., Gonzalez F.J., Peters J.M. Ligand activation of peroxisome proliferator-activated receptor beta inhibits colon carcinogenesis. *Cancer Res* (2006) 66(8):4394–4401.
- . 89 Harman F.S., Nicol C.J., Marin H.E., Ward J.M., Gonzalez F.J., Peters J.M. Peroxisome proliferator-activated receptor-delta attenuates colon

carcinogenesis. *Nat Med* (2004) 10(5):481–483.

. 90 Chaput E., Saladin R., Silvestre M., Edgar A.D. Fenofibrate and rosiglitazone lower serum triglycerides with opposing effects on body weight. *Biochem Biophys Res Commun* (2000) 271(2):445-50.

. 91 Buse J.B., Rubin C.J., Frederich R., Viraswami-Appanna K., Lin K.C., Montoro R., Shockey G., Davidson J.A. Muraglitazar, a dual (alpha/gamma) PPAR activator: a randomized, double-blind, placebo-controlled, 24-week monotherapy trial in adult patients with type 2 diabetes. *Clin Ther* (2005) 27(8):1181–1195.

. 92 Calkin A.C., Thomas M.C., Cooper M.E. MK-767. Kyorin/Banyu/Merck. *Curr Opin Investig Drugs* (2003) 4(4):444–448.

. 93 Fagerberg B., Edwards S., Halmos T., Lopatynski J., Schuster H., Stender S., Stoa-Birketvedt G., Tonstad S., Halldórsdóttir S., Gause-Nilsson I. Tesaglitazar, a novel dual peroxisome proliferator-activated receptor alpha/gamma agonist, dose-dependently improves the metabolic abnormalities associated with insulin resistance in a non-diabetic population. *Diabetologia* (2005) 48(9):1716–1725.

. 94 Pickavance L.C., Brand C.L., Wassermann K., Wilding J.P. The dual PPARalpha/gamma agonist, ragaglitazar, improves insulin sensitivity and metabolic profile equally with pioglitazone in diabetic and dietary obese ZDF rats. *Br J Pharmacol* (2005) 144(3):308–316.

. 95 Tanaka T., Yamamoto J., Iwasaki S., Asaba H., Hamura H., Ikeda Y., Watanabe M., Magoori K., Ioka R.X., Tachibana K., Watanabe Y., Uchiyama Y., Sumi K., Iguchi H., Ito S., Doi T., Hamakubo T., Naito M., Auwerx J., Yanagisawa M., Kodama T., Sakai J. Activation of peroxisome



proliferator-activated receptor delta induces fatty acid beta-oxidation in skeletal muscle and attenuates metabolic syndrome. *Proc Natl Acad Sci U.S.A.* (2003) 100(26):15924–15929.

. 96 Oliver W.R. Jr, Shenk J.L., Snaith M.R., Russell C.S., Plunket K.D., Bodkin N.L., Lewis M.C., Winegar D.A., Sznaidman M.L., Lambert M.H., Xu H.E., Sternbach D.D., Kliewer S.A., Hansen B.C., Willson T.M. A selective peroxisome proliferator-activated receptor delta agonist promotes reverse cholesterol transport. *Proc Natl Acad Sci U.S.A.* (2001) 98(9):5306–5311.

. 97 Liu K.G., Lambert M.H., Leesnitzer L.M., Oliver W. Jr, Ott R.J., Plunket K.D., Stuart L.W., Brown P.J., Willson T.M., Sternbach D.D. Identification of a series of PPAR gamma/delta dual agonists via solid-phase parallel synthesis. *Bioorg Med Chem Lett* (2001) 11(22):2959–2962.

. 98 Ramachandran U., Kumar R., Mittal A. Fine tuning of PPAR ligands for type 2 diabetes and metabolic syndrome. *Mini Rev Med Chem* (2006) 6(5):563–573.

. 99 Etgen G.J., Oldham B.A., Johnson W.T., Broderick C.L., Montrose C.R., Brozinick J.T., Misener E.A., Bean J.S., Bensch W.R., Brooks D.A., Shuker A.J., Rito C.J., McCarthy J.R., Ardecky R.J., Tyhonas J.S., Dana S.L., Bilakovics J.M., Paterniti J.R. Jr, Ogilvie K.M., Liu S., Kauffman R.F. A tailored therapy for the metabolic syndrome: the dual peroxisome proliferator-activated receptor-alpha/gamma agonist LY465608 ameliorates insulin resistance and diabetic hyperglycemia while improving cardiovascular risk factors in preclinical models. *Diabetes* (2002) 51(4):1083–1087.

- . 100 Miles P.D. et al. Improved insulin-sensitivity in mice heterozygous for PPAR-gamma deficiency. *J Clin Invest* (2000) 105(3):287–292.
- . 101 Olefsky J.M., Saltiel A.R. PPAR gamma and the treatment of insulin resistance. *Trends Endocrinol Metab* (2000) 11(9):362–368.
- . 102 Shang Y. et al.. Cofactor dynamics and sufficiency in estrogen receptor-regulated transcription. *Cell* (2000) 103(6):843–852.
- . 103 Rangwala S.M., Lazar M.A. The dawn of the SPPARMs? *Sci STKE* 2002(121):pe9.
- . 104 Berger J.P. et al. Distinct properties and advantages of a novel peroxisome proliferator-activated protein [gamma] selective modulator. *Mol Endocrinol* (2003) 17(4):662–676.
- . 105 Hubbard R.E. *Structure-Based Drug Discovery : an overview*. Royal Society of Chemistry (2006).
- . 106 Marks J.S., Burdette D.S., Giegel D.A. Homogeneous techniques for monitoring receptor-ligand interactions. *Methods Mol Biol* (2002) 190:51-63.
- . 107 Wu X., Glickman J.F., Bowen B.R., SILLS M.A.. Comparison of Assay Technologies for a Nuclear Receptor Assay Screen Reveals Differences in the Sets of Identified Functional Antagonists. *Journal of Biomolecular Screening* (2003) 8(4):381-92 .
- . 108 Niessen W.M. Progress in liquid chromatography-mass spectrometry instrumentation and its impact on high-throughput screening. *J Chromatogr A* (2003) 1000(1-2):413-36.

- . 109 Ebel C. Analytical ultracentrifugation for the study of biological macromolecules. *Progr Colloid Polym Sci* (2004) 127:73-82.
- . 110 Fernández C., Jahnke W. New approaches for NMR screening in drug discovery. *Drug Discov Today Technol* (2004) 1(3):277-83.
- . 111 Cliff M.J., Ladbury J.E. A survey of the year 2002 literature on applications of isothermal titration calorimetry. *J Mol Recognit* (2003) 16(6):383-91.
- . 112 Rich R.L., Myszka D.G. Why you should be using more SPR biosensor technology. *Drug Discov Today Technol* (2004) 1(3):301-8.
- . 113 Löfås S. SPRing screening. Surface plasmon resonance is increasingly useful in the study of biomolecular associations. *Mod Drug Discov* (2003) 6: 47-9.
- . 114 Baird C.L. and Myszka D.G. Current and emerging commercial optical biosensors. *J Mol Recognit* (2001) 14(5):261–268.
- . 115 Cottier K., Wiki M., Voirin G., Gao H., Kunz R.E. Label-free highly sensitive detection of (small) molecules by wavelength interrogation of integrated optical chips. *Sensors and Actuators B* (2003) 91(1-3):241–251.
- . 116 Huber W., Mueller F. Biomolecular interaction analysis in drug discovery using surface plasmon resonance technology. *Curr Pharm Des* (2006) 12(31):3999-4021.
- . 117 Weber P.C., Salemme F.R. Applications of calorimetric methods to drug discovery and the study of protein interactions. *Curr Opin Struct Biol* (2003) 13(1):115-21.

- . 118 Battye T.G., Kontogiannis L., Johnson O., Powell H.R., Leslie A.G. iMOSFLM: a new graphical interface for diffraction-image processing with MOSFLM. *Acta Crystallogr D Biol Crystallogr* (2011) 67(Pt 4):271-81.
- . 119 Navaza J. *AMoRe*: an automated package for molecular replacement. *Acta Cryst* (1994) A50, 157-163.
- . 120 Brünger A.T., Adams P.D., Clore G.M., DeLano W.L., Gros P., Grosse-Kunstleve R.W., Jiang J.S., Kuszewski J., Nilges M., Pannu N.S., Read R.J., Rice L.M., Simonson T., Warren G.L. Crystallography & NMR system: A new software suite for macromolecular structure determination. *Acta Crystallogr D Biol Crystallogr* (1998) 54(Pt 5):905-21.
- . 121 Adams P. D., Afonine P. V., Bunkóczi G., Chen V. B., Davis I. W., Echols N., Headd J. J., Hung L.-W., Kapral G. J., Grosse-Kunstleve R. W., McCoy A. J., Moriarty N. W., Oeffner R., Read R. J., Richardson D. C., Richardson J. S., Terwilliger T. C., Zwart P. H. *PHENIX*: a comprehensive Python-based system for macromolecular structure solution. *Acta Cryst* (2010) D66, 213-221.
- . 122 Kabsch W. XDS. *Acta Crystallogr D Biol Crystallogr* (2010) 66(Pt 2): 125–132.
- . 123 Murshudov G.N, Skubák P., Lebedev A.A., Pannu N.S., Steiner R.A., Nicholls R.A., Winn M.D., Long F., Vagina A.A. *REFMAC5* for the refinement of macromolecular crystal structures. *Acta Crystallogr D Biol Crystallogr* (2011) 67(Pt 4): 355–367.
- . 124 Chen V. B., Arendall III W. B., Headd J. J., Keedy D. A., Immormino R. M., Kapral G. J., Murray L. W., Richardson J. S., Richardson D. C. *MolProbity*: all-atom structure validation for macromolecular

crystallography. *Acta Cryst* (2010) D66, 12-21.

. 125 Kuwabara N., Oyama T., Tomioka D., Ohashi M., Yanagisawa J., Shimizu T., Miyachi H. Peroxisome proliferator-activated receptors (PPARs) have multiple binding points that accommodate ligands in various conformations: phenylpropanoic acid-type PPAR ligands bind to PPAR in different conformations, depending on the subtype. *J Med Chem* (2012) 55(2):893-902.

. 126 Jonsson U. and Malmqvist M. Real time biospecific interaction analysis. the integration of Surface Plasmon Resonance detection, general biospecific interface chemistry and microfluidics into one analytical system. *Adv Biosensors* (1992) 2:291-336.

. 127 Quinn J.G. Modeling Taylor dispersion injections: determination of kinetic/affinity interaction constants and diffusion coefficients in label-free biosensing. *Anal Biochem* (2012) 421(2):391-400.

. 128 Quinn J.G. Evaluation of Taylor dispersion injections: determining kinetic/affinity interaction constants and diffusion coefficients in label-free biosensing. *Anal Biochem* (2012) 421(2):401-410.

. 129 Rich R.L., Quinn J.G., Morton T., Stepp J.D., Myszka D.G. Biosensor-based fragment screening using FastStep injections. *Anal Biochem* (2010) 407(2):270-7.

. 130 Frostell-Karlsson A., Remaeus A., Roos H., Andersson K., Borg P., Hämäläinen M., Karlsson R. Biosensor analysis of the interaction between immobilized human serum albumin and drug compounds for prediction of human serum albumin binding levels. *J Med Chem* (2000) 43(10):1986-92.

- . 131 Myszka D.G., Morton T.A. CLAMP: a biosensor kinetic data analysis program. *Trends Biochem Sci* (1998) 23(4):149-50.
- . 132 van Marrewijk L.M., Polyak S.W., Hijnen M., Kuruvilla D., Chang M.R., Shin Y., Kamenecka T.M., Griffin P.R., Bruning J.B.. SR2067 Reveals a Unique Kinetic and Structural Signature for PPAR $\gamma$  Partial Agonism. *ACS Chem Biol* (2016) 11(1):273-83.
- . 133 Wang W., Devasthale P., Farrelly D., Gu L., Harrity T., Cap M., Chu C., Kunselman L., Morgan N., Ponticiello R., Zebo R., Zhang L., Locke K., Lippy J., O'Malley K., Hosagrahara V., Zhang L., Kadiyala P., Chang C., Muckelbauer J., Doweiko A.M., Zahler R., Ryono D., Hariharan N., Cheng P.T. Discovery of azetidinone acids as conformationally-constrained dual PPAR $\alpha$ /gamma agonists. *Bioorg Med Chem Lett* (2008) 18(6):1939-44.
- . 134 Thomsen R., Christensen M.H. MolDock: a new technique for high-accuracy molecular docking. *J Med Chem* (2006) 49(11):3315-21.
- . 135 Bernardes A., Souza P.C., Muniz J.R., Ricci C.G., Ayers S.D., Parekh N.M., Godoy A.S., Trivella D.B., Reinach P., Webb P., Skaf M.S., Polikarpov I. Molecular mechanism of peroxisome proliferator-activated receptor  $\alpha$  activation by WY14643: a new mode of ligand recognition and receptor stabilization. *J Mol Biol* (2013) 425(16):2878-93.
- . 136 Lee K.T., Sohn I.C., Kim D.H., Choi J.W., Kwon S.H., Park H.J. Hypoglycemic and hypolipidemic effects of tectorigenin and kaikasaponin III in the streptozotocin-induced diabetic rat and their antioxidant activity in vitro. *Arch Pharm Res* (2000) 23(5):461-6.
- . 137 Liu Y.W., Zhu X., Li W., Lu Q., Wang J.Y., Wei Y.Q., Yin X.X. Ginsenoside Re attenuates diabetes-associated cognitive deficits in rats.

Pharmacol Biochem Behav (2012) 101(1):93-8.

. 138 Bhavsar S.K., Singh S., Giri S., Jain M.R., Santani D.D. Effect of saponins from *Helicteres isora* on lipid and glucose metabolism regulating genes expression. J Ethnopharmacol (2009) 124(3):426-33.

. 139 Eu C.H., Lim W.Y., Ton S.H., bin Abdul Kadir K. Glycyrrhizic acid improved lipoprotein lipase expression, insulin sensitivity, serum lipid and lipid deposition in high-fat diet-induced obese rats. Lipids Health Dis (2010) 9:81.

. 140 Hu X., Li Z., Xue Y., Xu J., Xue C., Wang J., Wang Y. Dietary saponins of sea cucumber ameliorate obesity, hepatic steatosis, and glucose intolerance in high-fat diet-fed mice. J Med Food (2012) 15(10):909-16.

. 141 Lee K.T., Jung T.W., Lee H.J., Kim S.G., Shin Y.S., Whang W.K. The antidiabetic effect of ginsenoside Rb2 via activation of AMPK. Arch Pharm Res (2011) 34(7):1201-8.

. 142 Hostettmann K.M.A. Chemistry and pharmacology of natural products: Saponins. Cambridge University Press, UK edn (1995).

. 143 Kwon D.Y., Kim Y.S., Ryu S.Y., Choi Y.H., Cha M.R., Yang H.J., Park S. Platyconic acid, a saponin from *Platycodi radix*, improves glucose homeostasis by enhancing insulin sensitivity in vitro and in vivo. Eur J Nutr (2012) 51(5):529-40.

. 144 Lee E.J., Kang M., Kim Y.S. Platycodin D inhibits lipogenesis through AMPK $\alpha$ -PPAR $\gamma$ 2 in 3T3-L1 cells and modulates fat accumulation in obese mice. Planta Med (2012) 78(14):1536-42.

. 145 Li W., Yan X.T., Sun Y.N., Ngan T.T., Shim S.H. and Kim Y.H.. Anti-

Inflammatory and PPAR Transactivational Effects of Oleanane-Type Triterpenoid Saponins from the Roots of *Pulsatilla koreana*. *Biomol Ther (Seoul)* (2014) 22(4): 334–340.

. 146 Zhang Y., Yu L., Cai W., Fan S., Feng L., Ji G., Huang C. Protopanaxatriol, a novel PPAR $\gamma$  antagonist from *Panax ginseng*, alleviates steatosis in mice. *Sci Rep* (2014) 4:7375.

. 147 Wong H.R., Menendez I.Y. Sesquiterpene lactones inhibit inducible nitric oxide synthase gene expression in cultured rat aortic smooth muscle cells. *Biochem Biophys Res Commun* (1999) 262(2):375-80.

. 148 Ley K., Laudanna C., Cybulsky M.I., Nourshargh S. Getting to the site of inflammation: the leukocyte adhesion cascade updated. *Nat Rev Immunol* (2007) 7(9):678-89.

. 149 Avato P., Bucci R., Tava A., Vitali C., Rosato A., Bialy Z., Jurzysta M. Antimicrobial activity of saponins from *Medicago* sp.: structure-activity relationship. *Phytother Res* (2006) 20(6):454-7.

. 150 Calleri E., Fracchiolla G., Montanari R., Pochetti G., Lavecchia A., Loidice F., I A., Piemontese L., Massolini G., Temporini C. Frontal affinity chromatography with MS detection of the ligand binding domain of PPAR $\gamma$  receptor: ligand affinity screening and stereoselective ligand-macromolecule interaction. *J Chromatogr A* (2012) 1232:84-92.

. 151 Rich R.L., Hoth L.R., Geoghegan K.F., Brown T.A., LeMotte P.K., Simons S.P., Hensley P., Myszka D.G. Kinetic analysis of estrogen receptor/ligand interactions. *Proc Natl Acad Sci U.S.A.* (2002) 99(13):8562-7.



- . 152 Aronow W.S., Harding P.R., Khursheed M., Vangrow J.S., Papageorge's N.P., Mays J. Effect of halofenate on serum lipids. *Clin Pharmacol Ther* (1973) 14(3):358-65.
- . 153 Laghezza A., Montanari R., Lavecchia A., Piemontese L., Pochetti G., Iacobazzi V., Infantino V., Capelli D., De Bellis M., Liantonio A., Pierno S., Tortorella P., Conte Camerino D., Loiodice F. On the metabolically active form of metaglidazen: improved synthesis and investigation of its peculiar activity on peroxisome proliferator-activated receptors and skeletal muscles. *ChemMedChem* (2015) 10(3):555-65.
- . 154 Podolak I., Galanty A., Sobolewska D. Saponins as cytotoxic agents: a review. *Phytochem Rev* (2010) 9(3): 425–474.
- . 155 Tong X., Lin S., Fujii M., Hou D.X. Molecular mechanisms of echinocystic acid-induced apoptosis in HepG2 cells. *Biochem Biophys Res Commun* (2004) 321(3):539-46.
- . 156 Honore-Thorez D. Description, identification and therapeutic use of *Chrysanthellum "americanum"*: *Chrysanthellum indicum* DC. subsp *afroamericanum* B. L. Turner. *J Pharm Belg* (1985) 40(5):323-31.
- . 157 Itoh T., Fairall L., Amin K., Inaba Y., Szanto A., Balint B.L., Nagy L., Yamamoto K., Schwabe J.W. Structural basis for the activation of PPARgamma by oxidized fatty acids. *Nat Struct Mol Biol* (2008) 15(9):924-31.
- . 158 Carmona M.C., Louche K., Lefebvre B., Pilon A., Hennuyer N., Audinot-Bouchez V., Fievet C., Torpier G., Formstecher P., Renard P., Lefebvre P., Dacquet C., Staels B., Casteilla L., Pénicaud L. S26948: a new specific peroxisome proliferator activated receptor gamma modulator with

potent antidiabetes and antiatherogenic effects. *Diabetes* (2007) 56(11):2797-808.

. 159 Acton J.J. III, Black R.M., Jones A.B., Moller D.E., Colwell L., Doebber T.W., Macnaul K.L., Berger J., Wood H.B. Benzoyl 2-methyl indoles as selective PPARgamma modulators. *Bioorg Med Chem Lett* (2005) 15(2):357-62.

. 160 Gregoire F.M., Zhang F., Clarke H.J., Gustafson T.A., Sears D.D., Favelyukis S., Lenhard J., Rentzeperis D., Clemens L.E., Mu Y., Lavan B.E. MBX-102/JNJ39659100, a novel peroxisome proliferator-activated receptor-ligand with weak transactivation activity retains antidiabetic properties in the absence of weight gain and edema. *Mol Endocrinol* (2009) 23(7):975-88.

. 161 Rauch T., Hamilton B.S., Tsutsumi M. (Boehringer Ingelheim International GmbH), Int. PCT Pub. No. WO 2013167554 A1 20131114, 2013.

. 162 Hamilton B.S., Rauch T., Tsutsumi M. (Boehringer Ingelheim International GmbH), Int. PCT Pub. No. WO 2012059416 A1 20120510, 2012.

. 163 Allen T., Zhang F., Moodie S.A., Clemens L.E., Smith A., Gregoire F., Bell A., Muscat G.E, Gustafson T.A. Halofenate is a selective peroxisome proliferator-activated receptor gamma modulator with antidiabetic activity. *Diabetes* (2006) 55(9):2523-33.

. 164 Luskey K.L., Luo J. (Metabotex Inc., Hayward, U.S.A.), US Pat. No. 6.262.118B1, 2001.

. 165 Rangwala S.M., O'Brien M.L., Tortorella V., Longo A., Liodice F.,

Noonan D.J., Feller D.R. Stereoselective effects of chiral clofibric acid analogs on rat peroxisome proliferator-activated receptor alpha (rPPAR alpha) activation and peroxisomal fatty acid beta-oxidation. *Chirality* (1997) 9(1):37-47.

. 166 Laskowski R.A., Swindells M.B. LigPlot+: multiple ligand-protein interaction diagrams for drug discovery. *J Chem Inf Model* (2011) 51(10):2778-86.

. 167 Bruning J.B., Chalmers M.J., Prasad S., Busby S.A., Kamenecka T.M., He Y., Nettles K.W., Griffin P.R. Partial agonists activate PPARgamma using a helix 12 independent mechanism. *Structure* (2007) 15(10):1258-71.

. 168 Laghezza A., Pochetti G., Lavecchia A., Fracchiolla G., Faliti S., Piemontese L., Di Giovanni C., Iacobazzi V., Infantino V., Montanari R., Capelli D., Tortorella P., Loiodice F. New 2-(aryloxy)-3-phenylpropanoic acids as peroxisome proliferator-activated receptor  $\alpha/\gamma$  dual agonists able to upregulate mitochondrial carnitine shuttle system gene expression. *J Med Chem* (2013) 56(1):60-72.

. 169 Chan K.H., Niu T., Ma Y., You N.C., Song Y., Sobel E.M., Hsu Y.H., Balasubramanian R., Qiao Y., Tinker L., Liu S. Common genetic variants in peroxisome proliferator-activated receptor- $\gamma$  (PPARG) and type 2 diabetes risk among Women's Health Initiative postmenopausal women. *J Clin Endocrinol Metab* (2013) 98(3):E600-4.

. 170 Jeninga E.H., Gurnell M., Kalkhoven E. Functional implications of genetic variation in human PPARgamma. *Trends Endocrinol Metab* (2009) 20(8):380-7.

. 171 Tan G.D., Savage D.B., Fielding B.A., Collins J., Hodson L.,  
173

Humphreys S.M., O'Rahilly S., Chatterjee K., Frayn K.N., Karpe F. Fatty acid metabolism in patients with PPARgamma mutations. *J Clin Endocrinol Metab* (2008) 93(11):4462-70.

. 172 Al-Shali K., Cao H., Knoers N., Hermus A.R., Tack C.J., Hegele R.A. A single-base mutation in the peroxisome proliferator-activated receptor gamma4 promoter associated with altered in vitro expression and partial lipodystrophy. *J Clin Endocrinol Metab* (2004) 89(11):5655-60.

. 173 Li G. and Leff T. Altered promoter recycling rates contribute to dominant-negative activity of human peroxisome proliferator-activated receptor-gamma mutations associated with diabetes. *Mol Endocrinol* (2007) 21(4):857-64.

. 174 Monajemi H., Zhang L., Li G., Jeninga E.H., Cao H., Maas M., Brouwer C.B., Kalkhoven E., Stroes E., Hegele R.A., Leff T. Familial partial lipodystrophy phenotype resulting from a single-base mutation in deoxyribonucleic acid-binding domain of peroxisome proliferator-activated receptor-gamma. *J Clin Endocrinol Metab* (2007) 92(5):1606-12.

. 175 Guettier J.M., Park J.Y., Cochran E.K., Poitou C., Basdevant A., Meier M., Clément K., Magré J., Gorden P. Leptin therapy for partial lipodystrophy linked to a PPAR-gamma mutation. *Clin Endocrinol (Oxf)* (2008) 68(4):547-54.

. 176 Balamurugan B., Md. Roshan M.N.A., Shaahul Hameed B., Sumathi K., Senthilkumar R., Udayakumar A., Venkatesh Babu K. H., Kalaivani M., Sowmiya G., Sivasankari P., Saravanan S., Vasuki Ranjani C., Gopalakrishnan K., Selvakumar K. N., Jaikumar M., Brindha T., Michael D. and Sekar K.. PSAP: protein structure analysis package. *J Appl Cryst* (2007)

40:773-777.

. 177 Flocco M.M. and Mowbray S.L. Planar stacking interactions of arginine and aromatic side-chains in proteins. *J Mol Biol* (1994) 235(2):709-17.

. 178 Kimura Y., Okuda H., Arichi S. Effects of stilbenes on arachidonate metabolism in leukocytes. *Biochim Biophys* (1985) 834(2):275-278.

. 179 Sonnett T.E., Levien T.L., Gates B.J., Robinson J.D., Campbell R.K. Diabetes mellitus, inflammation, obesity: proposed treatment pathways for current and future therapies. *Ann Pharmacother* (2010) 44(4):701-711.

. 180 Qiang L., Wang L., Kon N., Zhao W., Lee S., Zhang Y., Rosenbaum M., Zhao Y., Gu W., Farmer S.R., Accili D. Brown remodeling of white adipose tissue by SirT1-dependent deacetylation of PPAR $\gamma$ . *Cell* (2012) 150(3):620-32.

. 181 Wang Z., Huang Y., Zou J., Cao K., Xu Y., Wu J.M. Effects of red wine and wine polyphenol resveratrol on platelet aggregation in vivo and in vitro. *Int J Mol Med* (2002) 9(1):77-79.

. 182 Naderali E.K., Doyle P.J., Williams G. Resveratrol induces vasorelaxation of mesenteric and uterine arteries from female guinea-pigs. *Clin Sci* (2000) 98(5):537-543.

. 183 Naderali E.K., Smith S.L., Doyle P.J., Williams G. The mechanism of resveratrol-induced vasorelaxation differs in the mesenteric resistance arteries of lean and obese rats. *Clin Sci* (2001) 100(1):55-60.

. 184 Labinskly N., Csiszar A., Veress G., Stef G., Pacher P., Oroszi G., Wu J., Ungvari Z. Vascular dysfunction in aging: potential effects of resveratrol,

an anti-inflammatory phytoestrogen. *Curr Med Chem* (2006) 13(9):989–996.

. 185 Inoue H., Jiang X.F., Katayama T., Osada S., Umesono K., Namura S. Brain protection by resveratrol and fenofibrate against stroke requires peroxisome proliferator-activated receptor alpha in mice. *Neurosci Lett* (2003) 352(3):203-6.

. 186 Bäckesjö C.M., Li Y., Lindgren U., Haldosén L.A. Activation of Sirt1 decreases adipocyte formation during osteoblast differentiation of mesenchymal stem cells. *J Bone Miner Res* (2006) 21(7):993-1002.

. 187 Costa C.S., Rohden F., Hammes T.O., Margis R., Bortolotto J.W., Padoin A.V., Mottin C.C., Guaragna R.M. Resveratrol upregulated SIRT1, FOXO1, and adiponectin and downregulated PPAR $\gamma$ 1–3 mRNA expression in human visceral adipocytes. *Obes Surg* (2011) 21(3):356–361.

. 188 Temporini C., Pochetti G., Fracchiolla G., Piemontese L., Montanari R., Moaddel R., Laghezza A., Altieri F., Cervoni L., Ubiali D., Prada E., Liodice F., Massolini G. and Calleri E. Open tubular columns containing the immobilized ligand binding domain of peroxisome proliferator-activated receptors  $\alpha$  and  $\gamma$  for dual agonists characterization by frontal affinity chromatography with MS detection. *J Chromatogr A* (2013) 1284:36–43.

. 189 Henke B.R., Blanchard S.G., Brackeen M.F., Brown K.K., Cobb J.E., Collins J.L., Harrington W.W. Jr, Hashim M.A., Hull-Ryde E.A., Kaldor I., Kliwer S.A., Lake D.H., Leesnitzer L.M., Lehmann J.M., Lenhard J.M., Orband-Miller L.A., Miller J.F., Mook R.A. Jr, Noble S.A., Oliver W. Jr, Parks D.J., Plunket K.D., Szewczyk J.R., Willson T.M. N-(2-Benzoylphenyl)-L-tyrosine PPAR $\gamma$  agonists. 1. Discovery of a novel series of potent antihyperglycemic and antihyperlipidemic agents. *J Med*

Chem (1998) 41(25):5020-36.

. 190 Porcelli L., Gilardi F., Laghezza A., Piemontese L., Mitro N., Azzariti A., Altieri F., Cervoni L., Fracchiolla G., Giudici M., Guerrini U., Lavecchia A., Montanari R., Di Giovanni C., Paradiso A., Pochetti G., Simone G.M., Tortorella P., Crestani M., Liodice F. Synthesis, characterization and biological evaluation of ureidofibrate-like derivatives endowed with peroxisome proliferator-activated receptor activity. *J Med Chem* (2012) 55(1):37-54.

. 191 Weidner C., de Groot J.C., Prasad A., Freiwald A., Quedenau C., Kliem M., Witzke A., Kodelja V., Han C.T., Giegold S., Baumann M., Klebl B., Siems K., Müller-Kuhr L., Schürmann A., Schüler R., Pfeiffer A.F., Schroeder F.C., Büsow K., Sauer S. Amorphutins are potent antidiabetic dietary natural products. *Proc Natl Acad Sci U.S.A.* (2012) 109(19):7257-62.

. 192 Pochetti G., Godio C., Mitro N., Caruso D., Galmozzi A., Scurati S., Liodice F., Fracchiolla G., Tortorella P., Laghezza A., Lavecchia A., Novellino E., Mazza F., Crestani M. Insights into the mechanism of partial agonism: crystal structures of the peroxisome proliferator-activated receptor gamma ligand-binding domain in the complex with two enantiomeric ligands. *J Biol Chem* (2007) 282(23):17314-24.

. 193 Tsukamoto T., Nakata R., Tamura E., Kosuge Y., Kariya A., Katsukawa M., Mishima S., Ito T., Inuma M., Akao Y., Nozawa Y., Arai Y., Namura S. and Inoue H. Vicianol C, a resveratrol tetramer, activates PPAR $\alpha$  and PPAR $\beta/\delta$  in vitro and in vivo. *Nutr Metab* (2010) 7:46.

. 194 Viji V., Shobha B., Kavitha S.K., Ratheesh M., Kripa K., Helen A. Betulinic acid isolated from *Bacopa monniera* (L.) Wettst suppresses

lipopolysaccharide stimulated interleukin-6 production through modulation of nuclear factor-kappaB in peripheral blood mononuclear cells. *Int Immunopharmacol* (2010) 10(8):843-9.

. 195 Viji V., Helen A., Luxmi V.R. Betulinic acid inhibits endotoxin-stimulated phosphorylation cascade and pro-inflammatory prostaglandin E(2) production in human peripheral blood mononuclear cells. *Br J Pharmacol* (2011) 162(6):1291-303.

. 196 de Melo C.L., Queiroz M.G., Arruda Filho A.C., Rodrigues A.M., de Sousa D.F., Almeida J.G., Pessoa O.D., Silveira E.R., Menezes D.B., Melo T.S., Santos F.A., Rao V.S. Betulinic acid, a natural pentacyclic triterpenoid, prevents abdominal fat accumulation in mice fed a high-fat diet. *J Agric Food Chem* (2009) 57(19):8776-81.

. 197 Hollis A., Sperl B., Gräber M., Berg T. The natural product betulinic acid inhibits C/EBP family transcription factors. *ChemBioChem* (2012) 13(2):302-7.

. 198 Zhang D.M., Xu H.G., Wang L., Li Y.J., Sun P.H., Wu X.M., Wang G.J., Chen W.M., Ye W.C. Betulinic Acid and its Derivatives as Potential Antitumor Agents. *Med Res Rev* (2015) 35(6):1127-55.

. 199 Choi J.H., Banks A.S., Kamenecka T.M., Busby S.A., Chalmers M.J., Kumar N., Kuruvilla D.S., Shin Y., He Y., Bruning J.B., Marciano D.P., Cameron M.D., Laznik D., Jureczak M.J., Schürer S.C., Vidović D., Shulman G.I., Spiegelman B.M., Griffin P.R. Antidiabetic actions of a non-agonist PPAR $\gamma$  ligand blocking Cdk5-mediated phosphorylation. *Nature* (2011) 477(7365):477-81.

. 200 Marciano D.P., Kuruvilla D.S., Boregowda S.V., Asteian A., Hughes












T.S., Garcia-Ordonez R., Corzo C.A., Khan T.M., Novick S.J., Park H., Kojetin D.J., Phinney D.G., Bruning J.B., Kamenecka T.M., Griffin P.R. Pharmacological repression of PPAR $\gamma$  promotes osteogenesis. *Nat Commun* (2015) 6:7443.

. 201 Pirat C., Farce A., Lebègue N., Renault N., Furman C., Millet R., Yous S., Speca S., Berthelot P., Desreumaux P., Chavatte P. Targeting peroxisome proliferator-activated receptors (PPARs): development of modulators. *J Med Chem* (2012) 55(9):4027-61.

# Appendix

RESEARCH ARTICLE

## Catechol-based matrix metalloproteinase inhibitors with additional antioxidative activity

Marilena Tauro<sup>1</sup> , Antonio Laghezza<sup>2</sup> , Fulvio Loidice<sup>2</sup> , Luca Piemontese<sup>2</sup> , Alessia Caradonna<sup>2</sup> , Davide Capelli<sup>3</sup> , Roberta Montanari<sup>3</sup> , Giorgio Pochetti<sup>3</sup> , Antonella Di Pizio<sup>4</sup> , Mariangela Agamenone<sup>5</sup>, Cristina Campestre<sup>5</sup>, and Paolo Tortorella<sup>2</sup>

<sup>1</sup>Department of Tumor Biology, H. Lee Moffitt Cancer Center and Research Institute, Tampa, FL, USA, <sup>2</sup>Dipartimento di Farmacia-Scienze del Farmaco, Università degli Studi "A. Moro" di Bari, Bari, Italy, <sup>3</sup>Istituto di Cristallografia, CNR, Monterotondo Stazione (Roma), Italy, <sup>4</sup>Institute of Biochemistry, Food Science and Nutrition, Robert H. Smith Faculty of Agriculture, Food and Environment, The Hebrew University of Jerusalem, Rehovot, Israel, and <sup>5</sup>Dipartimento di Farmacia, Università "G. d'Annunzio" Chieti, Chieti, Italy

### Abstract

New catechol-containing chemical entities have been investigated as matrix metalloproteinase inhibitors as well as antioxidant molecules. The combination of the two properties could represent a useful feature due to the potential application in all the pathological processes characterized by increased proteolytic activity and radical oxygen species (ROS) production, such as inflammation and photoaging. A series of catechol-based molecules were synthesized and tested for both proteolytic and oxidative inhibitory activity, and the detailed binding mode was assessed by crystal structure determination of the complex between a catechol derivative and the matrix metalloproteinase-8. Surprisingly, X-ray structure reveals that the catechol oxygens do not coordinate the zinc atom.

### Keywords

Antioxidants, inhibitors, metalloenzymes, structure–activity relationships, X-ray crystallography

### History

Received 6 June 2016  
Revised 18 July 2016  
Accepted 19 July 2016  
Published online 12 August 2016

### Introduction

Matrix metalloproteinases (MMPs) are a family of zinc-containing endopeptidases, capable to process all the extracellular matrix components. They can be classified in collagenases (MMP-1, MMP-8, MMP-13, MMP-18), gelatinases (MMP-2, MMP-9), and metalloelastase (MMP-12), based on the substrate that they process.

Their enzymatic activity is finely regulated in physiological conditions: MMPs are responsible for tissue regeneration and remodeling, as well as bioavailability of pro-factors that need proteolytic cut activation. Endogenous molecules such as tissue inhibitors of metalloproteinases (TIMPs) are responsible for the physiological fine regulation of the numerous isoforms<sup>1</sup>. However, several external factors (e.g. solar UV irradiation) or pathological conditions (cancer, metastasis, or chronic inflammation) are able to stimulate an overexpression of specific MMPs. Therefore, due to their implications in complex pathological processes, MMPs continue to be considered a pivotal target for therapeutic intervention<sup>2</sup>.

The selectivity still represents the main challenge in the MMP inhibitor design: the importance of selective targeting<sup>3,4</sup> has already been previously proved in MMP inhibition strategy<sup>5</sup> especially because in the last decade, a number of inhibitors failed in clinical trial phases<sup>6</sup>, mainly due to their broad spectrum activity.

Photoaging represents another process in which the proteolytic activity of MMPs has a notorious and critical role; collagenases, in particular, are responsible for the decomposition of particular types of collagen and other proteins in the extracellular matrix of the dermis<sup>7–10</sup>. The breakdown of dermal collagen and elastin is purported to be one of the major contributing factors to loss of skin's firmness and elasticity. Physiologically, the human skin expresses a number of MMPs, including MMP-1, -2, -3, -8, -9, and -13, all of which are capable of attacking native fibrillar collagen.

Chronic exposure to solar UV radiation is an accelerator factor for photoaging. UV irradiation is known to provoke oxidative stress through the generation of reactive oxygen species (ROS), which are responsible to interfere with physiological pathways and ultimately activate the overexpression of a number of proteolytic enzymes such as MMPs in skin cells, capable to destroy the dermal connective tissue. In addition, ROS can regulate pro-MMPs activation<sup>11–15</sup>.

Thus, the antioxidant activity associated with the inhibition of MMPs could represent a promising strategy to obtain new chemical entities capable to reduce photoaging and prevent wrinkles and damage of the skin, and be effective for other pathological conditions where oxidative stress occurs.

MMP inhibitors (MMPIs) are usually characterized by a backbone that interacts with the specificity pocket S1', coupled to a metal chelator portion that binds to the catalytic Zinc ion. To expand the library of potential MMPIs and to overcome some limitations of the hydroxamic acid moiety<sup>16,17</sup>, other zinc binding

Address for correspondence: Paolo Tortorella. E-mail: paolo.tortorella@uniba.it

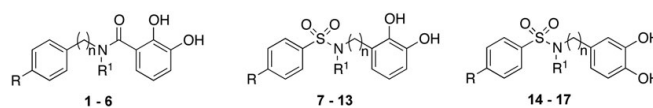


Figure 1. Catechol-based MMP inhibitors.

groups (ZBGs) as essential portion in MMP inhibitor molecule of new synthesis have been developed<sup>18–22</sup>.

Recently, a series of rosmarinic acid derivatives has been identified as micromolar MMP-1 inhibitors<sup>23</sup>. In addition, phenolic and polyphenolic compounds have already been used as antioxidants, and their activity seems to impact several different pathways. In particular, one of the most tested hypothesis is that they exert protective effects against cancer and other chronic diseases by reducing ROS levels<sup>13</sup>. Natural compounds derived from green tea (EGCG), mainly known for their antioxidant properties, have shown relevance when applied on wrinkles or fine lines caused by aging, due to their ability to enhance collagen levels and to inhibit MMPs<sup>24</sup>. Many other natural compounds, such as phytosterol, fucosterol, resveratrol, soy isoflavones, alpha-tocopherol, and vitamin E and C, are also able to inhibit MMPs and ROS and reduce the degradation of skin<sup>25–28</sup>. Some MMPis have been studied in topical cosmetic compositions to counteract the effect of photo and chronological skin aging. For example, their use has been reported in combination with UV blockers (e.g. octinoxate and zinc oxide)<sup>12</sup>, natural estrogen (e.g. 17-beta estradiol or an estrogen-like steroid)<sup>12</sup>, or antioxidants (Alpha Lipoic Acid, ALA)<sup>29</sup>.

In this study, we present a new class of MMPis obtained by combining a catecholic portion with a backbone able to reach the S1' specific pocket of the enzyme isoforms. All these compounds were tested toward MMP-2, -8, and -9 whereas their *in vitro* antioxidant activity was evaluated by DPPH assay. In order to better understand the interactions between MMPs and the chemical inhibitor, the X-ray structure of the complex between MMP-8 and one compound of the series was resolved.

## Results and discussion

Starting from the promising inhibitory activity values obtained testing catechol on different MMPs<sup>30</sup>, we decided to further investigate catecholic derivatives by focusing our attention on the backbone that, in the classical structure activity relationship (SAR) of MMPis, blocks the substrate access to the active site. Therefore, we report herein the synthesis and biological activity of three set of analogs (Figure 1) in which the catechol is connected through an amide (compounds 1–6) or a sulfonamide (compounds 7–17) group to a series of alkylaryl or aryl moieties in order to reach the S1' specificity pocket of the different enzyme isoforms.

Most compounds present a diphenyl or a phenoxyphenyl residue, based on the results obtained by our previous works in which these groups were linked to typical ZBGs<sup>3,4,19,22,31–34</sup>. The relative position of sulfonamide linking group as well as the importance of hydroxyl groups were evaluated. To this aim, we prepared a fourth set of compounds 18–22 (Figure 2) characterized by the lack of hydroxyl groups or the presence of a single hydroxyl group in different position of the aromatic ring.

Compounds 1–6 were obtained via condensation of dibenzoyloxybenzoic acid or corresponding chloride with the appropriate aniline or benzylamine and following by debenzoylation through catalytic hydrogenation (Scheme 1). N-(4-diphenylmethyl)-N-methyl-2,3-dibenzoyloxybenzamide (26) was obtained through

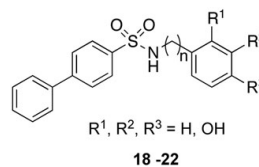


Figure 2. Catechol-based MMP inhibitors.

methylation of the sulfonamide nitrogen of the dibenzylate intermediate (25).

Compounds 7–13 and 18–22 were synthesized via condensation of the suitable aniline or benzyl amine with the appropriate sulfonyl chloride (Schemes 2 and 3). Subsequent deprotection under H<sub>2</sub> atmosphere in the presence of 10% Pd/C or with BBr<sub>3</sub> was needed to obtain the final compounds. N-(2,3-dihydroxyphenyl)-N-methyl-4-phenyl sulfonamide (10) and N-(2,3-dihydroxyphenyl)-N-methyl-4-phenoxy-phenyl sulfonamide (11) were obtained through methylation of the sulfonamide nitrogen of the dibenzylate intermediate.

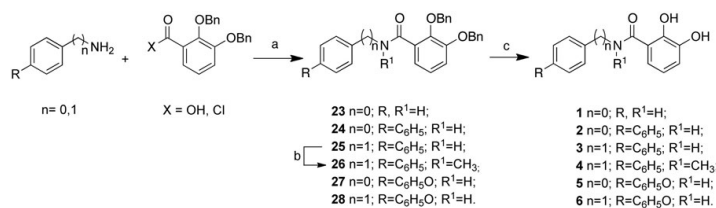
Compounds 14–17 were synthesized via condensation of 3,4-(methylenedioxy)aniline or benzylamine with the appropriate sulfonyl chloride (Scheme 4). Subsequent deprotection with BBr<sub>3</sub> was needed to obtain the final compounds.

All synthesized compounds 1–22 were tested against MMP-2, -8, and -9 (Tables 1 and 2). Compound 1 shows a very weak activity against all considered MMPs. As expected, the introduction of a diphenyl moiety (2) provides more potency and selectivity on MMP-2. A significant increase of activity toward all MMPs is obtained by inserting a methylene spacer (3), while the methylation of the amide nitrogen (4) reduces it. The introduction of an oxygen atom between the phenyl rings results in an increase of activity (5 versus 2) or selectivity for MMP-2 (6 versus 3).

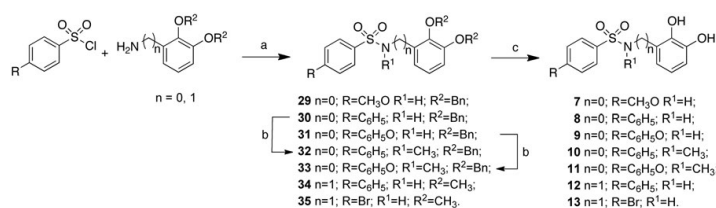
As well as for amide derivatives, compounds 7 and 8 still maintain good activity values toward MMP-2, showing an increased activity also on MMP-8 and -9. The introduction of the more flexible phenoxy phenyl structure (9) results in a slight increase of activity toward all the enzyme isoforms, with IC<sub>50</sub> values around 6 μM against all tested MMPs.

The methylation of the sulfonamide nitrogen still confirms its detrimental effects on MMP-8 and -9 (10 and 11), while no loss in activity results for these N-methyl derivatives against MMP-2. Compound 10 stands out for its very interesting selectivity toward MMP-2. The insertion of a methylene between the sulfonamide moiety and the catecholic portion (12) allows to obtain inhibition activity in the low micromolar range toward MMP-2, -8, and -9 and even the substitution of the phenyl ring with a bromine atom (13) maintains high activity values against all isoforms.

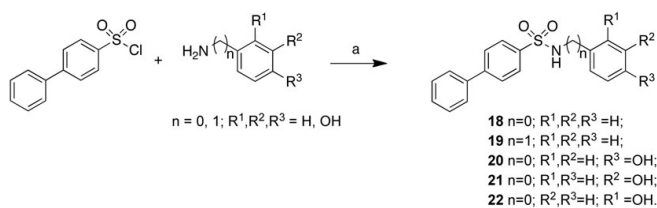
Moving the hydroxyl groups from the 2,3 to the 3,4 positions of the aromatic ring, it results a slight increase of activity when the sulfonamide moiety is directly linked to the phenyl residue (8 versus 14); in this case, the substitution of phenyl with bromine (15) reduces the activity on MMP-8 and MMP-9. The introduction



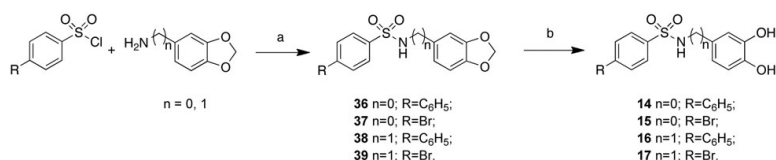
Scheme 1. Reagents and conditions: (a) anhydrous THF, r.t. or DMAP, DCC, CH<sub>2</sub>Cl<sub>2</sub>, r.t.; (b) dry DMF, NaH, CH<sub>3</sub>I, 0 °C; (c) H<sub>2</sub>, 10% Pd-C, CH<sub>3</sub>OH/THF 2:5, r.t.



Scheme 2. Reagents and conditions: (a) Et<sub>3</sub>N, CH<sub>2</sub>Cl<sub>2</sub>, reflux; (b) dry DMF, NaH, CH<sub>3</sub>I, 0 °C; (c) THF/MeOH, 10% Pd/C, H<sub>2</sub>, r.t. or BBr<sub>3</sub>, CH<sub>2</sub>Cl<sub>2</sub>, 0 °C 1 h.



Scheme 3. Reagents and conditions: (a) Et<sub>3</sub>N, CH<sub>2</sub>Cl<sub>2</sub>, reflux.



Scheme 4. Reagents and conditions: (a) Et<sub>3</sub>N, CH<sub>2</sub>Cl<sub>2</sub>, reflux; (b) BBr<sub>3</sub>, CH<sub>2</sub>Cl<sub>2</sub>, 0 °C 1 h.

of a methylene spacer into the structure of **14** gives **16** with lower activity toward all isoforms, whereas the same modification for **15** affords **17** showing reduced activity only against MMP-2.

In order to evaluate whether the presence of hydroxyl groups was essential for inhibitory activity, we prepared the

mono- (**20–22**) or non-substituted (**18, 19**) analogs (Table 2). However, these compounds show a complete loss of activity against all isoforms.

The *in vitro* antioxidant activity of these catecholic derivatives was also evaluated by DPPH assay (Tables 1 and 2), considered as

Table 1. MMP activity values expressed as IC<sub>50</sub> (μM) and antioxidant activity values expressed as EC<sub>50</sub> in DPPH assay and ARP.

Compounds	n	R	R <sup>1</sup>	MMP-2	MMP-8	MMP-9	EC <sub>50</sub> <sup>a</sup>	ARP <sup>b</sup>
Gallic acid							0.065 ± 0.012	15.4
<b>1</b>	0	H	H	>100	>100	>100	0.130 ± 0.041	7.7
<b>2</b>	0	C <sub>6</sub> H <sub>5</sub>	H	34 ± 6	>100	>100	0.163 ± 0.012	6.1
<b>3</b>	1	C <sub>6</sub> H <sub>5</sub>	H	4.0 ± 1.4	25 ± 4	56 ± 8	0.099 ± 0.009	10.1
<b>4</b>	1	C <sub>6</sub> H <sub>5</sub>	CH <sub>3</sub>	>100	>100	>100	0.112 ± 0.021	8.9
<b>5</b>	0	C <sub>6</sub> H <sub>5</sub> O	H	6.6 ± 1.2	26 ± 5	33 ± 5	0.104 ± 0.044	9.6
<b>6</b>	1	C <sub>6</sub> H <sub>5</sub> O	H	4.2 ± 0.9	94 ± 4	95 ± 5	0.119 ± 0.009	8.4
<b>7</b>	0	CH <sub>3</sub> O	H	12 ± 4	16 ± 3	19 ± 3	0.128 ± 0.013	7.8
<b>8</b>	0	C <sub>6</sub> H <sub>5</sub>	H	12 ± 3	8.7 ± 2.0	6.2 ± 0.4	0.101 ± 0.001	9.9
<b>9</b>	0	C <sub>6</sub> H <sub>5</sub> O	H	6.3 ± 2.3	6.2 ± 1.5	6.5 ± 2.0	0.112 ± 0.012	8.9
<b>10</b>	0	C <sub>6</sub> H <sub>5</sub>	CH <sub>3</sub>	9.5 ± 2.5	>100	>100	0.133 ± 0.023	7.5
<b>11</b>	0	C <sub>6</sub> H <sub>5</sub> O	CH <sub>3</sub>	17.5 ± 2.1	33.5 ± 0.7	29 ± 4	0.138 ± 0.004	7.2
<b>12</b>	1	C <sub>6</sub> H <sub>5</sub>	H	7 ± 2	2.5 ± 0.9	2.1 ± 1.0	0.166 ± 0.011	6.0
<b>13</b>	1	Br	H	4.4 ± 0.5	1.9 ± 0.4	2.0 ± 0.5	0.172 ± 0.025	5.8
<b>14</b>	0	C <sub>6</sub> H <sub>5</sub>	H	7.0 ± 0.2	3.1 ± 1.1	2.7 ± 0.8	0.143 ± 0.020	7.0
<b>15</b>	0	Br	H	5.6 ± 1.5	6 ± 2	5.5 ± 2.0	0.192 ± 0.042	5.2
<b>16</b>	1	C <sub>6</sub> H <sub>5</sub>	H	12 ± 2	6 ± 1	7.5 ± 1.5	0.167 ± 0.023	6.0
<b>17</b>	1	Br	H	10 ± 1	4.4 ± 0.3	2.5 ± 0.1	0.188 ± 0.002	5.3

<sup>a</sup>μmol of antioxidant/μmol of DPPH. <sup>b</sup>Antiradical power (ARP) = 1/EC<sub>50</sub>.Table 2. MMP activity values expressed as IC<sub>50</sub> (μM) and antioxidant activity values expressed as EC<sub>50</sub> in DPPH assay and ARP.

Compounds	n	R <sup>1</sup>	R <sup>2</sup>	R <sup>3</sup>	MMP-2	MMP-8	MMP-9	EC <sub>50</sub> <sup>a</sup>	ARP <sup>b</sup>
<b>18</b>	0	H	H	H	>100	>100	>100	>1	<1
<b>19</b>	1	H	H	H	>100	>100	>100	>1	<1
<b>20</b>	0	H	H	OH	>100	>100	>100	0.37 ± 0.09	2.7
<b>21</b>	0	H	OH	H	>100	>100	>100	>1	<1
<b>22</b>	0	OH	H	H	>100	>100	>100	0.15 ± 0.03	6.6

<sup>a</sup>μmole of antioxidant/μmol of DPPH. <sup>b</sup>Antiradical power (ARP) = 1/EC<sub>50</sub>.

one of the standard colorimetric method for the evaluation of antioxidant properties of pure compounds and is routinely practiced for assessment of free radical scavenging potential of an antioxidant molecule. Experiments were performed also with gallic acid, a naturally occurring plant phenol as the reference substance.

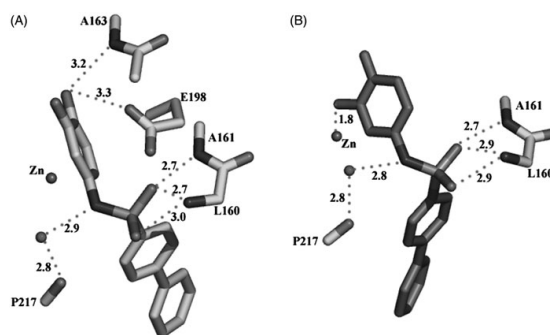
Several studies suggest that structure–antioxidant activity relationship for phenolic compounds depends on the position of hydroxyl groups, the presence of other functional groups in the whole molecule, and their conjugation to hydroxyl groups<sup>25</sup>.

For compounds 1–17, antioxidant activity could be mainly ascribed to the reducing power of the o-dihydroxy structure;

elimination of the hydroxy groups (**18** and **19**) or their substitution with methoxy ones (data not shown) results in a complete loss of activity. Derivatives with hydroxyl groups in positions 2, 3 show a better antioxidant activity with respect to the 3, 4 substitutions (**8** versus **14**).

The reduction of the o-dihydroxy structure to phenol (**20–22**) results in a decrease of the activity strongly dependent from the substituent position: only the 2-substituted analog (**22**) maintains an interesting antioxidant activity, while no or low activity is observed in the 3- or 4-substituted derivative, respectively (**20** and **21**). Therefore, it can be argued that the presence of two phenolic groups is not the only factor determining the antioxidant activity of our derivatives.

Figure 3. Hydrogen bond network of the catechol form (A) and the oxidized quinone form (B) of **14** (distances in Å).



Methylation of the nitrogen results in a reduction of activity for both the amidic (**4** versus **3**) and sulfonamide analogs (**10** versus **8** and **11** versus **9**). The presence of a methylene spacer increases ARP in the amide series (**3** versus **2**), while a strong reduction is observed for sulfonamide derivatives (**14** versus **16**).

Catechol was identified as a promising ZBG<sup>30</sup> but the introduction of aryl moieties aimed to reach the S1' specificity pocket of MMP enzymes does not lead to the expected potency improvement. In addition, at a first glance it is not obvious to derive a structure activity relationship (SAR) for the catechol analog series. To elucidate the binding mode of the catechol compounds, the inhibitor **14** was co-crystallized with MMP-8. Crystals of the complex MMP-8:**14** were grown as described in the Experimental Section. Surprisingly, the analysis of the Fo-Fc electron density map in the region of binding of **14** shows the presence of the catechol and its quinone oxidized form, both competing for the same binding site (S1' site). The refinement of the occupancy factors of the two forms reveals the predominance of the catechol with respect to quinone (77% versus 23%). The binding mode of the two forms in the S1' site is different at the level of the aromatic ring containing the zinc binding functions. As evidenced in Figure 3, only the quinone, with one of its oxygen atoms, bind the zinc ion with a distance of 1.84 Å giving rise to a distorted tetrahedral coordination, while one of the catechol oxygens makes H-bonds with the catalytic important E198 side-chain and the NH of A163, belonging to the antiparallel  $\beta$ -strand.

The sulfonamide NH group of both forms is engaged in a H-bond with a water molecule further bridged to the P217 CO group. The sulfonamide junction adopts a *g*-conformation in both forms ( $-86^\circ$  and  $-102^\circ$ , respectively), with one of the two oxygens turned toward the upper rim, giving rise to H-bonds with the A161 and L160 NH groups. Finally, the diphenyl group deeply protrudes into the S1' pocket, with its terminal part facing the charged R222 side-chain (closest distance of 3.1 Å), at the end of the pocket.

Integrating different computational approaches, we could identify the ligand features responsible for ligand-protein interaction and explain how small modifications in ligand structures can influence the inhibition potency. Through a pharmacophore-based analysis, the features that are needed for the MMP inhibition have been identified (Figure 4): one aromatic ring (R9), two acceptor H-bond groups (A1 and A3, respectively), and one donor H-bond group (D6). Compound **15** was automatically selected as the reference structure, with a Fit-value of 3.00.

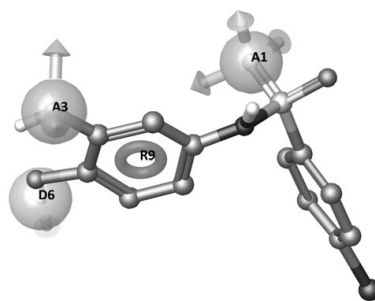


Figure 4. Pharmacophore model on the reference structure **15**.

The pharmacophore model highlights the importance of both hydroxyl groups for the MMP-8 inhibition and of their positions in relation to the aromatic ring. The resulting QSAR model works well in discriminating actives versus inactives (Figure 5), is robust and predictive (correlation values for the MMP-8 inhibition model,  $R^2$ : 0.8,  $Q^2$ : 0.8, F: 51.3, P: 3.3e-006, RMSE: 0.4, Pearson's  $R$ : 0.9).

The activity prediction is well correlated even with MMP-9 and MMP-2 (Figure 5B and C) experimental values; however, interestingly, the pharmacophore QSAR model underestimates the potency of compounds **3**, **5**, and **6** toward MMP-2. To investigate this difference and to characterize the interactions corresponding to the identified features, we integrate the pharmacophore-based analysis with a structure-based study.

Surprisingly, the X-ray structure of **14** in complex with MMP-8 reveals that the catechol oxygens contribute to a dense water network around the ligand (see Figure 6). Noteworthy, the quinone oxidized form of the ligand was found in the crystal complex, but not in the solution used for inhibition assay (see supporting information); therefore, we have considered activity values not related to the oxidized forms, which have been neglected in the computational studies. Apparently, catechol oxygen atoms prefer to enter in the water network rather than

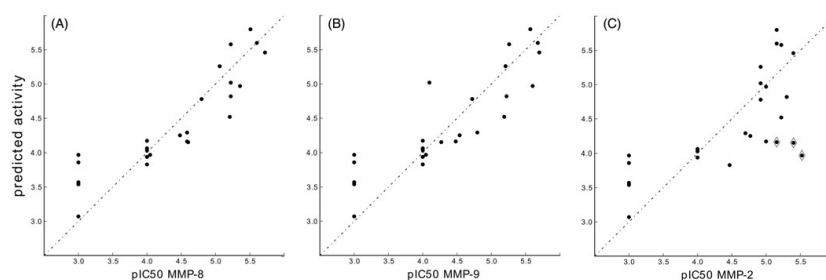


Figure 5. QSAR models for MMP-8 (A), MMP-9 (B), and MMP-2 (C) (test set + training set molecules).

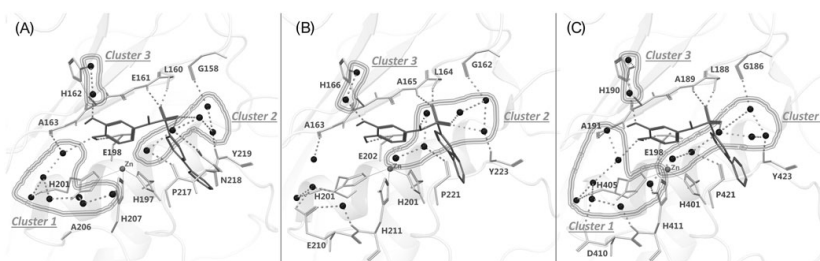


Figure 6. (A) MMP-8:14 X-ray complex ( $IC_{50}$ : 3.1  $\mu$ M, predicted total energy  $-395$  kJ/mol), (B) MMP-2:14 modeled complex ( $IC_{50}$ : 7.0  $\mu$ M, predicted total energy  $-379$  kJ/mol), and (C) MMP-9:14 modeled complex ( $IC_{50}$ : 2.7  $\mu$ M, predicted total energy  $-405$  kJ/mol). The ligand is represented as sticks and the water molecules as spheres. The network of water molecules is depicted with H-bonds reported as dashed lines and water clusters are encircled.

coordinate the zinc ion, suggesting a relevant role of water molecules in the binding and activity of catechol analogs toward MMP enzymes. It is well-known the role of water molecules in ligand–protein interaction, and this role becomes fundamental in the case of weak binders<sup>36</sup>. To clarify the role of the water molecules, the X-ray complex MMP-8:14 has been prepared and minimized with explicit waters with MacroModel Embrace Minimization<sup>37</sup>. The minimized complex reveals the interactions corresponding to the pharmacophore features: the donor feature (D6) is located on the OH group establishing an H-bond interaction with E198 side chain; the acceptor group A1 directly H-bonds with L160 NH and A161 NH; the acceptor group A3 is connected through two water molecules to H162 side chain; the aromatic feature (R9) is located above the zinc ion ensuring a good orientation for D6 and A3 interactions.

In addition, three relevant clusters of water molecules mediate the interaction between the ligand and MMP-8 (Figure 6A): (i) the oxygen bound to D6 is connected through seven water molecules to A163 CO on the top, H201 CO on the side and H207 side chain on the bottom; (ii) five water molecules connect the sulfonamide oxygen with P217 CO, N218 side chain and Y219 NH on the bottom, and G158 CO on the top; (iii) two water molecules mediate the interaction between the A3 feature oxygen and H162 side chain.

The structure determination of an enzyme bound to a potentially therapeutic inhibitor is usually aimed to design

optimized leads: starting from the identification of interactions involved in binding, moving to the analysis of possible additional or alternative interactions that can improve the potency. However, the complex described here highlights difficulties of theoretical prediction of binding energies and optimization process due to the fact that the binding involves hydrogen bonding through water molecules whose positions can change.

This observation prompted us to investigate the influence of the solvent in the binding of compound 14 with MMP-2 and MMP-9 (Figure 6B and C). We can observe similar interactions in all three complexes, but a different hydration by the solvent (Figure 6A–C). In the MMP-2:14 complex, the oxygen bound to D6 is not connected with the water molecule cluster 1 (Figure 6B). This difference is due to a sequence difference: A206 in MMP-8 is aligned to E210 in MMP-2. E210 side chain takes the place of the water molecule present in MMP-8:14 complex and shifts the water cluster 1 far away from the ligand (Figure 6B). In the case of MMP-9, we found in this position D410 (Figure 6C): since it is shorter than the glutamate present in this position in MMP-2, the cluster 1 water network is restored.

The structure-based analyses, taking into account all possible ligand–protein interactions and water contribution, ensure a more accurate prediction of the binding. Differently from what observed with the ligand-based analysis, the predicted binding energies of MMP-2:3, 5, and 6 ( $-303$  kJ/mol,  $-362$  kJ/mol and  $-366$  kJ/mol, respectively) are in a good correlation with the



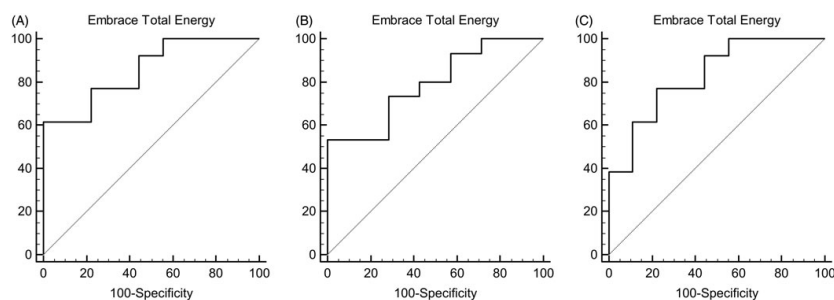


Figure 7. ROC curves (A) MMP-8-14 – AUC: 0.855. (B) MMP-2-14 – AUC: 0.790. (C) MMP-9-14 – AUC: 0.829.

experimental  $pIC_{50}$ . The ROC curves of all tested compounds toward MMP-8, MMP-2, and MMP-9 are shown in Figure 7.

### Conclusions

A new series of catechol-based compounds has been synthesized and tested for MMP inhibitory activity as well as antioxidant properties. Structure–activity relationship studies were implemented by X-ray analysis of the co-crystallization complex between MMP-8 and one of these new chemical entities (compound 14). Computational studies have been performed to identify a pharmacophore model and rationalize the influence of chemical structure on inhibition potency.

The activity of these molecules on both MMPs and ROS encloses a potential therapeutic strategy able to reduce the impact of these two important targets in degradation processes such as photoaging or inflammation, as well as to provide an additional treatment for degenerative phenomenon involving pathological enzymatic overexpression.

### Experimental section

#### Chemistry

Melting points were determined in open capillaries on a Gallenkamp electrothermal apparatus. Mass spectra were recorded on a HP MS 6890-5973 MSD spectrometer, electron impact 70 eV, equipped with a HP ChemStation or with an Agilent LC-MS 1100 Series LC-MSD Trap System VL spectrometer, electrospray ionization (ESI).  $^1\text{H-NMR}$  spectra were recorded using the suitable deuterated solvent on a Varian Mercury 300 NMR Spectrometer. Chemical shifts ( $\delta$ ) are expressed as parts per million (ppm) and the coupling constants ( $J$ ) in Hertz (Hz). Microanalyses of solid compounds were carried out with a Eurovector Euro EA 3000 model analyzer; the analytical results are within  $\pm 0.4\%$  of theoretical values. Flash column chromatography was performed using Geduran silica gel 60 Å (45–63  $\mu\text{m}$ ). Chemicals were purchased from Aldrich Chemicals (Milan, Italy) and were used without any further purification.

#### Preparation of 2,3-dibenzoyloxy-N-4-bromophenylbenzamide, 23 and 25

To a solution of 2,3-dibenzoyloxybenzoic acid (**30**) (2.27 mmol) in anhydrous toluene (35 mL), thionyl chloride (23.7 mmol) was added dropwise at  $0^\circ\text{C}$  under nitrogen atmosphere. The mixture was refluxed for 2 h and concentrated under reduced pressure.

The resulting oil was dissolved in dry THF (30 mL) and a solution of aniline or 4-phenylbenzylamine (7.12 mmol) in dry THF (1 mL) was added dropwise at  $0^\circ\text{C}$ . After 12 h at room temperature, the mixture was concentrated under reduced pressure and diluted with  $\text{CH}_2\text{Cl}_2$ . The organic layer was washed with HCl 1N, brine, dried over  $\text{Na}_2\text{SO}_4$ , and concentrated under reduced pressure. The residue was purified by column chromatography (n-hexane/ethyl acetate = 9:1) to give the title products.

#### 2,3-Dibenzoyloxy-N-phenylbenzamide (23)

53% yield;  $^1\text{H NMR}$  ( $\text{CDCl}_3$ ):  $\delta$  = 5.16 and 5.20 (2 s, 4H, 2  $\text{CH}_2\text{Ph}$ ), 7.03–7.09, 7.20–7.53, and 7.83–7.87 (m, 18H, aromatics), 10.01 (s, 1H, NH); MS (ESI)  $m/z$  (%): 432 [ $\text{M} + \text{Na}$ ] $^+$  (100)

#### 2,3-Dibenzoyloxy-N-(4-diphenyl)methylbenzamide (25)

71% yield;  $^1\text{H NMR}$  ( $\text{CDCl}_3$ ):  $\delta$  = 4.54 (s, 2H,  $\text{CH}_2\text{N}$ ), 4.99, and 5.15 (2 s, 4H, 2  $\text{CH}_2\text{Ph}$ ), 7.07–7.59 and 7.79–7.83 (m, 22H, aromatics), 8.38 (t, 1H, NH); MS (ESI)  $m/z$  (%): 522 [ $\text{M} + \text{Na}$ ] $^+$  (100), 340 (7).

#### 2,3-Dibenzoyloxy-N-4-bromophenylbenzamide

99% yield; mp: 122–124  $^\circ\text{C}$   $^1\text{H NMR}$  ( $\text{CDCl}_3$ ): 5.10 and 5.20 (2 s, 4H, 2  $\text{CH}_2\text{Ph}$ ), 7.10–7.50, and 7.80–7.86 (d, 17H, aromatics), 10.0 (s, NH); MS (ESI)  $m/z$ : 488 [ $\text{M} + 2 + \text{Na}$ ] $^+$  (100), 486 [ $\text{M} + \text{Na}$ ] $^+$  (100).

#### Preparation of 2,3-dibenzoyloxy-N-(4-diphenyl)benzamide (24)

A suspension of 2,3-dibenzoyloxy-N-4-bromophenylbenzamide (0.56 mmol), benzenboronic acid (1.6 mmol),  $\text{C}_5\text{S}_2\text{CO}_3$  (1.2 mmol), and  $[\text{Pd}(\text{PPh}_3)_4]$  (0.024 mmol) in anhydrous toluene (15 mL) was stirred at  $95^\circ\text{C}$  overnight under nitrogen atmosphere. Then, the mixture was diluted with 1N HCl (1 mL) and ethyl acetate (1.3 mL) at room temperature and filtered through a Celite pad. The resulting solution was washed with a saturated  $\text{NaHCO}_3$  solution ( $3 \times 15$  mL), brine, dried over  $\text{Na}_2\text{SO}_4$ , and concentrated under reduced pressure. The residue was purified by column chromatography (9:4:0.5:0.1 petroleum ether/ethyl acetate/IPA) to give the title product.

74% yield; mp: 121–124  $^\circ\text{C}$ ;  $^1\text{H NMR}$  ( $\text{CDCl}_3$ ):  $\delta$  = 5.18 and 5.21 (2 s, 4H, 2  $\text{CH}_2\text{Ph}$ ), 7.20–7.50, 7.70–7.73, 7.83–7.86, and 8.23–8.26 (d, 22H, aromatics), 10.0 (s, NH). MS(ESI)  $m/z$  (%): 508 [ $\text{M} + \text{Na}$ ] $^+$  (100).

**Preparation of compounds 27 and 28**

DCC (2.04 mmol) was added to a solution of 2,3-dibenzoyloxybenzoic acid (**30**) (1.5 mmol) in dichloromethane (30 mL) at 0 °C under nitrogen atmosphere. After 15 min, a solution of 4-DMAP (1.35 mmol) and 4-phenoxyaniline or 4-phenoxybenzylamine (1.38 mmol) in dichloromethane (4 mL) was added dropwise. The resulting mixture was allowed to warm to room temperature and stirred for further 22 h. The resulting precipitate was filtered off, and the organic layer was washed with a saturated NH<sub>4</sub>Cl solution (3 × 20 mL) and twice with brine, then dried over Na<sub>2</sub>SO<sub>4</sub>, filtered and the solvent removed *in vacuo* to yield a brown solid. Purification by flash chromatography (8:1.9:0.1 hexane/chloroform/IPA) and crystallization (THF/hexane) yielded the title compounds as a white powder.

**2,3-Dibenzoyloxy-N-(4-phenoxyphenyl)benzamide (27)**

73% yield; <sup>1</sup>H NMR (CDCl<sub>3</sub>): δ = 5.18 and 5.21 (2 s, 4H, 2 CH<sub>2</sub>Ph), 6.89–6.99, 7.05–7.10, 7.21–7.53, and 7.83–7.88 (m, 22H, aromatics), 9.99 (s, 1H, NH).

**2,3-Dibenzoyloxy-N-(4-phenoxyphenyl)methylbenzamide (28)**

69% yield; <sup>1</sup>H NMR (CDCl<sub>3</sub>): δ = 4.47 (d, 2H, CH<sub>2</sub>N), 4.99 and 5.15 (2 s, 4H, 2 CH<sub>2</sub>Ph), 6.88–7.48, and 7.76–7.82 (m, 22H, aromatics), 8.31 (t, 1H, -OH); MS (ESI) *m/z* (%): *m/z* 514 [M-H]<sup>-</sup> (100), 408 (9), 315 (9), 223 (9).

**General procedure for the preparation of 29–31, 34–39, and 18–22**

A solution of the suitable sulfonyl chloride (1.4 mmol) in CH<sub>2</sub>Cl<sub>2</sub> (5 mL) was added to a solution of the appropriate aniline (1.5 mmol) and Et<sub>3</sub>N (2.8 mmol) in CH<sub>2</sub>Cl<sub>2</sub> (5 mL). The mixture was refluxed for 4 h, cooled, diluted with CH<sub>2</sub>Cl<sub>2</sub> (10 mL), washed with 1N HCl and brine, dried over Na<sub>2</sub>SO<sub>4</sub>, and then evaporated *in vacuo*. The crude product was purified by flash column chromatography on silica gel using different mixtures as eluent (indicated in brackets) or was used for the next step without any purification.

**N-(2,3-dibenzoyloxy)phenyl-4-methoxyphenylsulfonamide (29)**

(Petroleum ether/ethyl acetate 9:1, 51% yield); <sup>1</sup>H NMR (CDCl<sub>3</sub>): δ = 3.79 (s, 3H, OCH<sub>3</sub>), 4.78 and 5.07 (2 s, 4H, 2 OCH<sub>2</sub>Ph), 6.70–6.97 (m, 4H, aromatics), 7.04 (bb, 1H, NH), 7.15–7.42 (m, 11H, aromatics), 7.63–7.68 (m, 2H aromatics); MS (ESI) *m/z* (%): 498 [M+Na]<sup>+</sup> (100), 407 (6), 304 (15).

**N-(2,3-dibenzoyloxy)phenyl-4-diphenylsulfonamide (30)**

(Petroleum ether/ethyl acetate/methylene chloride 9:0.5:0.5, 70% yield); <sup>1</sup>H NMR (CDCl<sub>3</sub>): δ = 4.79 and 5.07 (2 s, 4H, 2 OCH<sub>2</sub>Ph), 6.72–6.75, 6.94–7.00 (m, 2H, aromatics), 7.11 (bb, 1H, NH), 7.20–7.62, and 7.76–7.80 (m, 20H, aromatics); MS (ESI) *m/z* (%): 544 [M+Na]<sup>+</sup> (100), 304 (75).

**N-(2,3-dibenzoyloxy)phenyl-4-phenoxyphenylsulfonamide (31)**

(Petroleum ether/chloroform/IPA 9:0.9:0.1, 81% yield); <sup>1</sup>H NMR (CDCl<sub>3</sub>): δ = 4.81 and 5.09 (2 s, 4H, 2 OCH<sub>2</sub>), 6.72–6.75, 6.90–7.04, 7.16–7.47, 7.63–7.77 (m, 22H, aromatics and 1H, NH); MS (ESI) *m/z* (%): 560 [M+Na]<sup>+</sup> (100), 469 (5).

**N-(2,3-dimethoxyphenyl)methyl-4-diphenylsulfonamide (34)**

98% yield; mp: 120–121 °C; <sup>1</sup>H NMR (CDCl<sub>3</sub>): δ = 3.73 (s, 3H, OCH<sub>3</sub>), 3.76 (s, 3H, OCH<sub>3</sub>), 4.19 (d, *J* = 6.0 Hz, 2H, CH<sub>2</sub>NH), 5.30 (t, *J* = 6.0 Hz, 1H, NH), 6.72–6.79, 6.85–6.92, 7.38–7.50,

7.55–7.65, 7.83–7.88 (m, 12H, aromatics); <sup>13</sup>C NMR (CDCl<sub>3</sub>): δ 43.6, 56.0, 60.9, 112.6, 121.7, 124.3, 127.5, 127.7, 127.9, 128.7, 129.3, 130.0, 138.8, 139.6, 145.4, 147.1, 152.6.

**N-(2,3-dimethoxyphenyl)methyl-4-bromophenylsulfonamide (35)**

88% yield; mp: 125 °C; <sup>1</sup>H NMR (CDCl<sub>3</sub>): δ 3.72 (s, 3H, OCH<sub>3</sub>), 3.80 (s, 3H, OCH<sub>3</sub>), 4.15 (d, *J* = 6.0 Hz, 2H, CH<sub>2</sub>NH), 5.28 (t, *J* = 6.0 Hz, 1H, NH), 6.64–6.68, 6.76–6.80, 6.85–6.91, 7.47–7.51, 7.57–7.61 (m, 7H, aromatics); <sup>13</sup>C NMR (CDCl<sub>3</sub>): δ 43.8, 56.0, 60.8, 112.7, 121.7, 124.3, 127.4, 128.8, 129.6, 132.2, 139.4, 147.0, 152.6.

**N-(1,3-benzodioxol-5-yl)-4-diphenylsulfonamide (36)**

(CH<sub>2</sub>Cl<sub>2</sub>, 56% yield); mp: 145–146 °C; <sup>1</sup>H NMR (CDCl<sub>3</sub>): δ = 5.93 (s, 2H, -CH<sub>2</sub>), 6.46–6.50, 6.62–6.66, 6.72–6.74 (m, 3H, aromatic), 6.85 (bb, 1H, NH), 7.37–7.49, 7.55–7.67, 7.79–7.84 (m, 9H, aromatics); <sup>13</sup>C NMR (CDCl<sub>3</sub>): δ 101.8, 105.8, 108.5, 117.2, 127.5, 127.8, 128.1, 128.8, 129.3, 130.2, 137.6, 139.4, 146.0, 146.3, 148.3.

**N-(1,3-benzodioxol-5-yl)-4-bromophenylsulfonamide (37)**

62% yield; mp: 140–141 °C; <sup>1</sup>H NMR (CDCl<sub>3</sub>): δ = 5.94 (s, 2H, CH<sub>2</sub>), 6.41–6.45, 6.61–6.64, 6.67–6.81 (m, 3H, aromatics), 6.97 (bb, 1H, NH), 7.54–7.62 (m, 4H, aromatics); <sup>13</sup>C NMR (CDCl<sub>3</sub>): δ = 101.9, 105.8, 108.6, 116.6, 117.3, 128.4, 129.1, 132.6, 137.9, 146.6, 148.4.

**N-(1,3-benzodioxol-5-ylmethyl)-4-diphenylsulfonamide (38)**

(CH<sub>2</sub>Cl<sub>2</sub>, 98% yield); mp: 159–160 °C; <sup>1</sup>H NMR (CDCl<sub>3</sub>): δ = 4.08 (d, *J* = 6.0 Hz, 2H, CH<sub>2</sub>NH), 4.86 (t, *J* = 6.0 Hz, 1H, NH), 5.87 (s, 2H, CH<sub>2</sub>), 6.63–6.70, 7.39–7.52, 7.58–7.63, 7.67–7.62, 7.88–7.93 (m, 12H, aromatics); <sup>13</sup>C NMR (CDCl<sub>3</sub>): δ = 45.7, 101.4, 108.4, 108.7, 121.6, 127.6, 127.9, 127.9, 128.7, 129.3, 130.1, 138.7, 139.5, 145.8, 147.6, 148.1.

**N-(1,3-benzodioxol-5-ylmethyl)-4-bromophenylsulfonamide (39)**

(CH<sub>2</sub>Cl<sub>2</sub>, 97% yield); mp: 148–149 °C; <sup>1</sup>H NMR (CDCl<sub>3</sub>): δ = 4.04 (d, *J* = 6.0 Hz, 2H, CH<sub>2</sub>NH), 4.84 (t, *J* = 6.0 Hz, 1H, NH), 5.93 (s, 2H, -CH<sub>2</sub>-), 6.60–6.70, 7.59–7.71 (m, 7H, aromatics); <sup>13</sup>C NMR (CDCl<sub>3</sub>): δ = 45.4, 101.5, 108.5, 108.6, 121.7, 127.9, 128.9, 129.8, 132.6, 139.3, 147.6, 148.2.

**N-phenyl-4-diphenylsulfonamide (18)**

55% yield; mp: 126–127 °C; <sup>1</sup>H NMR (CDCl<sub>3</sub>): δ = 6.97 (bb, 1H, NH), 7.10–7.15, 7.22–7.29, 7.40–7.48, 7.53–7.58, 7.62–7.66, 7.83–7.86 (m, 14H, aromatics); <sup>13</sup>C NMR (CDCl<sub>3</sub>): δ = 121.8, 125.6, 127.7, 127.09, 128.1, 128.0, 128.8, 129.3, 129.6, 136.7, 137.7, 139.3, 146.1. MS (ESI) *m/z* (%): 308 [M-H]<sup>-</sup> (**18**), 244 (100). HR-MS [(C<sub>19</sub>H<sub>17</sub>NO<sub>2</sub>S-H)]<sup>-</sup>, *m/z* 308.0744 (calc. 308.0751).

**N-benzyl-4-diphenylsulfonamide (19)**

75% yield; mp: 134–135 °C; <sup>1</sup>H NMR (CDCl<sub>3</sub>): δ = 4.19 (d, *J* = 6.0 Hz, 2H, CH<sub>2</sub>NH), 4.74 (t, *J* = 6.0 Hz, 1H, NH), 7.20–7.31, 7.41–7.53, 7.59–7.63, 7.69–7.73, 7.91–7.95 (m, 14H, aromatics); <sup>13</sup>C NMR (CDCl<sub>3</sub>): δ = 47.6, 127.6, 127.9, 128.0, 128.1, 128.2, 128.4, 128.8, 129.0, 129.3, 136.4, 138.6, 139.5, 145.9. MS (ESI) *m/z* (%): 322 [M-H]<sup>-</sup> (**5**), 153 (100). HR-MS [(C<sub>19</sub>H<sub>17</sub>NO<sub>2</sub>S-H)]<sup>-</sup>, *m/z* 322.0903 (calc. 322.0907).

**N-(4-hydroxyphenyl)-4-diphenylsulfonamide (20)**

63% yield; mp: 212–214 °C; <sup>1</sup>H NMR (D<sub>2</sub>O/DMSO): δ = 6.58–6.61, 6.84–6.88, 7.40–7.82 (m, 13H, aromatics), 9.30 and 9.78

(bb, 2H, -OH and -NH);  $^{13}\text{C}$  NMR ( $[\text{D}_6]\text{DMSO}$ ):  $\delta = 116.0, 124.4, 127.5, 127.6, 127.8, 128.9, 129.0, 129.5, 138.8, 138.9, 144.4, 155.3$ . MS (ESI)  $m/z$  (%): 324  $[\text{M}-\text{H}]^-$  (100). HR-MS  $[(\text{C}_{18}\text{H}_{15}\text{NO}_3\text{S} + \text{Na})]^+$ ,  $m/z$  348.0665 (calc. 348.0665).

*N*-(3-hydroxyphenyl)-4-diphenylsulfonamide (21)

71% yield; mp: 258–259 °C;  $^1\text{H}$  NMR ( $[\text{D}_6]\text{DMSO}$ ):  $\delta = 5.85\text{--}6.30, 6.58\text{--}6.63, 7.31\text{--}7.73$  (m, 13H, aromatics), 8.51 (bb, 2H, -OH and -NH);  $^{13}\text{C}$  NMR ( $[\text{D}_6]\text{DMSO}$ ):  $\delta = 105.6, 107.8, 112.5, 126.6, 126.8, 127.2, 127.3, 127.5, 128.2, 128.8, 129.4, 139.8, 141.7, 157.8$ . MS (ESI)  $m/z$  (%): 324  $[\text{M}-\text{H}]^-$  (100). HR-MS  $[(\text{C}_{18}\text{H}_{15}\text{NO}_3\text{S}-\text{H})]^-$ ,  $m/z$  324.0694 (calc. 324.0700).

*N*-(2-hydroxyphenyl)-4-diphenylsulfonamide (22)

55% yield; mp: 155–157 °C;  $^1\text{H}$  NMR ( $[\text{D}_6]\text{DMSO}$ ):  $\delta = 6.66\text{--}6.73, 6.89\text{--}6.94, 7.14\text{--}7.17, 7.38\text{--}7.50, 7.68\text{--}7.80$  (m, 13H, aromatics), 9.43 (bb, 2H, OH and NH);  $^{13}\text{C}$  NMR ( $[\text{D}_6]\text{DMSO}$ ):  $\delta = 116.0, 119.4, 124.5, 125.0, 126.6, 127.4, 127.5, 127.8, 128.9, 129.5, 138.8, 140.0, 144.3, 150.7$ . MS (ESI)  $m/z$  (%) 324  $[\text{M}-\text{H}]^-$  (95), 217 (100);  $m/z$  (%): 348  $[\text{M} + \text{Na}]^+$  (100). HR-MS  $[(\text{C}_{18}\text{H}_{15}\text{NO}_3\text{S}-\text{H})]^-$ ,  $m/z$  324.0695 (calc. 324.0700).

General procedure for the preparation of 26, 32 and 33

**3a** or **30** or **31** (1 mmol) was dissolved in anhydrous DMF (20 mL) under argon atmosphere at 0 °C. Then, NaH (3 mmol, 95% powder) and, after 30 min,  $\text{CH}_3\text{I}$  (50 mL) were carefully added and the mixture was stirred overnight at room temperature. After evaporation of volatiles, the residue was dissolved in ethyl acetate and washed with 1N HCl (3  $\times$  50 mL) and brine (3  $\times$  40 mL), dried over  $\text{Na}_2\text{SO}_4$ , filtered, and concentrated *in vacuo* giving a yellow oil, that was used for the next step without any purification.

*N*-(4-diphenylmethyl)-*N*-methyl-2,3-dibenzoyloxybenzamide (26)

97% yield;  $^1\text{H}$  NMR ( $\text{CDCl}_3$ ):  $\delta = 2.76$  (s, 3H,  $\text{CH}_3\text{N}$ ), 3.00 (s, 2H,  $\text{CH}_2\text{N}$ ), 5.15 and 5.17 (2 s, 4H, 2  $\text{CH}_2\text{Ph}$ ), 6.92–7.55 (m, 22H, aromatics); MS (ESI)  $m/z$  (%) 536  $[\text{M} + \text{Na}]^+$  (100).

*N*-(2,3-dibenzoyloxyphenyl)-*N*-methyl-4-diphenylsulfonamide (32)

90% yield;  $^1\text{H}$  NMR ( $[\text{D}_6]\text{DMSO}$ ):  $\delta = 3.10$  (s, 3H,  $\text{CH}_3\text{N}$ ), 4.99 and 5.11 (2 s, 4H, 2  $\text{OCH}_2\text{Ph}$ ), 6.76–6.82, 6.95–7.02, and 7.20–7.88 (m, 22H, aromatics); MS (ESI)  $m/z$  (%): 558  $[\text{M} + \text{Na}]^+$  (100), 304 (7).

*N*-(2,3-dibenzoyloxyphenyl)-*N*-methyl-4-phenoxyphenylsulfonamide (33)

84% yield;  $^1\text{H}$  NMR ( $[\text{D}_6]\text{DMSO}$ ):  $\delta = 3.11$  (s, 3H,  $\text{CH}_3\text{N}$ ), 4.99, and 5.10 (2 s, 4H, 2  $\text{OCH}_2\text{Ph}$ ), 6.76–6.79, 6.94–7.05, 7.18–7.43, and 7.71–7.76 (m, 22H, aromatics); MS (ESI)  $m/z$  (%): 574  $[\text{M}-\text{Na}]^+$  (100), 319 (16), 228 (6).

General procedure for the preparation of compounds 1–6

A mixture of the appropriate dibenzoyloxybenzamide **23–28** (0.38 mmol) and 10% Pd-C (24 mg) in  $\text{CH}_3\text{OH}/\text{THF}$  2.5 (14 mL) was stirred at room temperature for 20 h under  $\text{H}_2$  atmosphere at 6 atm. The mixture was filtered through a Celite pad and concentrated *in vacuo* to give the title product as a white solid.

2,3-Dihydroxy-*N*-4-phenylbenzamide (1)

72% yield; mp: 114–117 °C;  $^1\text{H}$  NMR ( $\text{CDCl}_3$ ):  $\delta = 5.82$  (s, 1H, NH), 6.82–6.87, 7.05–7.12, 7.19–7.25 and 7.38–7.60 (m, 8H,

aromatics), 7.95 (s, 1H, OH), 12.34 (s, 1H, OH);  $^{13}\text{C}$  NMR ( $\text{CDCl}_3$ ):  $\delta = 114.3, 116.1, 118.6, 119.0, 121.3, 125.5, 129.2, 136.4, 146.1, 149.3, 168.4$ . MS (ESI)  $m/z$  (%): 228  $[\text{M}-\text{H}]^-$  (100). HR-MS  $[(\text{C}_{13}\text{H}_{11}\text{NO}_3-\text{H})]^-$ ,  $m/z$  228.0663 (calc. 228.0663).

*N*-(4-diphenyl)-2,3-dihydroxybenzamide (2)

38% yield; mp: 226–228;  $^1\text{H}$  NMR ( $\text{CDCl}_3$ ):  $\delta = 5.92$  (s, 1H, NH), 6.81–6.91, 7.09–7.12, 7.25–7.69, 7.76–7.88, 7.98–8.01 and 8.07–8.26 (m, 12H, aromatics), 9.53 (s, 1H, OH), 12.32 (s, 1H, OH); MS (ESI)  $m/z$  (%): 304  $[\text{M}-\text{H}]^-$  (100). HR-MS  $[(\text{C}_{19}\text{H}_{15}\text{NO}_3-\text{H})]^-$ ,  $m/z$  304.0972 (calc. 304.0972).

*N*-(4-diphenyl)methyl-2,3-dihydroxybenzamide (3)

79% yield; mp: 111–113 °C;  $^1\text{H}$  NMR ( $\text{CDCl}_3$ ):  $\delta = 4.68$  (d, 2H,  $\text{CH}_2\text{N}$ ,  $J = 5.49$ ), 5.80 (s, 1H, OH), 6.62 (bb, 1H, NH), 6.73–6.78, 6.89–6.91, 7.05–7.09, 7.34–7.47 and 7.57–7.71 (m, 12H, aromatics), 12.68 (s, 1H, OH);  $^{13}\text{C}$  NMR ( $\text{CDCl}_3$ ):  $\delta = 43.4, 113.8, 115.9, 118.2, 118.7, 127.1, 127.5, 127.7, 128.3, 128.8, 136.2, 140.5, 141.0, 146.0, 149.2, 169.9$ . MS (ESI)  $m/z$  (%): 318  $[\text{M}-\text{H}]^-$  (100). HR-MS  $[(\text{C}_{20}\text{H}_{17}\text{NO}_3-\text{H})]^-$ ,  $m/z$  318.1127 (calc. 318.1136).

*N*-(4-diphenyl)methyl-*N*-methyl-2,3-dihydroxybenzamide (4)

33% yield; mp: 160–163 °C;  $^1\text{H}$  NMR ( $[\text{D}_6]\text{DMSO}$ ):  $\delta = 3.14$  (s, 3H,  $\text{CH}_3$ ), 4.81 (s, 2H,  $\text{CH}_2$ ), 5.80 (bb, 1H, OH), 6.70–6.75, 6.89–7.01, 7.33–7.66 (m, 12H, aromatics), 10.2 (bb, 1H, OH); MS (ESI)  $m/z$  (%): 356  $[\text{M}-\text{H} + \text{Na}]^+$  (100). HR-MS  $[(\text{C}_{21}\text{H}_{19}\text{NO}_3 + \text{H})]^+$ ,  $m/z$  334.1435 (calc. 334.1438).

2,3-dihydroxy-*N*-(4-phenoxyphenyl)benzamide (5)<sup>38</sup>

84% yield; mp: 164–165 °C;  $^1\text{H}$  NMR ( $\text{CDCl}_3$ ):  $\delta = 5.82$  (s, 1H, NH), 6.81–6.87, 7.00–7.15, 7.14–7.39, and 7.51–7.55 (m, 12H, aromatics), 7.93 (s, 2H, OH);  $^{13}\text{C}$  NMR ( $\text{CD}_3\text{OD}$ ):  $\delta = 116.2, 118.1, 118.2, 118.5, 118.5, 118.8, 122.9, 123.1, 129.5, 133.1, 146.0, 148.4, 154.1, 157.5, 168.2$ . MS (ESI)  $m/z$  (%) 320  $[\text{M}-\text{H}]^-$  (100). HR-MS  $[(\text{C}_{19}\text{H}_{15}\text{NO}_4-\text{H})]^-$ ,  $m/z$  320.0923 (calc. 320.0928).

*N*-(4-phenoxyphenyl)methyl-2,3-dihydroxybenzamide (6)<sup>38</sup>

79% yield; mp: 113–114 °C;  $^1\text{H}$  NMR ( $\text{CDCl}_3$ ):  $\delta = 4.60$  (d,  $J = 5.66$ ,  $\text{CH}_2\text{N}$ , 2H), 5.82 (s, 1H, OH), 6.59 (bb, 1H, NH), 6.72–6.91, 6.97–7.14, and 7.29–7.37 (m, 12H, aromatics), 12.67 (s, 1H, OH);  $^{13}\text{C}$  NMR ( $\text{CD}_3\text{OD}$ ):  $\delta = 42.0, 115.3, 117.3, 118.2, 118.3, 118.3, 118.5, 122.9, 128.8, 129.4, 133.6, 145.9, 148.9, 156.4, 157.4, 170.0$ . MS (ESI)  $m/z$  (%): 334  $[\text{M}-\text{H}]^-$  (100). HR-MS  $[(\text{C}_{20}\text{H}_{17}\text{NO}_4-\text{H})]^-$ ,  $m/z$  334.1074 (calc. 334.1085).

General procedure for the preparation of compounds 7–11

To a stirred suspension of the appropriate intermediate (**29–33**) (0.41 mmol) in  $\text{THF}/\text{MeOH}$  (16 mL, 3:1), 10% Pd/C (26 mg) was added. After stirring overnight under hydrogen atmosphere (6 atm), the reaction mixture was filtered through a pad of Celite and concentrated under reduced pressure affording the desired product.

*N*-(2,3-dihydroxyphenyl)-4-methoxyphenylsulfonamide (7)

82% yield; mp: 147–149 °C;  $^1\text{H}$  NMR ( $[\text{D}_6]\text{DMSO}$ ):  $\delta = 3.78$  (s, 3H,  $\text{CH}_3$ ), 6.53–6.59, 6.98–7.01, 7.64–7.67 (m, 7H, aromatics), 8.87 (bb, 3H, 2 OH, NH); MS (ESI)  $m/z$  (%): 294  $[\text{M}-\text{H}]^-$  (100), 171 (59).  $^{13}\text{C}$  NMR ( $[\text{D}_6]\text{DMSO}$ ):  $\delta = 56.0, 112.8, 114.5, 114.7, 118.8, 125.6, 129.4, 132.6, 138.7, 146.0, 162.7$ . HR-MS  $[(\text{C}_{13}\text{H}_{13}\text{NO}_3\text{S}-\text{H})]^-$ ,  $m/z$  294.0436 (calc. 294.0442).

*N*-(2,3-dihydroxyphenyl)-4-diphenylsulfonamide (**8**)<sup>38</sup>

79% yield; mp: 182–183 °C; <sup>1</sup>H NMR (DMSO-d<sub>6</sub>): δ 6.45–6.63, 7.38–7.50, 7.69–7.82 (m, 12H, aromatics), 9.00 (bb, 3H, 2-OH, -NH); <sup>13</sup>C NMR (D<sub>2</sub>O/DMSO): δ = 113.0, 115.0, 118.8, 125.4, 127.5, 127.9, 128.9, 129.5, 138.9, 138.9, 139.9, 144.3, 146.1. MS (ESI) *m/z* 340 [M-H]<sup>-</sup> (93), 217 (100). HR-MS [(C<sub>18</sub>H<sub>15</sub>NO<sub>4</sub>S-H)]<sup>-</sup>, *m/z* 340.0643 (calc. 340.0649).

*N*-(2,3-dihydroxyphenyl)-4-phenoxyphenylsulfonamide (**9**)<sup>38</sup>

80% yield; mp: 176–178 °C; <sup>1</sup>H NMR (CDCl<sub>3</sub>): δ = 2.20–2.60 (bb, 3H, 2-OH and -NH), 6.54–6.58, 6.74–6.85, 6.93–6.96, 7.09–7.14, 7.28–7.33, 7.62–7.65 (m, 12H, aromatics); MS (ESI) *m/z* (%): 380 [M+Na]<sup>+</sup> (100). <sup>13</sup>C NMR (CD<sub>3</sub>OD): δ = 112.2, 114.8, 116.8, 118.6, 119.8, 124.5, 124.7, 129.3, 129.8, 133.3, 138.2, 145.3, 155.3, 161.5. HR-MS [(C<sub>18</sub>H<sub>13</sub>NO<sub>5</sub>S-H)]<sup>-</sup>, *m/z* 356.0594 (calc. 356.0598).

*N*-(2,3-dihydroxyphenyl)-*N*-methyl-4-diphenylsulfonamide (**10**)

57% yield; mp: 170–172 °C; <sup>1</sup>H NMR (CDCl<sub>3</sub>): δ = 3.22 (s, 3H, NCH<sub>3</sub>), 5.99–6.02, 6.62–6.67, 6.87–6.89, and 7.43–7.71 (m, 14H, aromatics and -OH); MS (ESI) *m/z* (%): 354 [M-H]<sup>-</sup> (100), 217 (61). <sup>13</sup>C NMR (CD<sub>3</sub>OD): δ = 37.6, 114.8, 118.4, 119.4, 126.9, 128.0, 128.1, 128.3, 128.7, 138.8, 139.2, 143.3, 145.4, 146.1. HR-MS [(C<sub>19</sub>H<sub>17</sub>NO<sub>4</sub>S-H)]<sup>-</sup>, *m/z* 354.0799 (calc. 320.0806).

*N*-(2,3-dihydroxyphenyl)-*N*-methyl-4-phenoxyphenylsulfonamide (**11**)

68% yield; mp: 150–152 °C; <sup>1</sup>H NMR (CDCl<sub>3</sub>): δ = 3.16 (m, 3H, NCH<sub>3</sub>), 4.99 (bb, 2H, OH), 5.99–6.02, 6.65–7.54 (m, 12H, aromatics); MS (ESI) *m/z* (%): 370 [M-H]<sup>-</sup> (100), *m/z* 340 [M+Na]<sup>+</sup> (100), 233 (81). <sup>13</sup>C NMR (CD<sub>3</sub>OD): δ = 37.5, 114.7, 116.9, 118.3, 119.4, 119.9, 124.6, 128.0, 129.9, 130.0, 131.8, 143.3, 146.1, 155.3, 161.7. HR-MS [(C<sub>19</sub>H<sub>17</sub>NO<sub>5</sub>S-H)]<sup>-</sup>, *m/z* 370.0749 (calc. 370.0755).

General procedure for the preparation of compounds **12–17**

To a solution of the appropriate sulfonamide **34–39** (1.36 mmol) in dry CH<sub>2</sub>Cl<sub>2</sub> (20 mL) was added a 1M solution of boron tribromide (3.26 mmol) in CH<sub>2</sub>Cl<sub>2</sub>, at 0 °C and under nitrogen atmosphere. After 1 h at room temperature, methanol (5 mL) was added dropwise carefully at 0 °C, and the mixture was stirred for additional 10 min. The crude was diluted with a 1:1 mixture of AcOEt/H<sub>2</sub>O, the organic phase was washed with brine, dried, and purified by flash chromatography on silica gel affording the desired product.

*N*-(2,3-dihydroxyphenyl)methyl-4-diphenylsulfonamide (**12**)

55% yield; mp: 154–155 °C; <sup>1</sup>H NMR (CD<sub>3</sub>OD): δ = 4.12 (s, 2H, CH<sub>2</sub>), 6.47–6.52, 6.58–6.63, 7.32–7.46, 7.57–7.66, 7.81–7.87 (m, 12H, aromatics); <sup>13</sup>C NMR (CD<sub>3</sub>OD): δ 42.2, 114.2, 119.1, 120.1, 123.6, 127.1, 127.2, 127.4, 128.2, 128.9, 139.3, 139.6, 143.3, 144.8, 145.2. MS (ESI) *m/z* (%): 354 [M-H]<sup>-</sup> (7), 234 (100). HR-MS [(C<sub>19</sub>H<sub>17</sub>NO<sub>4</sub>S-H)]<sup>-</sup>, *m/z* 354.0811 (calc. 354.0806).

*N*-(2,3-dihydroxyphenyl)methyl-4-bromophenylsulfonamide (**13**)

75% yield; mp: 179–180 °C; <sup>1</sup>H NMR (CD<sub>3</sub>OD): δ = 4.10 (s, 2H, CH<sub>2</sub>), 6.47–6.57, 6.61–6.64, 7.54–7.65 (m, 7H, aromatics); <sup>13</sup>C NMR (CD<sub>3</sub>OD): δ = 42.2, 114.3, 119.1, 120.2, 123.3, 126.7, 128.6, 131.9, 141.2, 143.3, 144.7. MS (ESI) *m/z* (%): 356 [M-H]<sup>-</sup> (1), 236 (100). HR-MS [(C<sub>13</sub>H<sub>12</sub>BrNO<sub>4</sub>S-H)]<sup>-</sup>, *m/z* 355.9591 (calc. 355.9598).

*N*-(3,4-dihydroxyphenyl)-4-diphenylsulfonamide (**14**)

88% yield; mp: 216 °C (dec.); <sup>1</sup>H NMR (CD<sub>3</sub>OD): δ = 6.37–6.41, 6.58–6.66, 7.31–7.44, 7.54–7.58, 7.62–7.66, 7.72–7.76 (m, 12H, aromatics); <sup>13</sup>C NMR (CD<sub>3</sub>OD): δ = 111.2, 114.8, 115.1, 127.0, 127.1, 127.7, 128.3, 128.9, 129.3, 138.4, 139.3, 143.4, 145.4. MS (ESI) *m/z* (%): 340 [M-H]<sup>-</sup> (11), 153 (100). HR-MS [(C<sub>18</sub>H<sub>15</sub>NO<sub>4</sub>S-H)]<sup>-</sup>, *m/z* 340.0632 (calc. 340.0649).

*N*-(3,4-dihydroxyphenyl)-4-bromophenylsulfonamide (**15**)

62% yield; mp: 209 °C (dec.); <sup>1</sup>H NMR (CD<sub>3</sub>OD): δ = 6.30–6.34, 6.57–6.61, 7.53–7.62 (m, 7H, aromatics); <sup>13</sup>C NMR (CD<sub>3</sub>OD): δ = 111.4, 115.0, 115.1, 127.1, 128.9, 128.9, 132.0, 138.9, 143.6, 145.4. MS (ESI) *m/z* (%): 342 [M-H]<sup>-</sup> (12), 157 (100). HR-MS [(C<sub>12</sub>H<sub>10</sub>BrNO<sub>4</sub>S+Na)]<sup>+</sup>, *m/z* 365.9400 (calc. 365.9406).

*N*-(3,4-dihydroxyphenyl)methyl-4-diphenylsulfonamide (**16**)

58% yield; mp: 189 °C (dec.); <sup>1</sup>H NMR (CD<sub>3</sub>OD): δ 3.92 (s, 2H, CH<sub>2</sub>), 6.47–6.51, 6.59–6.66, 7.37–7.50, 7.64–7.88, 7.72–7.76, 7.83–7.87 (m, 12H, aromatics); <sup>13</sup>C NMR (CD<sub>3</sub>OD): δ = 114.9, 115.2, 119.4, 127.2, 127.3, 127.4, 128.2, 128.7, 128.9, 139.6, 139.6, 144.7, 145.1, 145.3. MS (ESI) *m/z* (%): 354 [M-H]<sup>-</sup> (7), 234 (100). HR-MS [(C<sub>19</sub>H<sub>17</sub>NO<sub>4</sub>S-H)]<sup>-</sup>, *m/z* 354.0811 (calc. 320.0806).

*N*-(3,4-dihydroxyphenyl)methyl-4-bromophenylsulfonamide (**17**)

47% yield; mp: 124–125 °C; <sup>1</sup>H NMR (CD<sub>3</sub>OD): δ = 3.90 (s, 2H, CH<sub>2</sub>), 6.46–6.49, 6.61–6.5, 7.62–7.69 (m, 7H, aromatics); <sup>13</sup>C NMR (CD<sub>3</sub>OD): δ = 46.6, 115.0, 115.2, 126.8, 128.5, 128.6, 132.1, 140.3, 144.7, 145.1. MS (ESI) *m/z* (%): 356 [M-H]<sup>-</sup> (1), 236 (100). HR-MS [(C<sub>13</sub>H<sub>12</sub>BrNO<sub>4</sub>S-H)]<sup>-</sup>, *m/z* 355.9538 (calc. 355.9598).

## DPPH assay

The DPPH radical scavenging assay was performed in 96-well microplates according to the method reported by Blois with some modifications<sup>39,40</sup>. Briefly, a freshly prepared solution of DPPH in methanol (100 μM final concentration) was added to test compounds methanolic solution. The mixtures were shaken vigorously and left to stand in the dark for 30 min at room temperature, and then absorbance was read at 520 nm using a spectrophotometric plate reader (Victor 3 Perkin-Elmer). The antioxidant activity was determined as the RSA% (radical scavenging activity), calculated using following equation:

$$\text{RSA\%} = 100 \times [(A_0 - A_1)/A_0]$$

where, A<sub>0</sub> and A<sub>1</sub> are the DPPH absorbance in the absence or in presence of antioxidant, respectively. Different sample concentrations were used in order to obtain antiradical curves for calculating the EC<sub>50</sub> values. The value of EC<sub>50</sub> was expressed in terms of molar ratio of antioxidant to DPPH. ARP is inverse of EC<sub>50</sub> value, the larger the ARP the more efficient the antioxidant. The EC<sub>50</sub> values and statistical analyses were processed using GraphPad Prism<sup>41</sup> and are expressed as mean ± SEM of at least three independent measurements in triplicate.

## MMP inhibition assays

The catalytic domains of MMP-2, -8, and -9 were purchased from Enzo Life Sciences. The assays were performed in triplicate in 96-well white microtiter plates (Corning, NBS). For assay measurements, inhibitor stock solutions (DMSO, 25 mM) were diluted to six different concentrations (1 nM–250 μM) in fluorometric assay buffer (50 mM Tris-HCl pH 7.5, 200 mM NaCl, 1 mM CaCl<sub>2</sub>,

1  $\mu$ M ZnCl<sub>2</sub>, 0.05% Brij-35, and 1% DMSO). Enzyme and inhibitor solutions were incubated in the assay buffer for 15 min at room temperature before the addition of the fluorogenic substrate solution (OmniMMP = Mca-Pro-Leu-Gly-Leu-Dpa-Ala-Arg-NH<sub>2</sub>, Calbiochem, 2.5  $\mu$ M final concentration). After further incubation for 2–4 h at 37 °C, fluorescence was measured ( $\lambda_{\text{ex}} = 340$  nm,  $\lambda_{\text{em}} = 405$  nm) using a Perkin–Elmer Victor V3 plate reader.

Control wells lacked inhibitor. The MMP inhibition activity was expressed in relative fluorescence units (RFU). Percent inhibition was calculated from control reactions without inhibitor. IC<sub>50</sub> values were determined using GraphPad Prism<sup>41</sup> and are expressed as mean  $\pm$  SEM of at least three independent measurements in triplicate.

#### Expression and purification of the protein

The truncated form M80-G242 of the catalytic domain of MMP-8 was expressed in *E. coli* strain BL21 (DE3). At an OD<sub>600</sub> 0.5–0.6 expression of the collagenase was induced in a 1 l culture by adding IPTG to a final concentration of 0.5 mM. Inclusion bodies isolated and purified from harvested *E. coli* cells were resuspended in 20 mL of 6 M urea, 100 mM  $\beta$ -mercaptoethanol and 20 mM Tris, pH 8.5, and incubated at room temperature o/n under shaking to extract the solubilized collagenase. This extract was centrifuged for 30' at 40 000 rpm, and the supernatant was loaded onto a Mono Q-Sepharose column (GE Healthcare) previously equilibrated with the denaturing buffer.

Elution of the collagenase was carried out by applying a linear gradient of 0–1 M NaCl in the same buffer at a flow rate of 1 mL/min. The truncated form of MMP-8 was eluted at a salt concentration of 100 mM NaCl and could be purified to apparent homogeneity. A further step of purification was carried out by gel filtration using a HiLoadSuperdex 75 column (GE Healthcare) equilibrated with 6 M urea, 10 mM DTT, and 20 mM Tris, pH 8.5 at a flow rate of 0.5 mL/min. The collected protein was then refolded onto a HiLoadSuperdex 75 column in buffer MES-NaOH 3 mM, pH 6.0, 100 mM NaCl, 5 mM CaCl<sub>2</sub>, 0.5 mM ZnCl<sub>2</sub>, Na<sub>2</sub>S<sub>2</sub>O<sub>3</sub> 0.02% at a flow rate of 0.5 mL/min. The fraction containing the desalted and refolded protein was eluted after ca. 13 mL.

#### Protein crystallization

The inhibitor (stock solution 50 mM in DMSO) was immediately added to the fraction containing the refolded protein in the ratio 3:1 (final concentration of DMSO 1%) in order to prevent autoproteolysis during concentration. The MMP-8 protein with the inhibitor was then concentrated with Amicon-Ultra 15, to a final concentration of 6 mg/mL. Crystallization was performed by hanging-drop vapor diffusion method at 20 °C. Hanging droplets were made by mixing 2  $\mu$ L of protein/inhibitor solution with 5  $\mu$ L of PEG solution (10% (m/v) PEG6000, 0.2 M MES-NaOH, 0.02% Na<sub>2</sub>S<sub>2</sub>O<sub>3</sub>, pH 6.0). Droplets were concentrated against a reservoir buffer containing 1.0–2.0 M sodium phosphate, 0.02% Na<sub>2</sub>S<sub>2</sub>O<sub>3</sub>, pH 6.0. Crystals appeared after few days.

#### Data collection and processing

X-ray data were collected under cryogenic conditions (100 K) at the ID29 beamline of ESRF, Grenoble, using a wavelength of 0.976 Å and a Pilatus 6M\_F detector. The crystals were flash-frozen in the nitrogen stream after transferring them for few seconds into the mother solution containing 35% PEG400. Data were integrated and scaled using the programs MOSFLM and Scala<sup>42</sup>. The statistics of collection is given in Table 1 of the supporting Information.

#### Structure solution and refinement

Structure solution was performed with AMoRe<sup>43</sup> using the coordinates of the complex between MMP-8 and a non-zinc chelating inhibitor (PDB entry 3DPE)<sup>44</sup> as the starting model. The coordinates were then refined with CNS<sup>45</sup>. The statistics of refinement is summarized in Table 1 of the supporting Information.

#### Computational studies

**Ligand-based studies:** ligands reported in Tables 1 and 2 were manually built using the Built facility in Maestro<sup>37</sup>. 3D structures, stereoisomers, tautomers, and protomers at pH 7.0  $\pm$  0.5 were generated with LigPrep<sup>37</sup>. All synthesized analogs were aligned to the crystallographic coordinates of **14** with Phase Shape Screening<sup>37</sup> and, using the resulting aligned conformation, a pharmacophore-based QSAR model was built with Phase program. The minimum intersite distance between the features was set to be 1 Å. Molecules with pIC<sub>50</sub> < 4 toward MMP-8 were grouped as the inactive molecule set, while those with pIC<sub>50</sub> > 5 were grouped as the active molecules; all actives were set to be matched during the screening. The QSAR model was constructed using molecules **1**, **12**, **16**, **17**, **18**, and **21** as test set and all the others as training set. The best model has **15** as reference molecule, and is made of four features: 1 aromatic ring (R9), 2 acceptor groups (A1 and A3), and 1 donor group (D6). Excluded volume features were added around the shape of reference molecule.



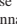





**Structure-based studies:** the hydrogen atoms of the X-ray complex–MMP-8:**14** has been added and optimized with the Protein Preparation Wizard tool from Schrödinger<sup>37</sup>. Then the complex with explicit waters was minimized to a derivative convergence of 0.05 kJ/mol Å using the Polak–Ribiere Conjugate Gradient (PRCG) minimization algorithm, the OPLS2005 force field, with MacroModel Embrace Minimization<sup>37</sup>. A shell of 15 Å around the catalytic zinc was set to be free to move, another shell of 5 Å minimized applying a force constant of 200 kJ/mol Å<sup>2</sup>.

The interaction energy between the receptor and each ligand was calculated with the Interaction energy mode implemented in Embrace. The same procedure was applied to calculate the interaction energies of MMP-2:**14** and MMP-9:**14**. Ligand coordinates were taken from the MMP-8 bound conformation of **14**. Protein and water coordinates were downloaded from the Protein Data Bank (PDB): 1GKC.pdb<sup>46</sup> and 1QIB.pdb<sup>47</sup> for MMP-9 and MMP-2, respectively. Then, interaction energies were calculated for all compounds reported in Tables 1 and 2 previously aligned to **14**. Calculated energies were used to derive ROC curves (see Figure 7). For the ROC curve calculations molecules with pIC<sub>50</sub> > 4 were considered active and all the others inactive.

#### Declaration of interest

The authors report no conflict of interest.

#### ORCID

Marilena Tauro  <http://orcid.org/0000-0003-2361-7364>  
 Antonio Laghezza  <http://orcid.org/0000-0001-6221-6155>  
 Luca Piemontese  <http://orcid.org/0000-0002-7980-5818>  
 Alessia Caradonna  <http://orcid.org/0000-0003-0072-8643>  
 Davide Capelli  <http://orcid.org/0000-0002-6716-3854>  
 Roberta Montanari  <http://orcid.org/0000-0002-7533-5425>  
 Giorgio Pochetti  <http://orcid.org/0000-0002-3980-3180>  
 Antonella Di Pizio  <http://orcid.org/0000-0002-8520-5165>

## References

1. Khokha R, Murthy A, Weiss A. Metalloproteinases and their natural inhibitors in inflammation and immunity. *Nat Rev Immunol* 2013;13:649–65.
2. Vandenbroucke RE, Libert C. Is there new hope for therapeutic matrix metalloproteinase inhibition? *Nat Rev Drug Discov* 2014;13:904–27.
3. Tauro M, Laghezza A, Loiodice F, et al. Arylamino methylene bisphosphonate derivatives as bone seeking matrix metalloproteinase inhibitors. *Bioorg Med Chem* 2013;21:6456–65.
4. Rubino MT, Agamennone M, Campestre C, et al. Biphenyl sulfonfylamino methyl bisphosphonic acids as inhibitors of matrix metalloproteinases and bone resorption. *ChemMedChem* 2011;6:1258–68.
5. Dufour A, Overall CM. Missing the target: matrix metalloproteinase antitargets in inflammation and cancer. *Trends Pharmacol Sci* 2013;34:233–42.
6. Tauro M, McGuire J, Lynch CC. New approaches to selectively target cancer-associated matrix metalloproteinase activity. *Cancer Metastasis Rev* 2014;33:1043–57.
7. Gupta A, Kaur CD, Jangdey M, Saraf S. Matrix metalloproteinase enzymes and their naturally derived inhibitors: novel targets in photocarcinoma therapy. *Ageing Res Rev* 2014;13:65–74.
8. Hwang KA, Yi BR, Choi KC. Molecular mechanisms and in vivo mouse models of skin aging associated with dermal matrix alterations. *Lab Anim Res* 2011;27:1–8.
9. Quan T, Qin Z, Xia W, et al. Matrix-degrading metalloproteinases in photoaging. *J Invest Dermatol Symp Proc* 2009;14:20–4.
10. Haar M, Gilchrist BA. Photoaging: mechanism, prevention and therapy. *Br J Dermatol* 2007;157:874–87.
11. Hsieh H-Y, Lee W-C, Senadi GC, et al. Discovery, synthetic methodology, and biological evaluation for anti-photoaging activity of bicyclic [1.2.3] triazoles: in vitro and in vivo studies. *J Med Chem* 2013;56:5422–35.
12. Ceccoli JD, Costello B, Hayward JA, Lahanas KM. Bath & Body Works Brand Management, Inc., USA, assignee. Topical compositions for inhibiting matrix metalloproteinases and providing antioxidative activities patent US20120058140A1; 2012.
13. Khan SB, Kong C-S, Kim J-A, Kim S-K. Protective effect of *Amphiroa dilatata* on ROS induced oxidative damage and MMP expressions in HT1080 cells. *Biotechnol Bioprocess Eng* 2010;15:191–8.
14. Gupta SK. Bioderm Research, Scottsdale, AZ, USA, assignee. Matrix metalloproteinase (MMP) inhibitors and their application in cosmetic and pharmaceutical composition patent US20060074108A1; 2006.
15. Yoon SO, Park SJ, Yoon SY, et al. Sustained production of H(2)O(2) activates pro-matrix metalloproteinase-2 through receptor tyrosine kinases/phosphatidylinositol 3-kinase/NF-kappa B pathway. *J Biol Chem* 2002;277:30271–82.
16. Rao BG. Recent developments in the design of specific Matrix Metalloproteinase inhibitors aided by structural and computational studies. *Curr Pharm Des* 2005;11:295–322.
17. Skiles JW, Gonnella NC, Jeng AY. The design, structure, and therapeutic application of matrix metalloproteinase inhibitors. *Curr Med Chem* 2001;8:425–74.
18. Campestre C, Agamennone M, Tauro M, Tortorella P. Phosphonate emerging zinc binding group in matrix metalloproteinase inhibitors. *Curr Drug Targets* 2015;16:1634–44.
19. Giustiniano M, Tortorella P, Agamennone M, et al. Amino acid derivatives as new zinc binding groups for the design of selective matrix metalloproteinase inhibitors. *J Amino Acids* 2013;178381, 12 p.
20. Agrawal A, Romero-Perez D, Jacobsen JA, et al. Zinc-binding groups modulate selective inhibition of MMPs. *ChemMedChem* 2008;3:812–20.
21. Jacobsen FE, Lewis JA, Cohen SM. The design of inhibitors for medicinally relevant metalloproteins. *ChemMedChem* 2007;2:152–71.
22. Campestre C, Agamennone M, Tortorella P, et al. N-Hydroxyurea as zinc binding group in matrix metalloproteinase inhibition: mode of binding in a complex with MMP-8. *Bioorg Med Chem Lett* 2006;16:20–4.
23. Yuan H, Lu W, Wang L, et al. Synthesis of derivatives of methyl rosmarinate and their inhibitory activities against matrix metalloproteinase-1 (MMP-1). *Eur J Med Chem* 2013;62:148–57.
24. Mahmood T, Akhtar N. Combined topical application of lotus and green tea improves facial skin surface parameters. *Rejuvenation Res* 2013;16:91–7.
25. Kim MS, Oh GH, Kim MJ, Hwang JK. Fucosterol inhibits matrix metalloproteinase expression and promotes type-1 procollagen production in UVB-induced HaCaT cells. *Photochem Photobiol* 2013;89:911–18.
26. Gweon EJ, Kim SJ. Resveratrol attenuates matrix metalloproteinase-9 and -2-regulated differentiation of HTB94 chondrosarcoma cells through the p38 kinase and JNK pathways. *Oncol Rep* 2014;32:71–8.
27. Kousidou OC, Mitropoulou TN, Roussidis AE, et al. Genistein suppresses the invasive potential of human breast cancer cells through transcriptional regulation of metalloproteinases and their tissue inhibitors. *Int J Oncol* 2005;26:1101–9.
28. Ricciarelli R, Maroni P, Ozer N, et al. Age-dependent increase of collagenase expression can be reduced by alpha-tocopherol via protein kinase C inhibition. *Free Radic Biol Med* 1999;27:729–37.
29. Alleva R, Tomasetti M, Sartini D, et al. alpha-Lipoic acid modulates extracellular matrix and angiogenesis gene expression in non-healing wounds treated with hyperbaric oxygen therapy. *Mol Med* 2008;14:175–83.
30. Rubino MT, Maggi D, Laghezza A, et al. Identification of novel matrix metalloproteinase inhibitors by screening of phenol fragments library. *Arch Pharm (Weinheim, Ger)* 2011;344:557–63.
31. Nicolotti O, Catto M, Giangreco I, et al. Design, synthesis and biological evaluation of 5-hydroxy, 5-substituted-pyrimidine-2,4,6-triones as potent inhibitors of gelatinases MMP-2 and MMP-9. *Eur J Med Chem* 2012;58:368–76.
32. Rubino MT, Agamennone M, Campestre C, et al. Synthesis, SAR, and biological evaluation of alpha-sulfonfylphosphonic acids as selective matrix metalloproteinase inhibitors. *ChemMedChem* 2009;4:352–62.
33. Biasone A, Tortorella P, Campestre C, et al. alpha-Biphenylsulfonfylamino 2-methylpropyl phosphonates: enantioselective synthesis and selective inhibition of MMPs. *Bioorg Med Chem* 2007;15:791–9.
34. Pochetti G, Gavuzzo E, Campestre C, et al. Structural insight into the stereoselective inhibition of MMP-8 by enantiomeric sulfonamide phosphonates. *J Med Chem* 2006;49:923–31.
35. Mishra KK, Pal RS, Arunkumar R, et al. Antioxidant properties of different edible mushroom species and increased bioconversion efficiency of *Pleurotus eryngii* using locally available casing materials. *Food Chem* 2013;138:1557–63.
36. Hummer G. Molecular binding: under water's influence. *Nat Chem* 2010;2:906–7.
37. LigPrep version 3.4, Maestro version 10.2, MacroModel, version 10.8, Phase version 4.3, Schrödinger, LLC, New York, NY; 2015.
38. Lauro G, Tortorella P, Bertamino A, et al. Structure-based design of microsomal prostaglandin E2 synthase-1 (mPGES-1) inhibitors using a virtual fragment growing optimization scheme. *ChemMedChem* 2016;11:612–19.
39. Mishra K, Ojha H, Chaudhury NK. Estimation of antiradical properties of antioxidants using DPPH[rad] assay: a critical review and results. *Food Chem* 2012;130:1036–43.
40. Sharma OP, Bhat TK. DPPH antioxidant assay revisited. *Food Chem* 2009;113:1202–5.
41. GraphPad Prism-5.0c: GraphPad Software Inc., San Diego, CA; 2009.
42. Batty TG, Kontogiannis L, Johnson O, et al. iMOSFLM: a new graphical interface for diffraction-image processing with MOSFLM. *Acta Crystallogr D Biol Crystallogr* 2011;67:271–81.
43. Navaza J. Amore – an automated package for molecular replacement. *Acta Cryst A* 1994;50:157–63.

44. Pochetti G, Montanari R, Gege C, et al. Extra binding region induced by non-zinc chelating inhibitors into the S1' subsite of matrix metalloproteinase 8 (MMP-8). *J Med Chem* 2009;52:1040-9.
45. Brunger AT, Adams PD, Clore GM, et al. Crystallography & NMR system: a new software suite for macromolecular structure determination. *Acta Crystallogr D Biol Crystallogr* 1998;54:905-21.
46. Rowsell S, Hawtin P, Minshull CA, et al. Crystal structure of human MMP9 in complex with a reverse hydroxamate inhibitor. *J Mol Biol* 2002;319:173-81.
47. Dhanaraj V, Williams MG, Ye QZ, et al. X-ray structure of gelatinase A catalytic domain complexed with a hydroxamate inhibitor. *Croat Chem Acta* 1999;72:575-91.

Supplementary material available online